TU
TECHNISCHE UNIVERSITÄT WIEN

Dissertation

Fast and radiation hard silicon detectors for the LHC-b Upgrade II

zur Erlangung des akademischen Grades
Doktor der technischen Wissenschaften im Fachbereich Physik

ausgeführt am
Atominstitut der TU Wien

in Zusammenarbeit mit
CERN

unter Betreuung von
Privatdoz. Dipl.Ing. Dr.techn. Christoph Schwanda

und
Dr. Heinrich Schindler (CERN)

durch
Dipl.Ing. Jakob Haimberger
Matr. Num.: 01325198

Gutachter: Prof. Dr. Lars Eklund (Uppsala University)

Dr. Michael Moll (CERN)

Wien, October 8, 2023

_____   _____
Jakob Haimberger   Christoph Schwanda

Abstract

High radiation tolerance will be a key prerequisite for the vertex detectors in future hadron-collider experiments such as the LHCb Upgrade II. It is therefore of utmost importance to understand the effects radiation has on the sensor performance and how they can be mitigated. The main scope of this thesis is the study of planar hybrid silicon sensors in the fluence range of the LHCb Upgrade II using measurements combined with TCAD simulations to understand the sensor behaviour at these fluences and provide possible detector scenarios for further radiation reduction.

Several test structures with a thickness of 50, 100, 200 and 300 µm respectively were produced and characterised before irradiation by IV and CV measurement. The results were compared to simulations and used to validate the used sensor model for further simulations. A comprehensive radiation campaign with proton and neutron irradiation was done covering a fluence range from 1×10^{15} n_{eq} cm^{-2} to 1×10^{17} n_{eq} cm^{-2}. After irradiation the change of leakage current and sensor signal was studied as a function of thickness and fluence. All measurements were compared to simulation using a state-of-the art radiation damage model.

In addition, a fast simulation tool was developed to study possible new detector layouts and validate their performance, in particular in terms of impact parameter resolution. Using this tool, alternative detector layouts were proposed, which would reduce the radiation damage of all sensors in the detector. An extensive discussion of the impact of the RF-foil on the impact parameter resolution of the detector is also presented.

Kurzfassung

Eine hohe Strahlungstoleranz wird eine entscheidende Voraussetzung für die Vertex-Detektoren in zukünftigen Hadronen-Beschleuniger-Experimenten wie dem LHCb Upgrade II sein. Daher ist es von größter Bedeutung, die Auswirkungen der Strahlung auf die Sensorleistung zu verstehen und zu ergründen, wie diese gemindert werden können. Der Hauptgegenstand dieser Arbeit ist die Untersuchung planarer Hybrid-Siliziumsensoren im Fluenzbereich des LHCb Upgrade II durch Verwendung von Messungen in Kombination mit TCAD-Simulationen. Diese Daten würedn dann genutzt um das Sensorverhalten bei diesen Fluenzen zu verstehen und mögliche Detektorszenarien für eine weitere Strahlungsreduzierung vorzuschlagen.

Es wurden mehrere Teststrukturen mit einer Dicke von jeweils 50, 100, 200 und 300 µm hergestellt und vor der Bestrahlung durch IV- und CV-Messung charakterisiert. Die Ergebnisse wurden mit Simulationen verglichen und zur Validierung des verwendeten Sensormodells für weitere Simulationen verwendet. Es wurde eine umfassende Strahlungskampagne mit Protonen- und Neutronenbestrahlung durchgeführt, die einen Fluenzbereich von 1×10^{15} n_{eq} cm^{-2} bis 1×10^{17} n_{eq} cm^{-2} abdeckte. Nach der Bestrahlung wurde die Änderung des Leckstroms und des Sensorsignals als Funktion von Dicke und Fluenz untersucht. Alle Messungen wurden mit Simulationen unter Verwendung eines Strahlungsschadensmodells verglichen.

Darüber hinaus wurde ein schnelles Simulationstool entwickelt, um mögliche neue Detektorlayouts zu untersuchen und deren Leistung, insbesondere im Hinblick auf die Auflösung des Stoßparameter, zu validieren. Mit diesem Tool wurden alternative Detektorlayouts vorgeschlagen, die den Strahlungsschaden aller Sensoren im Detektor reduzieren würden. Außerdem wird der Einfluss der RF-Folie auf die Auflösung des Stoßparameter des Detektors ausführlich erörtert.

Acknowledgements

I have to start here with an apology. A PhD is never easy and the frustration and loss of sleep made me not always the easiest person to work with. First of all I have to thank my parents and my brother, as without them, I probably would never made it until this point. Your help took a lot of my shoulders. Niki our talks on the phone were sometimes the closest I came to human contact I had during Covid pandemic and kept me sane. I would like to thank my university supervisor Christoph, who made sure that I was on time with all aspects of my thesis and prevented a lot of unnecessary stress for me. Another big thank has to go to my CERN supervisor Heinrich. I know it wasn't always easy with me, as you often had more faith in my work than I did. You were always there when I had some questions and kept my stubborn self in check. Paula, from the start you were always had an ear for me to voice my concern. Vagelis and Victor I have have to thank both of you for taught me important lessons for live. Efren and Andrea, the testbeams we did together were an experience I will never forget and probably will never experience again. Eloi, without you help with the measurements, I would have never been able to finished my PhD in time. Laurent I like to thank you for your help with my IP simulation results. I like to thank the SSD group at CERN, as they let me measure at their setup for weeks and without them I could not have done my PhD. I would like to thank Raphael for putting enough trust in me to let me have free access to his workshop. Jarl thank you for helping my two left hands with everything electrical. A special thanks has to go to Marius, as our discussion over any problem that came up and our frequent coffees kept me sane during my Phd. The countless hours we spent at work together were always fun.

Declaration

I declare that I have developed and written this thesis completely by myself, and have not used sources or means without declaration in the text. Any thoughts from others or literal quotations are clearly marked. This thesis was not used, in whole or in part, to achieve an academic degree.

Vienna, October 8, 2023

Jakob Haimberger

Der Konjunktiv ist die größte Erfindung der Menschheit.

Michael Köhlmeier

Table of contents

Introduction

1.1 The Standard Model

The Standard Model (SM) of particle physics is one of the greatest scientific achievements of the last century. Having been created in the 1970s and refined over the last decades, it has shown extreme accuracy and self-consistency in its predictions. Its main achievement is the explanation of three of the four elementary forces: electromagnetic, weak and strong interactions. Only the inclusion of the fourth elementary force, gravitation, is missing for the creation of a Grand Unified Theory. The SM describes the different properties of elementary particles and their interactions.

The elementary particles can be divided in two groups (see figure 1.1) according to the statistics applicable to them. Fermions follow Fermi-Dirac statistics, allowing no two particles in the same quantum state. For each fermion there exists an antiparticle with the same mass, but opposite additive quantum numbers. Fermions can be further subdivided into leptons and quarks and are organized in three families. Each particle has a counterpart in the other families with the same charge but different mass. Leptons are elementary particles with integer charge and can exist in an unbound state. Every family consists of a particle with charge -1 (for example the electron) and a charge 0 neutrino. Quarks on the other hand have either a charge of $-1/3$ or $+2/3$ and an additional property called color [1]. All quarks have to follow a rule called color confinement. It allows them to form bound states if the total color of the system is zero. This can be achieved by combining three quarks of different color or combining a quark and an anti-quark. As all non-elementary particles are made of a combination of different quarks, this limits the number of observable particles. Fermions may interact through the electromagnetic force, if they are charged, and weak force, with the latter allowing for transformation within the same particle family. Quarks additionally are bound together by the strong force [2].

Bosons on the other hand follow Bose-Einstein statistics, allowing for multiple particles in the same quantum state. Each boson corresponds to an excitation in a fundamental integer field, whereas fermions are excitations in half-integer fields. For vector fields, like the strong field, this leads to a spin 1 particle. For scalar fields like the Higgs field, the excitation results in a spin 0 particle. Currently, there are 12 known gauge bosons. Eight of them are gluons corresponding to the strong interaction. They act as mediators for color changing currents and obey the same confinement rules as the quarks. The photon corresponds to the electromagnetic interaction. It has neither charge nor mass, which in turn leads to the infinite range of the electromagnetic force. W^+, W^- and Z^0 are the only vector bosons with mass and there-
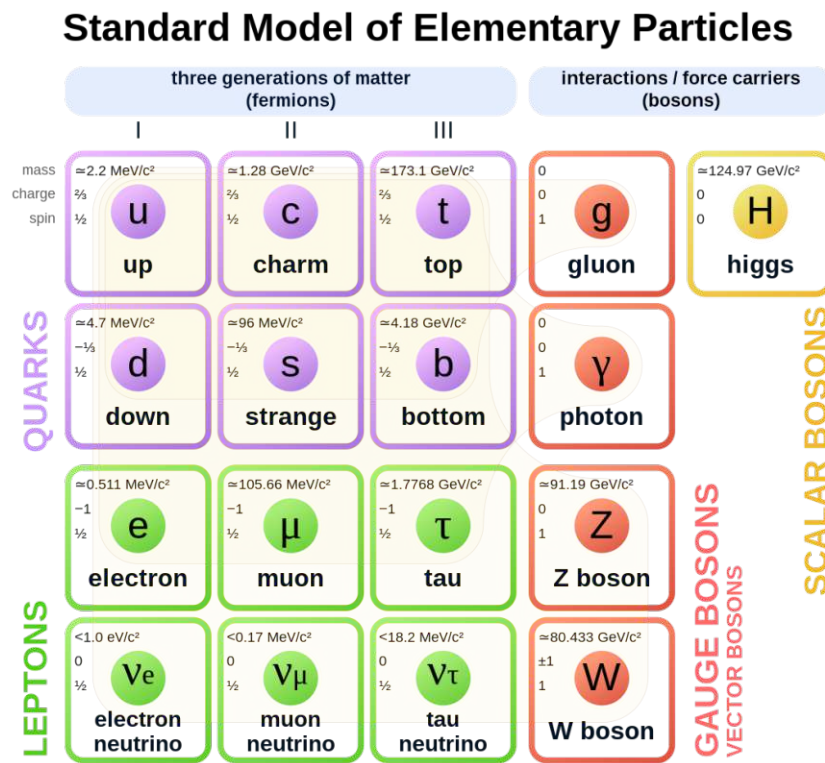
Standard Model of Elementary Particles

Fig. 1.1. Particles of the Standard Model. Reproduced from Ref. [3].

fore limit the effective range of the weak interaction. As W^+ and W^- are charged particles, they allow for the transformation into particles with different charges. The last particle is the Higgs boson, which is responsible for the mass of all particles [4].

As all-encompassing as the SM seems, there are still phenomena not explained within the model. Experimental results point to new forms of energy and matter, called dark energy and dark matter respectively, which do not fit in the current version of the standard model. Additionally, the non-zero mass of neutrinos leads to a chiral symmetry violation which cannot be explained by the standard model and is another indication for missing pieces inside the model [5]. Last but not least, the amount of Charge Parity (CP) violation incorporated in the SM is not sufficient to explain the imbalance between matter and anti-matter observed in the universe.

1.2 The Large Hadron Collider

The European Organization for Nuclear Research (CERN), located at the French-Swiss border on the outskirts of Geneva, was founded in 1953 [6] as a center for particle physics for Europe. Growing slowly over time, additional accelerator stages were introduced to achieve collision energies unreachable before. In this process every upgrade often profited from existing infrastructure as previously built accelerators were reused as injectors for the final stage.

The current complex can be seen in figure 1.2. The last accelerator in the chain is the Large
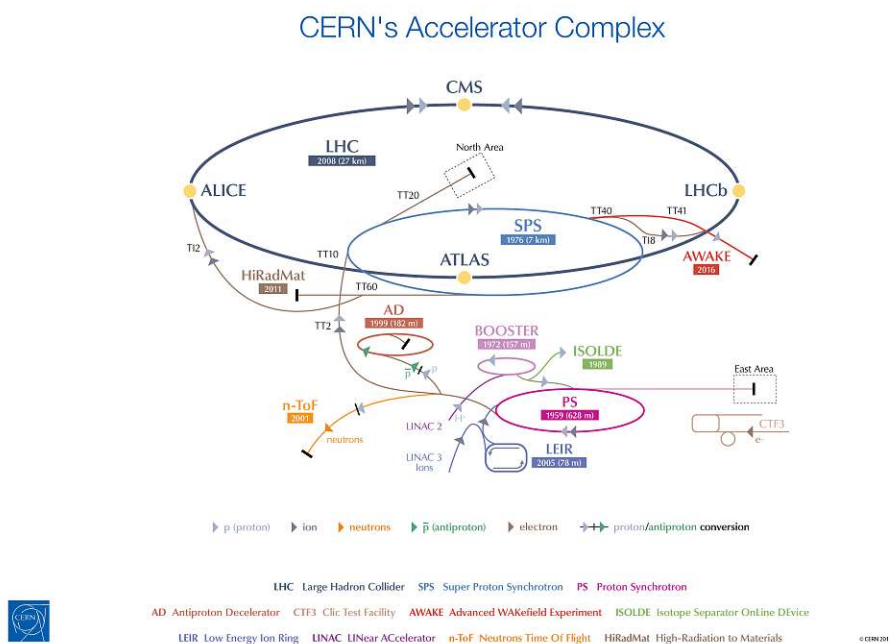

Fig. 1.2. CERN accelerator complex. Reproduced from Ref. [7].

Hadron Collider (LHC). It is a synchrotron with a total length of 26.7 km located between 45 to 170 m below ground level [8]. It is used to accelerate protons up to an energy of 6.8 TeV, but some of its run time is also dedicated to the collision of lead ions. For proton-proton collisions, the acceleration cycle starts by removing the outer electron from hydrogen atoms, supplied by bottles of hydrogen gas, producing the protons needed for acceleration. These are subsequently accelerated up to 140 MeV by a linear accelerator, the Linear Accelerator 4 (LINAC4) [9]. This step is followed by three stages of acceleration in synchrotrons. In the first stage, the protons are accelerated up to 1.4 GeV in the Proton Synchrotron Booster (PSB). When the particles reach their final energy they get injected into the Proton Synchrotron (PS), where they reach 25 GeV. The Super Proton Synchrotron (SPS) is the final stage before the particles get injected to the LHC, reaching particle energies of 450 GeV. To achieve a final center-of-mass energy of 13.6 TeV the protons need to be accelerated in opposite directions before the collision. Therefore two injection points at the LHC exist, where the particles can be inserted into one of two separated vacuum tubes where two beams circulate in opposite directions simultaneously. The particles are accelerated by 16 Radio Frequency (RF) cavities. Each beam has eight cavities, each delivering 2 MV at a frequency of 400 MHz. All cavities are located at a single location along the beam. To keep the charged particles on their track, 1232 superconducting dipole magnets are located around the accelerator. Due to the nature of the acceleration, particles are separated in bunches with varying spacing and intensity depending on the stage of the acceleration. To focus the particles inside the bunches both in momentum and space another 392 quadrupole magnets are used. Due to the frequency of 40.8 MHz of the RF cavities up to 3564 bunches are possible. For practical/technical reasons,

for example the time needed to adjust the kicker magnets, only 2808 bunches can be filled. The collection of bunches in the LHC are called fills. The bunches are organized in trains, with each train containing 72 bunches. Each bunch in a train is around 1 ns long and has a spacing of 25 ns to the next bunch. In the nominal design a bunch itself consists of 1.15×10^{11} protons [8] [10]. Spacing is a critical parameter for the experiments as it defines the maximal possible event rate. The tunnel for the LHC was constructed earlier for its predecessor the Large Electron Positron Collider (LEP). It has eight long straight sections where the two beam lines could cross. At four of these the four main experiments (ALICE[11], ATLAS[12], CMS[13] and LHCb[14]) are located.

An important parameter for the experiments is the *luminosity*. The instantaneous luminosity $\mathcal{L}$ describes the particle collision rate at a given collision point. For a collision of two Gaussian shaped beams it can be calculated as

$$\mathcal{L} = \frac{N_1 N_2 f}{4\pi \sigma_x \sigma_y} S, \tag{1.1}$$

with N_1 and N_2 representing the respective number of particles per bunch for two colliding beams, f the frequency of colliding bunches, σ_x and σ_y the size of the beams in x and y and S the luminosity reduction factor. The luminosity reduction factor originates from different effects, like non-zero crossing angles, which reduce the overall luminosity compared to a head-on scenario.

The integrated luminosity is, as the name implies, the integral of the instantaneous luminosity over a certain time interval. If the cross-section σ of a certain interaction is known, the integrated luminosity L can be used to calculate the number of interactions N expected in a given time interval with

$$N = L\sigma. \tag{1.2}$$

A commonly used unit for the integrated luminosity is $1\,\text{fb}^{-1} = 10^{39}\text{cm}^{-2}$. During Run 2 a maximal instantaneous luminosity of $2 \times 10^{34}\text{cm}^{-2}\,\text{s}^{-1}$ has been achieved at the LHC (figure 1.3). Another quantity closely related to the luminosity is the average number of visible interactions μ per bunch crossing.

The operation time of the LHC is divided into runs, technical stops (TS) and long shutdowns (LS). As the name suggests, during long shutdowns the operation of the accelerator is stopped to allow for repair or upgrades of the accelerator complex and/or the experiments. During runs the accelerators operate normally and the experiments are taking data. After every year of operation the accelerator is stopped for around 14 weeks, to allow access to the experiments and the accelerator (Year End Technical Stop). At the start of 2022, the second long shutdown (LS2) ended and a four-year period of operation (Run 3) started. The time table
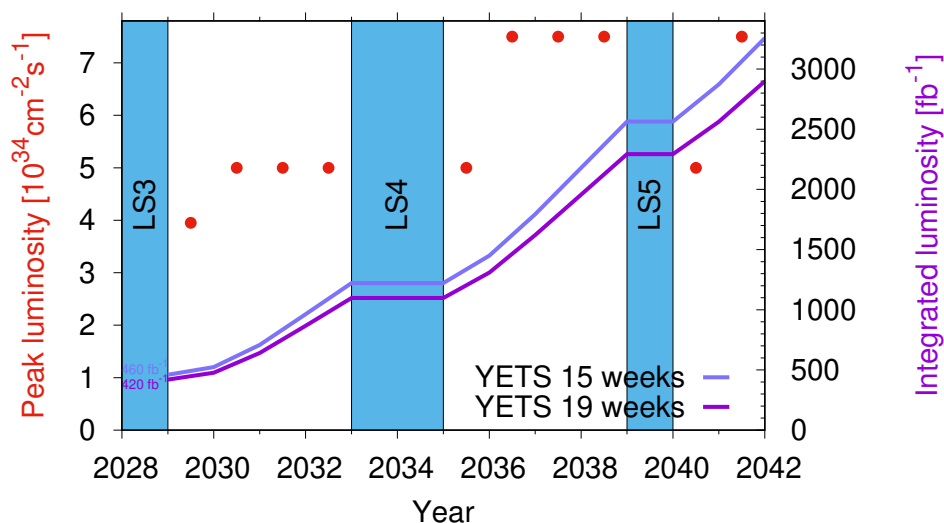
Fig. 1.3. Luminosity scenarios for ATLAS and CMS. Reproduced from Ref. [15].

after Run 3 can be seen in figure 1.3.

After Run 3 of the LHC, ATLAS and CMS will have collected a total of over $300\,\mathrm{fb}^{-1}$ integrated luminosity. At the same instantaneous luminosity, the experiments would have to take data for another 12 years beyond that point to achieve a meaningful increase in statistics, i.e. doubling the data sample. It was therefore decided to upgrade the LHC to achieve even higher luminosities. This upgrade, called the High Luminosity LHC upgrade, will take place during the Long Shutdown 3, while small changes have already been implemented during the Long Shutdown 2. The goal is to achieve an instantaneous luminosity of $5 \times 10^{34}\ \mathrm{cm}^{-2}\,\mathrm{s}^{-1}$ with a potential peak value of $2 \times 10^{35}\ \mathrm{cm}^{-2}\,\mathrm{s}^{-1}$ at the beginning of fills. This would deliver $250\,\mathrm{fb}^{-1}$ per year, collecting nearly the same amount of data per year as has been collected before in total ($300\,\mathrm{fb}^{-1}$) [16, 17].

6

Silicon detectors

2

Silicon detectors play a major role in particle detection. Their high density leads to a high energy loss per traversed distance, which in turn allows for high signals with relatively thin detectors. Due to using the same technology, they allow for an easy integration with the read-out electronics and detector sizes in the micrometer range. They are commonly used for tracking detectors, but also find application in other detectors like sampling calorimeters. In the following chapter a short introduction in their operation principle and the interaction of particle with them is given.

2.1 Particle interaction with matter

The mechanisms with which a particle can interact with a detector depend on the type of particle and its energy. For photons at low energies (above the UV range), the ejection of a bound electron through photoabsorption is the dominant effect. In the MeV energy range the most probable photon interaction is Compton scattering. Here only a part of the photon energy is transferred to an electron from an outer orbital. At high energies the dominant photon interaction is the creation of an electron-positron pair near a nucleus.

Except at high energies, charged particles lose energy predominantly through inelastic scattering with the atomic electrons of the material they traverse. The mean energy loss per unit length of a charged particle can be calculated by the Bethe-Bloch formula [18]

$$-\left\langle \frac{dE}{dx} \right\rangle = \frac{KZz^2\rho}{A\beta^2} \left[\frac{1}{2} ln \left(\frac{2m_ec^2\beta^2\gamma^2T_{max}}{I^2} \right) - \beta^2 - \frac{\delta(\beta\gamma)}{2} - \frac{C(\beta\gamma,I)}{Z} \right] \tag{2.1}$$

and

$$K = 4\pi N_A r_e^2 m_e c^2, \tag{2.2}$$

with N_A being the Avogadro constant, r_e the electron radius, γ the Lorenz factor and c the speed of light, z and β being the charge and the velocity of the particle, and Z and A the atomic number and the atomic mass number of the medium. I is the mean ionization energy and T_{max} is the maximal transferable energy onto a bound electron. The term δ is the density correction, which accounts for the saturation of the energy loss at high energy, while the term containing $\frac{C(\beta\gamma,I)}{Z}$ includes effects at low momenta. As can be seen from figure 2.1 the stopping power has a minimum around $\beta\gamma = 3$. Particles in this range of momentum are called Minimum Ionizing Particles (MIP) and play a key part in detector design, as they produce the smallest signal.
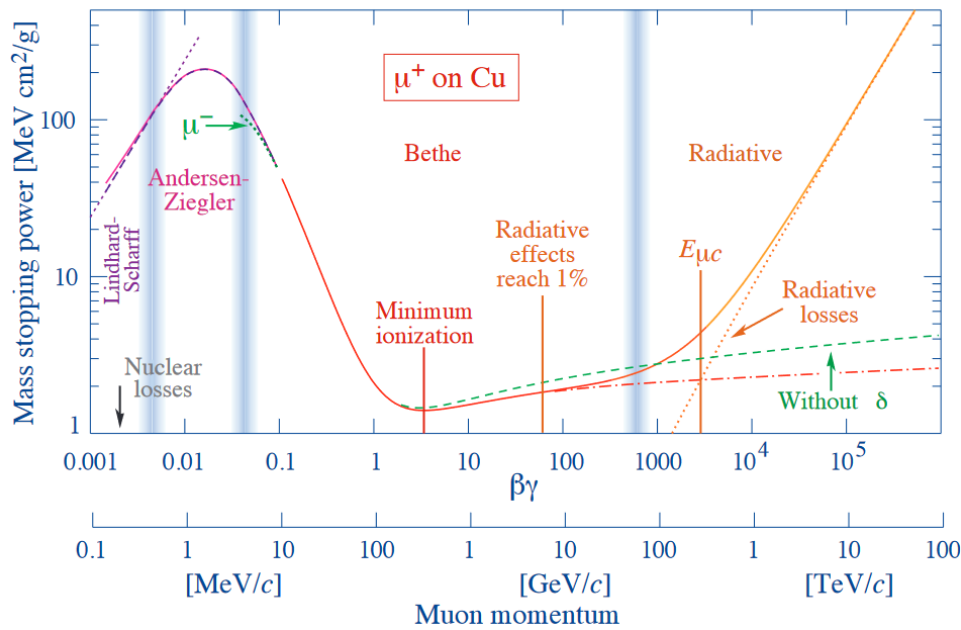
7

Fig. 2.1. Mean energy loss for positive muons in copper as a function of the muon momentum. Figure reproduced from Ref [18].

Due to the statistical nature of the interactions, the energy loss of a charged particle in a layer of material is subject to fluctuations. For thin layers, the energy loss distribution can be described by the convolution of a Gaussian and a Landau distribution [19]. The Landau distribution is asymmetric with a long tail at high energies. Due to the asymmetry the mathematical mean does not correspond to the most probable value. For most detector applications, the most probable value is a more relevant quantity than the mean energy loss. Figure 2.2 shows the scaled energy loss distribution for different target thicknesses. Part of the energy deposited by the charged particle is converted into ionisation. For silicon, the average energy loss to produce an electron-hole pair is 3.6 eV. In a 300 μm thick sensor, the most probable value of the charge deposition spectrum is 24 000 electrons (80 e/h pairs per μm). For a 50 μm thick sensor, the most probably value corresponds to 66 e/h pairs per μm [20]. It is also visible that at high energies the Bethe-Bloch formula underestimates the energy loss. This is due to Bremsstrahlung becoming relevant in this region. It describes the energy loss due to acceleration of a charged particle in the electric field of the nucleus or the atomic electrons. As this process is proportional to $\frac{1}{m^2}$ it is more relevant for light particles like electrons. A parameter describing the energy loss by Bremsstrahlung is the radiation length X_0. It describes the average length a particle has to traverse in a material until it reaches $1/e$ of its initial energy due to bremsstrahlung losses.

Multiple scattering of a charged particle in the Coulomb field of the nuclei leads to a deviation from its initial path (see figure 2.3) [22]. As the actual deviation is a statistical process, the final scattering angle probability (the deviation from its original direction) after traversing a material can be approximated by a Gaussian distribution with the σ_θ given by the "Highland-
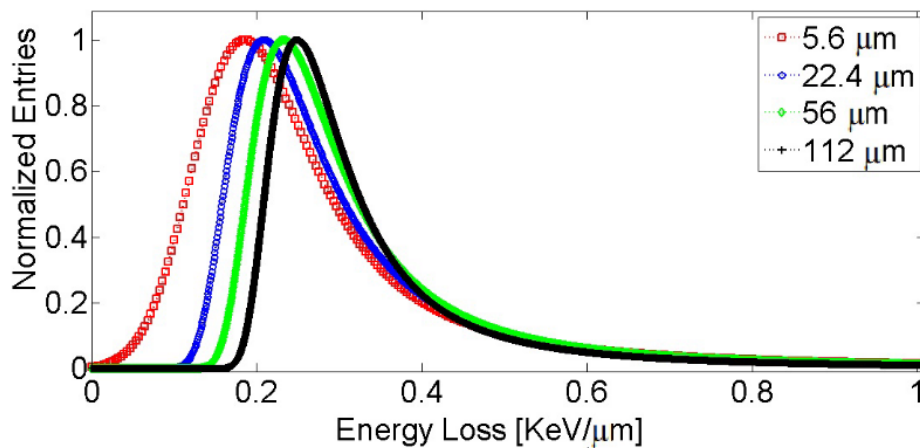
Fig. 2.2. Energy loss per μm for 12 GeV c^{-1} protons in sensors of different thicknesses. Figure reproduced from Ref [21].

Formula" [23]

$$\sigma_\theta = \frac{13.6\text{MeV/c}}{\beta p} z \sqrt{\frac{x}{X_0}} \left(1 + 0.038 ln \frac{x}{X_0}\right), \tag{2.3}$$

with p representing the momentum of the incoming particle, x the thickness of the scatterer and X_0 the radiation length of the material. Using this parameter the offset of the particle track y_{plane} can be calculated with

$$\langle y_{\text{plane}} \rangle = \frac{1}{\sqrt{3}} x \sigma_\theta. \tag{2.4}$$

Traversing particles not only generate a signal in the detector, but can also damage it over
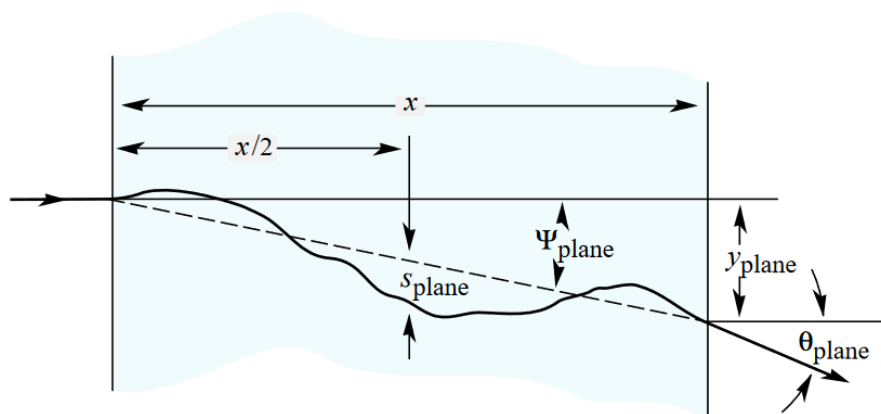

Fig. 2.3. Illustration of the change in path of a particle after traversing a scatterer. Figure reproduced from Ref. [18].

time. Bulk damage in silicon is mostly due to non-ionising energy loss by hadrons and is often parametrized as a function of 1 MeV neutron-equivalent (n_{eq}) fluence. A detailed explanation of radiation induced damage can be found in chapter 2.4.
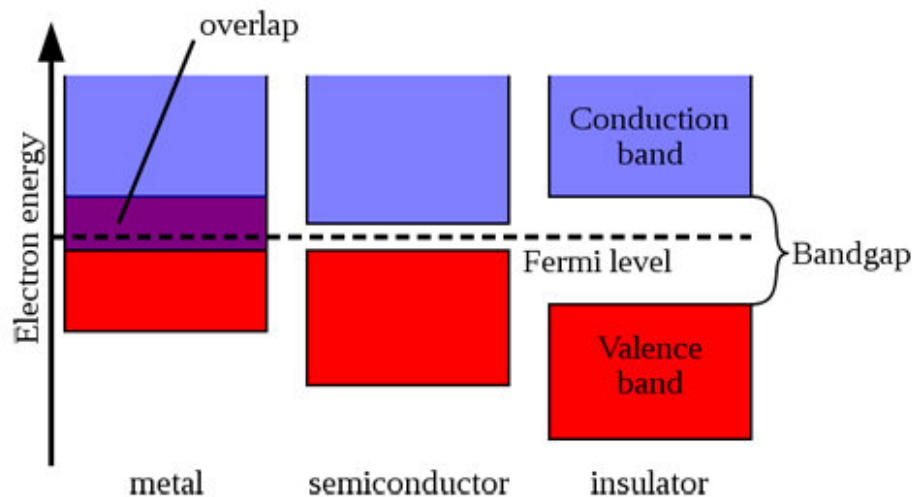
Fig. 2.4. Illustration of the band gap differences between isolators, metals and semiconductors. Figure reproduced from Ref. [24].

2.2 Band structure & pn-junction

When atoms form a solid they can either form a crystalline or amorphous structure. The difference lies hereby in the relative position of the atoms inside the solid to each other. In crystalline structures every atom has a well defined position in regard to all other atoms, whereas in an amorphous structure the positions follow a probability distribution. Crystalline materials are widely used in particle detection as they can be manipulated to change their characteristics and make them suitable for particle detection.

In a single atom the electrons have sharply defined energy levels. If several atoms are brought closer together, for example in a crystal lattice, these electrons start to interact with the electrons of other atoms. Through this interaction the energy levels start to split into several different levels around the initial energy level. If the density of these levels is high enough, they form a band of possible energies states. These bands can be separated by a region of zero state-density called a band gap. As size of the gaps and bands depends on the interaction of the atoms and therefore on their distance to each other they change with temperature due to the change in the inter-atomic distance. The band with the highest energy that still is filled with electrons at 0 K is called valence band. The next highest band is called conduction band. Depending on the band gap between the valence and conduction band a crystal can be classified as a metal, semiconductor or insulator (see figure 2.4)[22].

In insulators the band gap is big enough that no electron can be excited from the valence band into the conduction band under normal operation conditions. As all states are occupied by electrons in the valence band no free states are available for electrons to travel under the influence of an electrical field, prohibiting the flow of current.

In metals the two bands overlap or the states in the conduction band are partly occupied, hence allowing for the movement of charge through accessible free states.

In semiconductors the band gap is small enough that electrons can be excited to the conduction band by external electrical fields or thermal excitation. Here the concept of holes has to be introduced. If an electron moves from the valence band to the conduction band, it leaves behind a free state, which in turn allows the movement of electrons in the valence band. This collective movement of the electrons in the valence band is equivalent to a free state moving under an applied electrical field, similar to an electron, but in opposite direction. These states are called holes and can be treated like a particle similar to an electron with a positive charge. In a pure material the amount of electrons and holes is the same, but due to their different mobility, they do not contribute equally to the generated current. A typical example of a semiconductor is silicon, which is commonly used due its abundance. Its four outer electrons form four covalent bonds and create a diamond-like crystal structure. The band gap refers to the distance between the highest level of the valence band and the lowest of the conduction band. If they are located at the same momentum the band gap is called direct. If this is not the case it is called indirect and a phonon with the correct wave vector is needed to excite a electron. Silicon has an indirect band gap of 1.12 eV.

To know the conductive properties of a semiconductor the intrinsic free carrier concentrations n_i needs to be calculated. For this the number of states in the conduction band needs to be determined by integrating the density of states $Z(E)$ and the occupation probability of these states $f(E)$ from the lowest energy of the conduction band to its maximum using

$$n_i = \int_{E_{\min}}^{E_{\max}} Z(E)f(E)dE, \tag{2.5}$$

with the density of states being

$$Z(E)\,dE = 4\pi \left(\frac{2m_{\mathrm{eff}}}{h^2} \right)^{\frac{3}{2}} \sqrt{E}dE, \tag{2.6}$$

where m_{eff} is the effective mass, which reflects the reduced mobility of a carrier in the lattice and can be calculated from the energy-momentum relation of the carrier in the crystal. The occupation probabilities f_e, f_h for electrons and holes are given by the Fermi-Dirac distribution

$$f_e(E) = \frac{1}{e^{\frac{E-E_f}{k_b T}} + 1} \tag{2.7}$$

and

$$f_h(E) = \frac{1}{e^{\frac{E_f-E}{k_b T}} + 1}, \tag{2.8}$$

where T stands for the absolute temperature of the crystal, k_b for the Boltzmann constant and E_f for the Fermi-level. The Fermi-level is the energy at which the occupation probability is

50% for T > 0 K. At 0 K all states below this level are fully occupied and all above are empty. For intrinsic (not polluted by other elements) semiconductors it lies exactly in the middle of the band gap. Under the assumption $E - E_f \gg k_b T$, which is valid for a Fermi-level close to the middle of the band gap, the electron concentration n in the conduction band can be calculated

$$n = 2 \left(\frac{m_{\mathrm{eff,e}} k_b T}{2\pi\hbar^2} \right)^{\frac{3}{2}} e^{-\frac{E_L - E_f}{k_b T}} = N_L e^{-\frac{E_C - E_f}{k_b T}} \tag{2.9}$$

the hole concentration p in the valence band with

$$p = 2 \left(\frac{m_{\mathrm{eff,p}} k_b T}{2\pi\hbar^2} \right)^{\frac{3}{2}} e^{-\frac{E_f - E_V}{k_b T}} = N_V e^{-\frac{E_f - E_V}{k_b T}}, \tag{2.10}$$

with E_V being the highest energy of the valence band and E_C the lowest energy in the conduction band. N_V and N_C stand for the effective state density of the valence and conduction band, respectively. In the thermal equilibrium the product of the hole and electron concentration is constant leading to

$$np = n_i^2 = N_V N_C e^{-\frac{E_L - E_V}{k_b T}}. \tag{2.11}$$

For an intrinsic silicon semiconductor this results in a free carrier density of $1.01 \times 10^{10} \mathrm{cm}^{-3}$ at 300 K . It can be also seen that the carrier concentration does not depend on the Fermi-level and only on the band gap and the temperature.

The properties of a semiconductor can be changed by the introduction of impurities into the crystal. The impurities create new energy states in the band gap leading to a different electrical behaviour. This process is called doping. Depending on the element introduced, two types of doping can be defined: n- and p-doping. For n-doping, elements with more electrons in the outer shell than the semiconductor are used (see figure 2.5). For silicon this would be for example phosphorus or arsenic. This results in one or more unbound electrons, introducing a state close to the conduction band. The created states are called donor states. These states allow for an easy excitation of electrons from them to the conduction band, hence the number of free carriers and the conductivity increase. For p-doping elements with less outer electrons than the primary element are used (see figure 2.5), for example boron in the case of silicon. It creates empty states close to the valence band and increases therefore the number of holes. These states are called acceptors. As doping increases only the concentration of a single carrier type the concentration of the other decreases due to recombination. The carrier with the higher concentration becomes then the majority carrier, contributing relatively more to the conductivity, and the other becomes the minority carrier. In all cases the doping results in a movement of the Fermi-level closer to the introduced energy level.

 If two differently doped regions are brought in contact they form a diode, with the interface called pn-junction. Due to different carrier concentration in the regions the carriers start to
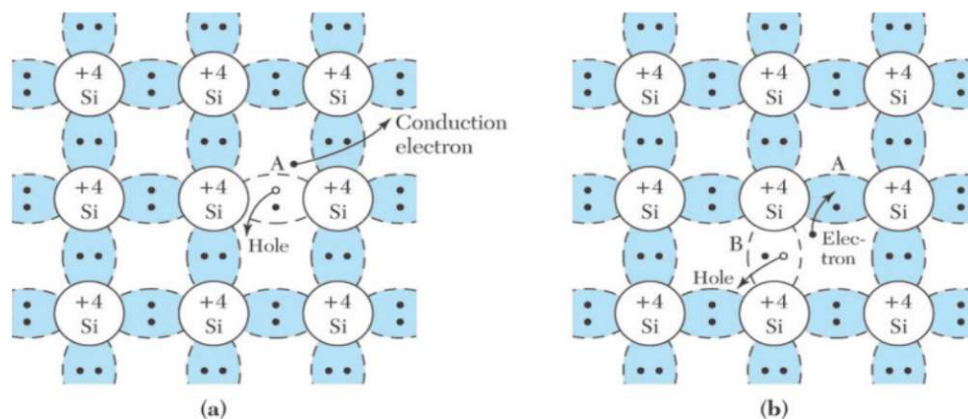
Fig. 2.5. Sketch of the bonding in (a) n-doped and (b) p-doped silicon. Reproduced from Ref. [25].

diffuse into the other region and start to recombine with each other. This leads to the previously neutral regions to develop a space charge due to the left behind ions. For the n-doped region this leads to a positive space charge, whereas the p-doped region becomes negatively charged (see figure 2.6). This charged region is called depleted region or space charge region. As as result an intrinsic electric potential (U_{diff}) is formed between the two sides of the pn-junction. The resulting electric field has its maximum at the interface of the doped regions and is oriented in the opposite direction of the diffusion current. The diffusion will hereby extend the space charge region until the diffusion current reaches an equilibrium with the current originating from the electric field. If the doping concentration in the two regions is not the same, as is the case for most semiconductors used for particle detectors, the depleted region will extend further into the zone of the lower concentration N_{low} to compensate the charge in the highly doped region. The depletion depth in the lower concentration region can be calculated with

$$d = \sqrt{\frac{2\epsilon\epsilon_0 U_{\text{diff}}}{qN_{\text{low}}}}. \tag{2.12}$$

If now an external bias voltage is applied, the size of the depletion zone changes, depending on the polarity and value of the applied voltage. If a positive voltage is applied to the p-side (forward bias) the diffusion potential is compensated and the depletion zone shrinks. If a positive bias is applied to the n-side the applied voltage has the same polarity as the diffusion current and the depletion region is increased. For particle detection the pn-junction is operated in reverse bias as the applied field allows the separation of generated electron hole pairs in the depleted region before they can recombine. Another positive effect is that the current flowing through the detector only originates from thermal excitations in the depletion region and if the detector is fully depleted further increase in bias voltages leads to an increase in electric field , but not in an increase in current. A diode has to be therefore operated at voltages where the full detector is depleted. Under the assumption that the diffusion voltage is much lower than the bias voltage, the voltage where a sensor of thickness d is fully depleted
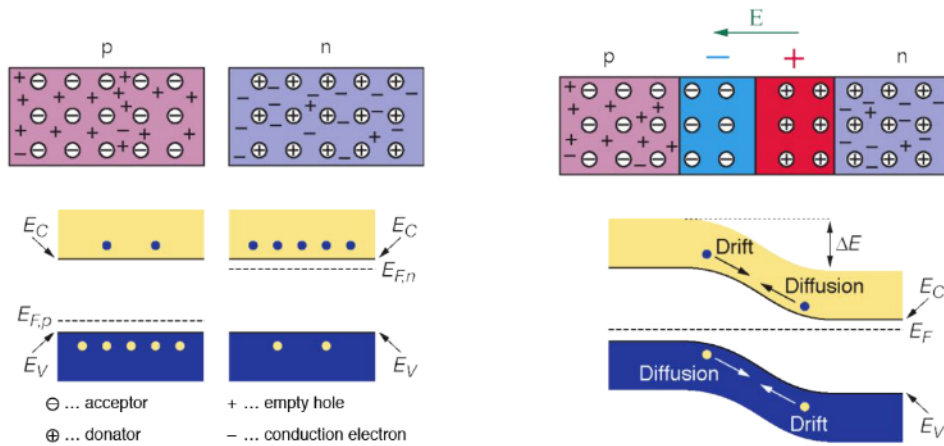
Fig. 2.6. Sketch of the energy levels and space charge of a n- and p-type doped region before and after they are brought into contact. Reproduced from Ref. [26].

can be calculated with

$$V_{dep} = \frac{qN}{2\epsilon\epsilon_0}d^2 \tag{2.13}$$

Due to the lack of free charge carriers in the depletion zone, a depleted diode can also be approximated as parallel plate capacitor, with the depletion region working as the dielectric. Using equation 2.13 we can then calculate the capacitance of a diode with an area A with

$$C = A\sqrt{\frac{\epsilon\epsilon_0 qN}{2U_{\text{bias}}}} \tag{2.14}$$

This equation only describes the capacitance until full depletion, as after, due to no possible further growth of the space charge region, the capacitance stays constant. Capacitance measurements are therefore a good tool to determine the depletion voltage.

2.2.1 Planar silicon sensors

Most silicon detectors are operated as diodes. They are called planar if the electrodes are parallel to the sensor surface A typical cross section of a planar silicon sensor can be found in figure 2.7. The biasing of and readout of the devices is done by applying a thin metal film on both sides of the diode, which work as the electrical contacts of the device. For the readout two types are possible, AC- and DC-coupled. In DC-coupled devices the readout electrode is in direct contact with the highly doped silicon implant and the generated charge can be evacuated directly by the electrode. In AC-coupled devices a thin insulation layer is applied between the electrode and the implant allowing the electrode to capacitively couple to the implant. To ensure a good electrical contact between the implant of the electrode and the metal a high implant concentration (in the order of 10^{19}cm^{-3} compared to 10^{12}cm^{-3} in the bulk) is used. This reduces the potential barrier between the metal and the bulk material and ensures an Ohmic contact. On the surface area where no electrode is present a layer of SiO_2

is grown to passivate the sensors.

To prevent large leakage currents originating from mechanical damage at the edge of the sensor and to contain the lateral spread of the depletion region guardrings are implemented around the active area. They can be either biased at the same potential to have a better control of the depleted volume or left floating. An example of a diode with several floating guardrings can be seen in figure 2.7.
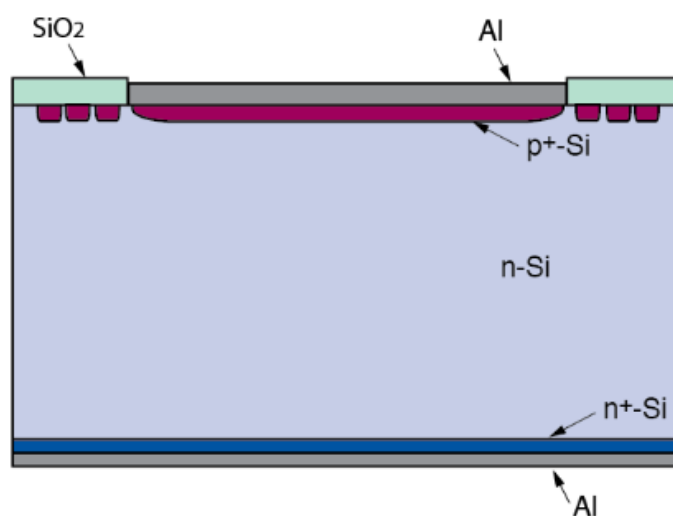

Fig. 2.7. Sketch of a planar silicon detector with 3 floating guard rings on each side of the readout electrode. Reproduced from Ref. [26].

Sensors that use the diode principle can be grouped in different types depending on the junction at the readout electrode. The nomenclature for the different types is x-on-y, where x stands for the type of doping at the readout electrode and y for the doping of bulk. For example, an n-on-p sensor has an n-type doped electrode in a p-doped bulk. As the pn-junction can also be located at the backside electrode used for biasing n-on-n or p-on-p sensors are possible. The doping of the electrode defines hereby in all cases the type of carrier collected.

For n-on-p another problem arises. This is due to the oxide that is used to separate the readout electrodes in segmented devices. During its growth it develops positively charged traps at the interface to the bulk. This leads to the accumulation of electrons at the interface with the bulk. The electron layer then shorts the different n-type electrodes together, creating a single electrode. To prevent this from happening, these sensors have an additional p-doping in the region between the readout electrodes. This is done either as a p-spray or p-stop. A p-spray is a uniform doping along the whole region with a concentration slightly above the expected electron layer concentration. A p-stop is a narrow but highly p-doped region between the electrodes. The difference to a p-spray is hereby the higher concentration and the fact that

the doping profile of the p-stop does not reach the electrode implant.

Silicon detectors are often used as position-sensitive devices. For this the readout electrode needs to be segmented. This can be either done in one dimension (strip) or in two (pixel). In the absence of charge sharing, the resolution of a detector with an electrode width p is given by the binary resolution calculated with

$$\sigma_{bin} = \frac{p}{\sqrt{12}}.$$ (2.15)

If the signal induced by a charged particle is shared between multiple electrodes and if other information, like the deposited charge, is available this can be improved further. Pixelated sensors are further divided in monolithic and hybrid sensors. In monolithic sensors the sensor and the readout electronic are constructed from a single wafer. In a hybrid sensor the sensor is soldered to a readout chip via small conductive balls, called bump bonds. This allows the separate development of the sensor and the readout.

2.2.2 Signal formation

The current induced on a readout electrode by a moving charge q with velocity v can be calculated using the Ramo-Shockley theorem [27]

$$i = qE_w\left(x\right)v,$$ (2.16)

where E_w is the weighting field. For a fully depleted sensor, the weighting field can be calculated by applying 1 V to the readout electrode and 0 V to the other electrodes. The weighting field is independent of the actual bias voltages and depends only on the geometrical layout of the detector. For an unsegmented pad sensor the weighting field is uniform. If the electrode size is small compared to the thickness of the device the weighting field becomes concentrated around the electrode, hence only charges reaching this region contribute meaningfully to the signal (see figure 2.8). As this effect increases with decreasing electrode size this becomes more prevalent when the detector is segmented like a strip or pixel detector.

2.3 Other detector designs

2.3.1 LGAD

Low Gain Avalanche Diodes(LGAD)[29] implement an additional doping lower below the doping layer of the readout electrode. This layer is of the same type as the bulk in the order of 10^{16} atoms cm^{-3}. This allows for a controlled impact ionization close to the readout electrode even at low bias voltages and a resulting internal gain. This allows to make LGADs to be
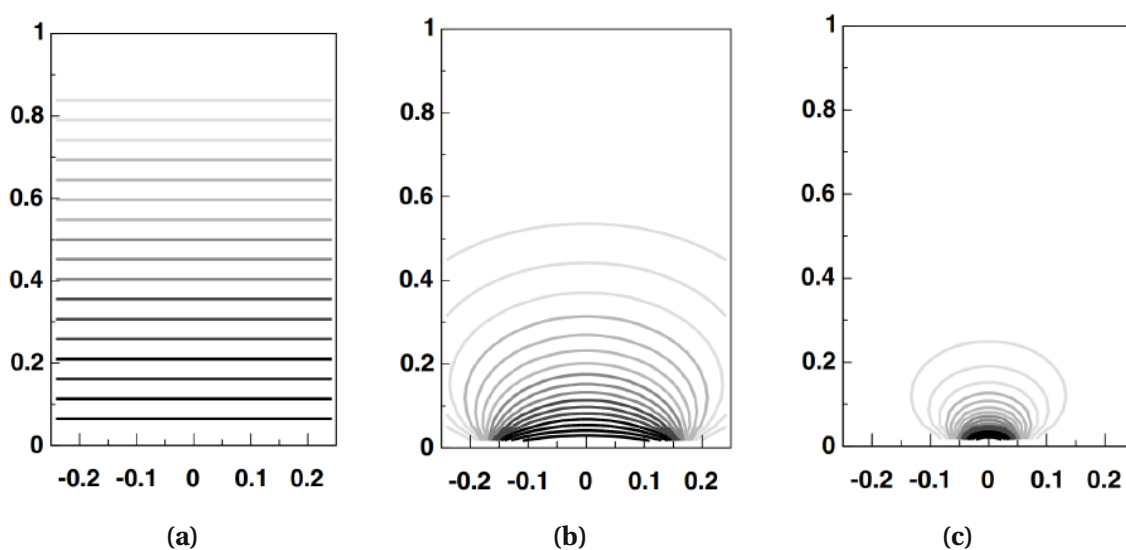
Fig. 2.8. Weighting fields for different electrode configurations: (**a**) parallel plate condensation (**b**) electrode size 1/3 of the sensor thickness (**c**) electrode size 1/10 of the sensor thickness. Reproduced from Ref. [28]

substantial thinner than normal diodes with similar signal heights reducing the material contribution of the sensor. Due to the high electrical field LGADs also achieve a time resolution in the region of 20 ps [30]. To increase the breakdown voltages of LGADs additional junction termination extensions (JTE)[31] are needed at the edge of the readout implant. As these regions are not collecting signals, the lead to an increased geometrical inefficiency, which becomes more critical for small pixel sizes.

2.3.2 3D sensors

In 3D sensors [32] the backside and readout are implemented by pillars which are perpendicular to the sensor surface. This allows to place them closer than in planar sensors. The advantage of this is that the sensor is depleted at relatively low bias voltages and the short drift distance leads to a good time resolution and radiation hardness. As the sensor thickness does not impact the timing and depletion anymore, it can be tuned independently to ensure a high enough deposited charge per traversing particle.

2.3.3 MAPS

In Monolithic Active Pixel Sensors (MAPS) the first stage of the readout electronics is included in the sensor wafer via CMOS processes [33]. As a result the noise until the first amplification stage is kept low as the bump-bonds are the main contributor in hybrid detectors. The CMOS technology makes also pixel sizes in the order of 20 µm possible. Their main drawback is their reliance on charge diffusion for signal collection. This results in a time resolution in the order

of ns.

2.4 Irradiation damage

Over time, the cumulative damage introduced by particles interacting with a detector can lead to significant performance changes. There are two main processes for radiation to interact with a detector. Non-ionizing interactions displace atoms from their crystal lattice positions, whereas ionization leads to the creation of electron/hole pairs [22]. When an atom is knocked-out of its position, due to non-ionizing damage, it creates a Frenkel-pair consisting of a vacancy and an interstitial atom (see figure 2.9). If the displaced atom is a dopant, it is removed from its electrically active lattice position and does therefore not contribute the doping. The vacancies and interstitials can interact to form new defects, for example divacancies by combining two vacancies, or with impurity atoms which then can be integrated into the lattice and change the electrical properties. All of these effects are called point defects. Some of the defects can heal out over time due to diffusion, most defects reach a stable state, which has to be treated to healing out.

The energy to create a Frenkel-pair in silicon is 25 eV [34]. If the energy transfer during the collision is higher than this threshold, the created interstitial can displace further atoms until its energy is lower than the threshold. This leads to a cascade of point defects along the particle track with a region of dense point defects at the end of the particle track. A conglomeration of point defects is called a cluster. The relation between the creation of point defects and clusters depends on the radiation energy and the type of particle used for irradiation. Due to additional possibility of coulomb scattering of charged particles, like protons, their mean transferred energy is much lower compared to neutrons. This leads to more clusters being produced in neutron irradiation compared to proton irradiation at the same particle energies and fluxes.
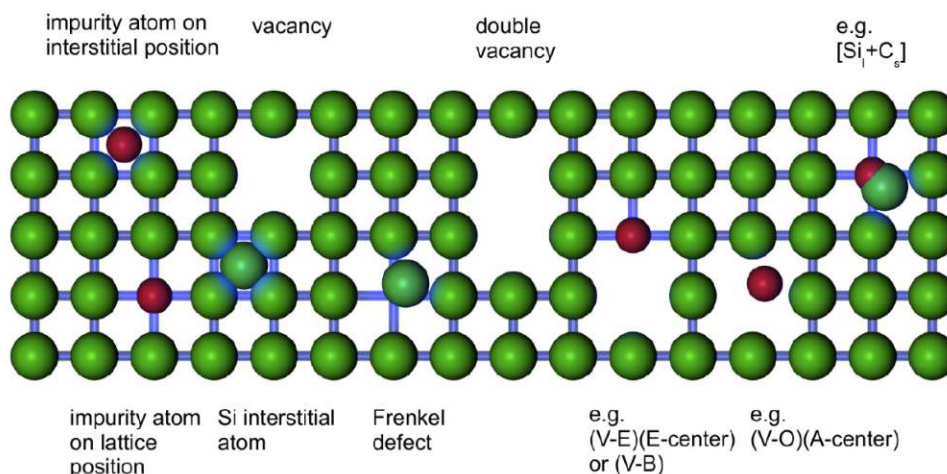
Fig. 2.9. Schematic sketch of the different types of point defects. Reproduced from Ref. [35]

2.4.1 Surface damage

Surface damage refers to damage introduced in the silicon oxide and its interface with the silicon bulk. For the oxide, only damage introduced by ionization plays a relevant role, as the amorphous structure of the oxide reduces the effect of displaced atoms on the lattice properties. In the case of ionizing interactions, most of the created e/h-pairs recombine shortly after creation, but some of the pairs can be separated by an electric field inside the oxide. This separation is due to the electron mobility being roughly 10^6 times higher than the hole mobility in the oxide [22] leading to them reaching a collection electrode before the holes. The lower hole mobility originates from shallow hole traps in the oxide, resulting in a slow movement from trap to trap for holes.

Due to the oxide growth process deep hole traps are created close to the interface of the oxide and the silicon. The created holes inside the oxide can then be trapped by these traps, leading to an increase in the positive charge accumulated close to the interface of the oxide. Ionizing radiation also leads to an increase of defects states in the interface region, by interaction with the dangling bond of the trivalent silicon atoms at the interface. This process introduces additional energy states in the band gap. The additional states can function as generation-recombination centres leading to an increase in leakage current. This defects can be either annealed out tunnelling of electrons from the bulk into the oxide recombining with the trapped holes or due annealing at at least 150 °C [36].

2.4.2 Bulk damage

Due to the highly ordered structure of the silicon and the higher mobility of holes compared to the oxide the predominant effect of radiation damage is the displacement of atoms and the resulting defects. As mentioned before the type and concentration of defects highly depends

on the energy and type of the irradiation particle making the comparison of different irradiation studies difficult. To be able to compare the different results the Non-Ionizing Energy Loss hypothesis (NIEL) is used [37]. It assumes that the change of detector parameters scales only with the energy lost by the projectile, independent of the exact cascade structure following the energy loss. Therefore, an energy dependent displacement damage cross-section $D(E)$ can be defined by integration of all possible interactions, that could lead to displacement damage

$$D(E) = \sum_{\nu} \sigma_{\nu}(E) \int_0^{E_R^{max}} f_{\nu}(E, E_R) P(E_R) dE_R, \tag{2.17}$$

where ν represents all the possible interactions that could lead to displacement damage (indexed with ν), σ_{ν} stands for the cross-section of the different processes, $f_{\nu}(E, E_R)$ is the probability of a particle with energy E, to create a secondary particle of energy E_R. $P(E_R)$ stands for the Lindhard partition function, which calculates the fraction of the recoil energy that is converted into displacement damage. Processes with recoil energies E_R which are below the threshold energy needed for displacement, are removed from the integral. The resulting displacement damage cross-section as a function of energy and particle type can be seen in figure 2.10.
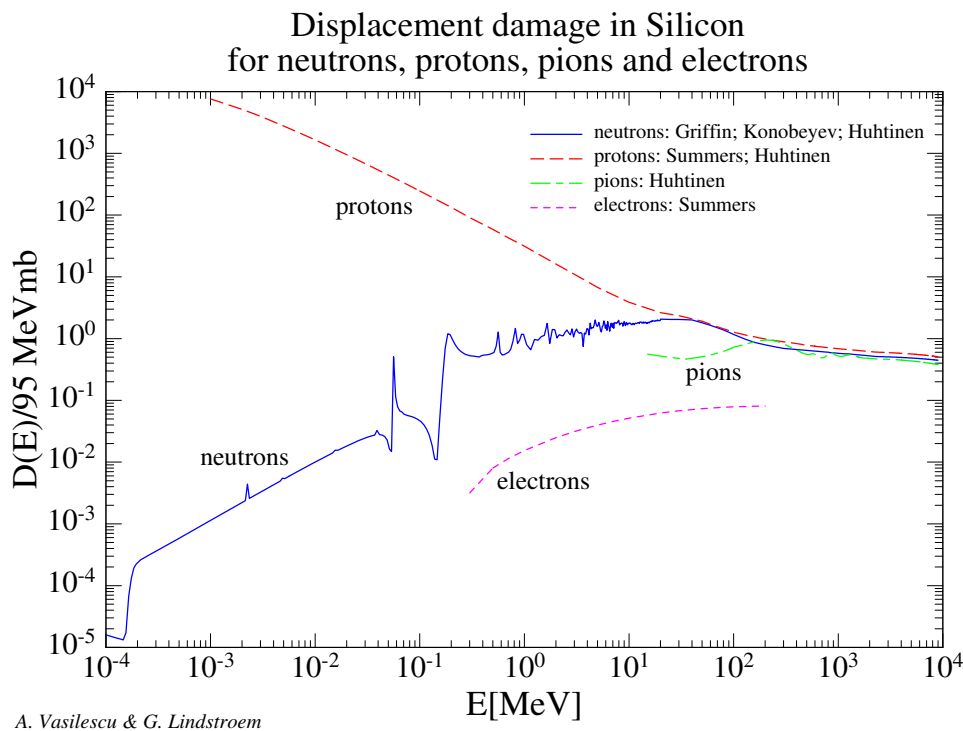
Fig. 2.10. Displacement damage cross-section $D(E)$ as a function of energy and particle type. Reproduced from Ref. [38].

$D(E)$ can then be used to define a scaling factor κ for each particle energy and type, that

allows to scale the measured fluence ϕ to a normalised fluence for comparisons with

$$\phi_{norm} = \kappa\phi. \tag{2.18}$$

The most commonly used reference is a mono-energetic neutron flux with a energy of 1 MeV. All fluences used in this thesis are converted to this reference fluence.

2.4.3 Effect of radiation on the detector

Each stable defect created by irradiation introduces a new energy level in the band structure of the crystal. Depending on their charge when they are occupied by an electron, they can be divided into two groups. Acceptor states are negatively charged when they are occupied and donor states are neutral when they have a trapped electron. In the other case the acceptor state is neutral and the donor state is charged negatively. The charge stage in thermal equilibrium depends on the position inside the band gap with respect to the Fermi level. If they are located above the Fermi level they are filled with an electron and have therefore the charge described before. Some defects can also have multiple states in the band gap. If these states contain donor and acceptor states the defect is called amphoteric.

The macroscopic effects of these states depend on the position in the band gap. Acceptor defects located above the Fermi level and donor defects located below the Fermi level are charged in the thermal equilibrium and contribute to the effective doping concentration in the bulk. In addition, the removal of dopants from the lattice due to radiation or the electrical deactivation of dopants due to their interaction with defects, can alter the N_{eff} of the bulk. This can lead to a change of electric field profile inside the bulk and to an increase in depletion voltage. As these effects scale with the concentration of the created defects, the observed macroscopic effects depend on the introduction rates of each defect state.

Due to a slight imbalance in the introduction rates of acceptor and donor states, a detector will be become increasingly p-doped due to the introduction of more acceptor states. For a previously n-doped bulk this leads to type inversion to a p-doped bulk at around 10^{12} n_{eq} cm^{-2} for high resistivity silicon (see figure 2.11). For p-doped silicon only an increase in N_{eff} is observed, leading to an increased bias voltage.
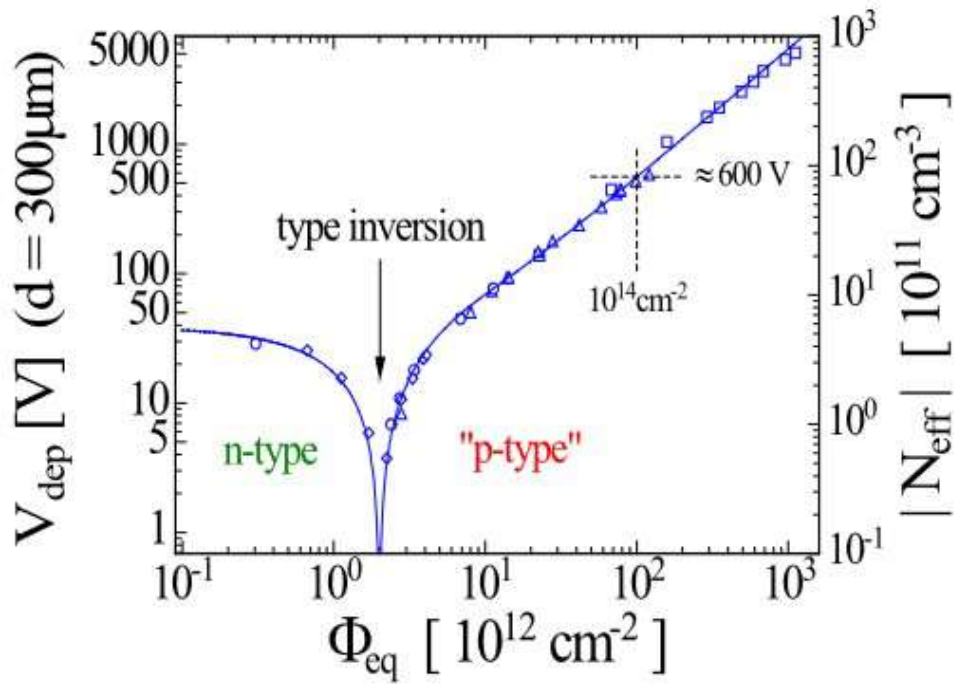
Fig. 2.11. Effective doping concentration as function of fluence. Reproduced from Ref. [39].

Defect states can also work as stepping stones allowing charge from the valence band to reach the conductive band more easily and vice versa, due to a lower threshold potential. These defects work now as generation/recombination centres and cause an increase in leakage current. The electron/hole pair generation rate G introduced by one trap is given by [37]

$$G = N n_i \frac{c_e c_p}{c_e e^{\frac{E-E_f}{k_b}T} + c_p e^{\frac{-E-E_f}{k_b}T}}.$$
(2.19)

E and N represent the energy level and concentration of the defect, respectively, E_f stands for the intrinsic Fermi level in the detector, c_e and c_p are the capture cross-sections of the defects for electrons and holes, and n_i stands for the intrinsic carrier density. As can been seen from equation 2.19, only defects with energy levels close to the middle of the band gap contribute significantly to the leakage current. As mentioned before, the concentration of defects states is observed to be linear with fluence (at least until 10^{16} n_{eq} cm^{-2}). Using equation 2.19 this leads to an expected linear increase in leakage current with fluence with a proportionality factor α, which is a collection of contributions of all defects states,

$$\delta I = \frac{\alpha \phi}{V}.$$
(2.20)

The current change is normalised to the depleted and therefore charge generating volume of the detector V. This factor was introduced to make the comparison of different sensors with different geometries possible. As can be seen in figure 2.12 this relation holds independent of the sensor studied. As seen in equation 2.19 the generation rate is temperature dependent.

The scaling factor α therefore has to be defined for a specific temperature. As a standard reference point 20° is used, which leads to an alpha factor of $3.99 \times 10^{-17}\,\mathrm{A\,cm^{-1}}$.
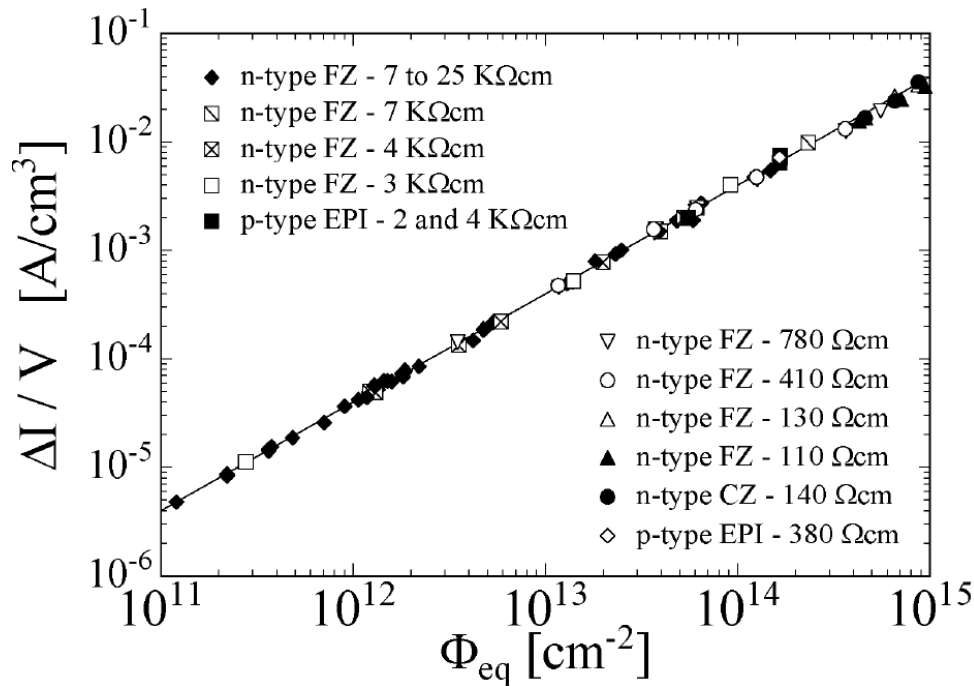
Fig. 2.12. Leakage current as a function of neutron equivalent fluence for different silicon detectors. Measured after 80 minute annealing at 60 °C. Reproduced from Ref. [37]

2.4.4 Annealing

The thermal budget introduced during irradiation and the handling of the sensors can have a substantial impact on the sensor performance, as it allows defects to form new defects or heal out due to enhanced diffusion and accessible energy. For the scaling factor of the leakage current this process can be modelled as the sum of exponential terms, which describe the healing out of all the different defects contributing to the generation of leakage current. As this does not explain the saturation of the change in leakage current after annealing times of over one year, an additional logarithmic term has been added, leading to

$$\alpha = \alpha_1 e^{-\frac{t}{\tau_I}} + \alpha_0 - \beta ln\left(\frac{\Theta\left(T_a\right)t}{t_0}\right). \tag{2.21}$$

The first term, corresponding to the short term annealing, is described using the two constants value α_1 and α_0, the annealing time t and a time constant τ_I. The logarithmic term consists of a scaling constant β, a temperature scaling factor $\Theta\left(T_a\right)$, the annealing time t and a reference annealing time t_0. It has to be mentioned here that all the parameters are defined for one reference temperature. In the cases of this thesis 80 °C is used as a reference. A table with the corresponding parameters can be found in 2.1.

α_1 [10^{-17} V cm^{-1}]	α_0 [10^{-17} V cm^{-1}]	β [10^{-18} V cm^{-1}]	t_0 [min]
1.23± 0.06	4.23	3.07± 0.18	1

Table 2.1. Parameters of current annealing with a reference temperature of 80°C for α_0. Reproduced from Ref. [37]

τ_I depends on the on the annealing temperature T_a as following

$$\frac{1}{\tau_I} = k_{0I}e^{\frac{E_I}{k_bT_a}},$$ (2.22)

with $k_{0I} = 1.2^{+5.3}_{-1} \times 10^{13}$ s^{-1} and $E_I = 1.11 \pm 0.05$ eV.

The factor $\Theta(T_a)$ was introduced to remove the temperature scaling behaviour of the α_0 parameter by scaling the annealing time and corresponds to

$$\Theta(T_a)t = e^{\frac{E_I^*}{k_b}\left(\frac{1}{T_a}-\frac{1}{T_{ref}}\right)},$$ (2.23)

with $E_I^* = 1.3 \pm 0.14$ eV and a reference temperature T_{ref} at which α_0 was measured.

If several annealing steps were done the annealing can be calculated as the product of the exponential and logarithmic term different annealing steps indicated by the index i with

$$\alpha = \alpha_1 e^{-\sum_i^n \frac{t_i}{\tau(T_{ai})_I}} + \alpha_0 - \beta ln\left(\sum_i^n \frac{\Theta(T_{ai})t_i}{t_0}\right).$$ (2.24)

2.4.5 Double junction

At fluences above 10^{15} n_{eq} cm^{-2} another effect is observed. Instead of the depletion region growing only from one side, the depletion region seems to grow from both sides of the detector simultaneously. In addition, higher fields are measured in this depleted region. An explanation is given by assuming only two defect states, one of them being an acceptor and one being a donor defect. In addition, these states have to be unoccupied in the thermal equilibrium. The occupation of these traps in the depleted space charge region depends on the concentration of free charge carriers. As these free carriers are created by thermal excitation the generation rate is uniform across the sensor. For the resulting electron and hole currents this is not the case. Due to the applied electric field in the space charge region the electron current is linearly increasing with proximity to the n+ electrode. The opposite is the case for the holes (see figure2.13). Due to this difference in free carriers, the trapping probabilities are not the same along the sensor, leading to a linear change of N_{eff} along the depth of the sensor. Using the Poisson equation, this leads to the double peaked electric field observed in the sensor. The reason for this effect to only appear at high fluences is due to the concentration of these trap states needing to be in the order of magnitude of the bulk doping. It has been shown in [40] that the growth in depth of the depletion zones can be again modelled with a

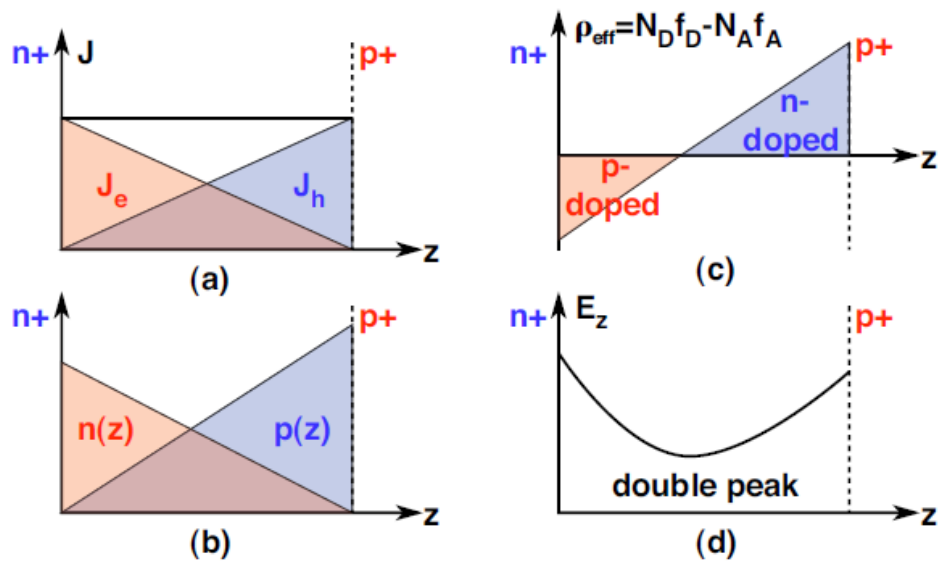$\sqrt{V_{Bias}}$ dependence up to 10^{16} n_{eq} cm^{-2}.

Fig. 2.13. Illustration of the creation of the double junction inside a p-in-n sensor.**a**: Electron and hole currents as a function of sensor depth. **b**: Free carrier concentration as a function of sensor depth. **c**: N_{eff} as a function of sensor depth. **d**: Electric field as function of sensor depth. Reproduced from Ref. [41]

LHCb

The LHC Beauty experiment (LHCb) [14] is one of the four main experiments located along the LHC. Unlike the general purpose experiments ATLAS [12] and CMS [13], it is optimized for studying heavy-flavor physics, indirect searches for physics beyond the Standard Model and measurements of Charge-Parity (CP) violations. For many of these phenomena $b\bar{b}$ pairs are key physics probes that can be used. In proton-proton collisions, the most prominent interaction that produces a $b\bar{b}$ is a parton-parton interaction in which one parton has much more energy than the other, leading to a high correlation in the flight path of b and $\bar{b}$. This in turn leads to a preferential production cross section in either beam direction with only small angles against the beam axis (see figure 3.1).
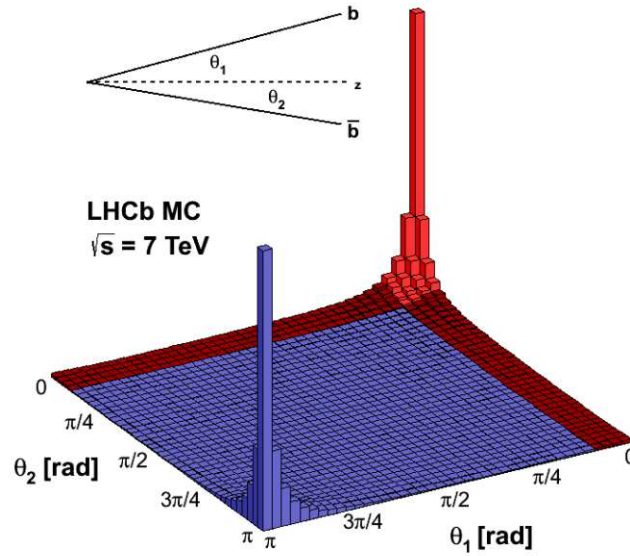
Fig. 3.1. Distribution of angle to the beam line for the two partons produced by $b\bar{b}$ pair production. The red area corresponds to the detection region of the LHCb experiment. Reproduced from Ref. [42].

In particle physics a common metric to describe the angle of a particle to the beam line is the pseudorapidity η,

$$\eta = -\ln\left[\tan\left(\frac{\theta}{2}\right)\right],\tag{3.1}$$

where θ represents the angle to the beam line. A pseudorapidity of zero would correspond to a track perpendicular to the beam while a parallel track would have infinite pseudorapidity. In this metric the LHCb acceptance covers the range $2 < \eta < 5$, corresponding to 14 to

250 mrad. Such a geometry allows for measuring at least 25% of all $b\bar{b}$ pairs produced, while substantially reducing the size of the detector [42]. The experiment covers only the forward direction as no asymmetries between forward and backward direction are expected.

The experiment runs at lower luminosity than the general-purpose experiments ATLAS and CMS. The process of luminosity reduction is called levelling. It can be achieved by increasing the offset or angle of the two beams at the interaction point or changing the beam profile a the collision point [43, 44]. Such an operating scheme allows one to reduce the combinatorial background by limiting μ and simplifies triggering. In addition this leads to an overall reduction in the radiation damage in the detectors and allows for constant luminosity throughout a fill (typically around 8 h).

The original LHCb experiment was operating from 2010 to 2018 collecting 9 fb^{-1} and reached a total radiation dose of 5×10^{14} n_{eq} cm^{-2} for the innermost region [45]. LHCb has published several significant measurements like the measurement of the rare decay of $B_s^0 \rightarrow \mu^+\mu^-$ [46][47], the measurement of the weak phase in B_s^0 oscillations [48] or the first observation of CP violation in B_s^0, the first observation of CP violation in charm [49] and the discovery of pentaquark [50] and tetraquark states [51].

Many of the measurements made by LHCb during Run 1 and Run 2 were still limited by statistics. To enable data taking at higher luminosity, a major upgrade (Upgrade I) [52] of the experiment took place during LS2. A key part of the upgrade was a redesign of the so-called trigger (event filtering) scheme. In the original LHCb experiment, the readout rate of most of the subdetectors was limited to 1.1 MHz, and a first-level hardware trigger was used to reduce the event rate from 40 MHz to 1.1 MHz. With an increase in luminosity, the threshold of the hardware trigger would have to be increased to comply with the 1.1 MHz readout limit. As this would reduce the yield for many hadronic channels, the decision was made to switch to a 40 MHz readout and to move to a full software trigger [53]. This required a redesign of all tracking detectors and an upgrade of the electronics of all subsystems. After this upgrade the instantaneous luminosity will be from $\mathcal{L} = 4 \times 10^{32}$ cm^{-2} s^{-1} to 2×10^{33} cm^{-2} s^{-1}. Under these new conditions a μ of 5.2 (figure 3.2) is expected, leading to the collection of 5 fb^{-1} of data per year. If no changes are made to run conditions during the lifetime of Upgrade I, a total collected data sample of 50 fb^{-1} is expected. The increase in luminosity compared to Run 1 and 2, together with the full software trigger, is expected to result in an increase in the signal yield by around ten for muonic B decays and twenty or more for heavy-flavor decays [54].

Figure 3.3 shows the layout of the upgraded experiment. The detector closest to the interaction point is the Vertex Locator (VELO), followed by the RICH1 and UT detectors and the dipole magnet. The detectors downstream of the dipole magnet are the Scintillating Fibre (SciFi) tracker, the RICH2 detector, the electromagnetic and hadronic calorimeters, and the
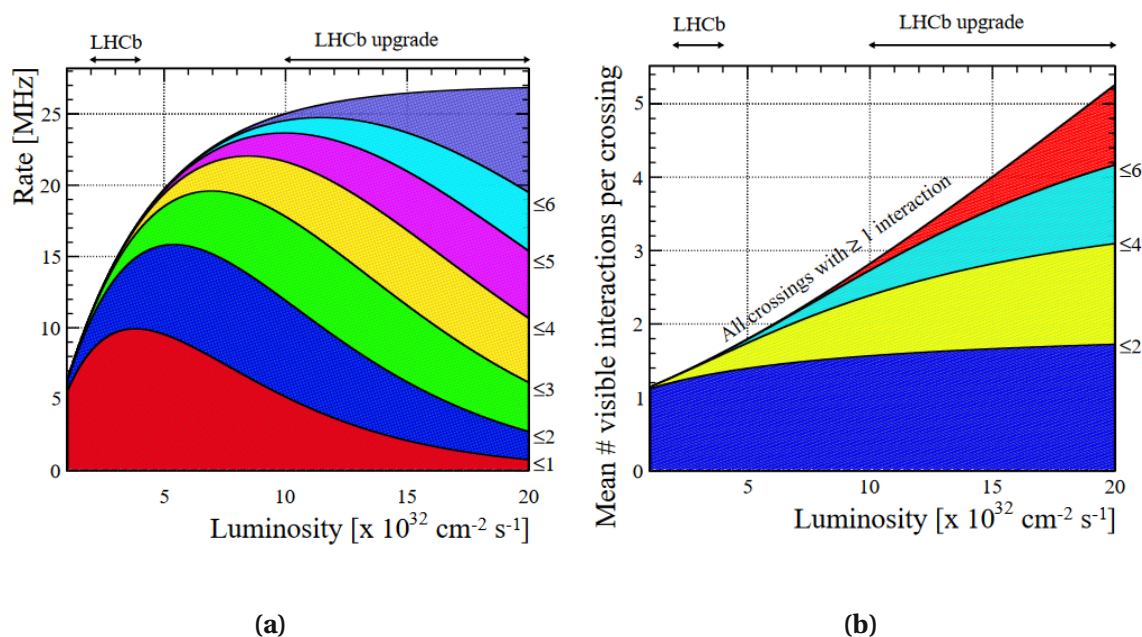
Fig. 3.2. a: Interaction rate as a function of instantaneous luminosity. Different color bands represent categories of number of interactions per event. **b**: Average number of visible interactions per bunch crossing as a function of luminosity, for events with at least one visible interaction. Reproduced from Ref. [55].

muon system.

The coordinate system used throughout the thesis and by the experiment has its origin at the interaction point and the z-axis pointing from the interaction point towards the muon system. The y-axis is pointing up and the x-axis is oriented to form a right handed coordinate system. The region between the interaction point and the magnet is referred to as the upstream region and the region after the magnet as the downstream region.

3.1 Tracking

Tracking is an integral part of all particle physics experiments. Its purpose is to reconstruct the trajectories of charged particles and measure their momenta. The momentum of a charge particle is measured by letting it fly through a magnetic field, perpendicular to the flight path. It will be deflected on a curved path, where the radius of the curvature r depends on the magnetic field B, the charge of the particle q and its momentum in the plane normal to the magnetic field p and can be calculated with

$$r = p/Bq. \qquad (3.2)$$

If the radius of the track curvature is measured, the charge and momentum can be determined. The LHCb dipole magnet provides a magnetic field of up to 1.1 T (see figure 3.4) with
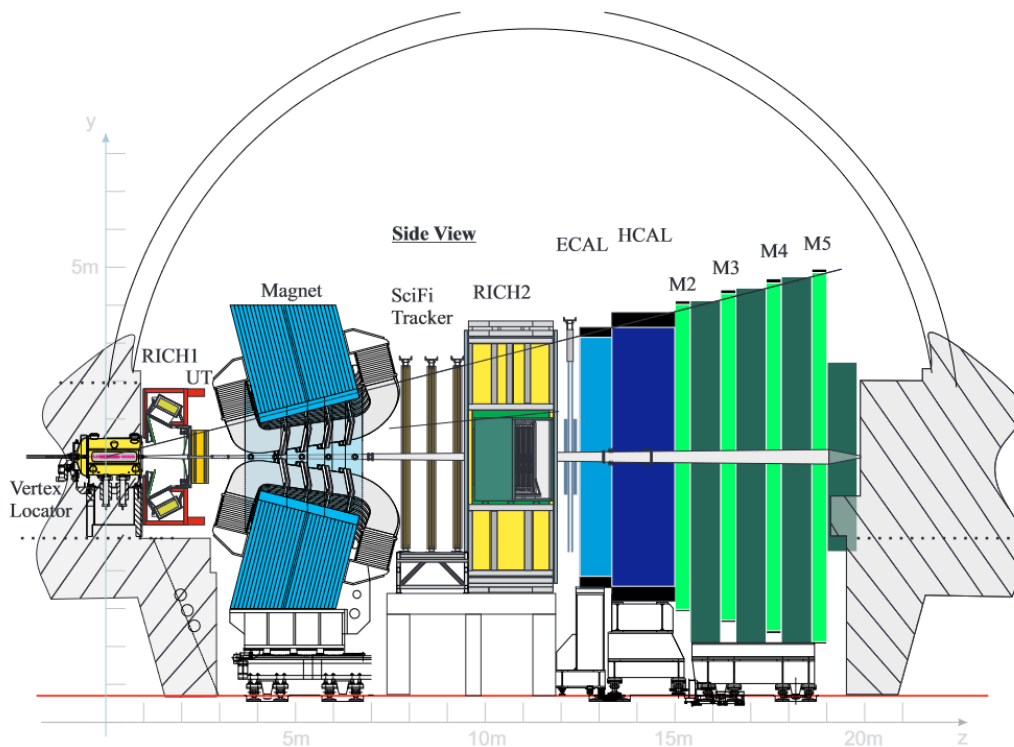
Fig. 3.3. A schematic view of the LHCb experiment (Upgrade I). Reproduced from Ref. [56].

an integrated field of 4 T m. To prevent biasing of results due to performance differences in the two sides of the detector the magnetic polarity is switched in regular intervals [57].

The tracking system of LHCb comprises the Vertex Locator (VELO) [55], the Scintillating Fiber tracker (SciFi) [58] and the Upstream Tracker (UT) [58]. The tracks can classified in different categories depending on which parts of the tracking system are used in the reconstruction (see figure 3.4) [59]:

- **Long tracks**: These are the most important tracks for physics, as they have hits both at the VELO and the SciFi.

- **Upstream tracks**: If a particle cannot pass the magnet, due to its low momentum or high initial track angle, it only leaves hits in the VELO and the UT.

- **Downstream tracks**: Downstream tracks have hits only on the tracking stations after the VELO. This can occur if the decay time of a particle is long enough to leave the Vertex Locator before decaying.

- **VELO Tracks**: If a particle has a higher track angle than the LHCb acceptance or flies in the backward direction it only leaves hits in the VELO. These tracks can be used to improve the vertex reconstruction.

- **T tracks**: If a track has only hits downstream of the magnet, it is called a T track.
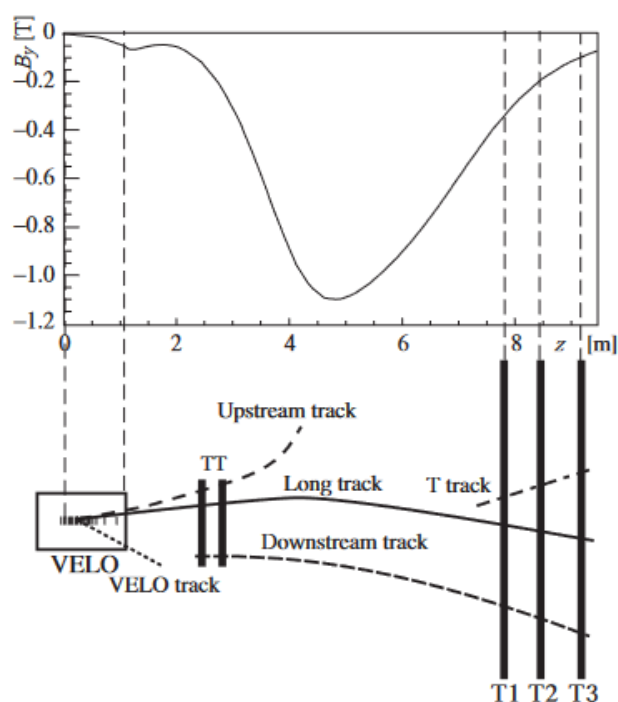
Fig. 3.4. Sketch of different track types in the LHCb experiment and the magnetic field as a function of z-position.[60].

3.1.1 VELO

The innermost detector of the LHCb experiment is the Vertex Locator (VELO). It is the first tracking detector and surrounds the interaction point, with the sensors placed at a distance of 5.1 mm from the beam line. Its close distance to the interaction point is essential to achieving a good primary and secondary vertex resolution. Because of its proximity to the interaction point it has the harshest restrictions in terms of radiation damage and hit rate out of all detectors in the LHCb experiment. In addition, the fluence is highly non-uniform along the detector (see figure 3.5), with the region closest to the interaction point receiving a fluence of around $8 \times 10^{15} \ n_{eq} \, \text{cm}^{-2}$ (after 50 fb^{-1}), whereas the outermost downstream sensor will receive only a fluence of $0.5 \times 10^{15} \ n_{eq} \, \text{cm}^{-2}$ [55].

The sensors are 200 μm thick silicon pixel sensors, with a pixel size of 55 × 55 μm. The 200 μm thickness was chosen to ensure a high charge collection efficiency after radiation, maintaining a high signal-to-noise ratio [61]. The sensors are n-on-p type sensors as they are shown to be radiation hard up to high fluences and unlike n-on-n or p-on-n do not suffer from type inversion. Additionally, time-walk is minimized as the signal carriers are electrons, which have a faster collection time than holes. The readout pixels are isolated from each other through p-stop implants. The pixel matrix has a total size of 42.46 × 14.08 mm. To prevent edge effects at the dicing line regions, a 450 μm wide inactive region is implemented at the edge of the sensor, including several guard rings for field termination. Each sensor tile is
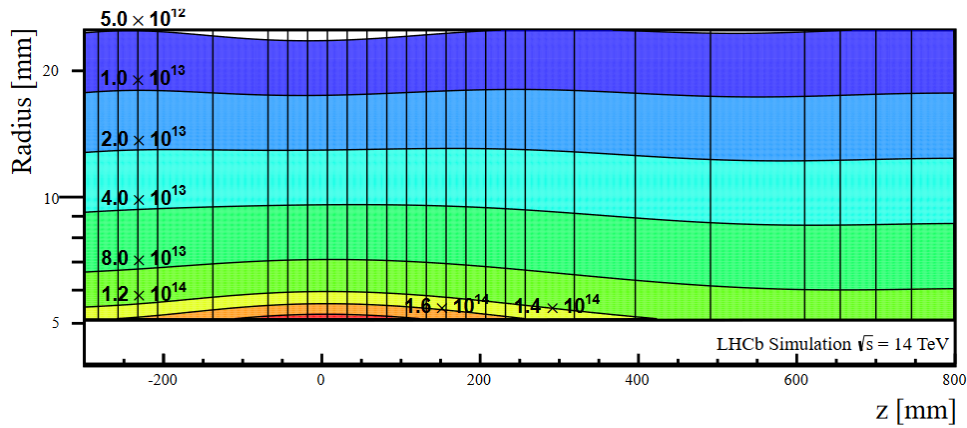
Fig. 3.5. Estimated integrated radiation dose per fb^{-1} for Upgrade I conditions in units of 1 MeV n_{eq} cm^{-2}. The vertical planes represent the position of the modules. Reproduced from Ref. [55].

bump-bonded to a row of three ASICS. To prevent an insensitive region between the ASICs, the two sensor pixels at the inter-chip borders are elongated to a total length of 137.5 μm to cover the inactive region.

With 8.5 hits per ASIC per event for the hottest region (see figure 3.6b), a special ASIC, called VeloPix [62], was designed to read out the signals. One ASIC is responsible for the readout of a 256×256 pixel matrix. The expected data rate the ASICs have to deal with is on average 10.2 Gbit s^{-1} for the hottest area, with a peak data rate of 15.1 Gbit s^{-1}. Such a rate is already significantly reduced by employing several data rate reduction techniques. Firstly, only binary hit data and a hit timestamp is transferred instead of the full signal information. Secondly, arrays of 2×4 neighbouring pixels are grouped to super pixels. The ASIC is thinned to 200 μm thickness to reduce its contribution to the material budget. The chip extends on three sides with respect to the matrix by 30 μm with the fourth side extending by 2.55 mm to allow space for digital processing and the wire-bonding pads [62]. The average power consumption per chip is 1.2 W, with a possible maximum of 1.9 W.

Four sensor tiles are used to form a module, with two tiles mounted on each side of the module [63]. Each of the tiles is glued, using a epoxy resin with alumina filler[1], to a 500 μm thick cooling substrate [64], which functions as the base of the module. The tiles are arranged in an L-shape, to allow the two sides to cover the full ϕ-range in the closed position. Due to its thickness, the cooling substrate introduces additional of scattering. To reduce this degradation of the reconstruction performance, the substrate does not cover the full area of the inner sensor and is instead retracted, compared to the sensors, from the beam line (see figure 3.8). To account for a sufficient cooling for the innermost sensor parts the substrate is only

---

[1] Henkel Loctite, Stycast 2850FT/Cat23LV

retracted by 5 mm. To prevent inactive regions in the detector due to the inactive edge of the sensor, two sensors are mounted on each side of the module. The overlap of the sensors on the different sides was chosen to be five active pixels, allowing to tracks with a maximum angle of 12 ° to the detector planes to transverse at least one sensor plane. For the outer tiles a gap still exists due to the inactive region at the edge of the tile and the spacing between two tile on the same side of the module (see figure 3.6a). The control of the ASICs, the readout of the signal and supply of power are provided by printed circuit hybrids glued to the outer parts of the substrate. The ASICs and hybrids are connected through wire bonds.

Inside the cooling substrate liquid CO_2 is evaporated. CO_2 was chosen as it offers excel-
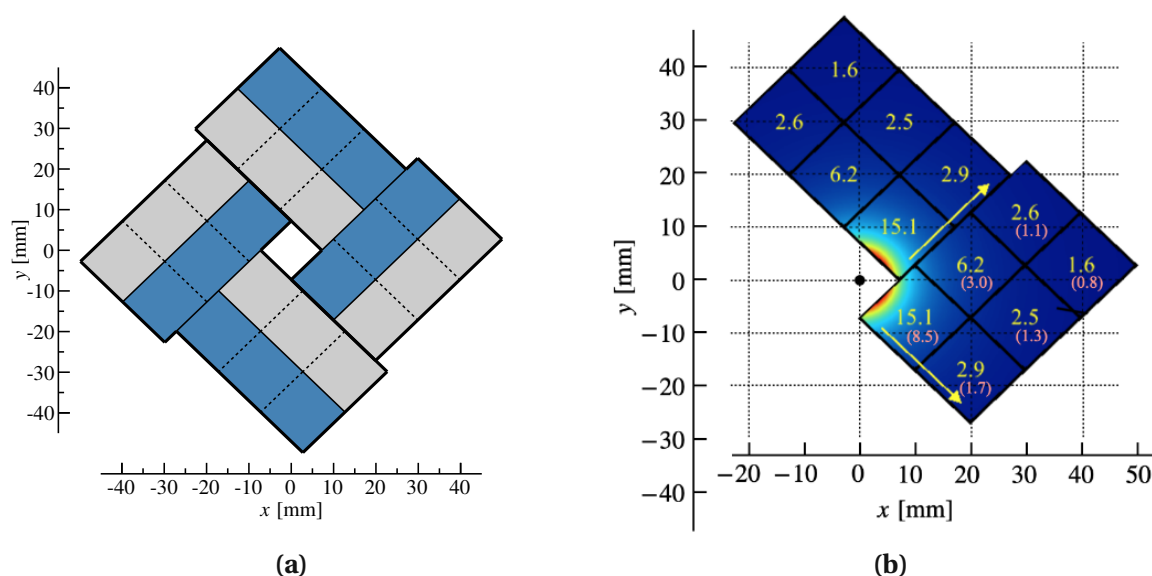
Fig. 3.6. a: Schematic of a module pair in the x-y plane. The colors represent sensor tiles mounted on different sides of the module. **b**: Peak data rate in Gbit s^{-1} (yellow) for the different ASIC positions. The red numbers represent the hits per ASIC per event. Arrows indicate the readout direction. Reproduced from Ref. [65].

lent heat capacity and radiation hardness. Running at an operation temperature of $-35\,°\text{C}$, it ensures that the temperature of sensors does not exceed $-20\,°\text{C}$ to avoid thermal runaway and degradation of sensor performance through reverse annealing. This solution allows to remove the 43 W of power dissipated by the electronics and the sensor of a module. Another important function of the cooling substrate is its mechanical stability as it is the core component of a module. The substrate is made out of two silicon wafers with 240 and 260 μm thickness, bonded together. In one of the substrates, micro channels are etched, in which the boiling CO_2 is circulated. The channels have dimensions of 120×200 μm with the first 40 μm of a channel being reduced to 60×60 μm to provide a uniform flow. Producing the cooling substrate out of silicon has additional benefits as it has the same thermal expansion as the other components mounted on the substrate to prevent thermal distortion [66].

The VELO as a whole consists of 52 modules oriented perpendicularly to the beam axis. It is split in two halves which can move in the horizontal direction such that they can be retracted away from the beam axis to avoid damage to the sensors and electronics during injection. The layout was optimized to ensure that 99% of all tracks inside the detector acceptance ($2 < \eta < 5$) have at least four hits in the detector. The exact position of the modules can be seen in figure 3.7. The modules are staggered in z-direction allowing for an overlap of the sensors of each side to close gaps in the acceptance due to the inactive edge of the sensor.
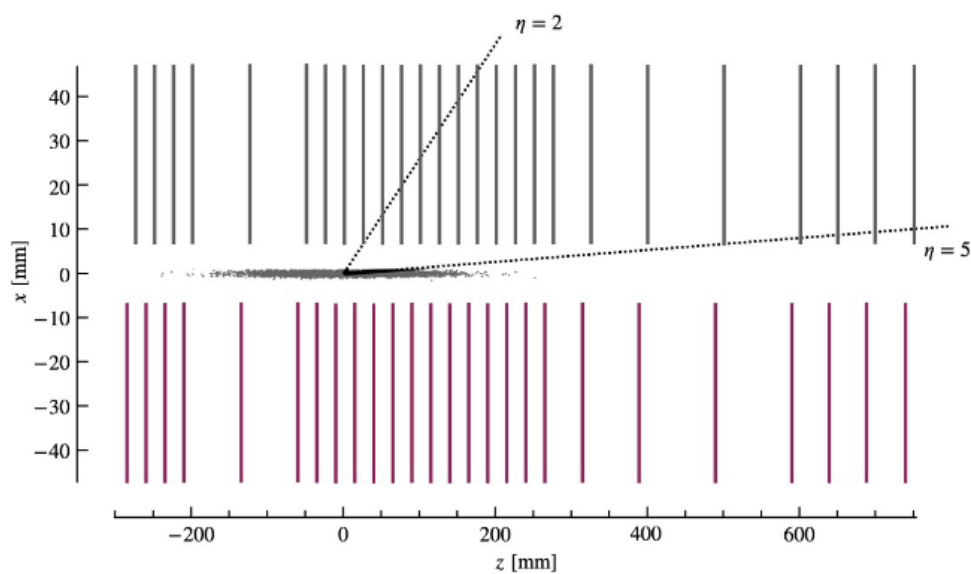
Fig. 3.7. Schematic view of the z - x plane of the VELO. The grey ellipsoid mark the luminous region. Reproduced from Ref. [65].
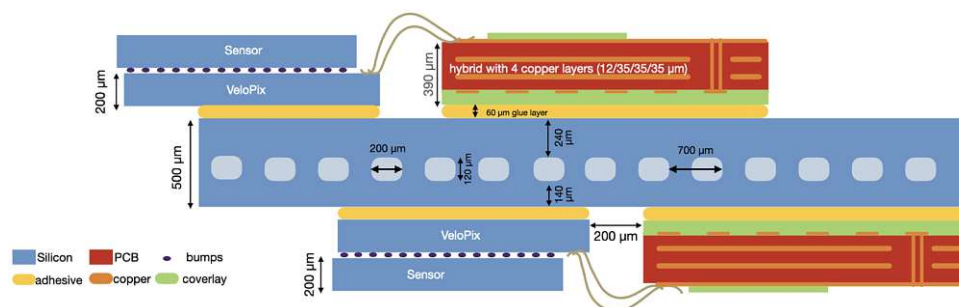
Fig. 3.8. Lateral cut through a module. Reproduced from Ref. [64].

Each half is encased in an RF-Box, which separates the detector vacuum from the beam vacuum (figure 3.9a). The sides of the RF-Boxes facing the beam are called RF-Foils. The RF-Foil is one of the most essential parts of the VELO detector. It has to separate the primary and secondary vacuum. Additionally, it should have a low impedance to conduct the beam mir-

ror current without sustaining thermal deformation, leading to a potential misalignment. It also has to shield the front end electronics from wake field excitations. Finally it is the main contributor to the material budget of the detector.

The foil is made out of cast aluminum alloy[2] due to its low contribution to the material budget and its electrical properties. The foil has a varying thickness between 250 μm in the thickest part and 150 μm in the thinnest part. In the region close to the beam line, the foil is constructed in a complex corrugated shape, folding around the sensor modules to minimise variations in the traversed material for most of the tracks (see figure 3.9b). Additionally, such a shape allows for an overlap of modules of opposite sides to close gaps in the acceptance. The innermost parts are 3.5 mm away from the beam line and the flat intersection between the modules is the furthest from the beam with 9 mm. Each module assembly is rotated by 45° to ensure that the region where the foils of the two sides overlap affects tracks of different ϕ equally. The complex shape is achieved by milling the foil to a thickness of 250 μm and then etching the innermost region down to 150 μm. The surface of the foil facing the interaction region is additionally coated with a 10 μm layer of torlon to ensure vacuum purity during operation. On the inside is coated with an 10 μm layer of polyamide to prevent an electrical breakdown between the modules and the foil.

(a)   (b)
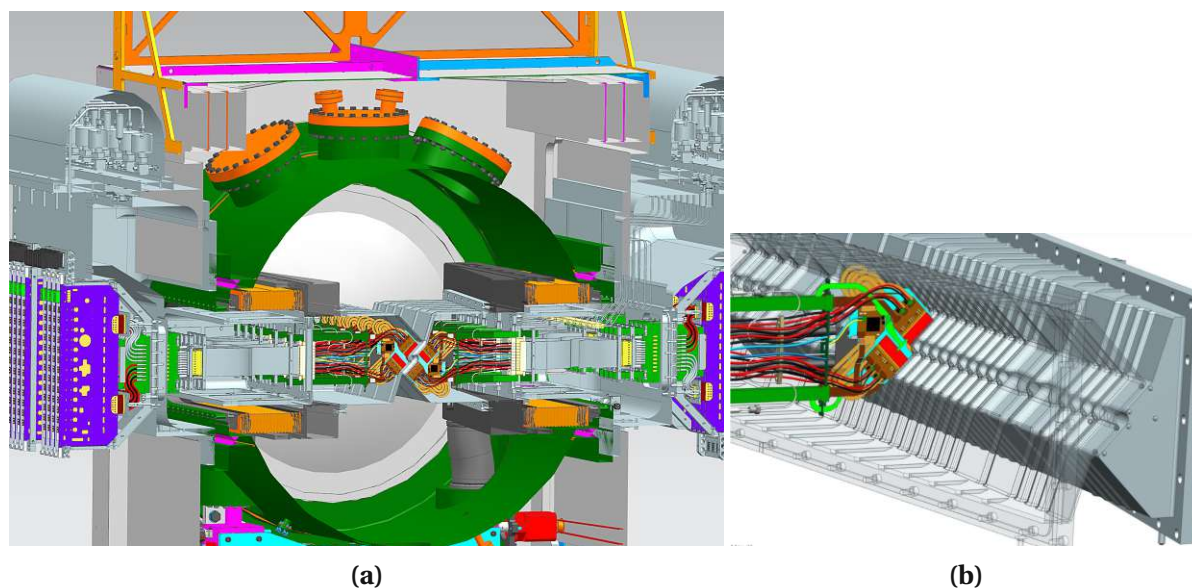
Fig. 3.9. a: Cut through the full VELO detector [67]. The vacuum tank is coloured in dark green and the sensors are coloured in red. **b**: Model of the RF-foil with a single module. Reproduced from Ref. [68].

On both ends of the RF-Boxes wakefield suppressors are mounted to ensure a smooth transition for the beam mirror current to the RF-foil. To be flexible enough to allow for the movement of the two sides, they are made out of 50 μm thick copper-beryllium sheets with a gold

---

[2]AlMg4.5Mn0.7 EN-AW5083

finish.

3.1.2 Upstream Tracker

The Upstream Tracker (UT) is located between the magnet and the RICH1. The UT can help reducing the amount of fake tracks (ghost tracks) by providing a first estimate of the momentum and charge. This is achieved by using the stray magnetic field of about 0.02 T in combination with a minimum of 3 hits in the UT. It allows to achieve a transverse momentum resolution σ_{p_T}/p_T of around 15 %, enough to determine the charge of the particle and reduce track finding time by a factor of three. Finally it can be used to reconstruct secondary vertices for particles with long decay times [58, 69].

The detector is built out of four planes, grouped together in two stations. The planes consist of silicon strip sensors, oriented along the y-axis. One of the planes per station is oriented vertically and the other is rotated by a 5° and -5° respectively. Such an implementation allows the measurement of the y-component of the hits and to reduce the number of ghost hits. Sensor modules are mounted on staves. The type of the silicon sensor depends on the position in the detector [69]. In the outermost region (marked in green in figure 3.10) the sensors are 320 µm thick p-in-n sensors with a pitch of 187.5 µm. Moving closer the beam, the type of sensor is changed to n-in-p and the thickness is reduced to 250 µm to cope with the higher radiation dose (marked in yellow in figure 3.10). Additionally, the strip pitch is reduced to 93.5 µm to accommodate the higher track multiplicity. This allows for the occupancy to never exceed 3%, even for the hottest region of the detector. For the region around the beam, the length of the sensor modules is reduced to 50 mm (marked in pink in figure 3.10). The sensor modules are mounted alternatingly on the two opposite sides of the staves (figure 3.10) with each side overlapping slightly to ensure no holes in the acceptance. The staves are also mounted with a slight offset in z-direction to allow for an overlap in y-direction. Read-out is performed by the newly developed SALT chip [70]. Communication and power are supplied through kapton flex cables. The modules are cooled by CO_2 evaporation using pipes in the support structures. The UT is expected to have a single hit efficiency of 98%, resulting in a 99.8% efficiency for tracks with at least three hits [58].

3.1.3 Scintillating Fiber Tracker

The tracking detector downstream of the magnet is called Scintillation Fiber Tracker (SciFi). This detector consists of scintillating fibers of 250 µm diameter. The fiber core is clad by two 7.5 µm thick layers of lower refractive index materials to ensure reflection of the signal along the fibre [71]. To compensate for the low light yield of the original material, a fluorescent dye was added. Additionally, a secondary dye used in the mixture functions as a wave length shifter to reduce the overall attenuation of signal in the scintillator, especially the part in the blue spectrum of the signal. At one end of each fibre a mirror is mounted, which allows to
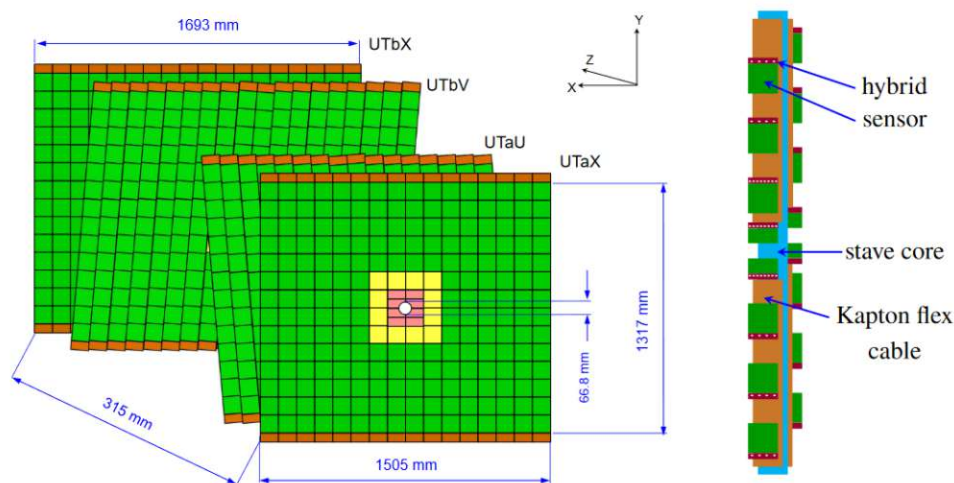
Fig. 3.10. Schematic layout of the four UT planes (left) and a UT stave (right). Different colors in the layout represent different sensors used. Reproduced from Ref. [69].

recover some of the non-collected photons by reflecting the signal back to the readout at the other end. The fibres are organized in six layers arranged in a hexagonal pattern and fixated by an epoxy matrix to form a mat. Eight mats make up a module and four modules are grouped to a station. The orientation of the modules in a station is the same as for the UT, with two modules arranged vertically and the other two rotated by $\pm 5°$. A sketch of a station can be seen in figure 3.11. The signal is detected by a 128-channel arrays of silicon photo-multipliers (SiPMs) located at the outer ends of the modules to reduce the received radiation dose an reduce the material inside the acceptance [72]. Their maximum peak efficiency is 45%, achieved for wavelengths of 450 nm. Their performance is expected to deteriorate due to radiation, especially with respect to the dark count rate. To mitigate this effect, the SiPMs are cooled to a temperature of -40 °C [73]. The readout is performed by a custom ASIC dubbed PACIFIC [58].

3.2 Particle identification

In addition to tracking, particle identification (PID) is a key aspect of particle physics experiments, and a major strength of LHCb. In LHCb, there are three systems that contribute to particle identification: the calorimeter [74] is used for identifying electrons and photons [65], the muon system [75] provides identification for muons and the RICH detectors [75] enable discrimination between charged hadrons (e. g. pions, kaons and protons).

3.2.1 RICH system

The discrimination of charged hadrons is critical for LHCb, allowing to reduce the background by being able to distinguish between different final states containing the same num-
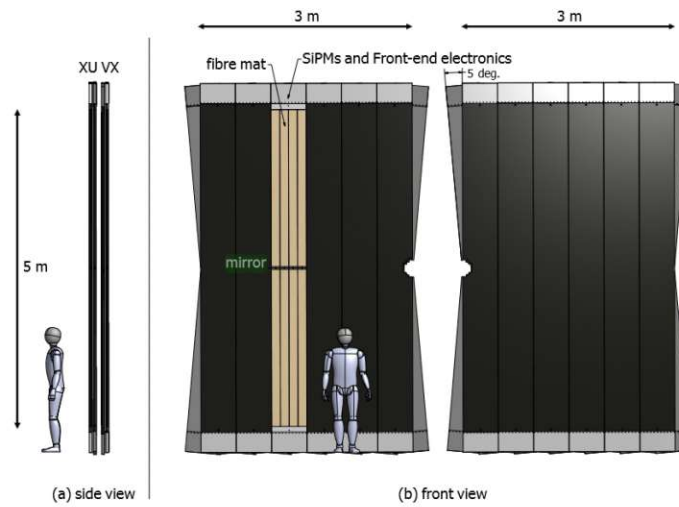
Fig. 3.11. a: SciFi station in a semi-open configuration **b**: Top Magnetic field as a function of z-position in the LHCb experiment. Reproduced from Ref. [71]

ber of hadrons. The main systems charged with this task are the Ring Imaging Cherenkov Detectors 1 (RICH1) and 2 (RICH2). Both detectors use a fluorocarbon gas as a radiator. To cover the full range of momenta, two types of radiators with different refraction indices are used. RICH1 is designed for detection in the low momentum range (2.6 to 60 GeV c^{-1}), using C_4F_{10} gas as radiator. RICH2 has instead CF_4 as a radiator and is responsible for the momentum range of 15 to 100 GeV c^{-1}. As the high momenta particles are produced predominately at high pseudorapidities (see figure 3.12a), RICH2 does not cover the full range of the LHCb acceptance and focuses instead only at the high η range. [76]. The Cherenkov photons are reflected out of the experiment's acceptance by a system of mirrors into the readout system. A quartz window is used to separate the radiator gas from the readout electronics. A schematic drawing of the layout can be found in figure 3.12b. For the readout, multi-anode photomultiplier tubes (MaPMT) [77] are used. To shield the MaPMTs from the fringe field of the magnet they are encased in iron boxes.

3.2.2 Calorimeter

When particles traverse matter, they lose energy and can produce secondary particles via interactions with atoms of the material. Such secondary particles, if created with high enough energy, can themselves repeat the effect. This cascade (shower) continues until all particles have transferred their energy to the material. The shape of these cascades depends on the particle type and its initial energy. If the shape of the showers is measured, the type of particle can be identified. The initial energy of a particle can be calculated by the sum of the total energy of the shower. This can be achieved by the calorimeters of the LHCb experiment.

In LHCb, there are two calorimeters. Both of them are made of alternating absorber and
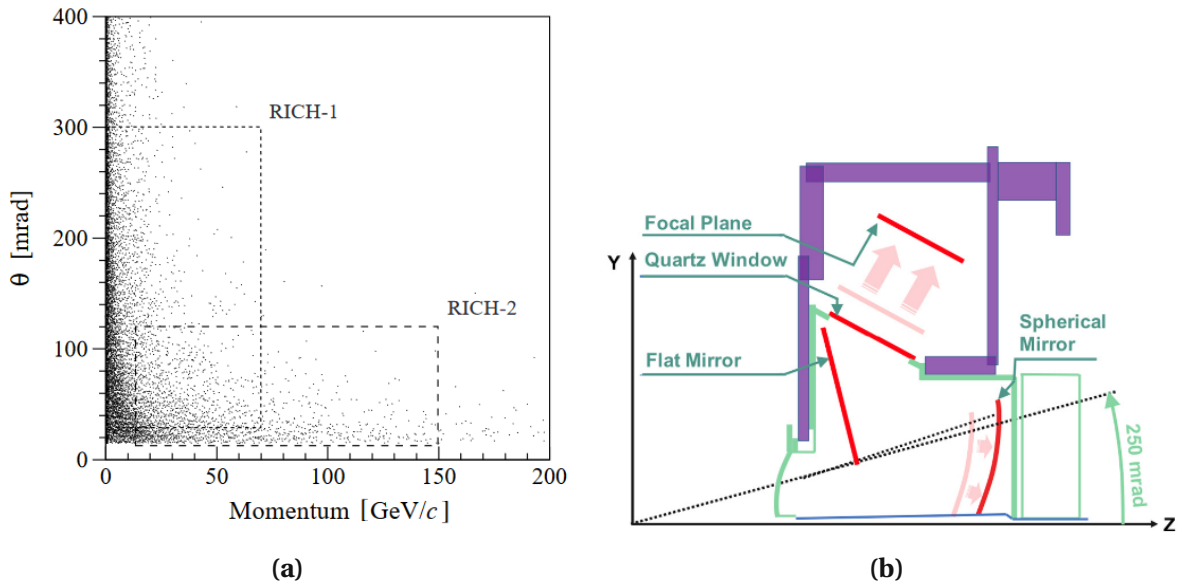
Fig. 3.12. a: Distribution of simulated $B_d^0 \to \pi^+\pi^-$ events as function of polar angle θ versus momentum. Dashed areas represent the acceptance of the two RICH detectors. Reproduced from Ref. [76]. **b**: Schematic layout of RICH1. Reproduced from Ref. [78].

scintillators layers. The absorber is a high density material used to create the shower in the calorimeter, whereas the scintillator is responsible for converting the deposited energy into photons, which are then guided by wave guides to photo multipliers for the read-out of the signal. On the way to the photo-multipliers the wavelength of the signal photons is shifted by wavelength shifters to ensure a maximal efficiency at the photo multipliers [74].

The first calorimeter is the electromagnetic calorimeter (ECAL) . It is composed of layers consisting of 2 mm of lead, 120 μm of reflective material and 4 mm scintillating fibers. The total length of the detector amounts to 42 cm which corresponds to 25 X_0, ensuring the total energy loss for electrons. It can achieve an energy resolution of

$$\frac{\sigma_E}{E} = \frac{9 \pm 0.5\%}{\sqrt{E}} \bigoplus 0.8 \pm 0.2\% \bigoplus \frac{0.003}{E \, sin \, (\theta)} (\text{E in GeV}), \tag{3.3}$$

where θ stands for the track angle to the beam. Due to the strongly varying hit density across the detector three different granularities are used.

The second calorimeter is the hadronic calorimeter (HCAL). As the name implies, its purpose is the measurement of the energy of hadrons. As hadrons are not stopped inside the ECAL, so an additional calorimeter is needed. To keep the size of the calorimeter limited, the thickness of the absorber layers is increased compared to the ECAL, consisting now of 16 mm iron layers. This leads to the detector being substantially larger, with a total thickness of 1.65 m [79].

In terms of radiation damage, most of the ECAL and HCAL are expected to continue working until the end of the Upgrade I phase without any meaningful performance losses. For

the innermost part of the ECAL on the other hand a substantial performance decrease is expected after a collected luminosity of 20-30 fb^{-1} [75]. For 30 fb^{-1}, a decrease in photon yield by a factor of 12 and a reduction in resolution by a factor of two is expected. This amount of radiation damage will be reached after the first years of Upgrade I, making a replacement necessary. The whole inner part is scheduled to be replaced during Long Shutdown 3.

3.2.3 Muon system

Since several channels studied by LHCb involve muons, a good muon detection system is essential. As muons have a increased mass compared to electrons, they are not stopped by most detectors. Building muon stations at the end of the experiment is therefore beneficial, as all other particles would be mostly stopped by the calorimeters, reduced the background in the muon stations. In the original LHCb design there were five muon stations label M1 to M5. M1 was removed for Upgrade I but the naming convention remained. Between M2-M5, absorber layers of 80 cm iron are placed to allow for a cut in particle energy, resulting in a minimal momentum of at least 6 GeV c^{-1} to traverse all stations. Each of the four stations is equipped with 276 multi-wire proportional chambers (MWPCs) [52]. MWPCs are gas filled detectors with a row of anode wires sandwiched between two cathode planes. When a particle passes through the gas it ionizes it and the produced electrons/ions drift to the anode/cathode, due to the applied electric field. Close to the wire the electric field is high enough for the electrons to accelerate and further ionize more molecules amplifying therefore the signal collected at the wire. In LHCb, MWPCs are filled with Ar/CO$_2$/CF$_4$ in a ratio of 40/55/5 and have a anode-wire spacing of 1.5 mm. The distance between the cathodes on each side of the anodes is 5 mm, resulting in an average of 50 primary ionisation electrons produced per traversing particle. The x coordinate is determined using groups of anode wires, while the y coordinate is established through the segmented cathodes [75].

3.3 The LHCb Upgrade II

After Run 4, many of the Upgrade I [52] detector components will reach the end of their lifetime and would need to be replaced to continue operating. As many physics channels will at this point be still limited by statistical uncertainties, a second major upgrade is proposed to reduce these uncertainties in a reasonable time frame. This new Upgrade (Upgrade II) [80] will make hereby use of the improved luminosity provided by the HL-LHC. The aim of this upgrade is to collect another 250 fb^{-1} of data, reaching a total of 300 fb^{-1}. It will be installed during the Long Shutdown 4 and should collect around 50 fb^{-1} per year during Run 5 and 6. Like with previous operating scenarios, during Upgrade II LHCb will run at a reduced luminosity to keep the pile-up and radiation damage at a manageable level. Several luminosity scenarios for LHCb are under consideration [81]. For this thesis only a baseline scenario of 1.5 $\times 10^{34}$ cm^{-2} s^{-1} is considered. This would allow to collect 49.5 fb^{-1} of integrated lumi-

nosity per year. In addition, this allows to run for the first 1.2 h of each fill with a constant luminosity, before beam burn off starts to exponentially decrease the luminosity.

One critical problem for the LHCb experiment in upgrade II will be the increase of μ from 5.2 to 42. This would lead to a mean primary vertex distance of 1.5 mm in z-direction. With the current layout and single-hit resolution this would mean a worse z pointing error resolution for tracks with $\eta > 4$ than the mean vertex distance (see figure 3.13a). Without changes to the detector layout, a reduction of the vertex reconstruction efficiency by 60 % (figure 3.13b) is estimated with more than double the amount of reconstructed ghost tracks. To mitigate this effect, the introduction of timing in the detector is necessary.
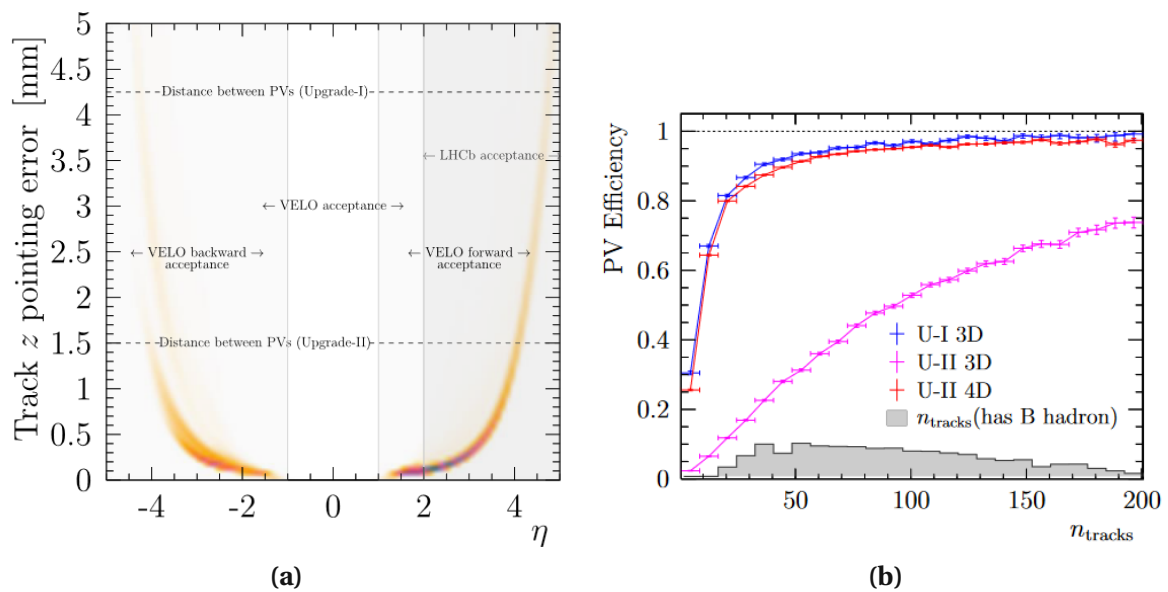
Fig. 3.13. a: Z pointing error as a function of track angle for the VELO detector. **b**: Primary vertex reconstruction efficiency with and without timing. Reproduced from Ref. [81].

The individual vertices in a bunch crossing are spread in time with a σ of 180 ps. If a timestamp can be added to each vertex, they can be separated and the combinatorial background can be reduced (figure 3.14). It has been shown that a 20 ps timestamp on each track would allow for a nearly full recovery of the reconstruction efficiency to Upgrade I levels (figure 3.13b) [82]. As the increase in statistics will improve precision on a wide range of physics param-
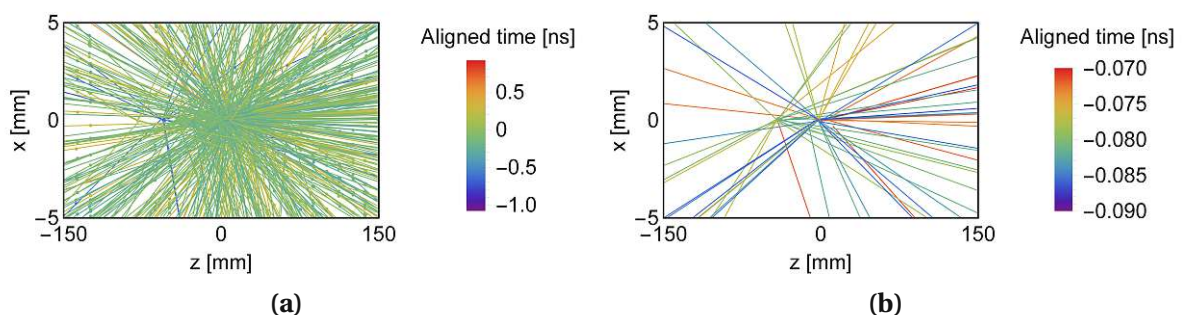
Fig. 3.14. Upgrade II track density for a 2 ns time window (**a**) and a 20 ps time window (**b**).

eters, only a small collection is mentioned in the following. The full expected range of improvements can be found in [81]. The increase would allow the LHCb experiment to probe the parameter γ and $|V_{ub}|/|V_{cb}|$ of the CKM unitary triangle with unprecedented resolution. For γ this means an improvement in resolution by from 4 ° (achieved at the end of Upgrade I) to 0.35 ° and for $|V_{ub}|/|V_{cb}|$ from 2% to 1%. The resulting improvement in the resolution can be seen in figure 3.15. For rare decays, an improvement of around 60% in the resolution of the branching fractions is expected. This allows for an unprecedented study of tree-level flavour changing neutral currents (FCNCs) transitions. As no source for them is provided within the SM, they therefore are good test for new physics (NP) models. Another test for NP models is the lepton flavour universality. Since in the SM universality can be calculated with high precision, it can be used as a probe for NP models where its violation is observed. For processes used for lepton flavour universality tests, an improvement of 60% is expected for Upgrade II .

(a)   **(b)**
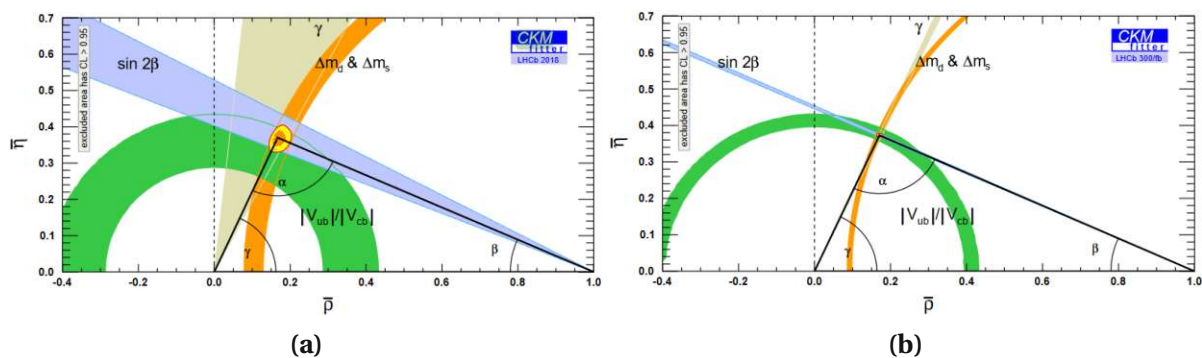
Fig. 3.15. Constraints from the dominant CKM observables to the apex of the unitarity triangle with (**a**) 9 fb^{-1} (status 2018) and (**b**) after 300 fb^{-1} of collected data. Reproduced from Ref. [83].

3.3.1 VELO

The design of the Upgrade II VELO faces two main challenges [82][81]. If the Upgrade I layout is kept, the fluence in the hottest point accumulated over the lifetime of the detector increases by a factor of 6 compared to Upgrade 1. To not be affected by a performance deterioration under such conditions, the sensors have to keep an efficiency of 99% over their lifetime. Due the non-uniformity of the fluence in the detector the expected performance changes have to be well understood in order to be able to compensate for them correctly. Lastly, the timing has to be introduced in the harsh radiation environment. Secondly, the increase in instantaneous luminosity would lead to an increase in hit rate, which among other things, would increase the needed data rate in the ASICs in addition to the increase to the introduction of timing information in the hit data package [82].

Timing

For the introduction of timing two approaches are considered. One would be the installation of dedicated timing planes around and at the end of the VELO. The second way would be the addition of timestamps to each hit at the ASIC level (4D tracking). A dedicated timing layer solution would benefit from a lower requirement on sensor spatial resolution, as only a single-hit resolution of $100\,\mu m$ would be necessary. Additionally, due to their distance from the interaction point, the sensor radiation hardness could be substantially lower compared to the ones used in the inner most layers. To allow for outlier rejection, at least three planes should be implemented. To find a viable solution, three scenarios were proposed:

- A set of three large timing planes placed before and after the detector, with each plane providing a time resolution of 25 ps. This would lead to an additional active area of $1.5\,m^2$ to cover the full VELO acceptance.

- Another solution would be to reduce the overall acceptance of the large timing layers with endcaps, which are technological equivalent, but only cover a region of $\eta \geq 2.8$. This would reduce the total material needed to $0.3\,m^2$

- The last option would be a endcap solution where the gap in the acceptance from previously mentioned solution is compensated by a barrel layer around the detector, but only for forward tracks. In addition, the timing resolution of the barrel layers need to be improved to 20 ps. The additional material needed would correspond to a total of $1.35\,m^2$.

All options will lead to the introduction of addition material which would degrade the performance of the detectors after VELO. As all planes are located at the end of the detector, an additional error would be introduced when extrapolating from the timing planes to the vertex, due to the different velocities of the particles.

For the 4D tracking option, no additional sensors are needed and the initial material budget of the detector can be maintained. For each hit, only a 50 ps time resolution has to be achieved to reach the desired 20 ps resolution per track. The challenge with this approach is maintaining performance at fluences of $5 \times 10^{16}\ n_{eq}\,cm^{-2}$ for the innermost sensors [81]. As can be seen in figure 3.16, all solutions would provide a similar primary vertex reconstruction efficiency, whereby the 4D solution provides the best resolution. Due to the smaller active area and reduced complexity, as well as overall better performance, this is the only solution considered in the scope of this thesis.

Sensor & ASIC considerations

For the implementation of 4D tracking, three silicon sensor technologies are under consideration: Hybrid pixel planar sensors, Low Gain Avalanche Diodes (LGADs) and 3D sensors.
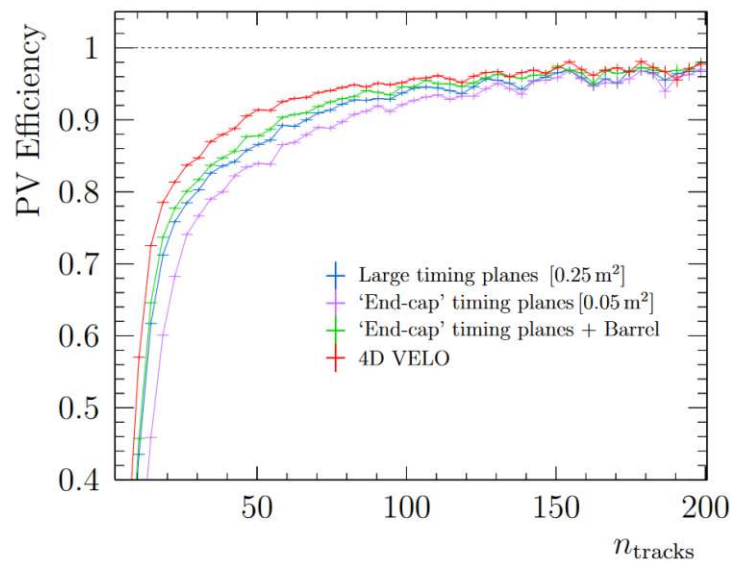
Fig. 3.16. PV reconstruction efficiency as a function of track multiplicity for the different timing implementations. Reproduced from Ref. [82].

Hybrid pixel planar detectors are currently used in Upgrade I. As they are widely used, they benefit from reduced cost and high availability. To achieve the desired timing performance, a reduced thickness of around 50–100 µm is considered. Thinner substrates will also improve radiation hardness, since shorter collection paths lead to less charge trapped in the bulk. Due to this decrease in signal charge, the signal to noise ratio poses the main challenge for this type of technology, especially after irradiation. A reduced thickness would also increase the ASIC input capacitance and therefore the electronic noise.

LGADs offer, due to the multiplication layer, a good signal to noise ratio. Such a gain layer poses challenges to fine segmentation as extra isolation implants are required between neighboring pads. Several new technologies, as iLGAD [84], deep gain layer [85] and trench isolation [86] can mitigate this issue. The main drawback of this type of sensors is the reduction of the gain layer by acceptor deactivation after irradiation. A total loss of gain is expected at fluences beyond 3×10^{15} n_{eq} cm^{-2} [87]. Currently studies are ongoing to improve the situation, for example by introducing lithium [88] .

3D sensors are a relatively new technology, in which the charge generation volume and drift distance are decoupled [89]. This allows for fast collection times, yielding excellent timing resolution, while maintaining a high deposited charge. Their main drawback is a relatively high capacitance and geometrical inefficiencies introduced through the electrodes.

On the ASIC front, the 28 nm process promises radiation hardness up to 10 MGy [90], while allowing for small pixel sizes. Smaller processes are not considered due to their prohibitive cost. Two candidate technologies are currently being explored. The Timespot ASIC offers a time resolution of 30 ps [91], while having a power budget of 1.5 W cm^{-2}. It is designed especially for 3D sensors. The other option currently being developed by the CERN microelectronics group is the PicoPix, designed to fit the specifications for Upgrade II.

Cooling considerations

As the time resolution of each ASIC can be improved by providing it with more power, new cooling is under consideration. As CO_2 cooling does not allow lower temperatures than $-56.6\,°C$, other possible coolants are under investigation. One promising candidate would be Krypton, which is radiation hard, and would allow cooling up to its triple point at $-157.4\,°C$. Further research is also under way to improve the critical bonding process of the silicon microchannel plates in order to prevent defects and allow for a reduction of production costs. If the sensors are to be replaced regularly, the possibility of 3D printed microchannels is appealing, since it allows for fast and cheap production of cooling substrates.

As these new technologies are implemented the current vacuum tank would need to be adjusted accordingly for different layouts. In case the secondary vacuum separation is removed, it has to ensure the purity of primary vacuum, while allowing for the movement of modules away from the beam during injection. If a decision is taken to replace sensors regularly, it has to be redesigned to facilitate fast switching of modules. With the redesign of the vacuum system new RF-foil designs are possible, like a wire mesh. This is essential as the RF-foil plays an important part in the detector performance (see chapter 4.2).

3.3.2 Upstream Tracker

For Upgrade II, the Upstream Tracker is going to replace its silicon strip sensors with silicon pixels. This would not only deal with the increase in occupancy, but also improve tracking due to the improved resolution in y-direction. For this MAPS are considered. MAPS could offer a relatively cheap way to tile the detector, while offering enough radiation hardness. To account for the inactive region of the MAPS, modules on different sides of the stave are staggered to ensure no inefficient regions in the tracking [81].

3.3.3 Mighty Tracker

In its current configuration the SciFi would see a reduction in tracking efficiency by 50% and increase in reconstruction time by a factor of 2 at Upgrade II conditions. It has therefore been proposed to replace the inner region with silicon detectors. This new combined detector will have the name Mighty Tracker. Each of the tracking stations will contain a silicon detector plane on each of their X-layers. Due to their pixelated structure no additional planes are needed in the other layers to achieve a reasonable resolution in y-direction. For the silicon sensors MAPS were chosen due to their low production costs, low material budget and radiation hardness. The scintillating fibres and SiPMs are going to need a replacement after Run 4. After irradiation, the attenuation change in the scintillating fibers is higher for blue-emitting than green-emitting ones. New green-emitting fibers are under investigation to replace the existing fibers. In addition, the implementation of micro lenses at the end of the fibers to focus the photons into the photo detectors improving the light yield is looked into. On the

SiPMs side, additional cooling is needed to keep the dark count rate after irradiation to a manageable level. This would also allow to reduce the detection threshold improving the overall light yield [81].

3.3.4 RICH

The main goal of the RICH detectors for Upgrade II is to achieve occupancies below 30% and a single-photon angular resolution σ_θ of less than 0.5 mrad. This already implies an improvement with respect to the current detector, while introducing new challenges due to the increase of luminosity of $1.5 \times 10^{34}\,\mathrm{cm^{-2}\,s^{-1}}$. To achieve this the currently used MaPMT photon detectors are planned to be replaced with SiPMs. Not only do they offer a high photon-detection efficiency, but are insensitive the stray magnetic field of the magnet, needing in turn no magnetic shielding. SiPM with a pixel size of $1 \times 1\,\mathrm{mm^2}$ would lead to the same occupancy compared to the $2.8 \times 2.8\,\mathrm{mm^2}$ MaPMTs used currently. This would allow reaching a peak pixel occupancy of 18% and 0.15/0.07 mrad resolution for RICH1/RICH2 under Upgrade II conditions. A negative point of SiPMs is the high dark count rate expected after irradiation. To compensate for the increase, the SiPMs need to be cooled. Another way to improve angular resolution would be to reduce the tilt of the spherical mirrors, but as this would make a rearrangement of the flat mirrors in the detector acceptance necessary, decreasing the photon yield. The effect of this on performance is currently studied. Due to the fast response time of SiPMs, inclusion of timing in the RICH would be possible. As the arrival of a particle at the RICH system can be calculated from the tracking information with at least a resolution of 20 ps, RICH hits can be used to reduce the combinatorial background and contribute to the determination of primary vertex times[81].

3.3.5 TORCH

TORCH (Time Of internally Reflected Cherenkov light) [92] is a new Time-of-flight detector located upstream of RICH2. This position was chosen to increase the time of arrival difference between different particle types at the detector plane. It uses a 1 cm thick quartz window as a Cherenkov radiator, in which the created photons are reflected internally to the top edge of the window. A mirror is then used to direct them into Micro-Channel Plate photon detectors (MCPs), where they are read out. As the measurement of the arrival time is critical in this detector, the time resolution of the MCPs plays a critical role. To achieve a time resolution of 15 ps per track, the MCPs need at least a resolution of 70 ps per photon, assuming a mean of 30 created photons per track. TORCH will offer excellent momentum resolution for low momentum particles, complementing the current RICH system. Its introduction could improve the yield for exotic hadron spectroscopy by 30%, while improving flavour tagging by 25-50% [54].

3.3.6 ECAL

The Upgrade II would not only lead to an increase in occupancy for the ECAL, but in overlapping electromagnetic showers. For most regions a reduction in granularity would be enough to compensate, but in the inner region an additional reduction of the Moliere radius is necessary. The introduction of timing is also needed to suppress background introduced by the higher pile-up. To account for the increase in granularity, a new Spaghetti Calorimeter is foreseen [93]. In such a configuration, scintillators act also as their own light guides and are oriented along beam direction. The new design would allow to define the granularity by the amount of fibers bundled and read out together. To deal with the high pile-up the detector is going to be separated along the beamline in two halves divided by a mirror. As the density of showers increase longitudinally in the detector, the timing data of the upstream half can be used to help the reconstruction in the downstream halve. To cope with the high radiation environment in the inner region crystal fibers are considered, while in the outer regions polystyrene fibers are deemed sufficient. To improve timing resolution of the ECAL, dedicated timing planes could be placed in the gap between the two halves of the detector.

3.3.7 Muon system

The main challenges for the Muon System for Upgrade II are the increase in rate, the corresponding increase in occupancy and dead time induced efficiencies. For the inner region this means a replacement of the MWPCs with a new technology with finer granularity. A promising candidate would be a new type of Micro-Pattern Gaseous Detector called μ-RWELL showing promising results in regards to radiation hardness. Another way to reduce the data rate is to increase shielding in front of the M2 station. As this space is currently occupied by the HCAL, this option is only viable if the HCAL is not deemed necessary for the Upgrade II. For the outer regions most of the MWPC can be reused. To minimize the amount of ghost tracks a new readout will be implemented, which reads out every cathode pad separately. For the MWPCs that need replacement, similar MWPCs with finer granularity are foreseen.

IP simulation

A key limiting factor for the design of the Upgrade II VELO is the fluence to which it is exposed. It is roughly inversely proportional to the square of the distance from the beam line. More precisely, the 1 MeV neutron equivalent fluence ϕ as a function of the radial distance r can be parametrised as

$$\phi \propto r^{-\kappa}.$$

Near $z = 0$, the exponent κ is 2.3. It decreases with increasing z and reaches 1.9 at the end of the VELO ($z = 82.5$ cm). At $r = 5.1$ mm (inner edge of the active area in the Upgrade I VELO), the fluence accumulated over the lifetime of the Upgrade I detector (50 fb^{-1}) is 8×10^{15} n_{eq} cm^{-2}. If we want to limit the fluence after 300 fb^{-1} to the same value, the sensors need to be retracted to $r \sim 11.1$ mm (see figure 4.1).

Without any compensatory measures, increasing the distance of the sensors from the inter-
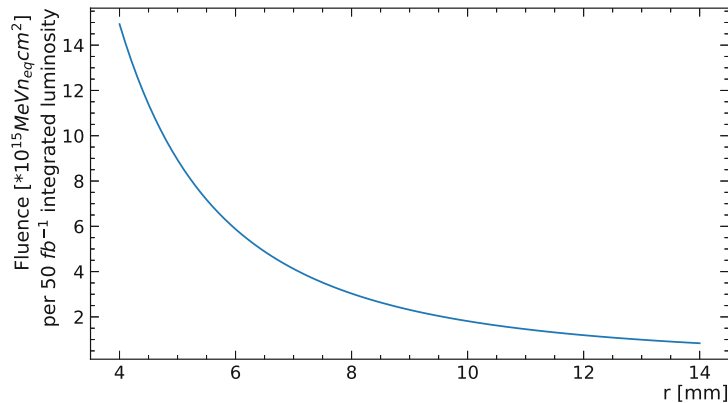
Fig. 4.1. Calculated fluence per 50 fb^{-1} at $z = 0$ as a function of the radial distance from the beam line.

action point will however worsen the impact parameter (IP) resolution in x and y direction, which we will use in the following as the main figure of merit for characterising the performance of the VELO. The impact parameter in x and y direction describes the distance of a track to the corresponding primary vertex at the z-position of the vertex (figure 4.2). As the single-hit resolution is the same in x and y and the sensor layout is symmetric with respect to the x- and y-axis, the IP resolution is the same in x and y. In this study therefore only the resolution in the x-direction is shown.

Assuming that only two points are used for extrapolating a track to the origin vertex, one
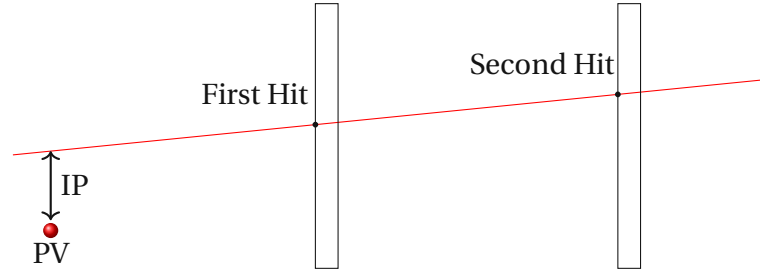
Fig. 4.2. Impact Parameter for a track reconstructed from two hits. The red line represent the reconstructed track.

can derive [94] an analytic expression for the impact parameter resolution

$$\sigma_{IPx}^2 = \underbrace{\frac{\sigma_0^2[(z_1 - z_v)^2 + (z_2 - z_v)^2]}{(z_2 - z_1)^2}}_{\text{extrapolation}} + \frac{1}{p_{\mathrm{T}}^2} \underbrace{\left(R^2 \frac{13.6\,\mathrm{MeV}}{\beta c} q \sqrt{\frac{x}{X_0}} \left[1 + 0.038 \ln\left(\frac{x}{X_0} \right) \right] \right)^2}_{\text{multiple scattering}}, \quad (4.1)$$

where σ_0 is the single-hit resolution, z_1, z_2 are the z-coordinates of the two hits, z_v is the z-position of the primary vertex, R is the radial distance of the first measurement from the beam line, p_{T} is the transverse momentum of the particle, q is the particle charge, βc is the velocity of the particle and x/X_0 is the relative radiation length traversed by the particle up to the second measured hit.

The first term describes the extrapolation error due to the finite resolution of the two hits. The second term incorporates the extrapolation error due to multiple scattering of the particle. Moving the sensors away from the beam line increases the distance of the two measurements to the primary vertex and, consequently, both the extrapolation and the multiple scattering term.

Figure 4.3 shows the IP resolution of the Upgrade I VELO as a function of p_{T}^{-1}, calculated using the simulation tool described in Chapter 4.1, and fitted with a straight line. It can be seen that in the limit of low p_{T}^{-1} the IP resolution converges to the hit resolution, while for $p_{\mathrm{T}}^{-1} = 3\,\mathrm{GeV}^{-1}$ c it degrades to 50 µm. If the inner radius of the sensors has to be increased without worsening the IP resolution, the other free parameters in equation 4.1 need to be improved . This means an improvement in single-hit resolution σ_0 and a reduction of the material budget x/X_0.

As a start two extreme layout scenarios are considered to define the limits of the parameter space:

- Scenario A: Sensors are kept at a distance of 5.1 mm from the beam line. Such an approach leads to an increase of the fluence by a factor of 6 and the hit rate by a factor of 7.5 with respect to Upgrade I [81]. The detector layout and the RF-foil can be kept the same, while new sensors and ASICs that can withstand the harsh environment have to be developed. To mitigate radiation hardness constraints, the detector can be designed for periodic replacements of the modules.
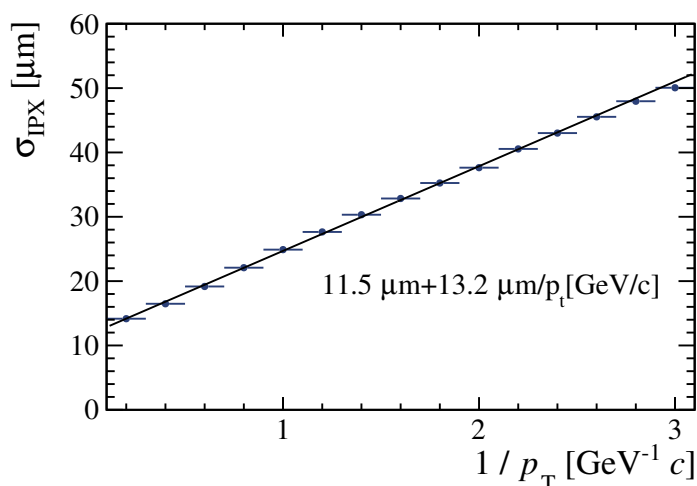
Fig. 4.3. Simulated IP resolution of the Upgrade I VELO.

- Scenario B: In this scenario the sensors are moved to 11.1 mm. The fluence accumulated in the "hottest" region of the sensor is then the same as for the Upgrade I detector (after $50\ \text{fb}^{-1}$). The hit rate will slightly increase compared to Upgrade I. As discussed later, this would impose a reduction of the thickness of the RF-foil, sensors and/or ASICs. The overall layout of the detector would have to be adjusted to maintain the required acceptance ($2 < \eta < 5$). Depending on the sensor shape, this could lead to the addition of stations and an increase in detector length.

As these two scenarios represent the limits of the parameter space, solutions in-between can also be considered as a compromise.

To get an estimate of the possible parameter-space, we use Eq. (4.1) in combination with ray-tracing simulation. The two terms of Eq. 4.1 were calculated separately to illustrate the dependencies of each term. The IP resolution was calculated by taking the mean of 1000 tracks for the whole ϕ range, whereby the starting z-positions are randomly drawn from a Gaussian distribution with its mean at the interaction point and a standard deviation of the luminous region (6.3 cm for Upgrade I). The ray-tracing was used to determine the radii and z-positions of the hits on a track. For the hit determination a simplified description of the active area of the detector is used. It was approximated by a square with a central quadratic cut-out with a side length of 2 times the inner radius. The side length of the outer square is chosen to be 56 mm longer than that of the inner square to keep the active area for all inner radii roughly the same. As pixel resolution the mean Upgrade I resolution of 12.5 μm was implemented. To improve the agreement with the results shown in the Upgrade I TDR [55], the first and last hit on a track were used for calculating the extrapolation term. This is due to the fact that the full simulation uses all hits along the track, which results in a better resolution. For simulating layouts with an inner radius larger than 5.1 mm the planes were

moved further out in r but not in z. The material encountered up to the second hit is taken from literature [55]. As the IP behaviour strongly depends on η each plot represents a fixed η value. The presented value of 3.5 was chosen as it represents a mean behaviour between low and high η tracks. The results can be seen in figure 4.4 for the two contributors to the resolution. The black lines represent isolines of equal IP resolution. The background color illustrates the fluence as a function of radius. For the calculation of the fluence at a certain radius, only a radial dependence of r^{-2} was assumed.

The top plot in figure 4.4 illustrates the extrapolation term. A linear relation between the hit resolution and the inner radius is observed if the same IP resolution must be kept the same as Upgrade I. For example, if the sensors are moved to 11.1 mm, the single-hit resolution of 10 µm is needed to achieve the same performance as Upgrade I. An improvement of the IP resolution by a factor two would require a pixel resolution of around 5 µm. The three scenarios marked in the plots represent the three working points that were considered in this thesis and are discussed in detail at a later point in this chapter.

The bottom plot illustrates the effect of multiple scattering on the IP resolution. It can be seen that, even if the radial distance is only increased a little, a drastic reduction in the material budget must be implemented. Only at high radii this effect becomes less pronounced. For 11.1 mm this means a reduction of the material by 70%.

Due to several reasons the results should only be considered as starting points for the simulation. Firstly, only tracks for a single η are taken into account. Secondly, the calculation does not include the improvement in IP resolution by using all the hits of a track or account for the use of any filter to improve the track fit. Thirdly, the z-layout of the planes is not re-optimised for the different radii. Lastly, the scattering is modelled as a single continuous scatterer containing all the encountered material along the track. An in-depth discussion on the parameters driving the IP resolution can be found in section 4.2.
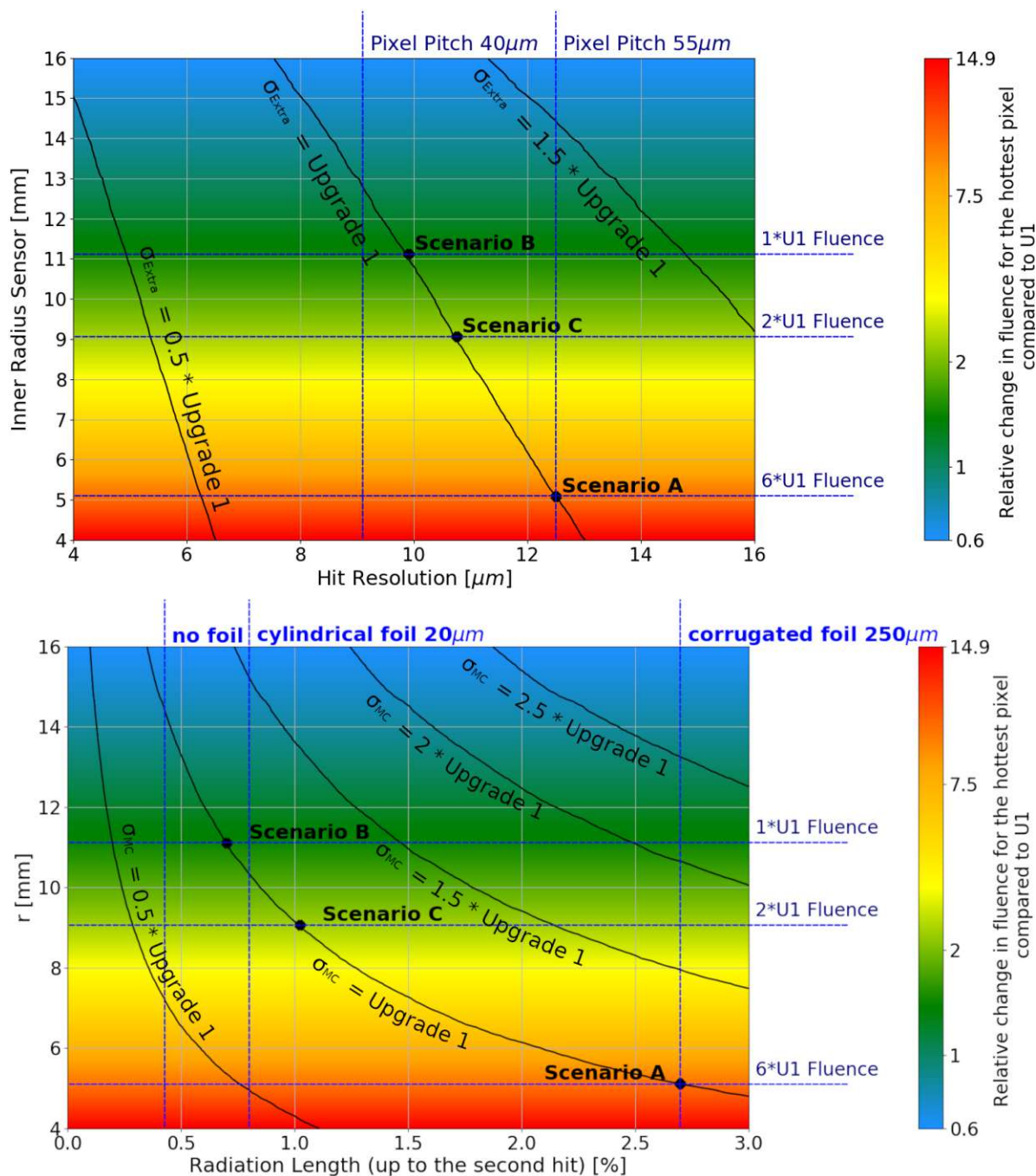
Fig. 4.4. Analytic calculation of the different terms of the IP resolution for $\eta = 3.5$. Black lines represent areas of constant IP resolution. Scenario C represents a solution between A and B. An in detail explanation of it can be found in section 4.5. **Top**: Extrapolation term of the IP resolution. **Bottom**: Multiple scattering term of the IP resolution.

4.1 Simulation method

The main topic of this section will be the simulation setup developed for this study. The development of a new tool was deemed necessary, as the full LHCb simulation and reconstruction

framework was too specialised to enable a fast turn-around for new detector designs. It will give an overview about the structure and the different steps of the simulation and introduce all simplifications that were made. As the Upgrade I detector is used as the baseline of new geometries and simulation, table 4.1 summarizes some key design parameters of the Upgrade I VELO.

4.1.1 Detector description

The detector geometry is described using the DD4HEP [95] C++ tool kit [96]. For each geometry a compiled factory is created, which contains the instructions on how to build the detector from primitive geometrical shapes and defines the hierarchy of these objects and their properties used later for the simulation of particle-matter interaction. As a starting point for all new models, an existing DD4HEP model of the Upgrade I VELO (figure 4.5a) was used. As this initial model was still in development, it contained several errors which were corrected until the material scan was equal to the DDDB (Detector Description DataBase)[1] model of the Upgrade I VELO.

To make the detector easily modifiable, a DD4HEP model with reduced complexity was designed to be used for all further simulations. Therefore, parts that are outside the acceptance such as the vacuum tank, the RF box, the module support structures and the wake field suppressors were removed. The sensors, ASICs, bump bonds, glue layers and cooling substrates were replaced by slabs of the corresponding material, with thicknesses of 200, 200,20,70 and 500 μm to keep the encountered material along the track the same. This slightly increases the covered area of the sensor as seen in figure 4.5b but does not affect the IP resolution substantially. The simplified model also does not include the sensor tiles on both sides of the cooling substrate. This was done as the tiling is highly dependent on the size of the ASICs and sensors and the simulations should be as universal as possible. This change leads, compared to the Upgrade I detector, to a small difference in the distance of the first hit from the primary vertex depending on whether the sensor is located upstream or downstream of the cooling substrate. To compensate for this, the silicon planes are moved a little closer to the middle of

---

[1]DDDB is the detector description tool kit used in the simulation framework [97] of the initial LHCb experiment. It is currently being replaced by DD4Hep.

Mean hit resolution	12.5μm
Width of inactive edge around sensor tile	0.45 mm
Closest distance of the sensor to the beam line	5.1 mm
Closest distance of the RF foil to the beam line	3.5 mm
z position of the last module	750 mm

Table 4.1. Key parameters of the Upgrade I Vertex Locator.

(a)   **(b)**
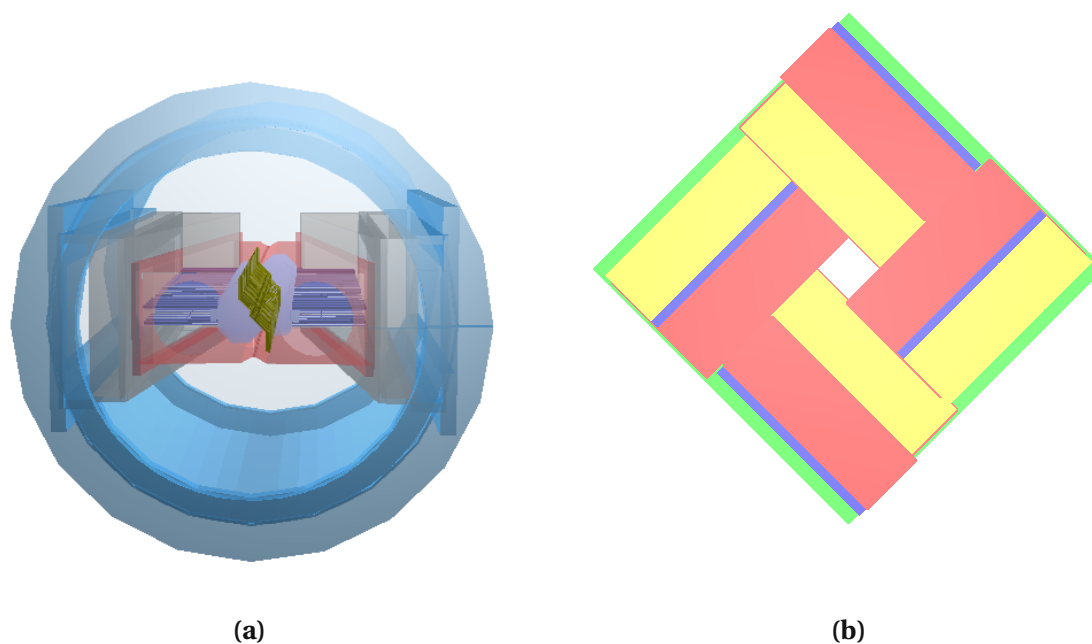
Fig. 4.5. a: DD4HEP model of the Upgrade I VELO. **b**: Coverage of the VELO sensor compared to the simple sensor (green).

the station to ensure the same mean value for the radius of the first measured point r_F.

To validate the geometry models, a set of benchmark plots was used. One important parameter for the design of a new detector is the radiation length encountered along tracks. As the fraction of a radiation length traversed by a particle influences the amount of multiple scattering it experiences, it should be kept as small as possible. To calculate the radiation length, ray tracing was used. Tracks are created for η and ϕ in the acceptance range with a starting point at the origin. The endpoint of these tracks is chosen by defining a z coordinate corresponding to the end of the VELO. For the layout used in Upgrade I this corresponds to 82.5 cm. A comparison of the results of the tool using the reduced DD4HEP model to a similar scan done using the DDDB model used for the full reconstruction can be seen in figure 4.6.

No difference is seen between the DDDB and DD4HEP model. The reduced geometry shows a lower material budget up to the first hit, with the difference to the full geometry being higher for low η and decreasing with increasing η. This is due to the fact that in the simplified geometry the sensors are placed only on one side of the cooling substrate, whereas for the full simulation they are placed on both. This causes particles that hit sensors on the downstream side of the substrate to traverse the ASIC before the first hit. As the distance that is traversed in the ASIC increases with decreasing η, this leads to an η dependent difference. The relative high discrepancy between the full model and the reduced one for the full detector scan at low η is due to the fact that all the support structures are not included in the reduced model, but would be included when a track is extrapolated to the final z-position. Additionally, the mate-
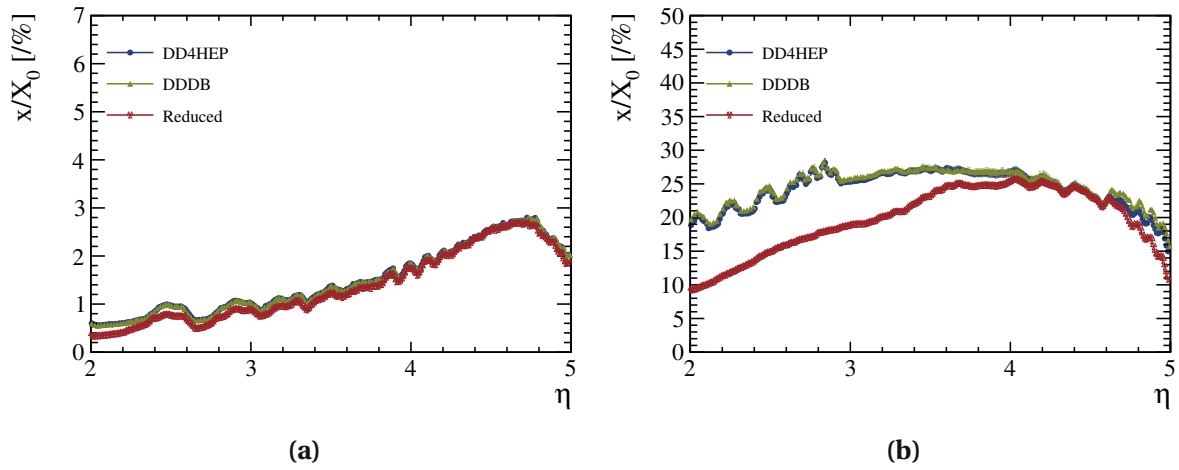
Fig. 4.6. Material up to the first measured point (a) and up to $z = 82.5$ cm (b) for the Upgrade I DDDB, DD4HEP model and the reduced geometry as function of η.
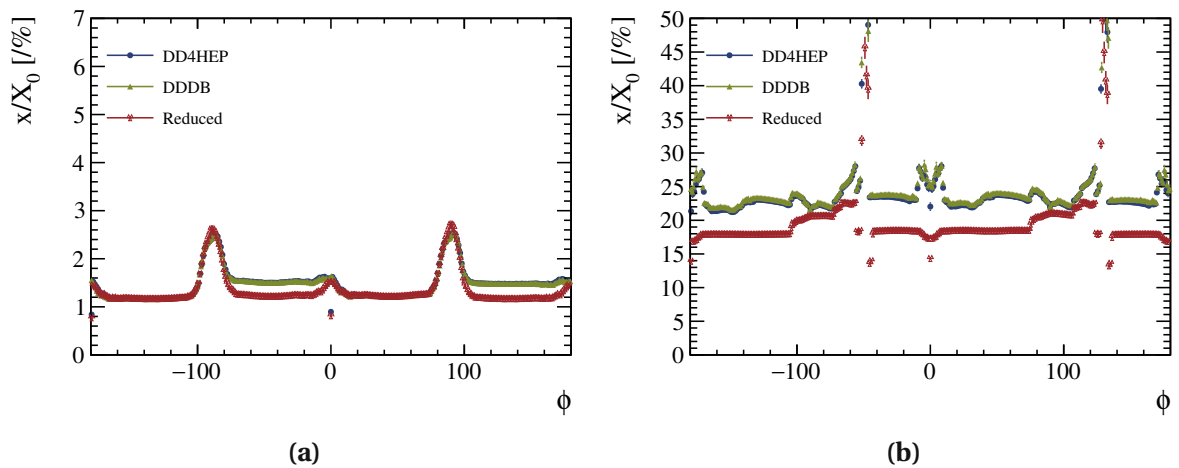
Fig. 4.7. Material up to the first measured point (a) and up to $z = 82.5$ cm (b) for the Upgrade I DDDB, DD4HEP model and the reduced geometry as function of ϕ.
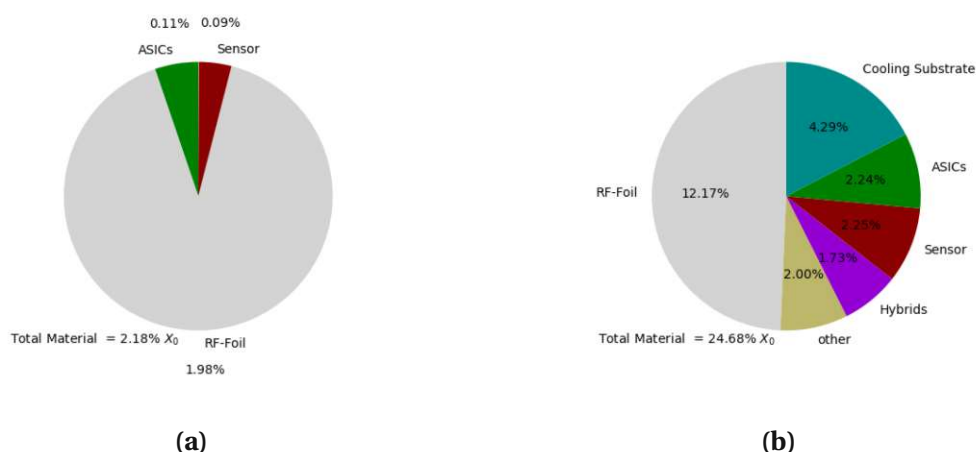
Fig. 4.8. Encountered material for the different components of the Upgrade I VELO up to the first measured point (a) and up to $z = 82.5\,\mathrm{cm}$ (b).

rial between the two geometries should only differ in the region of $-90°$ to $0°$ and $90°$ to $180°$ in ϕ, where the sensors on the downstream side are located. As can be seen in figure 4.7 this is the case. For the overall material the difference is expected to be substantial as in the reduced geometry all the support structures are not modelled. This should be more prevalent in the low η region as all the material contributions of the additional components are amplified due to the high track angle. The increased difference in the high η region is due to the RICH1 exit window, which is not implemented in the simplified model. The contribution of different detector parts to the material budget can be seen in figure 4.8. For the full detector the RF-foil contributes nearly 50% to the total material budget, followed by the cooling substrate with 17%. The ASICs and sensors each contribute 9% to the total material budget.

The calculation of the acceptance range is done similarly to the material budget, as it uses ray tracing to count the hits. For each combination of η and ϕ several tracks are simulated, where the starting z-positions are randomly drawn from a Gaussian distribution with its mean at the interaction point and a standard deviation given by the σ of the luminous region (see table 4.2). At least four hits on the track are needed to count as reconstructible. Figure 4.9 shows that the fraction of reconstructible tracks calculated using this method corresponds to the nominal acceptance ($2 < \eta < 5$).

4.1.2 Event simulation

The LHCb simulation application (Gauss on Gaussino [98]) was used to generate minimum-bias pp collision events using Pythia and transport the resulting particles through the detector geometry (described using DD4HEP) using Geant4 [99]. All events are generated at Upgrade II conditions (Table 4.2). For each energy deposit by a charged particle in a sensitive region of
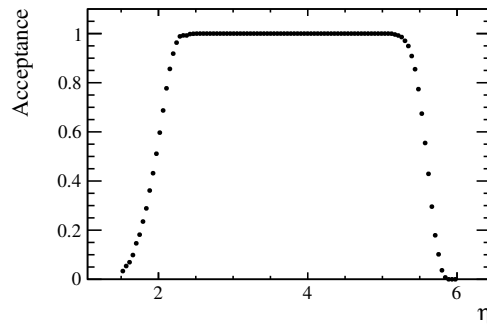
Fig. 4.9. Fraction of tracks with at least four hits as function of η, calculated using the DD4HEP model.

	Upgrade I	Upgrade II
Luminosity [cm^{-2} s^{-1}]	2×10^{33}	1.5×10^{34}
Bunch RMS [mm]	90	76.1
σ_{lum} [mm]	63	44.7
Interactions per bunch crossing	5.2	42

Table 4.2. Parameter used for sample generation in Gauss. Bunch RMS stands for the longitudinal extend of the simulated bunches and σ_{lum} for the longitudinal extend of the interaction region

the detector, the simulation application creates a Monte Carlo hit (MCHit) object, which contains information about the entry and exit point of the particle and a link to the corresponding Monte Carlo particle (MCParticle) object. An MCParticle contains information about the kinematic properties of the particle and a link to the associated vertex (MCVertex). For each event, the MCHits, MCParticles and MCVertices are saved to an output file.

4.1.3 Reconstruction

As discussed in section 3.1, the most relevant tracks for physics analyses are so-called long tracks which have measurements both in the VELO and the tracking stations downstream of the magnet. For calculating the IP resolution in the fast simulation, which only includes the VELO, we apply a set of cuts to select a sample of particles with similar kinematic properties as long tracks. Specifically, we select particles that:

- have a pseudorapidity in the LHCb acceptance ($2 < \eta < 5$),

- have a momentum greater than 2.5 GeV c^{-1},

- originate from a vertex close to the primary vertex,

- leave at least four MCHits in the VELO.

To validate these cuts, we compare the distribution of tracks as function of different track parameters in the full simulation and the fast simulation. To make these two comparable the distributions are scaled to the same number of events. By looking at the distribution of η and p_T^{-1} a reasonable agreement between the two simulations is seen. The drop of tracks at $\eta \sim 4$ (figure 4.10) is due to a loss of particles which interact with a structure downstream of the VELO. In the momentum distribution the full simulation has slightly more particles with higher momentum. This is due to a loss of low momentum particles which are deflected by the magnet and therefore do not have enough hits in the downstream region.
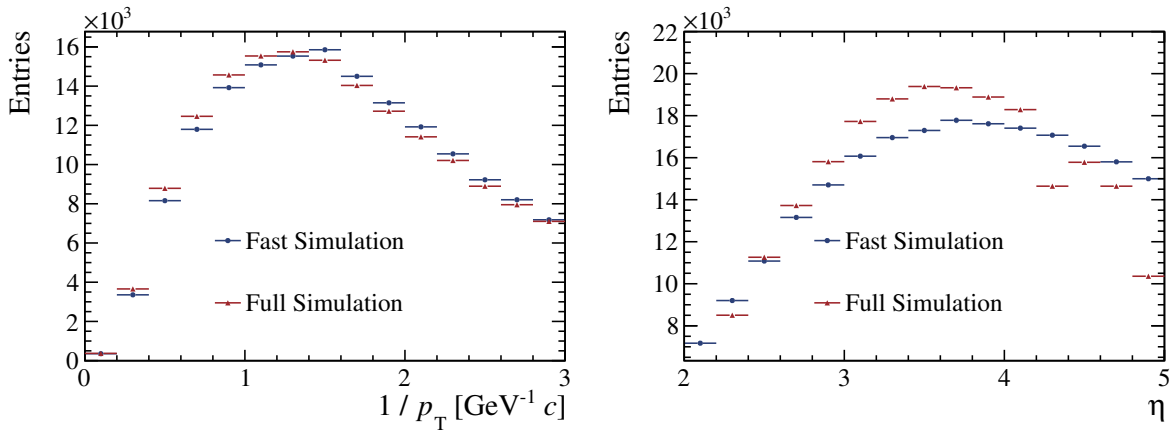
Fig. 4.10. Comparison of parameters of reconstructed particles between full simulation and fast simulation.

For the calculation of the IP resolution the program groups all MC hits of one particle to a track. The measurement process is approximated by smearing the x- and y-positions of each hit by the pixel resolution according to a Gaussian distribution. For all Upgrade I simulations a single hit resolution of 12.5 μm is assumed, which corresponds to the mean cluster resolution. Hits in the inactive region of the sensors are discarded during track reconstruction.

Mathematically, a track is defined by a collection of state vectors. A state vector contains the x, y and z coordinates of a hit on the track and the track slope in x and y at the z-position of the hit. As a starting point the track state is calculated using a straight-line fit. A Kalman filter then takes the initial state calculated by the linear fit and iterates over each measurement, starting from the most downstream one, calculating an improved estimated state, by taking the encountered perturbation terms and measurement error into account [100]. The perturbation term originates from the multiple scattering along the track, which leads to a wrong assumption of the track slope. The measurement error originates, as the name implies, from the finite spatial resolution of the hits and leads to errors for the slope and the x and y coordinates. For the calculation of the multiple scattering error after each hit the simulation uses the x/X_0 calculated from the DD4HEP model between the two hits and the true particle momentum to calculate the standard deviation of the track angle distribution using Molière's theory of multiple scattering (Eq. 2.3). When the first hit (closest hit to the interaction point) in a track is reached, it is then extrapolated to the z-position of the vertex using the state of

(a)

(b)
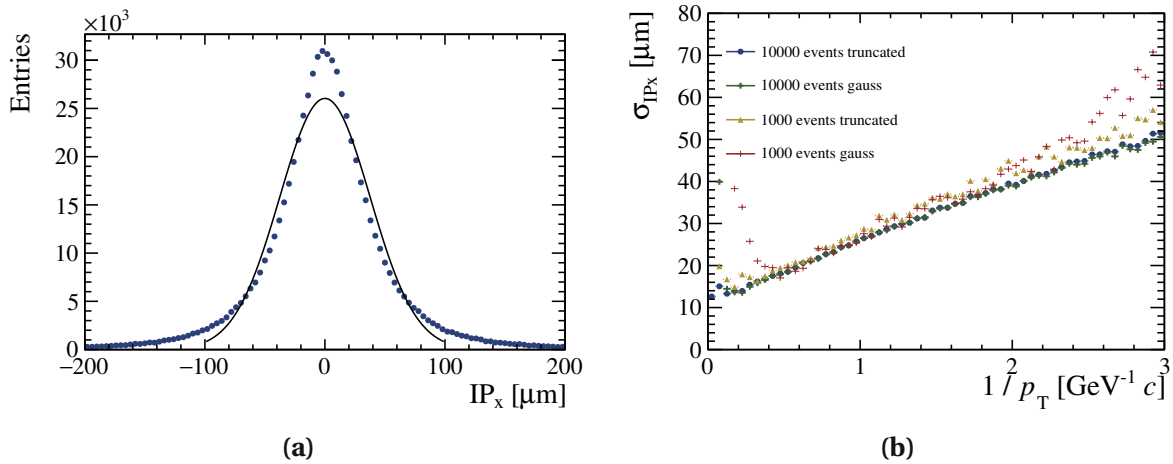
Fig. 4.11. a: Example of a IP distribution with an applied Gaussian fit for the region between -100 and 100 µm. **b**: Comparison of the IP resolution for Upgrade I calculated by different methods and number of simulated events.

the first hit. As a last step the impact parameter is calculated using the true (MC) vertex and all relevant parameters of the track are saved in a ROOT tree.

Figure 4.11a shows a typical distribution of the IP with an applied Gaussian fit. Two methods were evaluated for calculating the impact parameter resolution from the impact parameter distribution. The first method is fitting the IP distribution with a Gaussian distribution, but this is not an optimal solution as the IP distribution is not Gaussian and has a long tail (figure 4.11a). The second method calculates the RMS, removes entries further away than three standard deviations and repeats the process until the change in RMS between two steps is smaller than 0.01 %. The difference between the two methods for different sample sizes can be seen in figure 4.11b. The truncated RMS method is more stable, even for small data sets and was therefore used for all further simulations.

4.1.4 Validation

First, the results from the fast simulation were compared to the full LHCb simulation framework. For this all simulation steps were done in the fast simulation framework with the full detector geometry. The results were then compared to the full simulation of the same geometry in DDDB and the same generation parameters. As can be seen from figure 4.12, the IP resolution as function of p_T^{-1} calculated using the fast simulation is in close agreement with the full simulation. Only for tracks with high momentum the IP resolution is worse.
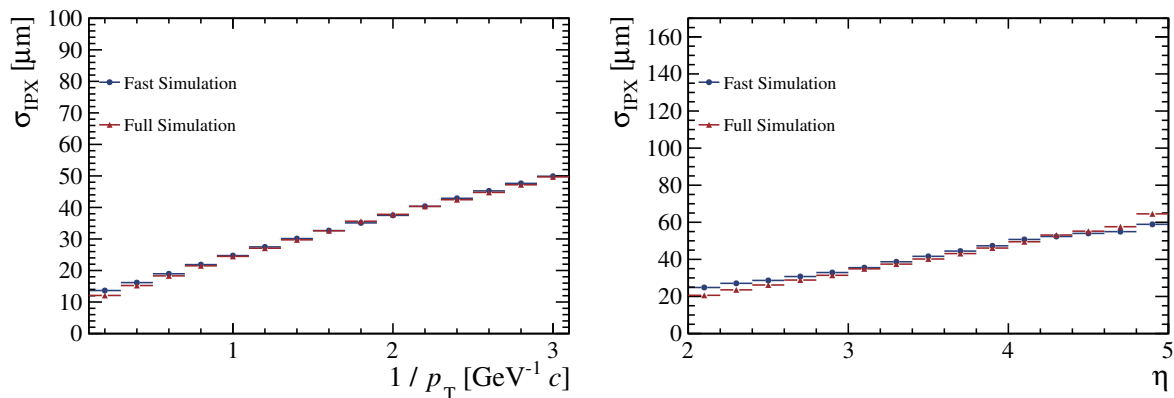
Fig. 4.12. Comparison between the IP resolution calculated using the full simulation and the fast simulation.

To evaluate the impact of reduction in complexity of the geometry, simulations of the simplified geometries are compared to the IP resolution using the full model of the Upgrade I VELO. As can be seen in figure 4.13, these simplifications do not lead to a significant increase or decrease in IP resolution compared to the full geometry.
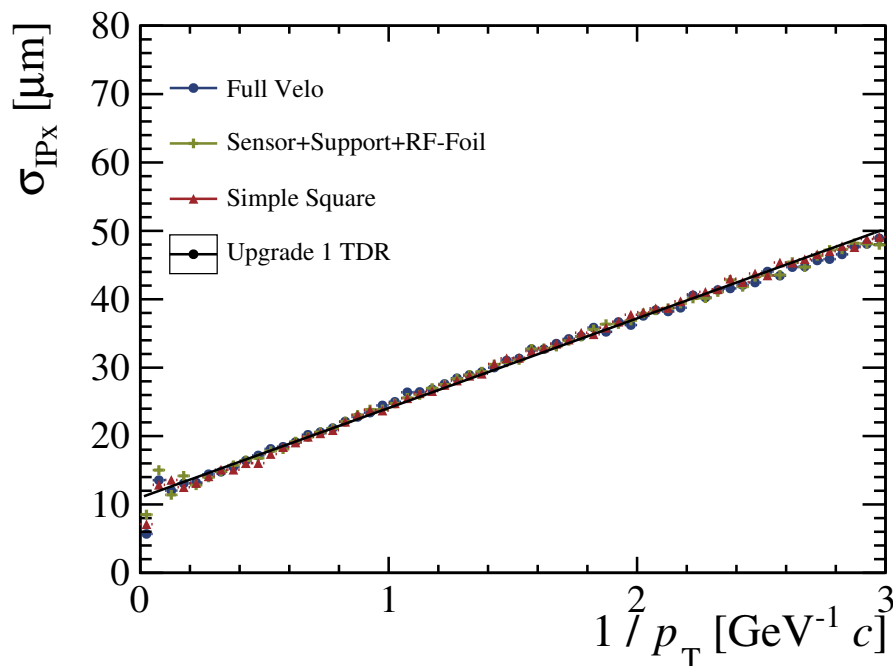
Fig. 4.13. IP resolution for different levels of simplification of the VELO geometry [54] description.

The particle momentum is an important parameter in the Kalman filter to estimate the scattering angle. In the full LHCb simulation and reconstruction framework, the momentum measured using the tracking system is used. In the fast simulation, the true momentum of the generated particle is used. To study the effect of not using the calculated momentum of

the track, the simulation was run one time using the true momentum and the other time using a smeared momentum. The smeared momentum was obtained by applying a Gaussian error of 1% on the true momentum [101]. It can be seen in figure 4.14 that the effect is small and does not affect the validity of the simulation.
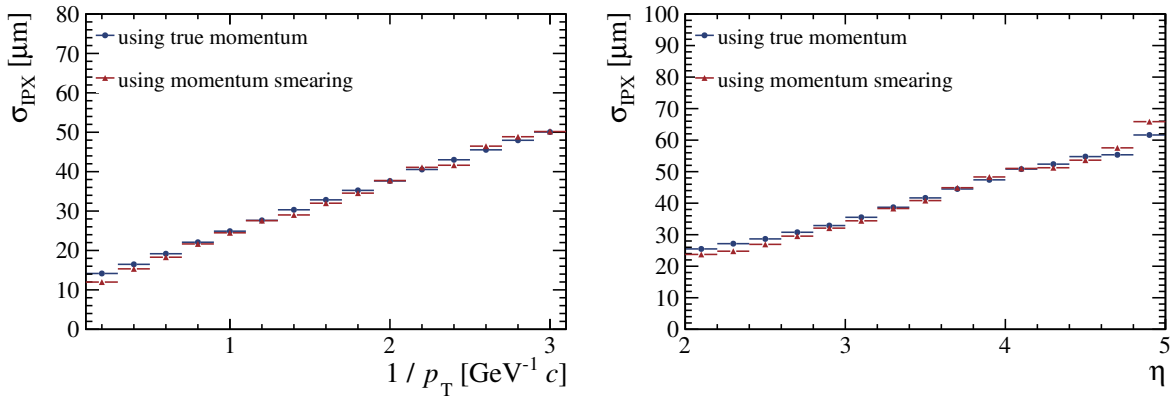
Fig. 4.14. Comparison of IP resolution using the true momentum and a reconstructed momentum.

As the guard-ring's position and shape depends on the sensors that are developed for the different shapes, this simulation does not include it in the DD4HEP model. Instead, an exclusion region for the hits in the guard-ring section that is closest to the beam is defined and applied during the track reconstruction. This ensures that the first hit cannot be closer than the first pixel. No exclusion region is defined for the other guard-ring parts. To assess the impact of tracks that have hits in the active part of the guard-ring, a model including the full Upgrade I guard-ring was compared to a simulation using an active guard-ring with an exclusion zone. Due to the low relative area of the active guard-ring not modelling the guard-ring does not lead to a substantially better IP resolution (figure 4.15).
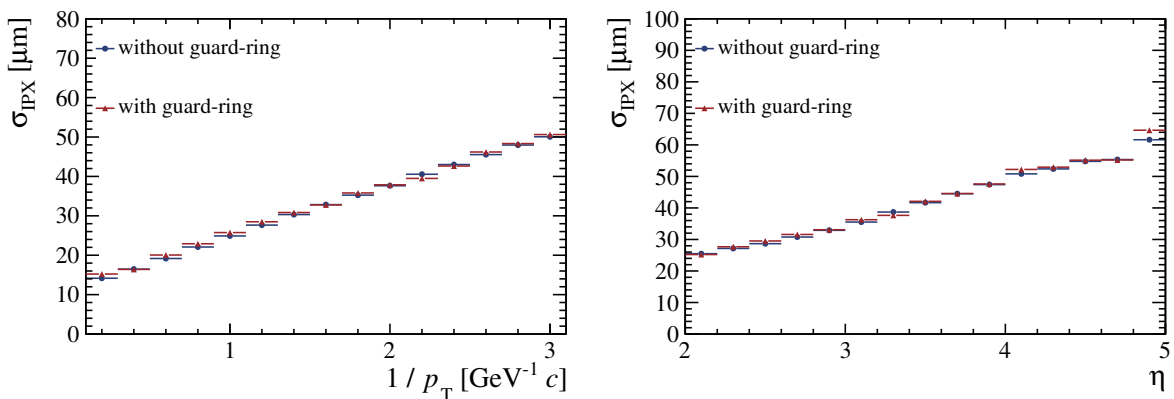
Fig. 4.15. Comparison of IP resolution using guard rings implemented in the model and approximated ones.

4.2 The impact of material on the IP resolution

One of the most important parts of the detector is the RF-foil. It is the first part a particle interacts with inside the detector. The particle scatters in the foil and introduces the first extrapolation error when the measured track is extrapolated back to the primary vertex. To visualize the effects of this scattering two different foils were simulated. Firstly, a corrugated foil with a uniform thickness of $250\,\mu m$, which introduces a relatively uniform material encountered up to the second hit as a function of pseudorapidity. Secondly, a cylindrical foil of $250\,\mu m$ thickness, which shows a strong dependence of encountered material as a function of η. The thickness of the foils was chosen to make the relevant effects more visible, while still being in a realistic range. For the corrugated foil the closest distance to the beam line is 3.5 mm. The cylindrical foil therefore also has an inner radius of 3.5 mm. For easier comparison all simulation results using the cylindrical foil are plotted in red using triangular markers, whereas results using the corrugated foil are plotted in blue using circles. The grey curve displays the relative population of each bin. A comparison of the encountered material of the two different foils can be found in figure 4.16. In the following the terminology *material up to the first hit* and *material up to the second hit* does not include the material of the corresponding sensor.
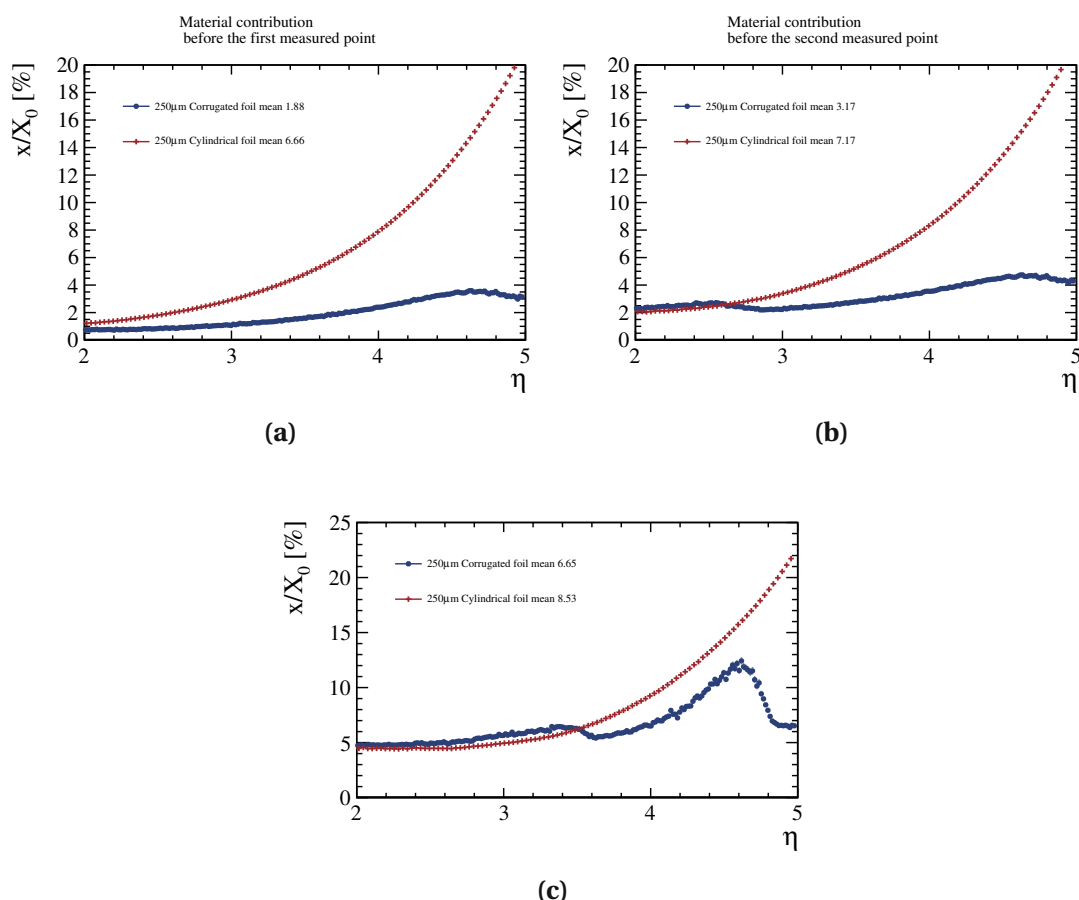
Fig. 4.16. Comparison of encountered material for different RF-foil shapes. **a**: Material up to the first hit. **b**: Material up to the second hit. **c**: Material encountered along the whole track.

To design a new layout the contribution of the different detector parts on the IP resolution must be well understood. In this section a slow increase in model complexity is used, to illustrate the different effects at play. This is done starting from a single hit and adding slowly all steps of the track reconstruction. In addition, a brief explanation is provided why only the cylindrical foil is considered for all new designs in this thesis. For this study the sensor planes were placed at the same location as defined for Upgrade 1.

First only the first hit in a track is used for the IP calculation. As the slope of the particle after scattering in the foil was not directly accessible in the simulation framework, an approximation had to be found. For this the slope between the entry and exit point in the sensor of the first hit was used. This includes the scattering in the sensor itself. Due to the small thickness of $200\,\mu m$, this introduces only an additional material budget of around $0.2\%\,X_0$ for tracks inside the η acceptance and can be therefore ignored. The difference in encountered material inside the sensor is small and does not influence the η dependence of the resolution. In the following plots the IP resolution is shown as a function of the inverse transverse momentum $1/p_T$, the pseudorapidity η, the angle of the track in the x-y plane ϕ and the momentum of the particle p. To exclude the impact of the pixel resolution only the MC hits were used for the position of the hit. As can be seen by comparing figure 4.17 and figure 4.16 the IP resolution generally follows the trend of the encountered material but in the range $2 < \eta < 2.6$ the IP-resolution of the corrugated foil is equal to the one of the cylindrical foil, despite the encountered material being lower. This can be explained by the fact that the entry point for a corrugated foil is closer to the sensor than for the cylindrical foil. Due to this longer lever arm between the primary vertex and the hit in the RF foil the extrapolation error made in this case is more significant. A sketch of this effect can be found in figure 4.18a a, whereby the green line represents the track extrapolated from the hit and the blue line the true particle track. This is especially important in the region mentioned before, as the overall distance to the primary vertex is negligible compared to higher η tracks. The slight change in distance has therefore a bigger and more visible impact in this region. The increase in r_F as function of η (figure 4.18b) does not play a significant role in this case, as it is compensated by the track angle and will lead to roughly the same foil entry point.

Until now only a perfect sensor with a perfect position resolution was considered. Now a finite position resolution was included by setting it to $12.5\,\mu m$, which corresponds to the mean hit resolution after clustering for Upgrade 1. As expected, this led to a worse IP resolution as another uncertainty was introduced (see figure 4.19). No other effects can be seen, as for this case the pixel resolution does not affect the extrapolation of the track.

In the next step the second hit was included and a linear extrapolation of the two hits was used to calculate the IP resolution. Again, first a perfect sensor was simulated. For the cylindrical foil only the material of the sensor module is added, while for a corrugated foil the foil
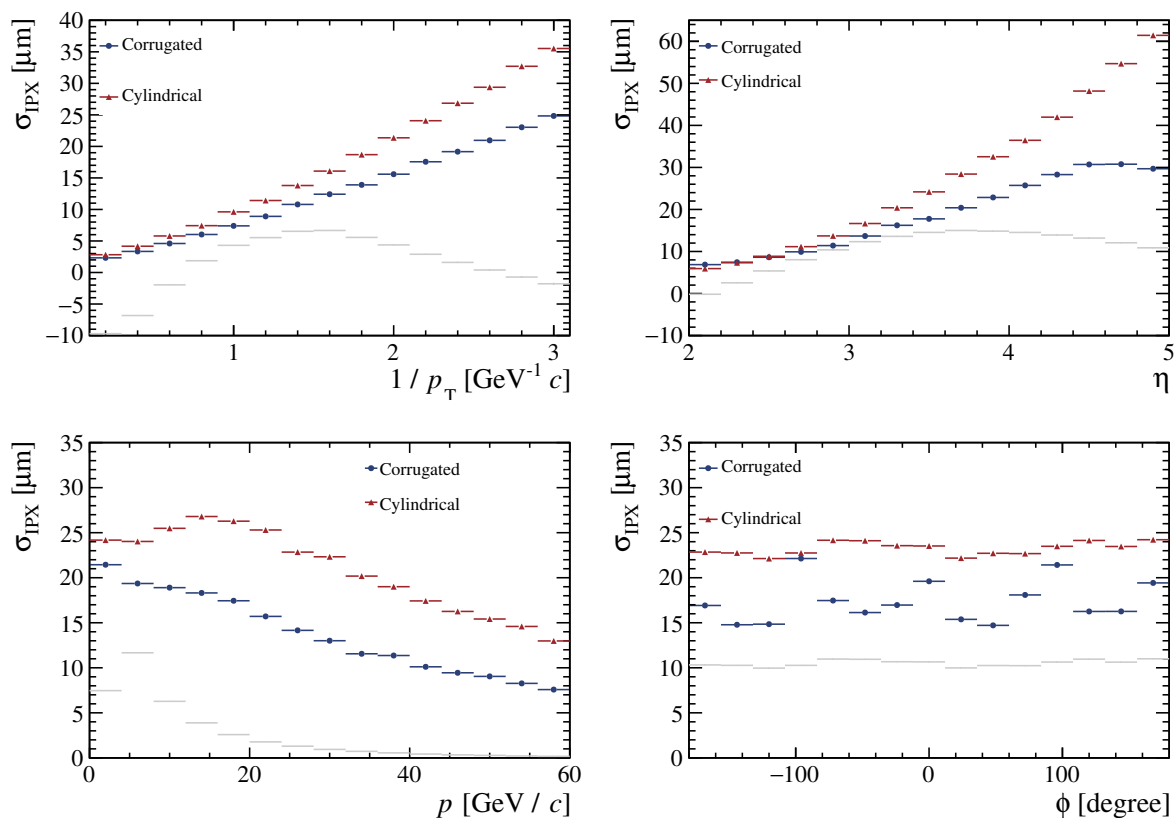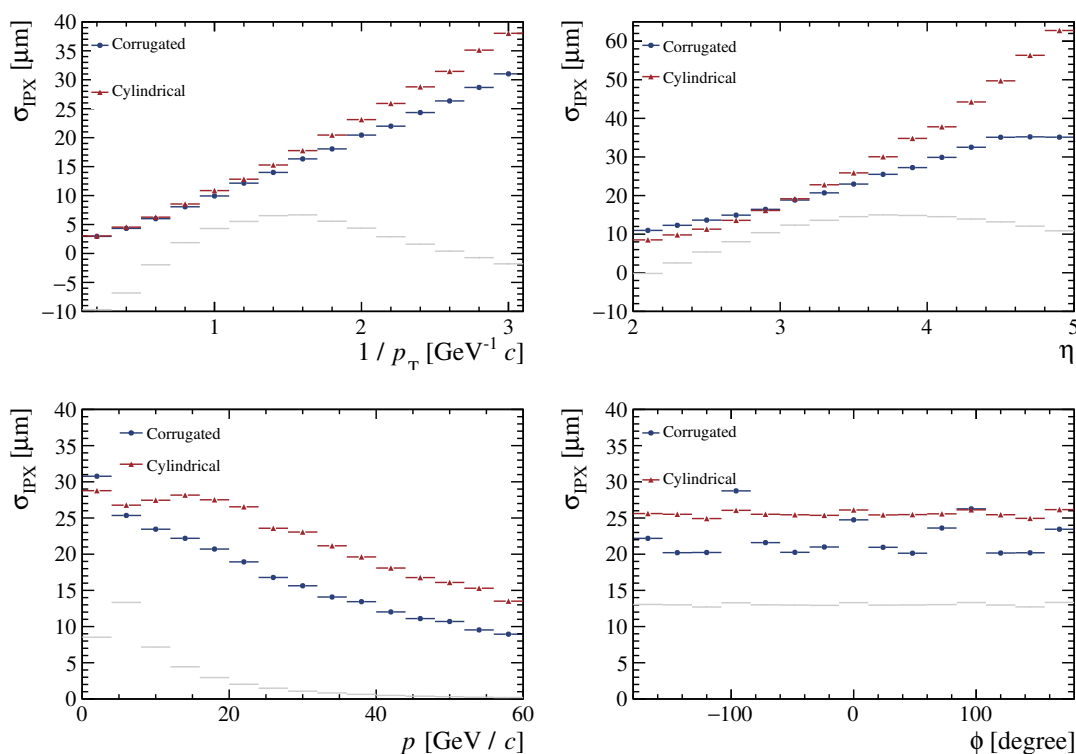
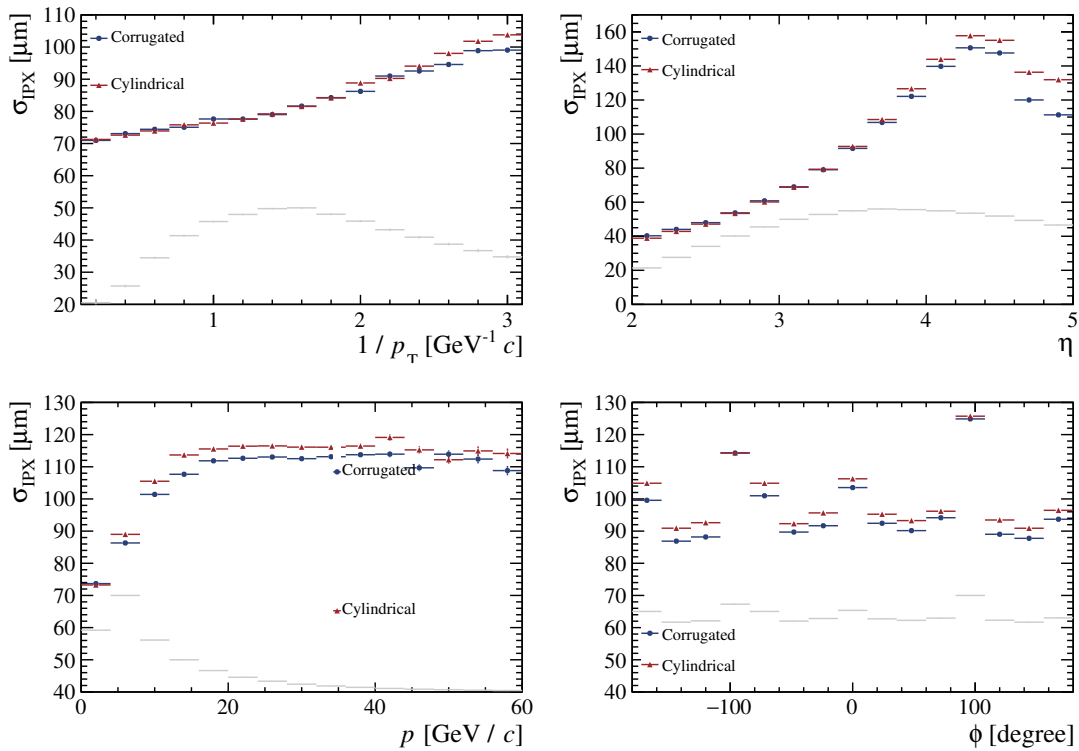**Fig. 4.17.** Comparison of the IP-resolution between a 250 μm corrugated (blue) and a 250 μm cylindrical foil (red) for true hits (1 hit). It is plotted against the inverse transverse particle momentum, η, true particle momentum and polar angle of the track.


(a)   **(b)**
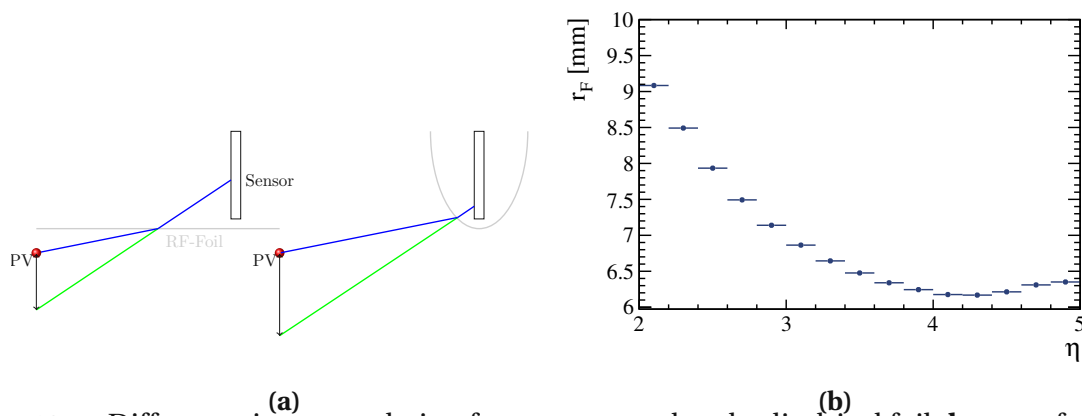
Fig. 4.18. a: Difference in extrapolation for a corrugated and cylindrical foil. **b**: r_F as function of η.

is traversed up to two more times. This leads to less material for a cylindrical foil up to $\eta = 2.6$ (figure 4.16 b). For the corrugated foil the additional scattering centers lead to a larger cumulative scattering error compared to a single scatterer with the same material [102]. This results in a better IP resolution of the cylindrical foil compared to the corrugated one, even far past η of 2.6, as expected from the material distribution (figure 4.20).
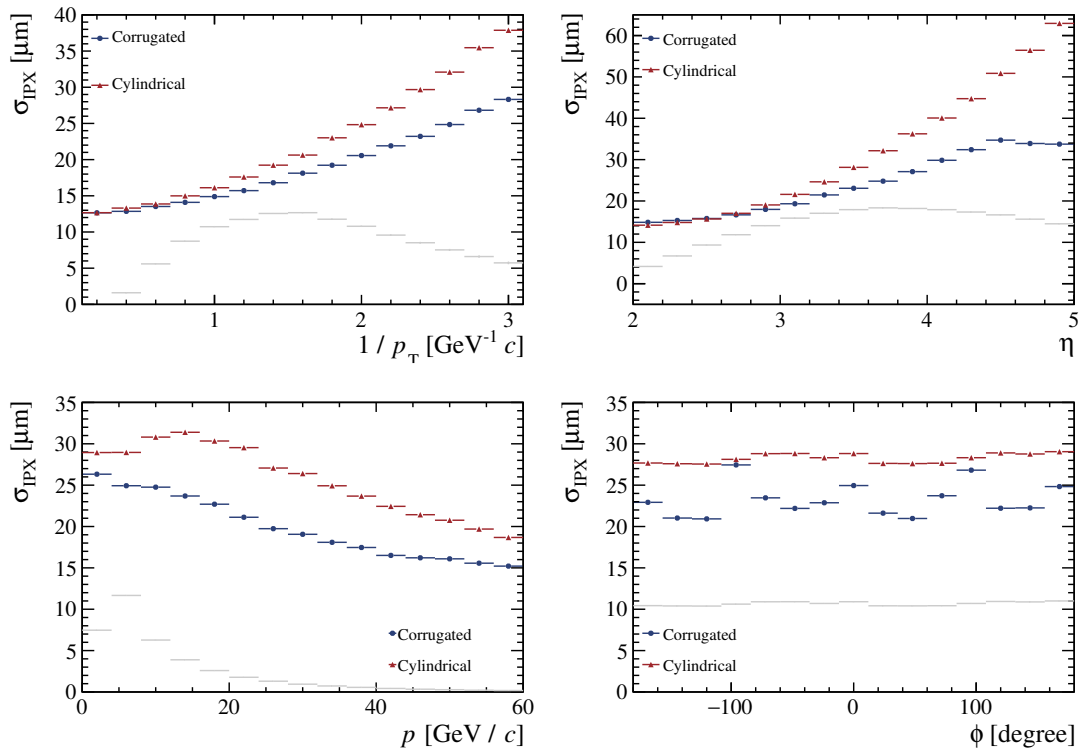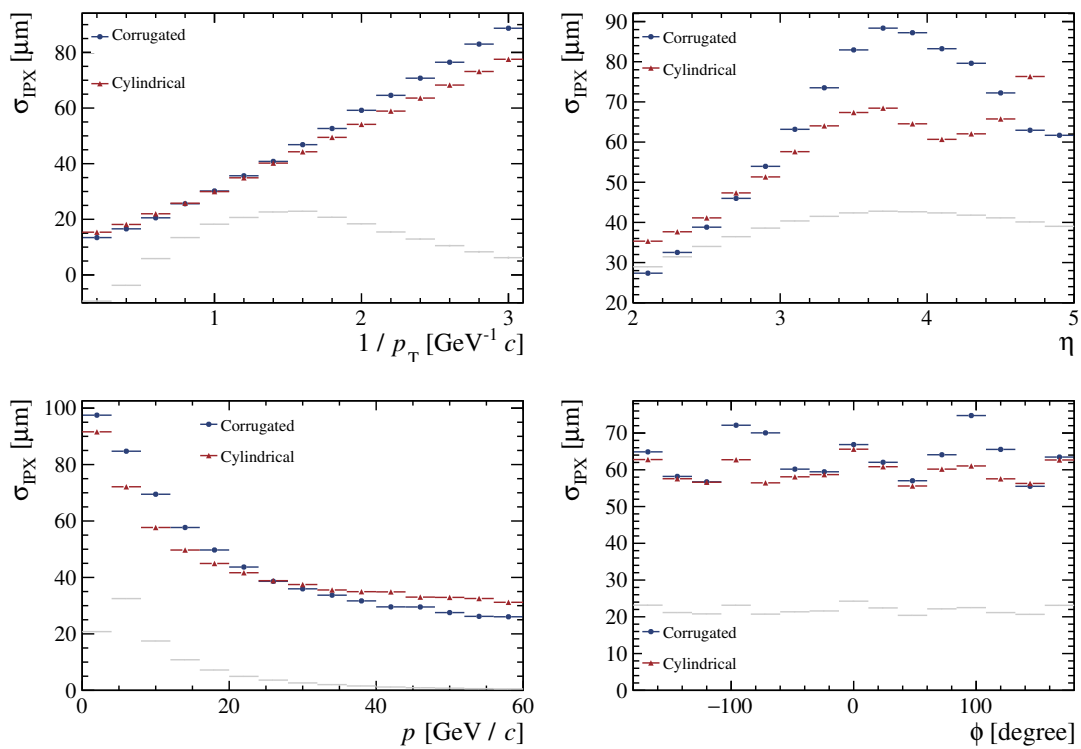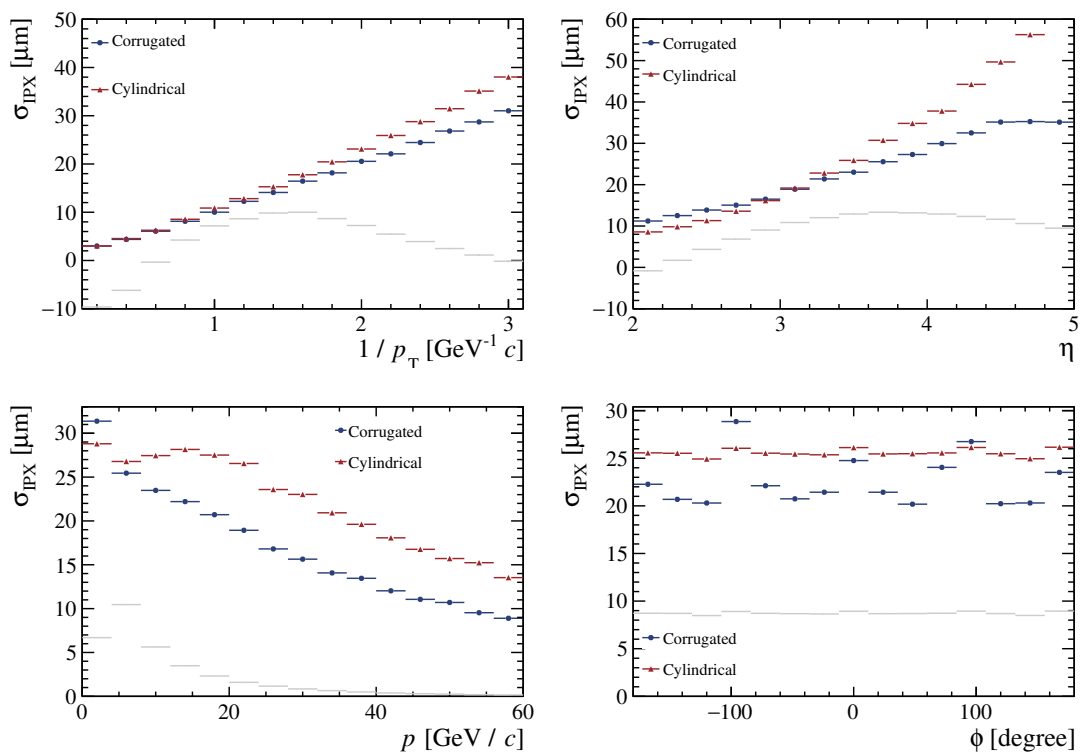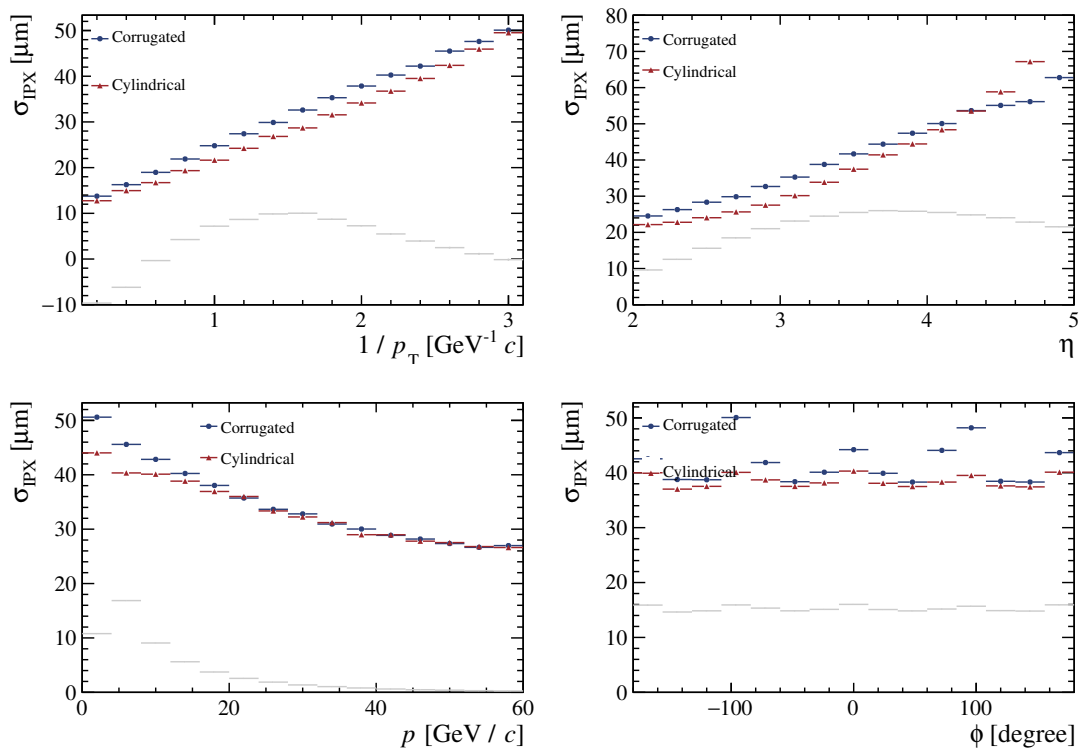
Fig. 4.19. Comparison of the IP-resolution between a 250 μm corrugated (blue) and a 250 μm cylindrical foil (red) with a finite pixel resolution (1 hit). It is plotted against the inverse transverse particle momentum, η, true particle momentum and polar angle of the track.

If now the pixel resolution is also included, it can be observed that in this regime the pixel resolution is by far the dominant factor (figure 4.21). The change in IP resolution after the introduction of the pixel resolution is non-uniform as a function of η. This has two reasons. First, as mentioned before, the increased material budget and secondly, due to the increase in mean distance of the first hit to the primary vertex, the interpolation error contribution to the IP-resolution due to a finite hit resolution is magnified. The small dip in resolution for high η tracks can be explained by the fact that in this region the distance between the sensor planes increases. This increases the lever arm between hits for extrapolation. Due to the nature of the measurement, the impact parameter cannot be treated as a simple addition of the difference between the true vertex and the reconstructed vertex introduced by the pixel resolution and multiple scattering. The resulting additional increase leads to a worse IP resolution. A sketch of the difference in the IP can be seen in figure 4.22a.

At last, all the hits of a track are used. Again, first only the true hits are used for IP-resolution calculations and a linear fit is applied to calculate the track state at the first hit. From the material scan (figure 4.16 c) it is visible that the corrugated foil shows lower material than the cylindrical one only for high η. In the case of the IP resolution, the behaviour is different from the material (figure 4.23). In the range around $\eta = 3.6$, both foils even exhibit a quite worse IP resolution than expected. This can be explained by the material distribution along the track. So far only a small number of scattering centers were assumed so that the effect of

Fig. 4.20. Comparison of the IP-resolution between a 250 µm corrugated (blue) and a 250 µm cylindrical foil (red) for true hits (2 hits). It is plotted against the inverse transverse particle momentum, η, true particle momentum and polar angle of the track.

their relative positions on each other can be ignored. If all hits are included, every additional plane traversed results in a worse IP resolution for each plane that follows. This can be clearly seen by comparing the IP resolution and the mean number of hits per track (figure 4.22b) as a function of η. The IP resolution depends now mostly on the number of scattering planes traversed and only for the cylindrical foil at high η the material budget of the first hit becomes the dominant term again. The lower relative effect of the material budget can also be seen in the fact that the corrugated foil shows a worse resolution than its cylindrical counterpart, even in regions with comparatively lower total material budget, due to the introduction of additional scattering centers from its corrugations. Introducing the pixel resolution introduces an offset in the resolution (figure 4.24), depending on the number of hits per track, but in this case the additional hits lead to an improvement of the resolution, as the interpolation of the hits can compensate to a certain degree the error made through incorrect measured positions.

As a last step a Kalman filter was introduced to compensate for the afore mentioned error contributions (except for the scattering before the first measured point). For true hits (figure 4.25) it can be seen that the Kalman filter can reduce the additional effect introduced by the multiple scattering centers on the IP resolution. This is due to the fact that it is putting most of its weight on the first hit. This leads to a better IP resolution for a corrugated foil, compared to a cylindrical one, as the filter puts most of the weight on the first true hit.

Fig. 4.21. Comparison of the IP-resolution between a 250 mm corrugated (blue) and a 250 mm cylindrical foil (red) with a finite pixel resolution (2 hits). It is plotted against the inverse transverse particle momentum, η, true particle momentum and polar angle of the track.

(a)   **(b)**
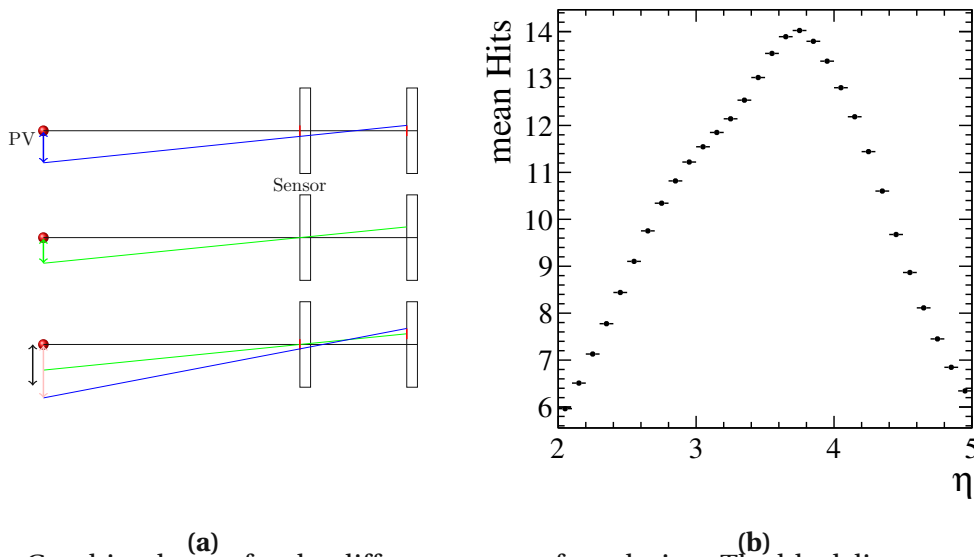
Fig. 4.22. a: Combined error for the different terms of resolution. The black line represents an un-scattered track, a green line an extrapolated track after scattering and a blue line a track with additional extrapolation errors due to finite pixel resolution. The IP distance marked in black represents the square sum of the two contributions above. **b**: Mean hits per track as a function of η.
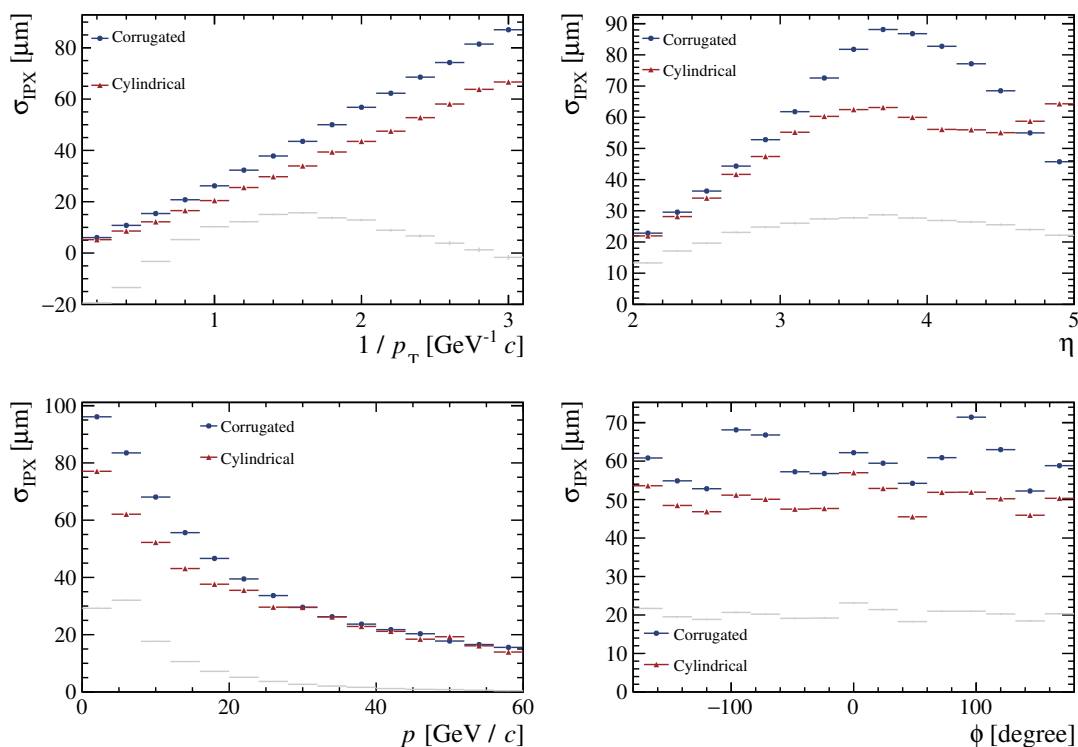
Fig. 4.23. Comparison of the IP-resolution between a 250 μm corrugated (blue) and a 250 μm cylindrical foil (red) for true hits (linear). It is plotted against the inverse transverse particle momentum, η, true particle momentum and polar angle of the track.

If the pixel resolution is also considered (figure 4.26) , the IP resolution of the corrugated foil exhibits a decrease in IP resolution, which scales with increasing η, while for the cylindrical foil the decrease is nearly constant.

Fig. 4.24. Comparison of the IP-resolution between a 250 μm corrugated (blue) and a 250 μm cylindrical foil (red) with a finite pixel resolution (linear). It is plotted against the inverse transverse particle momentum, η, true particle momentum and polar angle of the track.

Fig. 4.25. Comparison of the IP-resolution between a 250 μm corrugated (blue) and a 250 μm cylindrical foil (red) for true hits (Kalman). It is plotted against the inverse transverse particle momentum, η, true particle momentum and polar angle of the track.

Fig. 4.26. Comparison of the IP-resolution between a 250 μm corrugated (blue) and a 250 μm cylindrical foil (red) with finite pixel resolution (Kalman). It is plotted against the inverse transverse particle momentum, η, true particle momentum and polar angle of the track.

For the corrugated foil the particle experiences more scattering after the first hit. The Kalman filter therefore puts more weight on the first hit of the track and decreases the effective number of hits per track. This decreases the possible reduction of pixel resolution errors due to the interpolation of multiple hits. The reason this is more prevalent for high η tracks is due to the increased interpolation lever arm between the primary vertex and the first hit (first discussed for 1 hit tracks). This effect should scale with the pixel resolution itself, as the combination of pixel resolution and multiple scattering introduces a worse IP resolution (see two hit example) and the multiple scattering itself. To prove the first effect, simulations were done with pixel resolutions of 1, 5 and 12.5 µm and differences with respect to the results obtained using the true hit positions were plotted. Looking at figure (4.27) the diverging behavior between the corrugated foil and the cylindrical one is clearly visible. In addition, the scaling behavior between the different pixel resolutions is seen. To study the effect of scattering, the difference in IP resolution is plotted against the momentum of the particles. Since momentum and pseudorapidity are correlated, we make separate plots, one for the pseudorapidity range $2 < \eta < 2.5$ and one for the range $4.5 < \eta < 5$ (see figure 4.28). For the low η range the difference is quite small, due to the small lever arm between the primary vertex and the first scattering point in the RF foil. For high η the difference is clearly visible and increases with decreasing momentum.
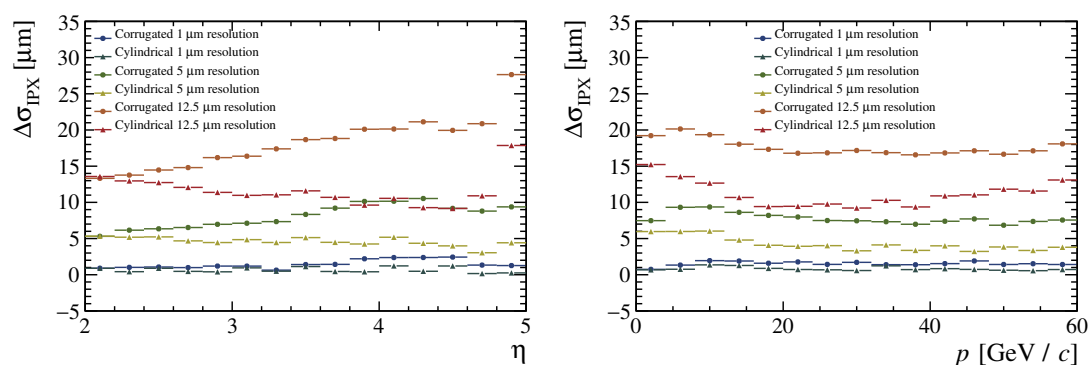
Fig. 4.27. Comparison of the IP-resolution difference of different pixel resolutions compared to the true hit results.

(a) **(b)**
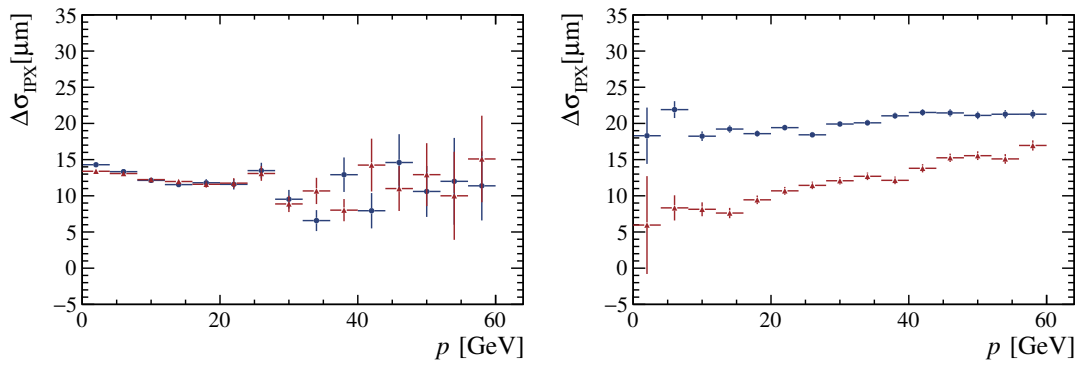
Fig. 4.28. Comparison of the IP-resolution difference(true hit and $12\,\mu$m resolution) between a $250\,\mu$m corrugated (blue) and a $250\,\mu$m cylindrical foil (red) with a finite pixel resolution. **a**: Tracks with $2 < \eta < 2.5$. **b**: Tracks with $4.5 < \eta < 5$.

So far, the focus was mostly on the effect of scattering and the intrinsic introduction of a measurement error on the IP resolution was discussed. In the next step a focus is put on the relative contributions of the measurement error itself. As shown before, they cannot be studied independently as their interaction changes the final results. To improve a layout, it is of interest if either a reduction of pixel resolution or of material budget would lead to the most significant improvement in the IP resolution. As the phase space of potential material distributions is near infinite, only the two foil scenarios from before are studied. For each of these layouts a "perfect" resolution scenario with $1\,\mu$m pixel resolution was simulated. For this scenario the scattering term is expected to be the main contributor to the IP resolution. Then the pixel resolution was decreased successively and compared to the initial simulation. When the IP resolution decreases by at least a factor of $\sqrt{2}$, it can be assumed that the extrapolation term becomes the dominant term. The resolution where the transition point is reached is called critical resolution. This critical resolution is then plotted as a function of η and p_{T}^{-1}. To estimate the effect on the total IP resolution, the number of simulated particles is shown for each bin in figure 4.29a.

For the corrugated foil most bins have a critical resolution below 12.5 μm (see figure 4.29b). This indicates that an improvement in pixel resolution with respect to 12.5 μm would lead to the most significant improvement in IP resolution. It can be also seen that the critical resolution decreases with the number of hits per track. This is in accordance with the observed decrease in IP resolution due to combination of extrapolation and scattering error. If a corrugated foil is used for Upgrade II, the focus should be put on improving the spatial resolution as much as possible.

For the cylindrical foil (figure 4.30) the extrapolation term is the dominant one only for $\eta < 4$. A clear dependency on the material is seen: with increasing η and decreasing particle momentum the spatial resolution becomes less important due to drastic scattering before the first hit. The empty bins at the top right corner of the diagram originate from the fact that
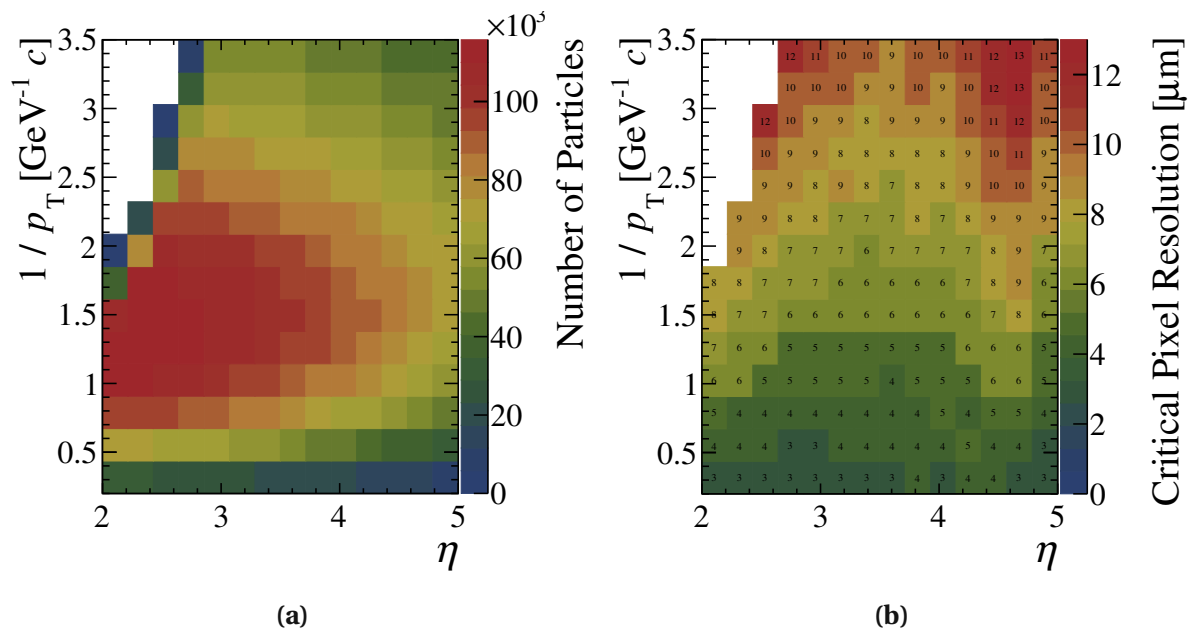
Fig. 4.29. a: Event population as a function of p_{T}^{-1} and η used for the study of the IP resolution. **b**: Critical resolution as a function of p_{T}^{-1} and η for a 200 μm thick corrugated RF-foil.
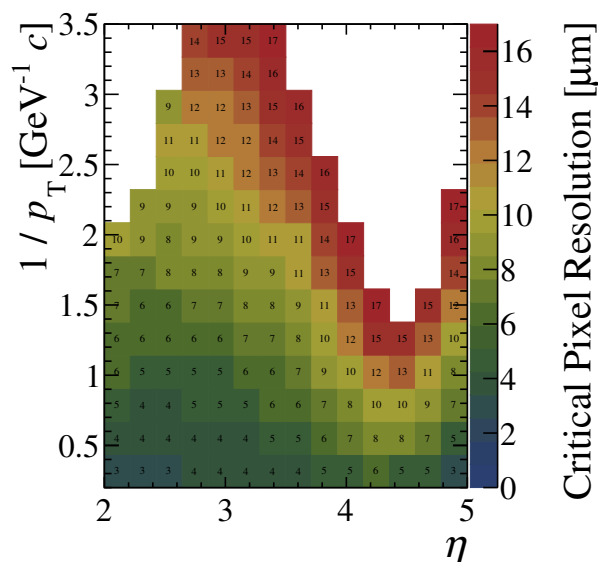
Fig. 4.30. Critical resolution as a function of p_{T}^{-1} and η for a 200 μm thick cylindrical RF-foil.

simulations were done up to 17 μm and the critical resolution in this region lies above this value. Due to the distribution of particles, improving the spatial resolution will still lead to a substantial improvement of the IP resolution. It must be mentioned here that a direct comparison between the critical resolutions of the corrugated and cylindrical foil is not possible, as they do not share the same baseline IP resolution.

4.3 Scenario A

As mentioned in the introductory section of this chapter, one option ("Scenario A") for the Upgrade II VELO is to keep the sensors at the same distance from the beam line as in Upgrade I (5.1 mm). In the following, we investigate if the IP resolution can be further improved with respect to Upgrade I by changing the shape of the RF foil. For this purpose, the Upgrade I detector is compared to a similar one with a cylindrical foil of 78 μm thickness instead of a corrugated one. The thickness was chosen to achieve the same mean material up to the second hit for all tracks in the acceptance range as a 200 μm corrugated foil. The pixel resolution is kept the same as for Upgrade I. As shown in figure 4.31 the IP resolution would improve drastically, which would in turn improve PV reconstruction efficiency. It is worth noting, that even without any change to the detector, the IP resolution is slightly better for Upgrade II conditions than for Upgrade I conditions. This improvement can be explained by the fact that the RMS of the luminous region decreases from 63 mm to 44.7 mm. This implies that a larger fraction of tracks with low p_T^{-1} traverse the densely packed inner region and therefore have a larger number of hits per track and a decreased r_F. This effect is less prevalent for tracks with low momentum as multiple scattering is the main contributor. Looking at the η dependence only at the ends of the acceptance range a slight increase is visible, with an improvement of 2.1% for $\eta = 2$ and 5.7% for $\eta = 5$. Plotting the IP resolution as function of momentum it is clearly visible that the improvement increases with momentum, as discussed before.

Comparing with the 78 μm foil it can be seen that the resolution improves by 9% for low p_T^{-1} tracks and 23% for high p_T^{-1}. Looking at the IP resolution as a function of η it can be seen that the improvement follows the difference in encountered material with a peak around $\eta \sim 3.5 \ldots 4.5$ where the corrugated foil exhibits a maximum in encountered material. As the encountered material increases with η the resolution improvement drops from 14.6% for $\eta = 2$ to 6.4% for $\eta = 5$. Due the uniform shape of the cylindrical foil the variation of the IP resolution with ϕ is reduced compared to a corrugated foil.
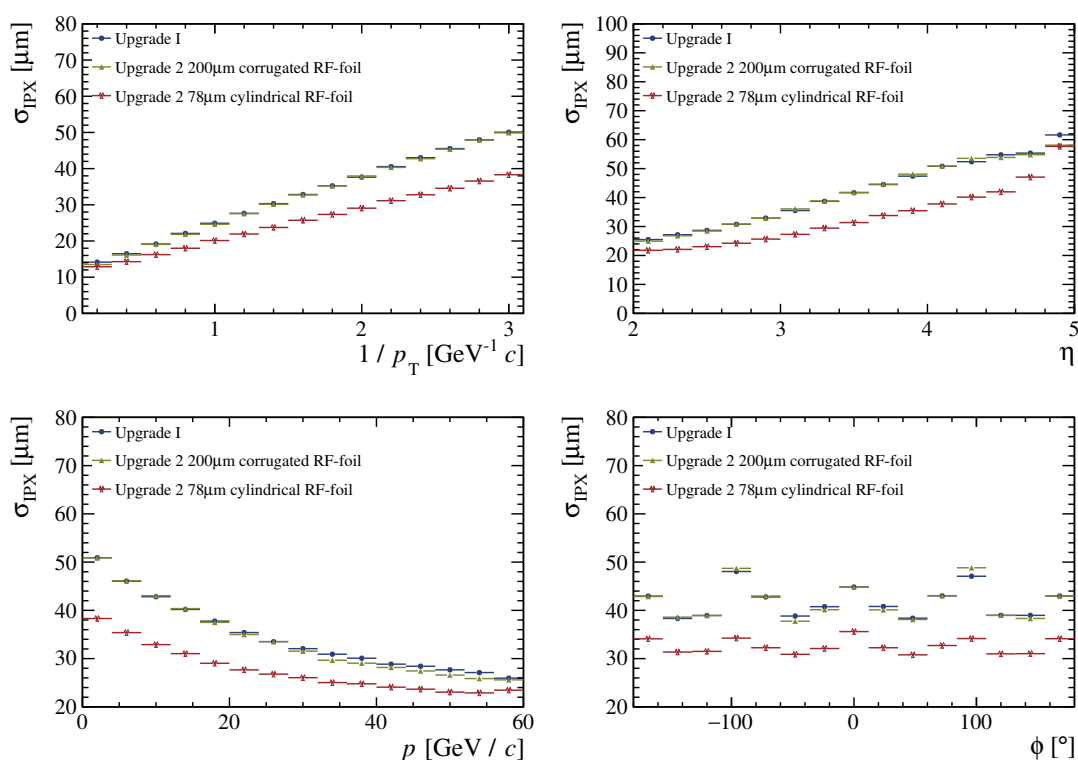
Fig. 4.31. IP resolution for Scenario A for different RF-foils compared tot he current upgrade I layout.

4.4 Scenario B

4.4.1 Layout

To keep the maximum fluence the same as in Upgrade I, the active area of the "hottest" sensors close to the interaction point should start at a distance of 11.1 mm from the beam line. This scenario is called scenario B. In the following the design process of new layouts for the modules of the VELO detector is discussed. For every new layout it is required that 99% of the particles originating from $|z| < 2\sigma_{lum}$ and being within the LHCb acceptance ($2 < \eta < 5$) leave at least four hits in the VELO. This is the first limitation around which an initial layout is designed. For all layouts in this chapter only particles flying in the downstream direction are considered.

The layout of the region around the interaction point is designed to satisfy the acceptance requirements of tracks with $\eta = 2$. The upstream starting point of this region is decided by tracks with $\eta = 2$ originating from $z_{start} = -2\sigma_{lum} = -8.94$ cm. To keep the size of the detector as compact as possible this track should hit the sensor exactly at the inner edge. Its z-position

can be therefore calculated using

$$z = \frac{R_{\text{in}}}{\tan \theta} - 2\sigma_{\text{lum}}, \tag{4.2}$$

where R_{in} is the minimum of the inner radial distance of the closest sensor to the beamline (called inner radius from now on) and θ is the track angle [103]. For an inner radius of 11.1 mm and $\eta = 2$ we obtain a z-position of -8.64 cm. The endpoint of this region can be calculated using

$$z = \frac{R_{in}}{\tan \theta} + 2\sigma_{\text{lum}}, \tag{4.3}$$

It must be mentioned here that the inner radius is not constant as a function of ϕ for a non-circular inner hole. For the calculation of the position of the endpoint the minimal inner radius was assumed. The implications of this are discussed later.

The requirement for the tracks to have at least four hits until they leave the detector leads to the following distance between planes in the inner region

$$\Delta z = \frac{R_{\text{out}} - R_{\text{in}}}{4 \tan \theta}, \tag{4.4}$$

where R_{out} represents the outer radius of the sensor. It is set to 39.05 mm to achieve the same distance between inner and outer radius as the Upgrade I detector. Additionally, three planes must be placed after the last plane to ensure that the track it was optimized for, still has at least four hits. Using the minimum radius for the calculation leads to some of the tracks, which originate from the most upstream part of the acceptance range and would hit the sensor close to the corner, to have less than four hits. This can be corrected by designing the layout with the maximum inner radius in mind. This would shift all the planes slightly in the downstream region but would lead again to a loss of hits for tracks that start in the left-most part and hit the sensor close to the minimum radius. A compromise to include the most tracks would be to design the first position with the minimum inner radius in mind and the last with the maximum. Additionally, the spacing can be varied around the calculated value to optimize further. These calculations were done by ray-tracing. The results can be seen in figures 4.32 and 4.33a.

As the overall material budget of the detector should be kept as small as possible, the number of planes should be also minimized. Figure 4.33a shows that the sensors can be placed further apart if the start plane is calculated using the minimum inner radius and the maximum inner radius is used to calculate the last plane. The maximum distance between planes without the loss of acceptance in this scenario is 2.56 cm and was used for all further layouts. The layout of the downstream stations is determined by tracks with $\eta = 5$. For these tracks we calculate the furthest z-position of the first hit of a track possible, which depends, as mentioned before, on the inner radius. The largest inner radius is encountered in the corners of the inner hole. With equation 4.2 the position of the first of the four last planes calculates to 126. cm. The relation between the inner radius and the position can be seen in figure 4.33b.
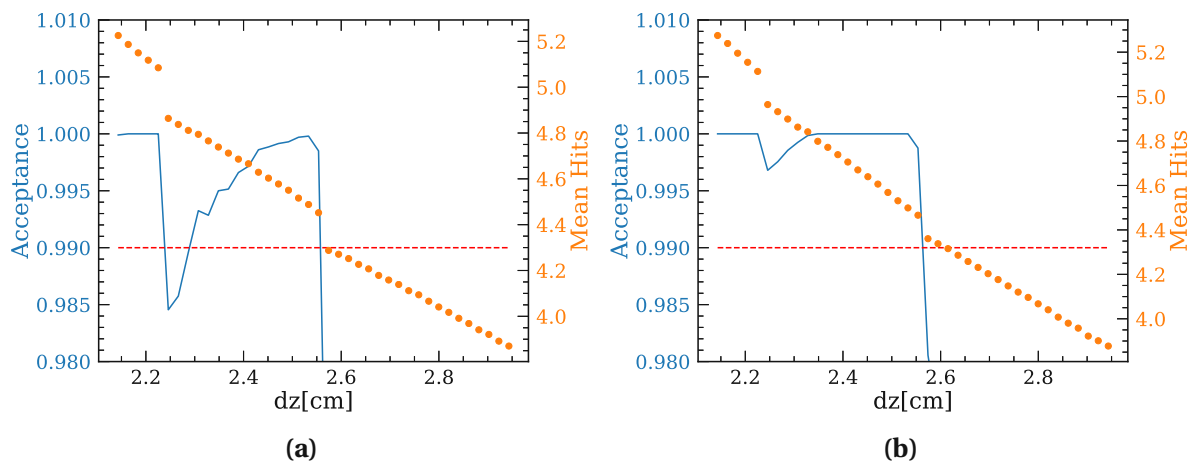
Fig. 4.32. Ray-tracing simulations for different calculated layouts for the inner region of the detector. The red line represents the required acceptance. For the calculation of the start and end plane different inner radii are used **a**: Start: R_{in} min/End:R_{in} min. **b**: Start:R_{in} max/End:R_{in} max

For tracks with $\eta = 5$, the spacing must be at most 5.2 cm to ensure four hits per track.
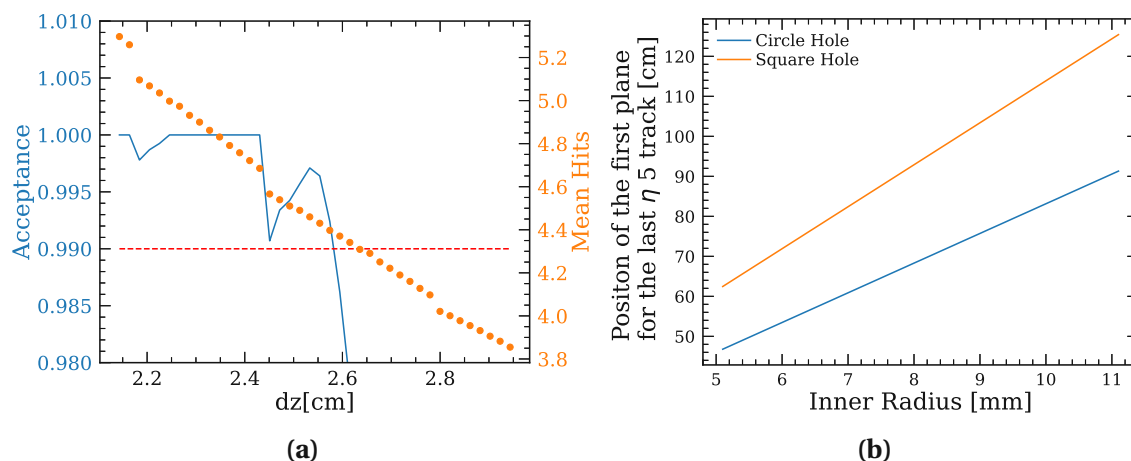
Fig. 4.33. a: Ray-tracing simulations for different calculated layout for the inner region of the detector. The red line represents the required acceptance. For the calculation of the start and end plane different inner radius are used: Start: R_{in} min/End: R_{in} max. **b**: Relation between the maximum inner radius and the resulting position of the first plane hit by the last η=5 track.

Reducing the spacing will result in a decrease of the distance between hits for these tracks, which should affect the IP resolution of these tracks negatively but would lead to a small overall effect due to the low density of tracks in this region. As the length of the detector should be minimised, the planes also need to be placed as close as possible. As both criteria cannot be satisfied at the same time, it was decided to place them at a distance of 2.5 cm apart from each other. This value was chosen as it was the closest distance between planes in the Upgrade I layout.

As mentioned before the shape of the inner hole defines the minimal size of the detector. A circular hole would be the optimal solution, but is difficult to realise in terms of ASIC layout. Two inner hole geometries are considered in this thesis: the first one featuring a hexagonal aperture and the second one an octagonal one. The hexagonal shape has the advantage that it can be achieved by tiling with no unwanted overlap (figure 4.34). While the octagonal shape would allow a more compact design, it would lead to extensive overlap if more than one sensor row is used. For the rest of the layout calculations an octagonal sensor is used as an example. It is worth noting that an octagonal shape can be also approximated by using
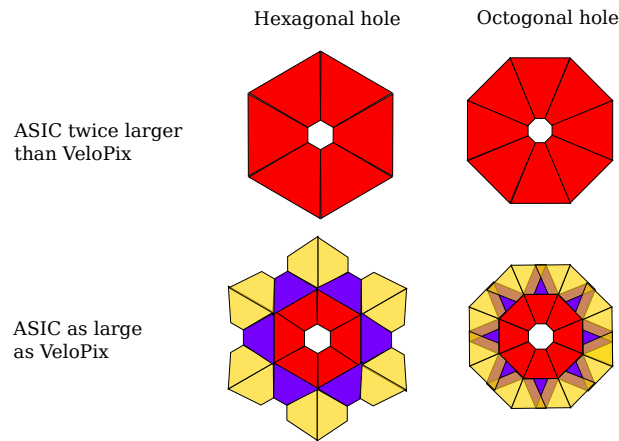
Fig. 4.34. Possible tiling option for Scenario B resulting in hexagonal and octagonal inner holes. **top**: Implementation with only a single row with sensor tiles and ASICs substantially larger than in Upgrade I. **bottom**: Implementation using ASIC and sensors tiles of similar size as upgrade I in two rows. Different colors are used to visualize possible overlaps.

modules with a square cut-out and rotating every second station by 45°. For this layout, additional sensor planes are needed, therefore increasing the overall material budget, but would lead to comparable values of r_F.

The number of the planes between the central and the downstream region is determined in first order by ray tracing calculations of the acceptance of the layout. First three additional planes are placed in the region. This number was chosen as it is equal to the number of planes placed in the same region for Upgrade I. Two of them are placed close to the central region as the density of tracks is higher in this region and the distance in z a track travels before it leaves the detector region is small, due to the high amount of low η tracks. One plane is placed in the middle of the region between these two planes and the last planes in the detector. As can be seen this leads to a drastic drop in acceptance around $\eta = 3.5$ (figure 4.35a). To compensate for this a plane is placed so that tracks which originate from z = 0 and have the same η as the minimum in the acceptance hit the sensors in the middle of the placed plane. This ensures that most tracks in this η region have an additional hit (figure 4.35b). Then all the planes are varied by a small distance around their original position until a layout is found that maximizes the acceptance. These steps are repeated until a layout is found which fulfills the LHCb acceptance. If multiple local minima are encountered which are spaced far apart the minima

at lower η is treated first, as it can affect higher η tracks, which is not the case the other way around. Placing a total of six planes leads to the desired acceptance. The resulting layouts are illustrated in figure 4.37a. In the next step the IP resolution was taken into consideration.

(a)   **(b)**
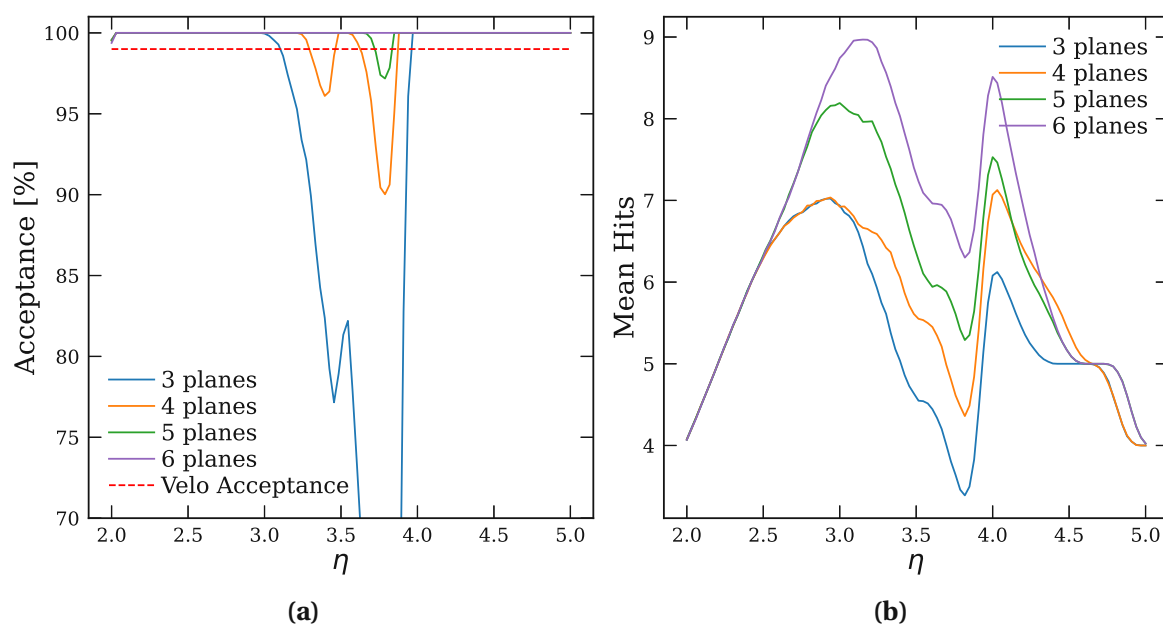
Fig. 4.35. Acceptance (**a**) and mean number (**b**) of hits for different number of planes added between the central and downstream region for an octagonal sensor layout at 11.1 mm. The red line in the acceptance plot represents the required acceptance.

Looking at the IP resolution as a function of η it can be seen that the resolution is starting to degrade compared to Upgrade I around $\eta = 4.5$ (figure 4.36a), which comes from the fact that in this region r_F increases (figure 4.36b) due to a low plane density. To compensate for this an additional plane is placed in this region so that tracks with $\eta = 5$ starting at $z = 0$ hit the sensor at the inner edge. The increase of IP resolution at $\eta = 5$ originates from the increased material due to the RF-foil shape. As this effect scales too with r_F (see 4.35), it can be reduced by placing additional planes in the region traversed by corresponding tracks. Adding additional planes has only a marginal effect on the IP resolution. This is since the decrease in r_F is small, and the closer distance of planes leads to a worse resolution due to extrapolation. The change of layout during the implementation of new planes for an octagonal sensor layout at 11.1 mm can be seen in figure 4.37b. For all new layouts, the increase in size is substantial and all of them would extend into the RICH detector. If this extension is not possible, additional changes must be implemented to reduce the size. As the fluence not only decreases with the distance from the beam line but also with the z distance from the interaction point, sensors further away from the interaction point could be placed closer to the beamline. If a point is defined in z after which the inner radius of the sensor planes is reduced, the overall length of the detector decreases. The step in inner radius size was chosen to be at 60 cm as the decrease of fluence after 60 cm as a function of z is quite low (figure 4.38a), so the decrease in length would be minuscule. Additionally, introducing the step at lower z position would decrease r_F and therefore improve the IP resolutions for a wider range of tracks. Only
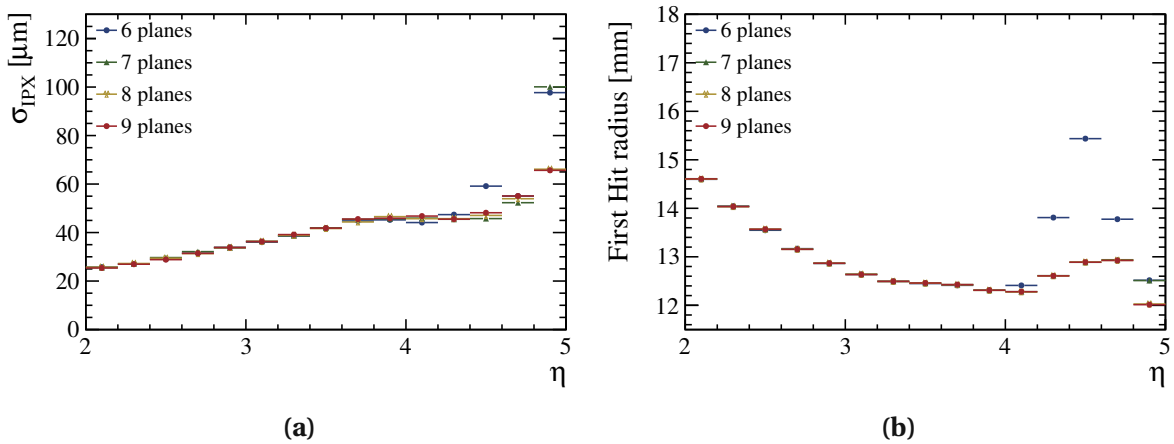
Fig. 4.36. IP resolution (**a**) and r_F (**b**) for different number of planes added between the central and downstream region for an octagonal sensor layout at 11.1 mm.
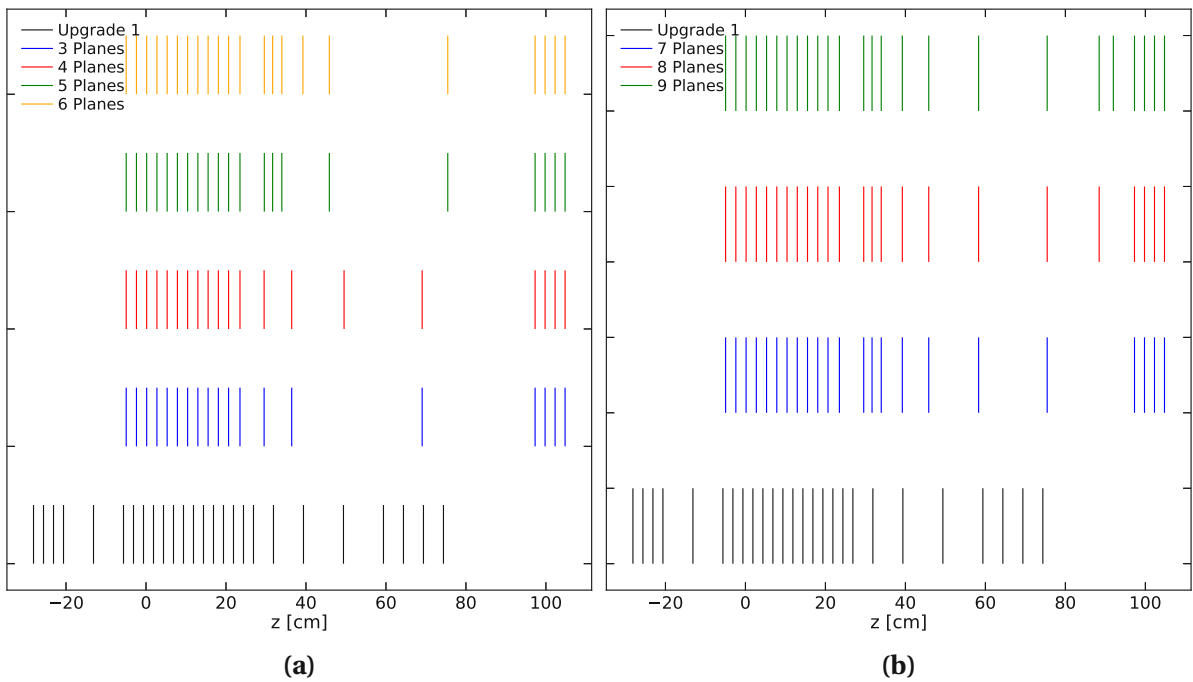
Fig. 4.37. Illustration of the layout at the different layout optimization steps for each additional added plan for scenario B with an octagonal inner hole. **a**: After each acceptance optimizations step. **b**: After each IP optimization step.

the last step influences the size of the layout, so only one step is considered. Further steps in the radius in-between would lead to a better IP resolution, but also increase the number of different ASIC and sensor shapes that must be developed and produced and were therefore not considered. Figure 4.38b shows the difference in detector length achieved by moving the last sensors closer to the beam.

Another option to additionally reduce the size of the detector would be to reduce the η ac-

(a) **(b)**
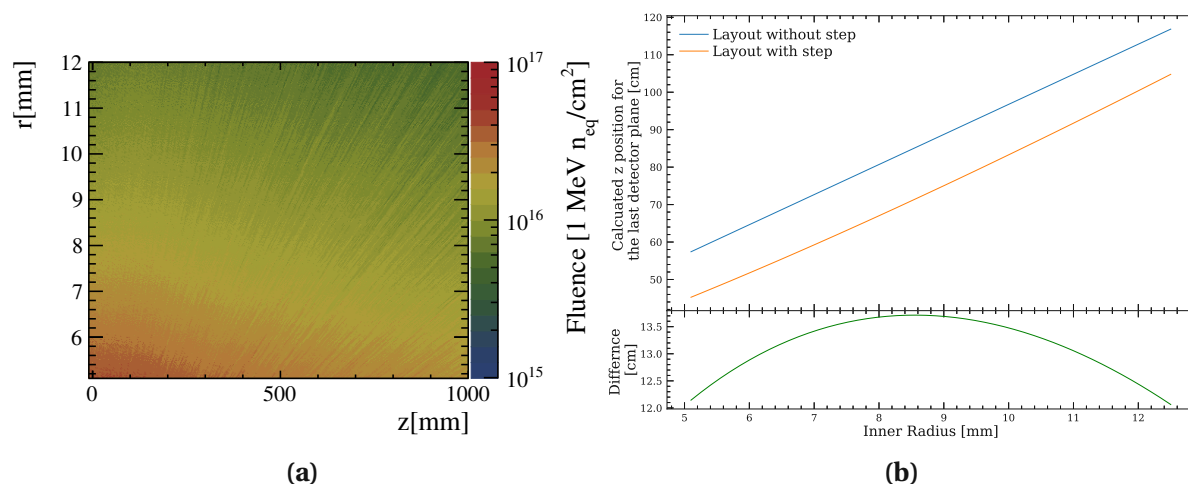
Fig. 4.38. a: Fluence calculation as function of z position and radius to beam line for Upgrade II conditions. **b**: Difference of the position on the last plane with and without a step in inner radius at $z = 60$ cm for an octagonal sensor design.

ceptance of the detector. Even a small reduction in the η coverage can lead to substantial decreases in the size of the detector. Figure 4.39a shows the z-position of the first downstream station as a function of the highest pseudorapidity to be included in the acceptance. If the size of the VELO should stay the same, decreasing the η coverage would allow the sensors to be placed a little further from the beam. The maximal possible η for the same length as the current detector for different inner radii is shown in figure 4.39b. As the viability of a decrease in the η-acceptance must be carefully studied, this possibility was not further investigated in this study.

The z position of each plane for the different scenario B options are shown in figure 4.40.

To maintain the same IP resolution as in Upgrade I at low p_{T}, the material budget of the VELO needs to be reduced. This implies that the RF foil, which is the dominant contributor to the material budget of the Upgrade I VELO, needs to be thinner. Apart from its thickness, the shape of the foil and its distance to the beam line also affect the IP resolution.

A corrugated foil is not chosen for this scenario for two main reasons. First, the increase in radius for the scenarios discussed moves the sensors completely out of the corrugations of the current foil (see figure 4.41). Due to this, the particles traverse the full material of the foil, especially the corners of the foil, before the first hit, which increases the material compared to a cylindrical foil with the same thickness. Extending the corrugations to the sensor to prevent particles from traversing the corners of the foil before the first hit, would only increase the material budget and is therefore not viable. The multiple different scattering centers before the first hit would additionally degrade the resulting IP resolution. A cylindrical foil also provides a uniform material distribution as a function of ϕ.
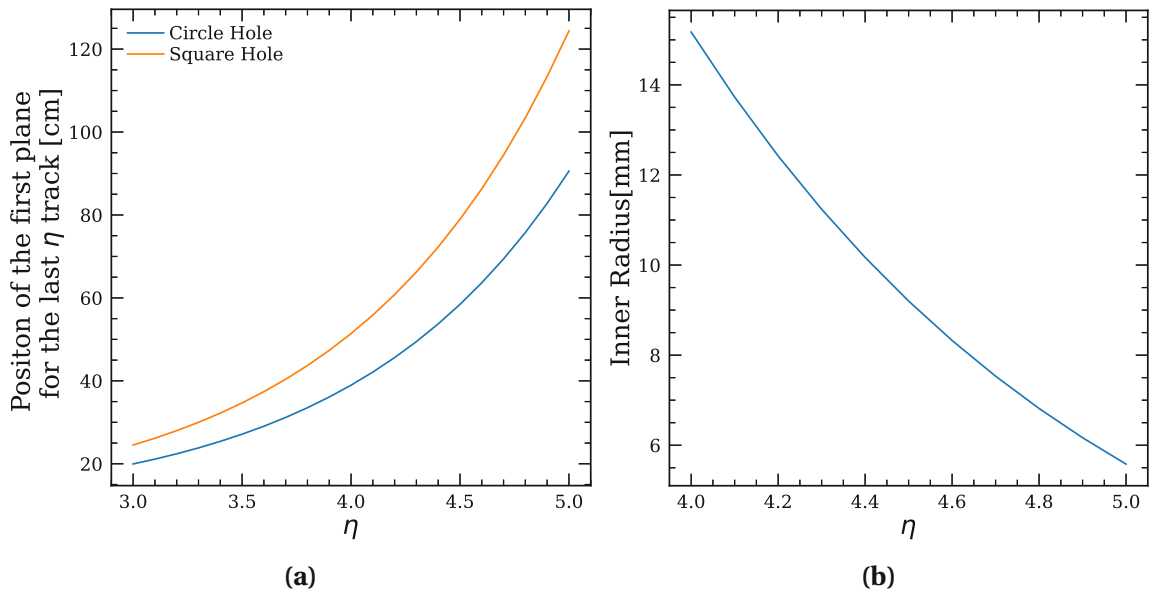
Fig. 4.39. a: Relation between the maximum η and the resulting position of the first plane of the last η 5 track for an inner radius of 11.1 mm. **b**: Relation between the inner radius of the sensor planes and the highest accepted η if the detector is kept at the same length as the Upgrade I VELO.
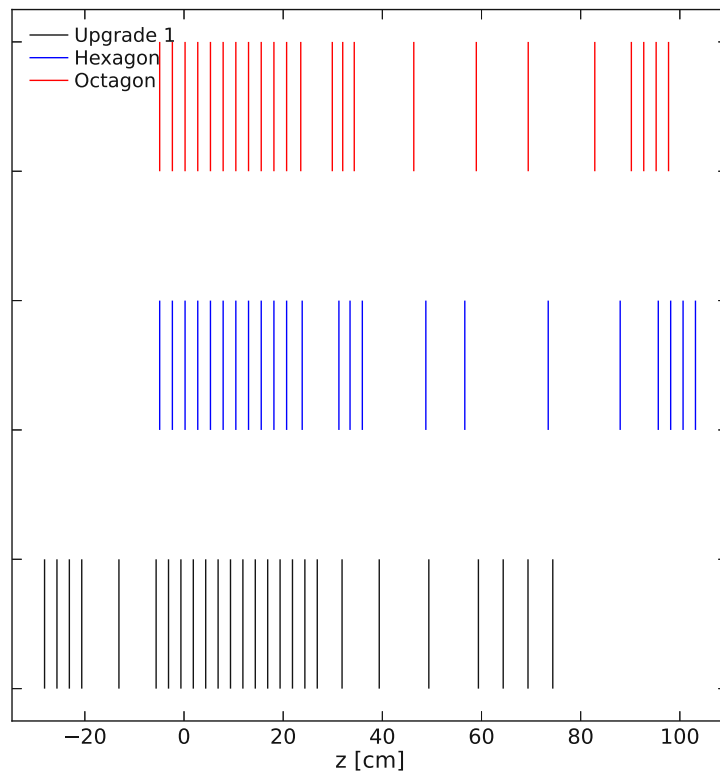
Fig. 4.40. Optimized Layouts for Scenario B with a hexagonal and octagonal inner hole compared to the current upgrade I layout.

A key function of the RF foil is to shield the sensitive elements of the detector from the electromagnetic field of the LHC beams. The (exponential) attenuation of an electromagnetic
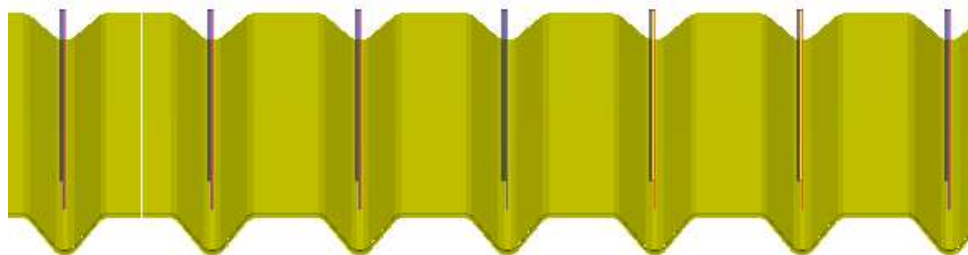
Fig. 4.41. Cut through the detector for a Scenario B sensor position. The RF-Foil is colored yellow and the sensor tiles are colored red.

wave with angular frequency ω in a material with resistivity ρ and permeability μ is characterized by the skin depth [104]

$$\delta = \sqrt{\frac{2\rho}{\omega\mu}}. \tag{4.5}$$

For $\omega = 2\pi \times 40$ MHz the skin depth of aluminum is $\delta \sim 13$ µm, which was considered a lower limit to the allowable thickness of the foil. To increase structural integrity of the foil and to achieve an attenuation of 80% 20 µm was instead chosen as the lowest possible RF-foil thickness. In the following two inner radii of the RF foil are considered: 3.5 mm, which is the same distance to the beam as the closest point to the beam of the Upgrade I corrugated foil and 8.6 mm. The reason for placing the foil at 8.6 mm will be discussed in section 4.5.

Comparing the material budget of the Scenario B with the (reduced) Upgrade I geometry (figure 4.42) it is clearly visible that Scenario B leads to a decrease in material by roughly a factor two, because of the multiple crossings of the corrugated foil. The steep increase of material at $\eta \sim 3.9$ originates from the additional planes that were placed there to increase the IP resolution.

(a)

(b)
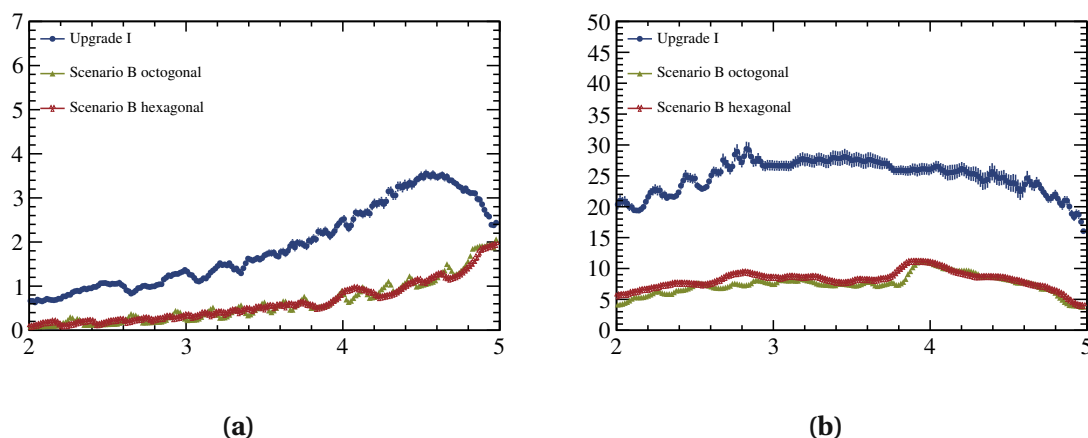
Fig. 4.42. Material budget for Scenario B compared to the reduced Upgrade I model. **a**: up to the first hit **b**: until the end of the detector

4.4.2 IP resolution

Due to the large parameter space in the following only solution which exhibit the same or slightly better IP resolution as Upgrade I are discussed. For both layouts, the average distance between the primary vertex and the first measurement point increases significantly with respect to Upgrade I (figure 4.43). To keep the IP resolution at high p_T the same as in Upgrade I, a single-hit resolution of $\sim 9\mu$m is needed, which, assuming binary resolution, corresponds to a pixel pitch of ~ 31 µm. By only decreasing the foil thickness to 20 µm only the octagonal layout shaped sensors with a foil at 3.5 mm has an IP resolution that is not worse than in Upgrade I. For this configuration, the IP resolution degrades by 0.6% compared to the Upgrade I detector for low p_T^{-1} and exhibits a 2.9% improved resolution at high p_T^{-1} (figure 4.44).

For all other layouts the slope of the IP resolution is significantly higher, while at low p_T^{-1} the
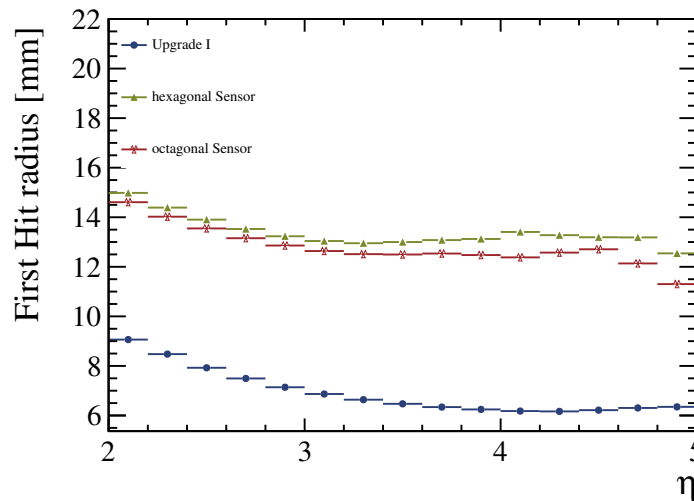
Fig. 4.43. Mean radius of the first measured point on a track in Scenario B, for sensors with octagonal and hexagonal aperture.

same as resolution as Upgrade I is achieved. Therefore, the material contribution must be reduced. As mentioned before a further reduction of the material of the RF-foil is not possible, so the material of the modules themselves must be reduced. A reduction of the thickness of cooling substrate is not possible without moving to new cooling solutions or a decrease in cooling capability and is therefore not considered. For the Upgrade II timing will play an important part in the reconstruction. If on-hit timing is implemented using planar silicon sensors, thinning of sensors is expected to lead to an overall better timing resolution due to shorter collection times. Additionally, a reduction of the ASIC thickness can be considered as most of its thickness originates from the support wafer. So, to improve the performance of the hexagonal sensors with the foil at 3.5 mm was simulated where the thickness of the sensor is reduced from 200 to 100 µm. For the other two layouts also the thickness of the ASIC had to be reduced to 100 µm.

The IP resolution for the hexagonal sensors with the foil at 3.5 mm improves by 5.6% compared to the Upgrade I detector for low p_T^{-1} and exhibits a 3.5% improved resolution at high p_T^{-1}.

For the η dependence it can be seen that Scenario B even exhibits a better IP resolution in the region $4 < \eta < 4.6$. This is due to the additional planes that were introduced to limit the degradation of the IP resolution due to the material dependence of η of the cylindrical foil. For $\eta = 5$ the layouts with the closer foil exhibit a 10% worse resolution for the octagonal sensors, compared to the 34 % of the hexagonal layout. For low η the hexagonal sensors lead to an improved resolution by 3 %, due to reduced sensor thickness whereas the octagonal sensors lead to the same performance as Upgrade I. Overall the octagonal sensors only show a slightly worse performance with an mean improvement of 1.7% compared to 2.3% of the hexagonal ones, despite the thicker sensors.
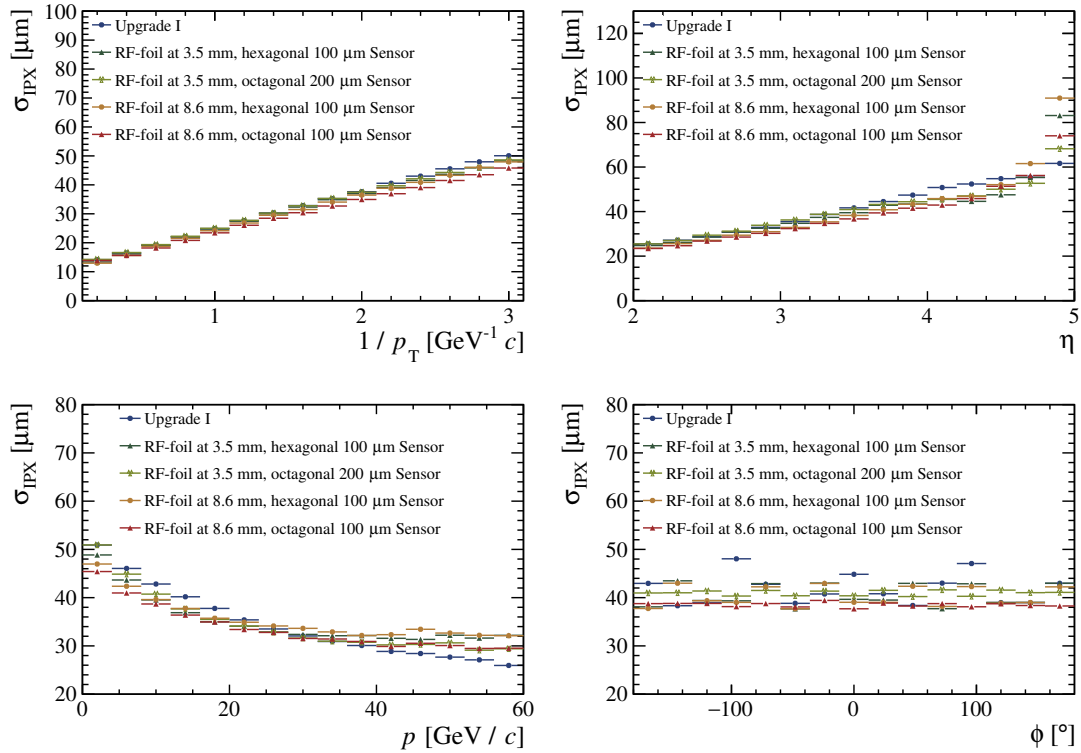
Fig. 4.44. IP resolution for different layouts for Scenario B using a 20 µm thick cylindrical RF-foil and a 9 µm pixel resolution. The ASICs have a thickness of 200 µm for a foil at 3.5 mm and 100 µm for a foil at 8.6 mm.

Looking at the momentum of the particle octagonal and hexagonal sensors outperform the current layout up to 30 GeV c^{-1}. For momenta around 60 GeV c^{-1} the resolution of the hexagonal and the octagonal layout degrade by 24% and 13% respectively. This originates from the increased distance of the sensors from the primary vertex. For low momenta the resolution improves by 4% for the hexagonal sensors and stays at Upgrade I level for the octagonal one.

For the layouts with the foil at 8.6 mm the octagonal sensors perform better at high p_T^{-1} (8.5% to 4.2%) and the hexagonal one at low p_T^{-1} (8.6% to 2.1%). For the mean improvement the octagonal one has 6.8% and the hexagonal one 4%. Looking at the η-dependence the octagonal sensor outperformed the hexagonal ones within all regards with an improved IP resolution of 8% al low η and a degradation of 20.1% at high η, compared to 7.5% and 47.6%, respectively. In total the octagonal layout improves the IP resolution by 7.1% and the hexagonal by 2.4%.

Due to the reasonable improvement in IP resolution for the two octagonal layouts, a thicker RF-foil can be considered, if only the same performance as Upgrade I must be achieved. This is only simulated for the octagonal sensors, as the possible increase in thickness is expected to be the highest. Using hexagonal sensors would lead to comparable results if the thickness were slightly reduced compared to the octagonal layout. For a foil placed at 3.5 mm the thick-
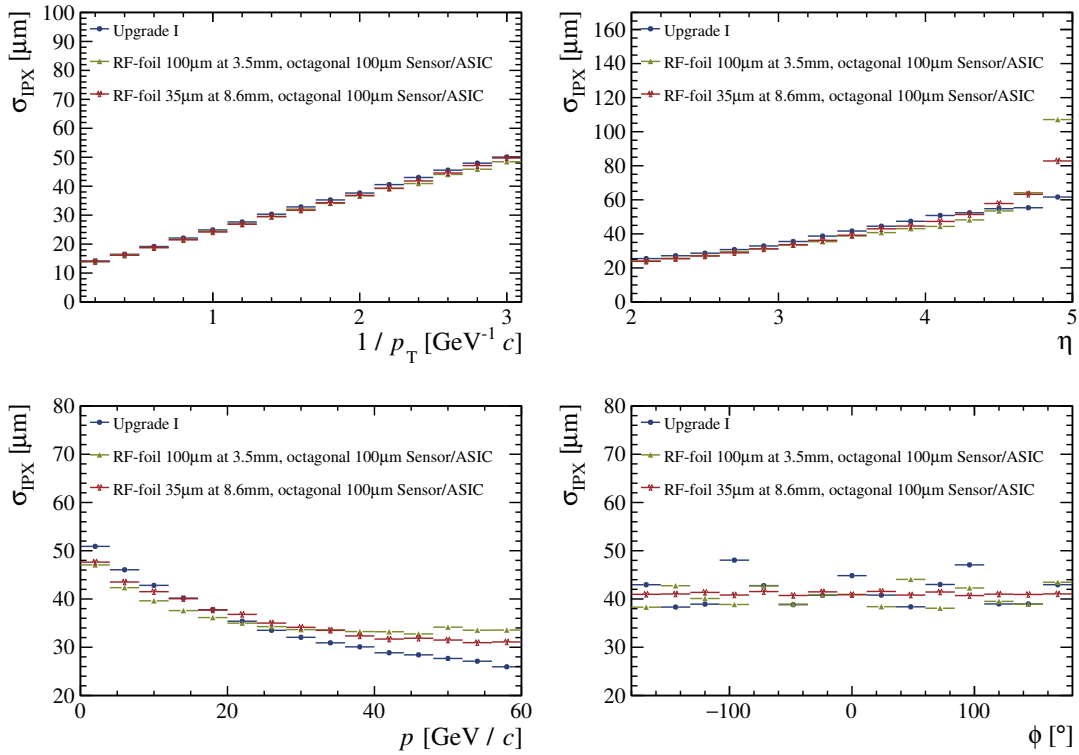
Fig. 4.45. IP resolution for layouts with reduced ASIC and sensor thickness of 100 μm for scenario B. The foil thickness is increased until the same performance as Upgrade I was achieved.

ness can be increased to 100 μm. This achieves a 1.2% improvement for low and 3.1% for high p_T^{-1}. Leading to a mean improvement of 2.7%. Looking at the resolution as function of η (figure 4.45) a clear degradation of resolution due to the increased foil material is visible after $\eta = 4.6$, which cumulates in a 73.8% degradation for η around 5. Not taking these outliers into account a mean improvement of 6.6% is achieved. Only a marginal increase from 20 to 35 μmis possible if the foil is placed at 8.6 mm. With 1.6% a similar performance increase as the closer foil is achieved at low p_T^{-1}, whereby the improvement at high p_T^{-1} is negligible with

0.6%. Overall, the mean improvement sits at 2.3%. For the η dependency, the degradation of the resolution starts earlier due to the increased distance for the interaction point at η=4.4 but degrades less at high η with only a 34% degradation. In general, thicker foils should only be considered if the reconstruction of high η tracks becomes less important.

A summary of the parameters of layouts that lead to a similar IP resolution to Upgrade I for scenario B can be found in table 4.3.

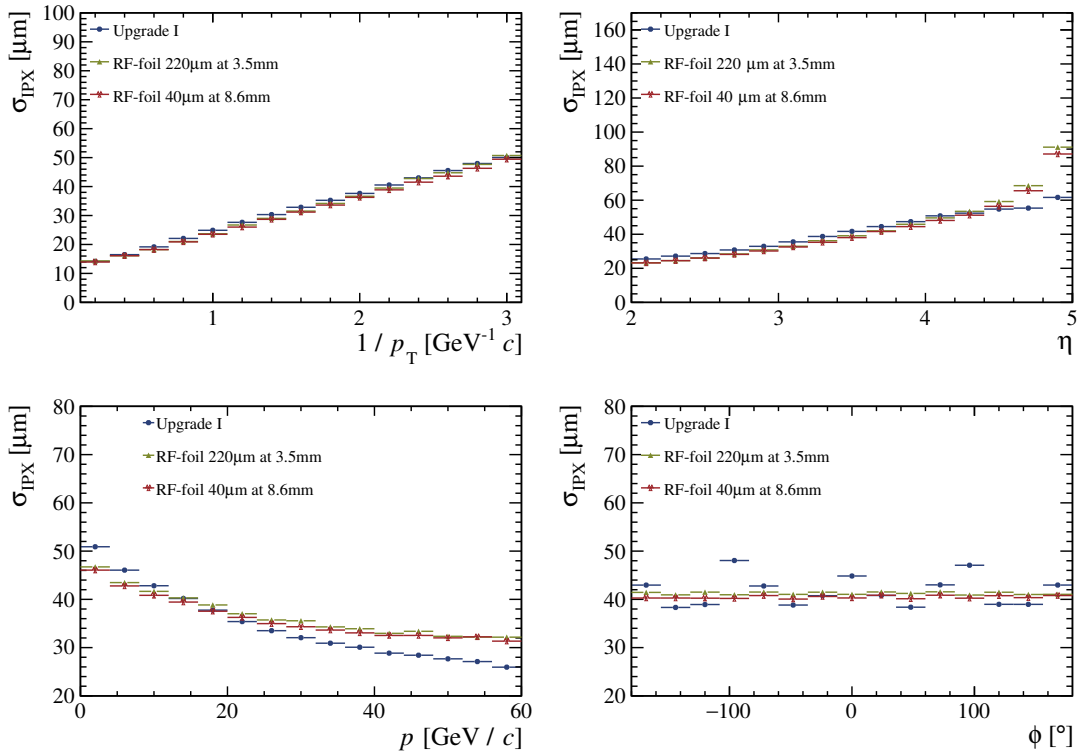| Cut-out	Sensor thickness [µm]	Sensor resolution [µm]	ASIC thickness [µm]	Foil radius [mm]	Foil thickness [µm]
Octagon	200	9	200	3.5	20
Octagon	100	9	100	8.6	20
Hexagon	100	9	200	3.5	20
Hexagon	100	9	100	8.6	20
Octagon	100	9	100	3.5	100
Octagon	100	9	100	8.6	35

Table 4.3. Scenario B configurations which achieve similar IP resolution as Upgrade I.

4.5 Scenario C

4.5.1 Layout

As discussed in chapter subsection 4.4.1 the size increase of the VELO would be substantial, if the same acceptance as Upgrade I has to be achieved. To reduce these limitations a layout was designed which puts the sensors closer to the beam compared to scenario B. The corresponding increase in radiation damage can then be compensated by replacing the sensors once in the experiment's lifetime. Currently, the RF foil is made of two movable parts, this is because the foil has to be moved away from the beam during injection to prevent the beam from hitting the foil. If the distance of the foil from the beamline is big enough it would be possible to construct it out of one single piece. This would reduce the overall complexity and cost of the detector. To define a safe distance from the beamline during injection the safe distance around each beam has to be calculated. As defined in [105, 106] a distance of 12.6 nominal beam RMS (σ_{beam}) would be sufficient. Assuming an emittance ϵ of 2.5 µm, a beta-value at the interaction point β^* of 10 m and an injection energy of 450 GeV σ_{beam} can be calculated with

$$\sigma_{\mathrm{beam}} = \sqrt{\frac{\beta^* \epsilon}{\beta \gamma}}. \tag{4.6}$$

This leads to a needed safety distance of 2.8 mm around each beam. Next the orbital error of the HL-LHC has to be added. It is expected to be 2 mm or better. Due to the vertical crossing angle of 0.32 mrad an additional 0.26 mm has to be added to prevent interference at 80 cm. Finally the beam separation of 3.5 mm has to be included. This results in a safe distance to the beamline of 8.6 mm. With an error margin for alignment errors of the sensors and RF foil of 0.45 mm and an inactive edge of 0.45 mm of the sensors, the first pixel can be placed at 9.5 mm, which still would lead to the last plane placed at $z = 120$ cm for the same sensor shape as the current Upgrade I. To decrease this even further different hole shapes were again considered (figure 4.46).
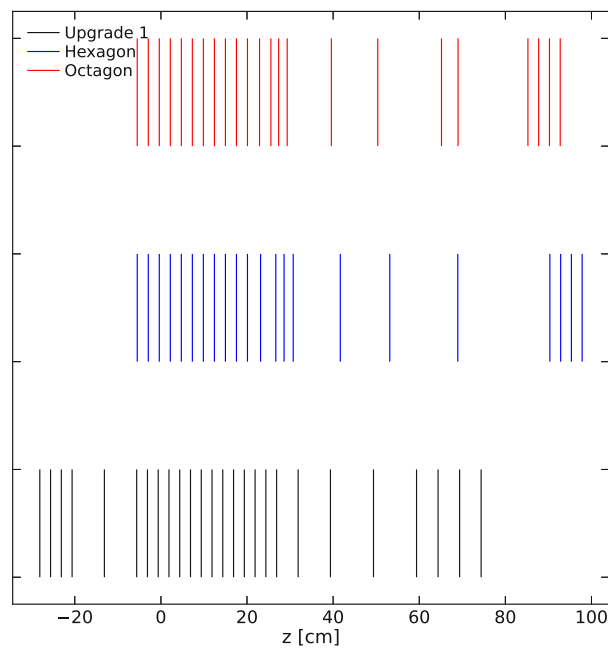
Fig. 4.46. Optimized Layout for scenario C for a hexagonal and octagonal inner hole compared to the current upgrade I layout.

The possibility of moving the last planes is not considered due to the close distance of the foil to the sensors. An illustration of these optimized layouts for this radius can be seen in figure 4.46. The exact positions of the planes of the hexagonal and octagonal configuration can be found in table 11.3 and 11.4. Different hole shapes were again considered (figure 4.46).

4.5.2 IP resolution

As can be seen in figure 4.47 the mean first hit radius decreases for scenario C, compared to scenario B, allowing the use of a worse single-hit resolution of 10 μm. As a starting point, we consider configurations with a 20 μm thick cylindrical foil, 200 μm thick sensors and 200 μm thick ASICs. The resulting IP resolution can be seen in figure 4.48. For the Upgrade I foil position this leads to an IP resolution improvement for low p_T^{-1} to 4.4% for hexagonal sensors and leads to 1% for octagonal ones. For high p_T^{-1} the improvement is 6.6% and 8.%

respectively. For a single piece foil at 8.6 mm the IP resolution degradation is measured of 0.1% for the hexagonal layout, whereby for the octagonal layout an improvement of 0.3% is observed. In the high p_T^{-1} region the differences for both layouts are smaller than one percent. For high η the configuration with a hexagonal cut-out shows a better IP resolution than their octagonal counterpart with a degradation of 11.1 % for the 3.5 mm foil and 27.8 % for the 8.6 mm foil compared to 13.8% and 32% for the octagonal ones. Despite this the octagonal sensors show a better mean performance by around 1% in both. The layouts which include
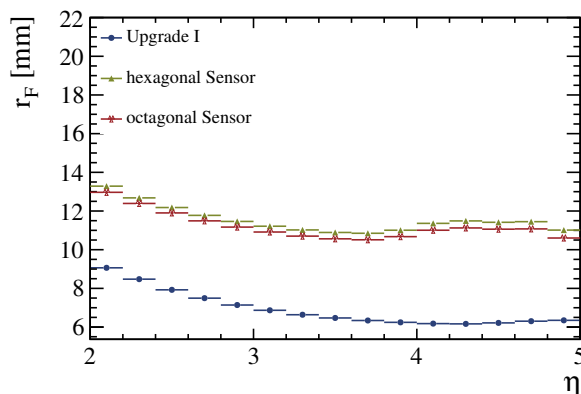
Fig. 4.47. Mean radius of the first measured point on a track in Scenario C, for sensors with octagonal and hexagonal aperture.

the single piece foil would lead therefore to the same resolution as in Upgrade I, while for the old foil layout a small improvement of the IP resolution can be achieved. It can also be seen that the difference between the octagonal and hexagonal sensors is negligible due to the closer distance to the beamline.
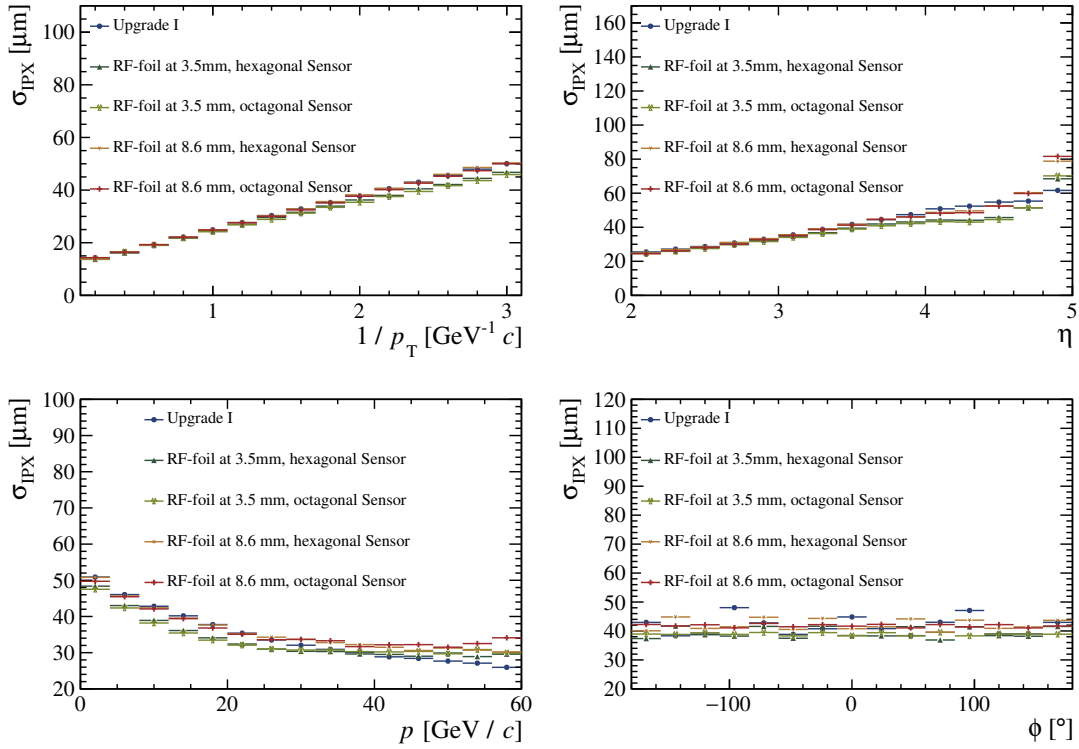
Fig. 4.48. IP resolution for different layouts for Scenario C with a pixel resolution of 10 μm and a cylindrical foil of 20 μm thickness. The sensors and ASIC have a simulated thickness of 200 μm.

Similar to Scenario B a thinner sensor and ASIC can be considered also in this case. As the different sensor shapes exhibit the same IP resolution this is only done for the octagonal sensors, as the hexagonal should achieve the same performance with the same implemented changes. For Scenario C the foil thickness can be increased to 220 μm in case of the 3.5 mm foil and 40 μm for the 8.6 mm foil. It can be already seen that the foil can be thicker compared to Scenario B, and in case of the closer foil the increase is substantial.

For the closer foil the resolution degrades by 1% and 1.3% for low and high p_T^{-1} respectively, but this degradation is only visible at both ends of the p_T^{-1} range. The mean resolution improves by 2.5%. In case of the single piece foil the resolution improves by 1.5 % for low p_T^{-1} and 1.2% for high. The overall improvement is 4%. Both cases start degrading after $\eta = 4.4$ with 42% in for a single piece foil and 47% for a foil at 3.5 mm. The smaller difference between the different foil positions compared to Scenario B, can be explained by the fact that a closer distance of the sensor to the foil leads to a shorter extrapolation lever compared to Scenario B and therefore to increased extrapolation error from the first hit to the primary vertex. A summary of the parameters of all layouts that lead to a similar IP resolution to Upgrade I for scenario C can be found in table 4.4.

Fig. 4.49. IP resolution for layouts with reduced ASIC and sensor thickness of 100 µm and increased foil thickness so that the same performance could be achieved as Upgrade I for Scenario C. The Simulated spatial resolution is 10 µm

Cut-out	Sensor thickness [µm]	Sensor resolution [µm]	ASIC thickness [µm]	Foil radius [mm]	Foil thickness [µm]
Hexagon	200	10	200	3.5	20
Hexagon	200	10	200	8.6	20
Octagon	200	10	200	3.5	20
Octagon	200	10	200	8.6	20
Octagon	100	10	100	3.5	220
Octagon	100	10	100	8.6	40

Table 4.4. Scenario C configurations that achieve a similar performance as Upgrade I.

4.6 Summary

In this chapter the design of a new detector layout and its influence on the IP resolution was discussed. For this a new fast simulation was developed to allow for the fast testing of new geometries. The setup was validated against the full LHCb simulation framework and the

implication of all simplifications were discussed. A scenario B was proposed which puts the first active pixel at a distance of 11.1 mm from the beamline. To reduce the needed increase in length of the detector the modules after a distance of 60 cm from the interaction are moved from 11.1 mm to 10.5 mm and two different inner aperture shapes (hexagonal and octagonal) were introduced. To achieve the same IP resolution as Upgrade I several other parameters had to be adjusted. The spatial resolution needed to be improved from 12.5 µm to 9 µm. In addition, substantial decreases in material budget had to be implemented. Several options for achieving this have been presented, all of which use a cylindrical foil instead of the corrugated foil of Upgrade I. A study of the impact of the different parameters of the IP resolution and its interaction with a Kalman filter was presented. It was concluded that the combination of scattering error and extrapolation error to the IP resolution led to a worse resolution than their simple square sum. In addition, it was shown that the amount of scattering centres plays a critical role in the IP resolution, especially after the implementation of a Kalman filter, and they should be kept as low was possible. An extensive discussion of the IP resolution has been presented and it has been shown that by using a cylindrical foil of the same thickness the IP resolution can be improved compared to a layout with a corrugated foil. The corrugated foil offers only for high η tracks an improved resolution. It must be mentioned here that this only considers the case in which the corrugated foil thickness is uniform along the whole foil. Local thinning can reduce the difference. Furthermore, no "tails" were simulated for the cylindrical foil. This effect has only a marginal effect on the difference, as can be seen by plotting the IP resolution as a function of ϕ. Even for regions with angles away from the tails, the cylindrical foil shows better resolution. It has been shown that for both types of foil a reduction in pixel resolution leads to the most significant improvement of the IP resolution. A scenario C, with the sensors at 9.5 mm, was proposed as a compromise between the limitations on the material budget, detector length, pixel resolution and the radiation damage. Again, the two types of apertures were discussed. In addition, a scenario where the RF-foil is placed at 8.6 mm is discussed. This allows the foil to be made of a single piece since at this distance it does not need to be retracted from the beam during injection. Again, several viable solutions are presented in table 4.4. Lastly the improvement of the same layout as Upgrade I for Upgrade II with a cylindrical foil were discussed.

Sensor design

To study the effect of radiation damage and timing on planar n-on-p sensors, several test structures were designed and produced by ADVACAM[1]. Non-oxygenated wafers of four different thicknesses (300, 200, 100 and 50 μm) were produced with a bulk resistivity of around 10 kΩ cm. Each wafer was produced using the same masks. The production layout of each wafer can be seen in figure 5.1. The 300 μm wafers were processed without thinning, whereas the thinner wafers were first processed on the backside and then attached to a support wafer for the top side processing. This was done to prevent the breaking of the wafers during the process steps. The support wafer was removed before the metallization step.
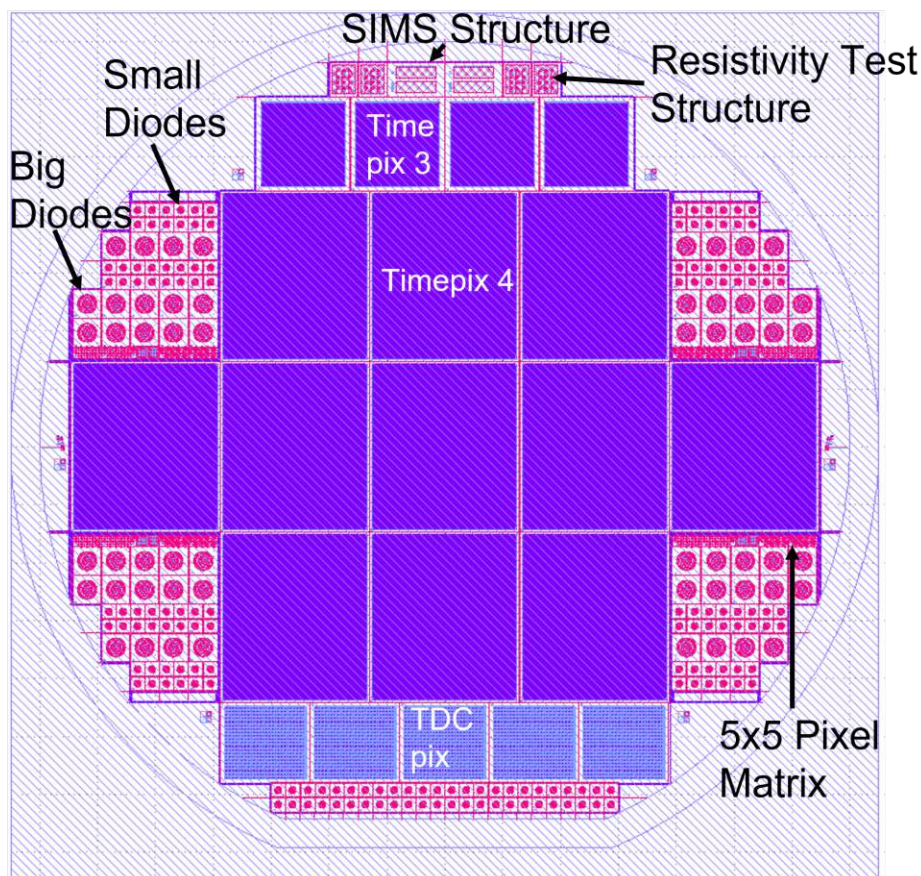
Fig. 5.1. Mask layout of the wafers produced by ADVACAM. Metallization masks are coloured blue. Implant masks are coloured red.

The main area of the wafer is dedicated to pixel matrices (Timepix 4, Timepix 3 and TDCpix),

---

[1]ADVACAM Oy. Espoo, Finland
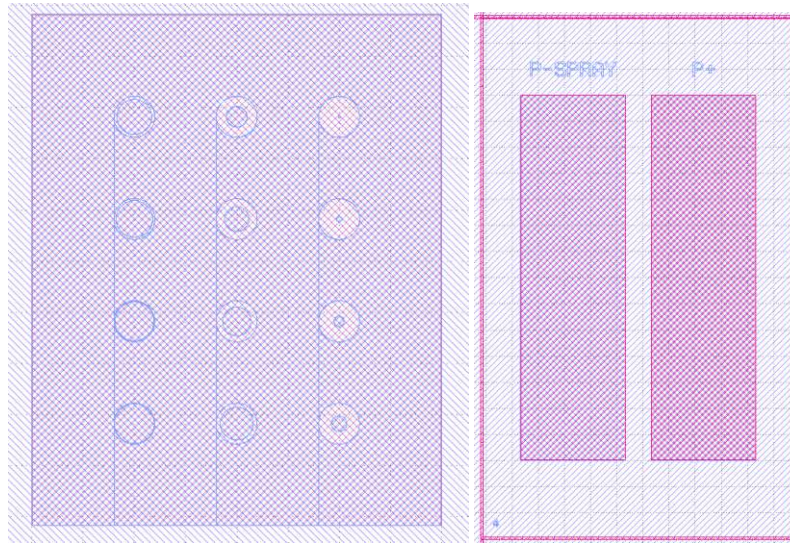
Fig. 5.2. Left: Layout of the resistivity test structures. **Right**: Layout of the SIMS test structures. Blue regions represent the metallization, red ones the implant.

which were bump-bonded to ASICs. To measure the surface resistivity of the n+ doped region, special structures were designed consisting of a metallized implant region with ring-like cut-outs of different widths. The resistivity can then be measured for different distances of the inner electrode and the outer metallization. For secondary Ion Mass Spectroscopy measurements, dedicated structures are implemented in each wafer consisting of region dedicated to the p-spray and the n+ implant (see figure 5.2) [88]. To enable the study of charge sharing the wafer also includes 5x5 planar pixel matrices with a $55 \times 55 \, \mu\text{m}$ pixel pitch.

Circular diodes were implemented to avoid field edge effects and simplify simulations by exploiting rotational symmetries. Each of them has a guard-ring to shield the main electrode from currents originating from defects introduced during dicing and to ensure a well-defined depleted volume. The readout electrode (pad) consists of three concentric rings connected through metal bridges of 15 μm width. The split of the electrode was done to prevent a lower time resolution in pad areas far away from the electrode. The backside is fully metallized with periodic holes to allow for laser illumination (see figure 5.4). Two sizes of diodes were produced to account for different measurement requirements of the different parameters studied. The big diodes (figure 5.3b) have a central implant with a diameter of 3 mm and a 50 μm wide guard ring implant. The gap between these implants measures 85 μm. For the small diodes (figure 5.3a) the diameter of the central implant is 1 mm and the width of the guard ring is 25 μm, with a gap of 60 μm. The metal electrodes are created with a 10 μm overhang over the oxide to ensure a smooth transition of the junction line into the oxide to prevent early breakdown [107]. For IV and CV measurements bigger diodes lead to increased leakage current and capacitance, which enables more precise measurements of these quantities. The smaller diodes are used for timing measurements as the lower capacitance and leakage current lower the noise, which is especially relevant for the thinner sensors. For the present study only the circular diode structures located at the outer edge of the wafers are used.
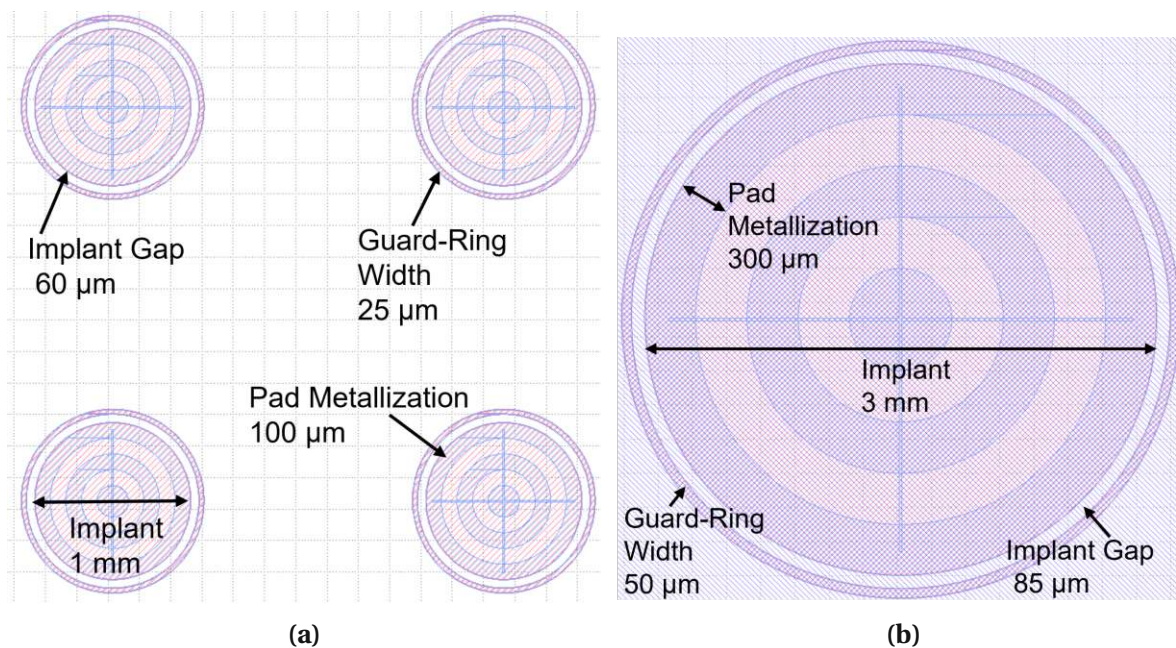
Fig. 5.3. Layout of the circular diodes. Blue regions represent the metallization, red ones the implant. **a:** Small Diode. **b:** Big Diode.
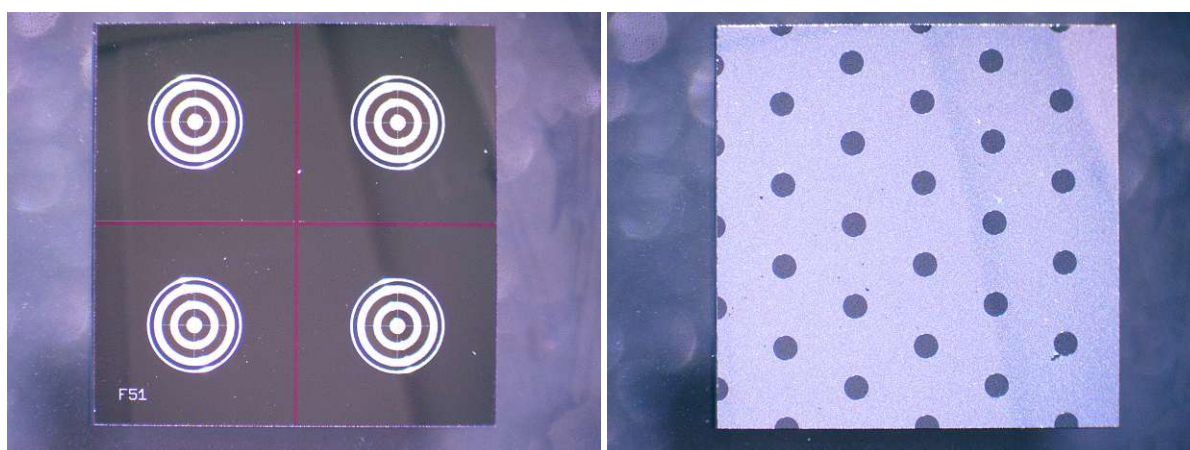
Fig. 5.4. Picture of the front (left) and back side (right) of a small diode sample.

5.1 Secondary ion mass spectroscopy

As the field inside the sensor is shaped by the dopant profiles, good knowledge of the latter is necessary for accurate device simulations. Using Secondary Ion Mass Spectroscopy (SIMS) one can precisely determine the implant concentration within the device. It allows one to quantify the doping layers up to a depth of 10 μm [108]. As the doping profiles are expected to have a depth of 1-2 μm, this range is adequate. In addition, SIMS also delivers information about interface layers on top of the silicon substrate, which may be the cause of potential abnormal device behaviour. All measurements were performed at the laboratory of the GEMaC group (Group d'Etude de la Matière Condensée) of the University of Versailles [109].

5.1.1 Experimental setup

In SIMS, atoms are removed from the sample's surface through sputtering with an ion beam. These atoms are subsequently redirected into a mass spectrometer where the intensity for a certain mass window can be measured. A sketch of the setup can be found in figure 5.5. SIMS
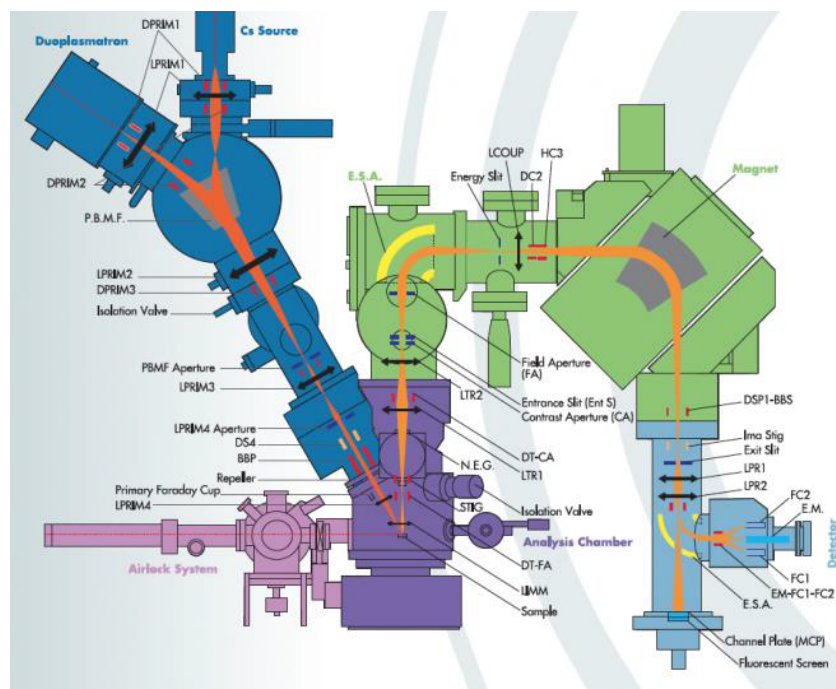
Fig. 5.5. Overview of a SIMS system. Reproduced from Ref. [110].

is a destructive process. To ensure no contamination and to minimize scattering of the primary ions used for sputtering, the whole process has to be conducted in vacuum (in this case 6.3×10^{-10} mbar). The primary ions are generated using a duoplasmatron source [111] and are subsequently accelerated towards the sample by an electric field. The impact of the primary ions on the sample surface leads to the release of secondary particles and/or molecules into the gas phase. Only charged particles are of interest as they can be extracted and guided

to the detector system using an extraction field. The yield and polarity of the created particles depends on the type of primary ion. Oxygen for example increases the yield of positive ions due to its high electron affinity and ionization potential, as it binds electrons in the ionization process. Caesium on the other hand, leads, due to its accumulation on the sample surface during sputtering, to accessible electrons during the ionization process and therefore to a higher yield of negative ions. During the sputtering process, positive charge accumulates on the sample surface reducing the production yield of negative ions. This effect leads to a deterioration of beam focusing and increases the needed potential for secondary ion extraction. For conductive samples, surface charge accumulation is not an issue since the additional charge can be redistributed across the sample surface. For non-conductive samples compensation has to be implemented either by introducing an electron cloud through a secondary electron gun, coating the sample surface with a conductive layer or using negatively charged primary ions [112]. The electron beam was hereby calibrated during the measurements to compensate the accumulated charge in the case of Cs primary beams. To calibrate the intensity of the electron beam a conductive surface is needed to be used as a reference potential. This surface is achieved by using Plasma-Enhanced Chemical Vapor Deposition to deposit a 44.5 μm thick gold layer over the whole sample.

Once the secondary ions leave the sample surface, they are directed into a mass spectrometer. In it a specific mass is selected, either by the time of flight in the detector or by a selection magnet, to be directed into the readout system [113]. For the determination of the abrasion speed of the beam, the depth of the crater created by the ion beam has to be measured. This is done using a mechanical profilometer. It measures the depth by moving its tip across the sample surface while applying a constant force. The change in vertical position is recorded along the path of the tip. For each crater at least three measurements were performed. The height was determined by fitting a straight line at the surface and at the bottom of the crater and calculating the difference between the two. An example of a measured profile can be seen in figure 5.6.
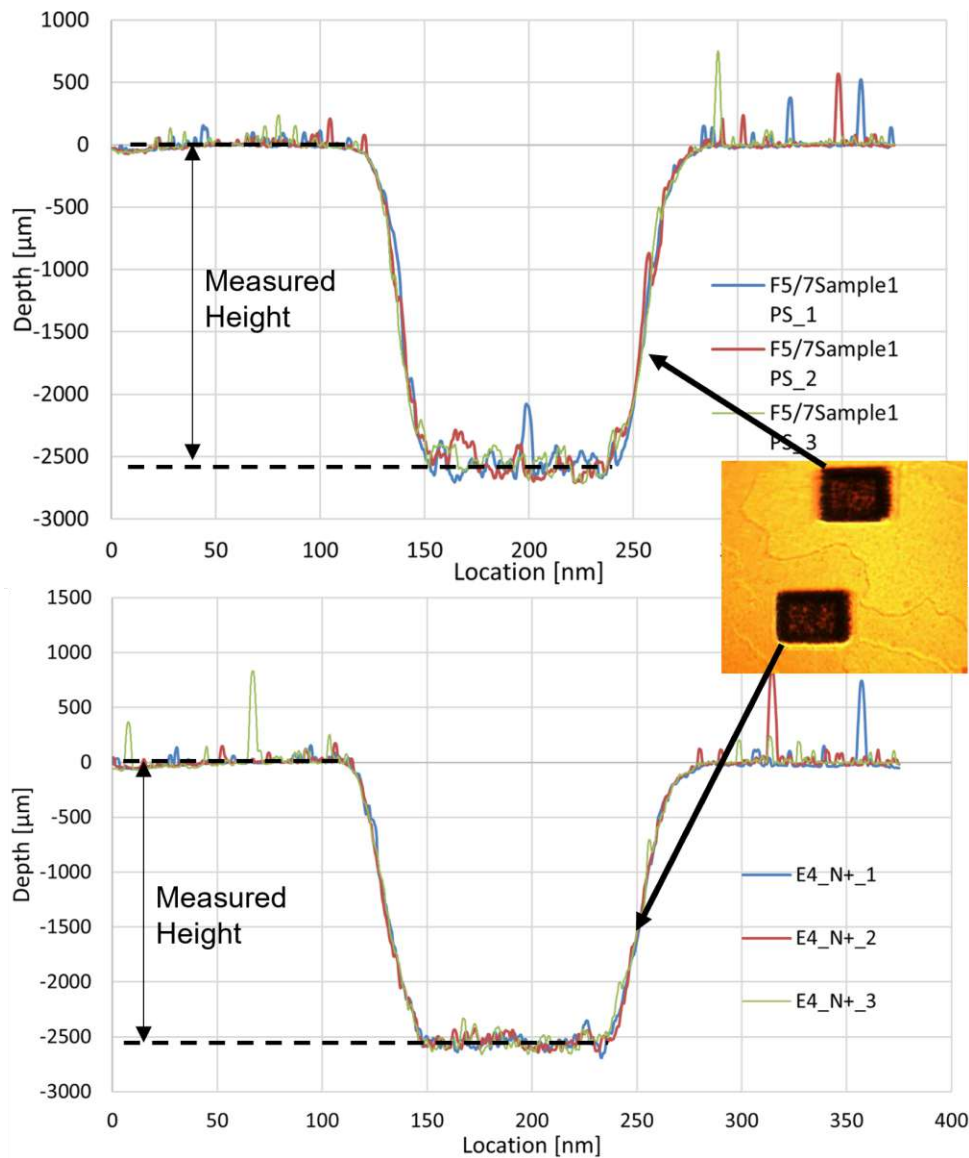
Fig. 5.6. Depth profile measurement for different SIMS craters in regions for different roughness. **Top**: Measurement in the light region of the metallization. **Bottom**: Measurement on dark regions of the metallization.

5.1.2 Method

As the production process should be the same for all different thicknesses, only one sample was measured. The two main elements of interest in our sample are phosphorus and boron, as they are used for the n+ implant and the backside/p-spray doping respectively. For phosphorus, caesium ions can be used to increase the yield of negative phosphorus ions, whereas oxygen is used to determine the boron concentrations.

Due to the continuity of the beam a compromise between the integration time, the abrasion speed, the number of followed elements and the analysed area has to be found. A fast abra-

sion speed would allow for a fast measurement, but increase the sputtered depth between two measurement points for a single element, thus increasing the depth uncertainty. The same goes for an increased integration time and an increased amount of observed elements. The size of the sputtered area affects the impact of sputtering the edge of the crater, where a smaller area leads to a better resolution of the transition points at the cost of the resolution of the followed elements.

The signal of the sputtered-ions is measured by directing the secondary ion beam to an electron multiplier. To convert the electronic signal to a concentration for the desired element, a scaling factor has to be applied, the Relative Sensitivity Factor (RSF). This factor not only depends on the beam conditions but also on the measured element itself and the matrix it is embedded in. It therefore has to be calculated anew whenever one of these parameters is changed. For RSF calculations dedicated calibration samples are used which have to be measured at exactly the same beam conditions as the sample under test. The calibration sample itself has to consist of the same element implanted in the same matrix as the sample under test. In addition, the implanted profile in the calibration sample has to be well defined. The RSF can be determined from the mean concentration of the element to be analyzed in the reference sample (C_{Element}), the mean current of the analyzed element (I_{Element}) and the matrix element (I_{Matrix}) [88]

$$RFS = C_{\mathrm{Element}} \frac{I_{\mathrm{Element}}}{I_{\mathrm{Matrix}}}. \tag{5.1}$$

The mean current can be calculated by dividing the integral of the signal ($S_{\mathrm{Element}}, S_{\mathrm{Matrix}}$) by the total measured time T with

$$I_{\mathrm{Element}}^{\mathrm{mean}} = \frac{\int_0^T S_{\mathrm{Element}} dt}{T} \tag{5.2}$$

and

$$I_{\mathrm{Matrix}}^{\mathrm{mean}} = \frac{\int_0^T S_{\mathrm{Matrix}} dt}{T}. \tag{5.3}$$

To get the mean concentration, the known implanted dose of the reference sample (K) has to be divided by the measured crater depth D,

$$C_{\mathrm{Element}} = \frac{K}{D}. \tag{5.4}$$

It has to be mentioned that for the final calculation of concentrations with the help of equation 5.1 both the signal of the matrix and the element have to be used. The uncertainty of the RFS (δRSF) can be estimated, due the independence of the different parameters, with error propagation of equation 5.1 [114] as

$$\delta RSF = \sqrt{A + B} \tag{5.5}$$

with

$$A = \frac{(S_{\text{Matrix}} T \delta K)^2 + (K S_{\text{Matrix}} \delta T)^2 + (\delta S_{\text{Matrix}} T K)^2}{(S_{\text{Element}} T D)^2} \tag{5.6}$$

and

$$B = \left(\frac{K S_{\text{Matrix}} T}{S_{\text{Element}} T D} \right)^2 \left(\left(\frac{\delta D}{D} \right)^2 + \left(\frac{\delta S_{\text{Element}}}{S_{\text{Element}}} \right)^2 + \left(\frac{\delta T}{T} \right)^2 \right) \tag{5.7}$$

The uncertainty of the current can be split in contributions from the signal measurement uncertainties and time measurement uncertainties. The uncertainty of the total measured time is the square sum of the uncertainties of the time of the first and last measured point, which in turn are half the time difference of two adjacent measured points,

$$\delta T = \left| \frac{t_{i+1} - t_i}{2} \right|. \tag{5.8}$$

The resolution of the depth consists of the intrinsic resolution of the profilometer used to measure the depth δD_{cal} (5.3 nm) and the standard deviation of the depth measurements δD_{stat},

$$\delta D = \sqrt{\delta D_{\text{cal}}^2 + \delta D_{\text{stat}}^2}. \tag{5.9}$$

For the uncertainty of the implanted dose (δK) the standard deviation of the tail of the calibration profile is used. The uncertainty of the dose integral consists of the square sum of the time difference between the measurement of two points of the same element δt and the counting uncertainty, which is considered 1, and can be calculated with

$$\delta S = \sqrt{\sum_{k=0}^{n} \delta t^2 + 1}. \tag{5.10}$$

Not only the change of concentration, but also its position in the sensor is of interest. As the SIMS measurement only return the time of measurement, it has to be converted to a position. For this purpose, the abrasion speed v has to be calculated. Under the assumption of a stable beam during the measurement, a constant abrasion speed is assumed for a certain uniform layer. The abrasion speed can be calculated by measuring the depth of the crater created by the primary ion beam and dividing it by the total measurement time. The speed can then be used to extrapolate the depth of every measured point.

The abrasion speed not only depends on beam parameters, but also on the sputtered material itself. For samples consisting of stacks of layers of different compositions, an abrasion speed has to be calculated for each layer and can be only applied to the corresponding layer. The position of layer transitions can be determined by looking at the measured counts of the observed elements. Depending on the interface types a sharp change in intensity should be visible for specific elements. To estimate the exact interface position, the first derivative of the signal is calculated for each of the monitored elements. For an abrupt layer transition, the secondary ion intensity follows a step function and the derivative is delta function
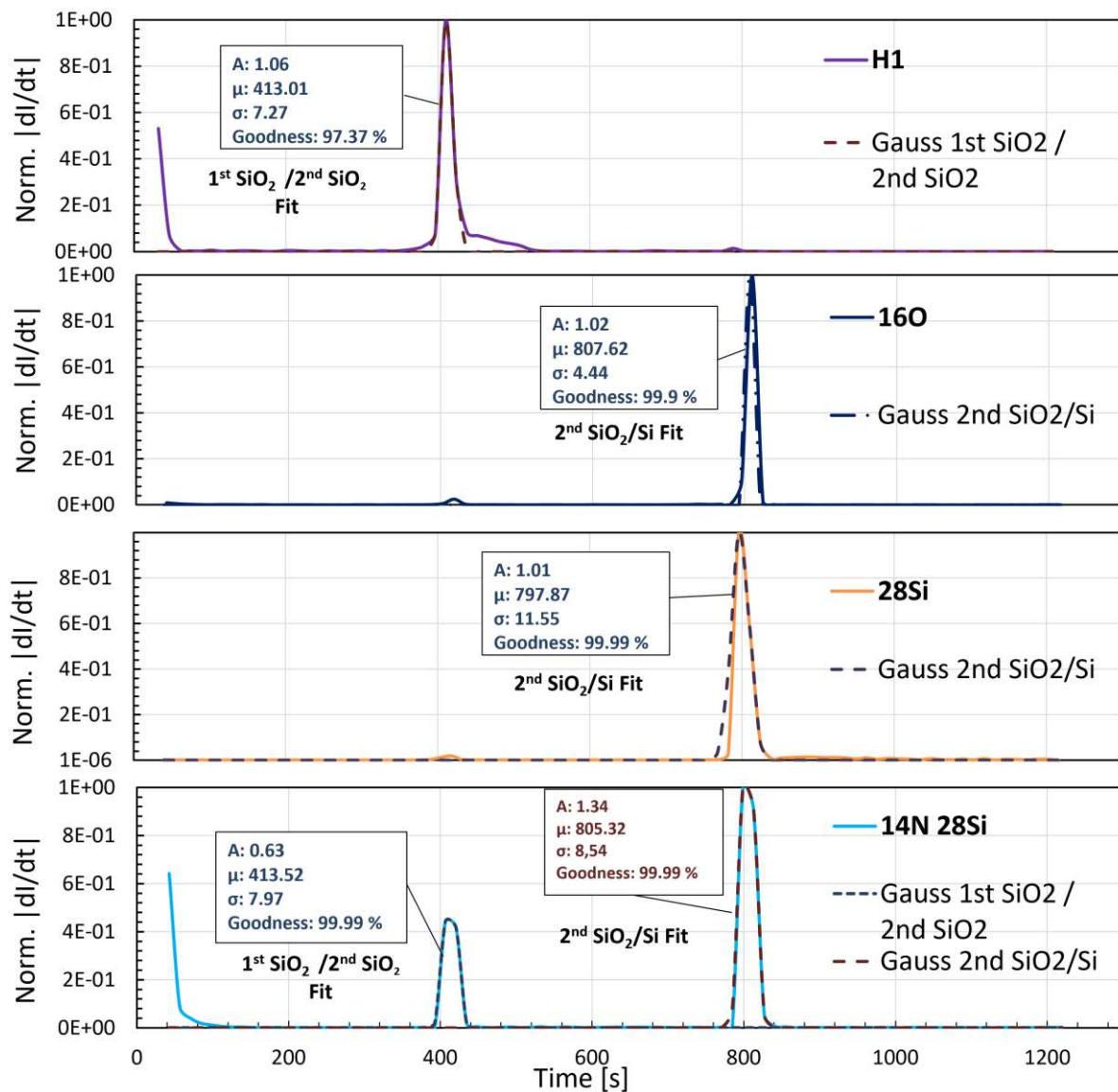
Fig. 5.7. First derivation of intensities of the count rate for different elements normalized to the highest value for a measurement in-between the dedicated doping areas. Transition points are fitted with gaussian curves. The fit parameters are displayed next to the first.

the. Due to the finite resolution of the measurement time and inter-layer diffusion effects, a Gaussian-like first derivative shape is expected with its mean at the interface point and standard deviation corresponding to the uncertainty in measurement of the layer transition (see figure 5.7) [115]. A Gaussian fit is performed in the first derivative of the signal of the monitored elements. For each layer the mean of all fitted curves is used to estimate the interface position, whereas the resolution includes the uncertainty of the time measurement. For each layer the depth d_i is calculated in relation to the previously determined interface transition

time T_{i-1}, while the measured depth of all previous layers D_j is added, as

$$d_i = \sum_{j=0}^{j=i-1} D_j + (t_i - T_{i-1})\, v_i. \tag{5.11}$$

The uncertainty of the depth calculation can be split in two terms. The first originates from the extrapolation of the layer interface. The second originates from the uncertainties in the depth measurements of the previous layers and the resolution of the determination of the starting point of the layer, with the final equation being

$$\delta d_i = \sqrt{(t_i - T_{i-1})^2\, \delta v_i^2 + v_i^2 \delta t_i^2 + \sum_{j=0}^{j=i-1} \delta D_j^2 + v_i^2 \delta T_{i-1}^2}. \tag{5.12}$$

5.1.3 N^+ region

To have a good resolution in the layer transition, a smooth surface is a necessary prerequisite. As was discussed at the beginning of chapter 5, the over-etching of the top metal layer resulted in a a rough surface causing a degraded resolution in the measurement of layer transition interfaces. Under the microscope the metal surface exhibits several dark and light structures, corresponding to regions of more or less surface roughness (see figure 5.6). To ensure a good resolution, measurements of the layer transitions are only performed, when possible, in the dark regions, which exhibit much smoother transitions, whereas mass calibration and test measurements are done in the light regions. This strategy was adopted as a compromise due to the limited number of regions with smooth surfaces big enough for measurements.

As mentioned before, the continuous nature of the beam imposed limitations on the number of followed elements. For this measurement hydrogen, carbon, oxygen, aluminum, phosphorus, silicon and silicon nitride are chosen. Hydrogen is an indicator for the type of oxide used, with wet oxide containing a much higher hydrogen concentration than dry oxide. Oxygen can be used to identify oxide layers, whereas increased aluminium presence characterizes the metallization layers. Silicon and phosphorus need to be followed as they are the matrix and doping element, respectively. Silicon nitride can be used to determine the existence of nitride layers.

For the first test measurements a high count rate of phosphorus was observed deep inside the silicon bulk. As phosphorus is implanted, its concentration is expected to have a peak close to the silicon interface and a drop down to the detectable limit after a certain depth. As this is not the case an interference of molecules with a similar mass to charge ratio was suspected to be responsible for the measured constant phosphorus concentration in the bulk. It was therefore decided to switch to a higher mass resolution, which would increase the required signal collection time, thus doubling the overall measurement time. As can be seen

in figure 5.8, in a high mass resolution mode, the expected baseline phosphorus resolution is obtained.
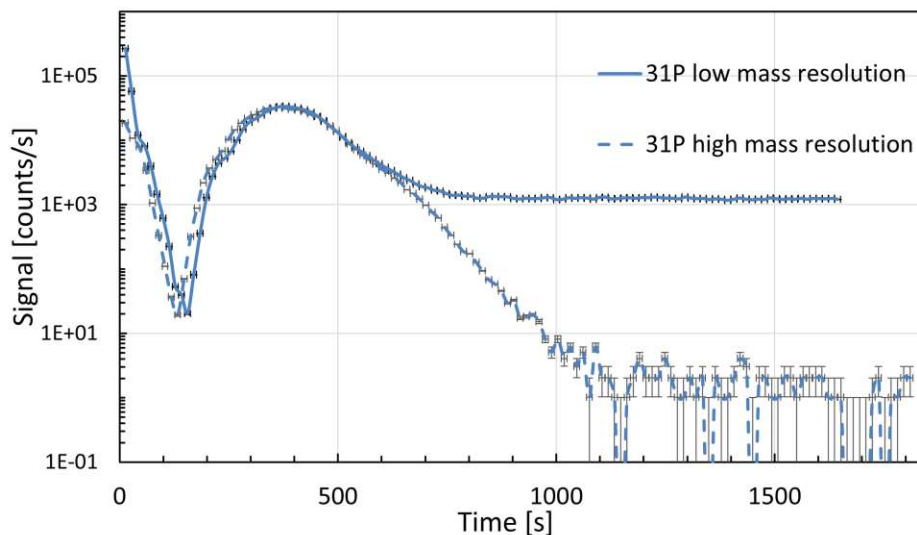
Fig. 5.8. Comparison of the phosphorus signal measured with high and low mass resolution of the n+ region.

For all measurements of the n^+ sample, Cs primary ions with a primary beam current of 40 nA are used. The beam was scanning an area of 125×125 µm^2 whereby only the central area the size of 87×87 µm^2 was used for the analysis. This corresponds to roughly 50 % of the sputtered area and was done to reduce the effect of the edge of the crater on the measurement. A table containing the beam parameters for all measurements can be seen below (table 5.1). Using a dedicated phosphorus calibration sample, a RSF of $1.28 \pm 0.0483 \times 10^{23}$ atoms cm^{-3} was calculated. Additionally, the measurement of the calibration sample is used to determine the sensitivity as previously described. For these specific beam conditions, a resolution of $6.09 \pm 0.731 \times 10^{14}$ atoms cm^{-3} was achieved, as shown in figure 5.9.

Measurement	Primary Current [nA]	Raster Size [µm]	Analysis Size [µm]	Primary Ion Type
n^+	40	125	87	Cs
p-spray caesium	40	125	75	Cs
p-spray oxygen	100	125	75	O
backside	100	125	62.5	O
in-between	40	125	87	Cs

Table 5.1. Beam parameters for the different SIMS measurements.
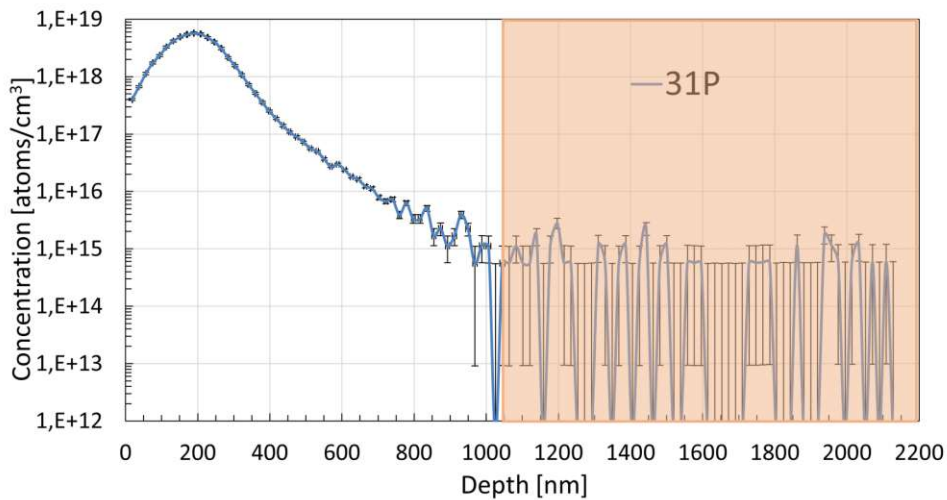
Fig. 5.9. Doping profile of the phosphorus calibration sample. Sensitivity estimated by a Gaussian fit at the tail of the sample (orange region).

To evaluate different layers and determine the transition point, two different measurements were performed (figure 5.10 and 5.11). During this process, hydrogen, oxygen, silicon and silicon nitrite were monitored. Aluminum could also be a good candidate as is should exhibit a sharp transition at the end of the metal layer, but due to the roughness associated with the over-etching of the latter, it was excluded. The first layer that is visible in this probe is the aluminum layer used as the contact electrode which extends up to a thickness of 334 $\pm$ 22 nm. This is followed by two layers of silicon oxide indicated by the high silicon and oxygen content in these regions, reaching a total thickness of 295 ± 25 nm. The relatively high concentration of hydrogen indicates the use of wet oxidation [116], which typically leads to a rougher interface between the oxide and the silicon, increasing the probability of defects in the transition region. The fits used to determine the transition points can be seen in figure 11.1 and 11.2.

The depth of the layers was estimated using the two separate measurements, where sputtering was stopped when the transition point was reached. A calculation of the different abrasion speeds can be seen in table 5.2. For the aluminum, a mean abrasion speed of $1.67 \pm 0.17 \, \mathrm{nm\,s^{-1}}$ was calculated, while for the oxide $1.7 \pm 0.21 \, \mathrm{nm\,s^{-1}}$ was determined. The larger error associated to the oxide abrasion speed originates from the relative uncertainty in the layer transition depth. For silicon, a slower rate of $1.33 \pm 0.02 \, \mathrm{nm\,s^{-1}}$ is calculated. For the profile of the phosphorus inside the silicon two measurements were combined by averaging the measured points (see figure 5.12).
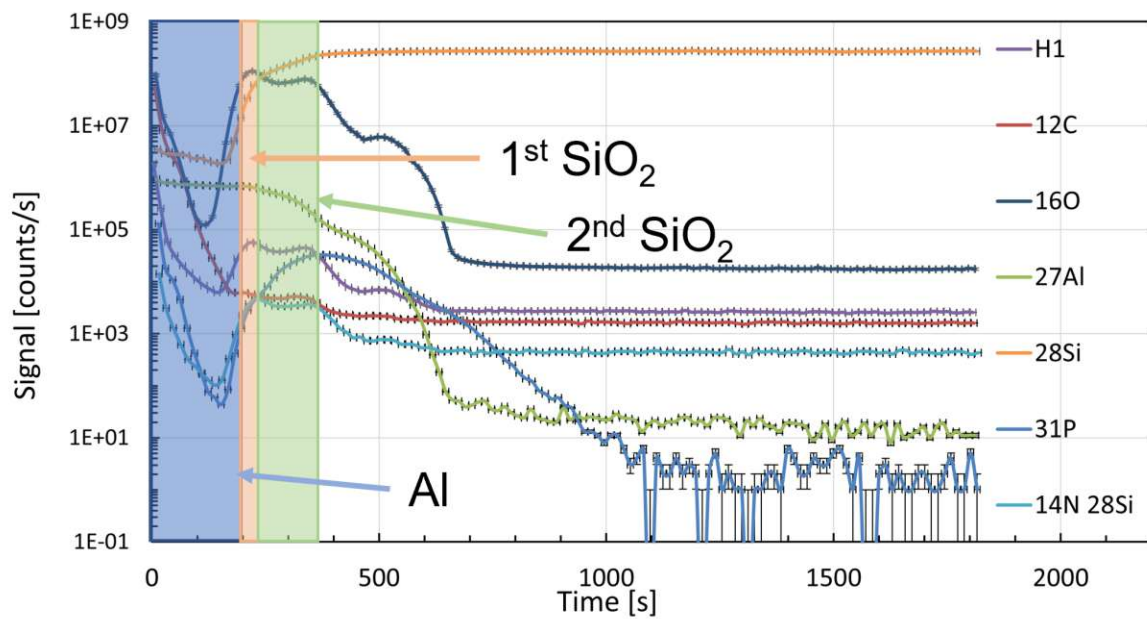
Fig. 5.10. First SIMS measurement in the n^+ region. Pre-silicon layers are marked with coloured boxes.
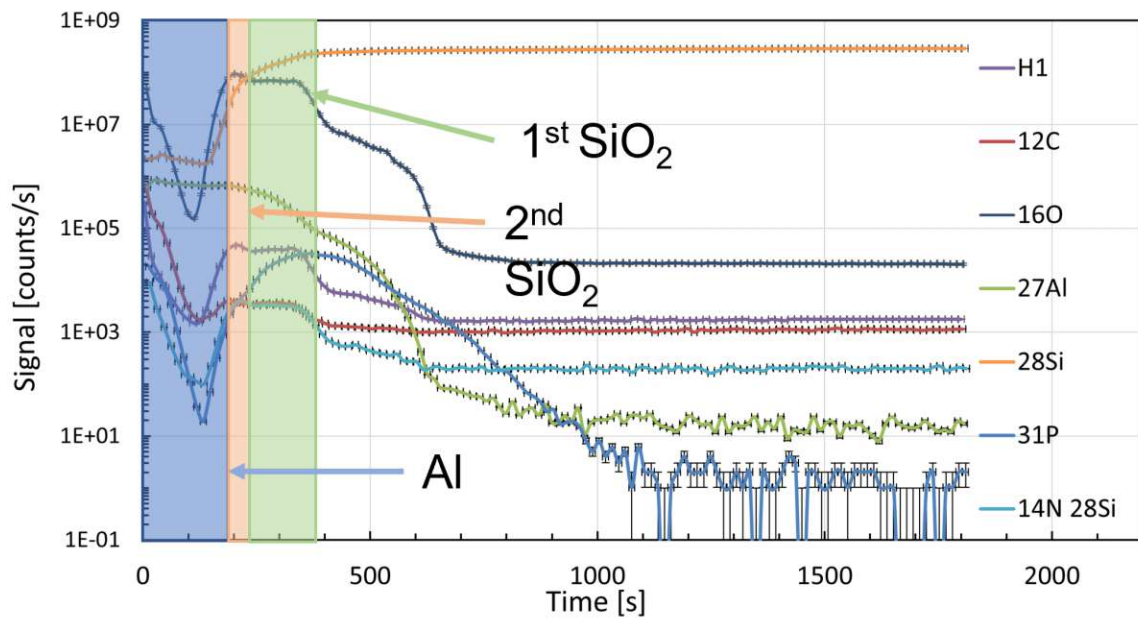
Fig. 5.11. Second SIMS measurement in the n^+ region. Pre-silicon layers are marked with coloured boxes.

	Abrasion Speed [nm s^{-1}]	Error [nm s^{-1}]
Al Measurement 1	1.75	0.19
SiO$_2$ Measurement 1	1.65	0.26
Si Measurement 1	1.32	0.02
Al Measurement 2	1.59	0.17
SiO$_2$ Measurement 2	1.74	0.29
Si Measurement 2	1.34	0.03

Table 5.2. Abrasion speeds calculated for the different layer present in the n^+ region.
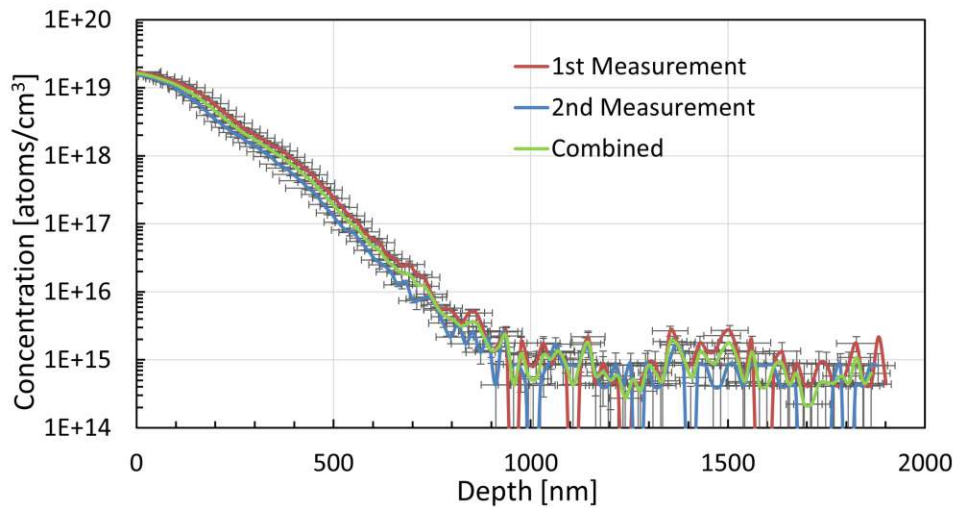
Fig. 5.12. Measured doping profile for the phosphorus implant in the n^+ region. The "Combined" plot represents the mean of the two measurements.

5.1.4 P-Spray

Oxygen primary ions were used for the p-spray measurement to increase the yield of boron ionization (used as an implant). Due to the electronegativity of the primary ions, accumulation of negative charge during the measurements at the sample surface occurs. Since charge compensation for negative ions is not possible, charge accumulation in the silicon oxide is inevitable. This accumulation of negative charge in the oxide layer can cause signal loss (see figure 5.13), which impacts the determination of the layer transition. As the expected boron concentration is substantially lower compared to the phosphorus, two calibration measurements were performed to try and improve the sensitivity: One with the same beam conditions as for the phosphorus calibration and one where only boron and silicon were followed while the total analysed window was reduced to 75×75 µm to limit the effect of the edge of the sputtering crater on the measurement even further. The relevant parameters for these two measurements can be found in figure 5.1.
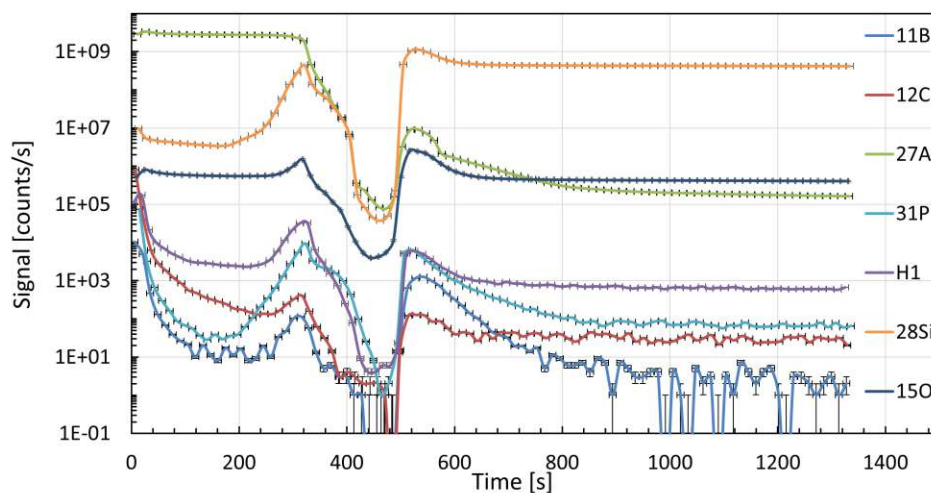
Fig. 5.13. SIMS measurement of the p-spray region using oxygen primary ions. The signal loss between 400 and 500 s in the SiO_2-layer happens due to charge accumulation.

The calibration measurements before and after the reduction of followed elements can be seen in figure 5.14. For the calculated abrasion speed and RSF factor both measurements are in agreement within their respective uncertainty range. The sensitivity was slightly improved from $4.17 \pm 0.295 \times 10^{14}$ atoms cm^{-3} to $3.11 \pm 0.256 \times 10^{14}$ atoms cm^{-3} . The last configuration was therefore used for all further p-spray measurements.

Due to the charge effects detailed previously, layer estimation was performed using Cs primary ions. For the layer transition measurement high mass resolution was used again. As can be seen in figure 5.15 only one oxide layer is visible with twice the thickness of the combined oxide layers in the n^+ region of 595 ± 39 nm. This can be explained by its function as a screening oxide during the implantation of phosphorus, where the additional layer thickness
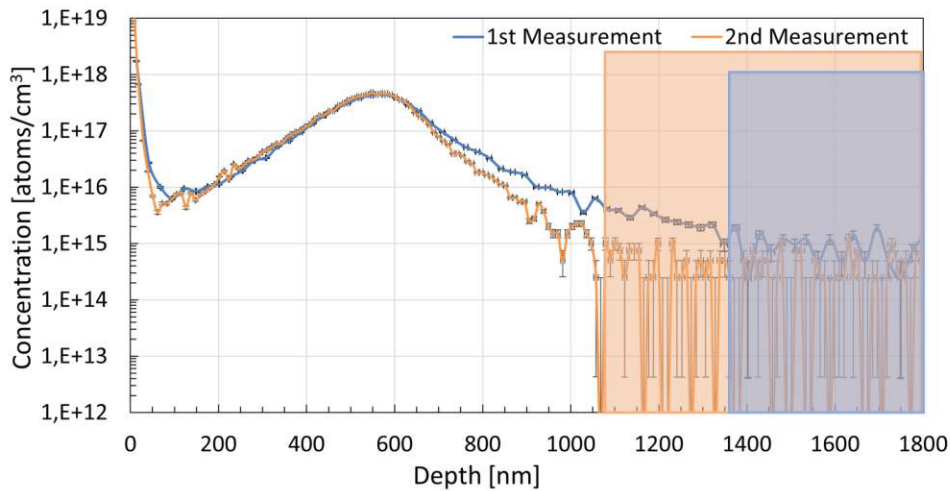
Fig. 5.14. Boron calibration using oxygen primary ions. Highlighted areas are used for sensitivity calculations of the corresponding measurement.

is used to stop the phosphorus ions from reaching the silicon. Another indication for this is the increased phosphorus signal in the oxide. The increase in the aluminum thickness to 461 $\pm$ 23 nm is a result of the measurement carried out on a raised (light) area.
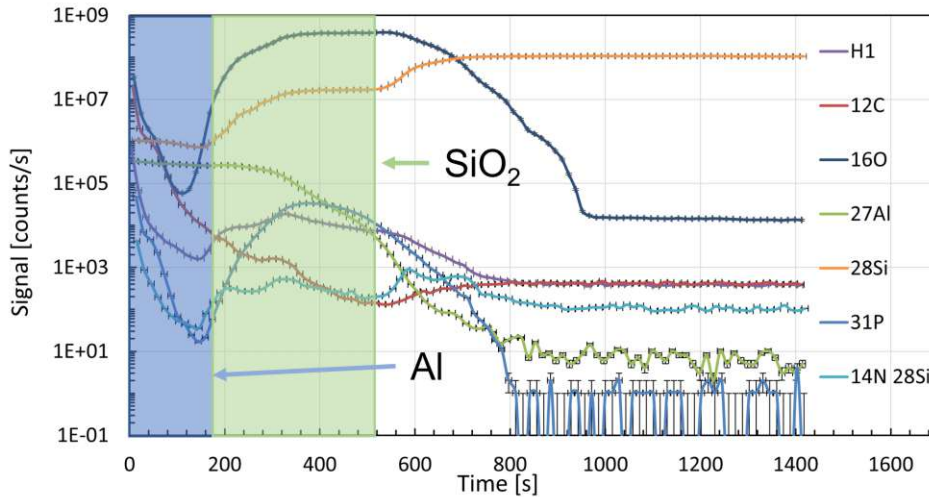
Fig. 5.15. Layer transition for the p-spray region. Pre-silicon layers are marked with coloured boxes.

Additionally, two craters which were sputtered until the silicon interface using Cs primary ions, were done to allow for a precise layer transition and to be later used for the measurement of the boron profile. For the measurement of the profile, the ion source was switched back to oxygen and prepared craters were used. The calculated abrasion speeds for the aluminum and oxide agree within their uncertainty with the speed calculated for the n^+ region (see figure 5.3). The abrasion speed for silicon, 2.46 ± 0.08 nm s^{-1}, is substantially higher

compared to the n^+ sample. This can be explained by the switch to much higher beam energies necessary for the oxygen primary ion configuration. The implant was again estimated as the combination of the two measurements in the same way as described in the n^+ section (see figure 5.16).

	Abrasion Speed [nm s^{-1}]	Error [nm s^{-1}]
Al	1.47	0.09
SiO$_2$	2.13	0.2
Si Measurement 1	2.5	0.1
Si Measurement 2	2.42	0.05

Table 5.3. Abrasion speeds calculated for the different layer present in the n^+ sample.
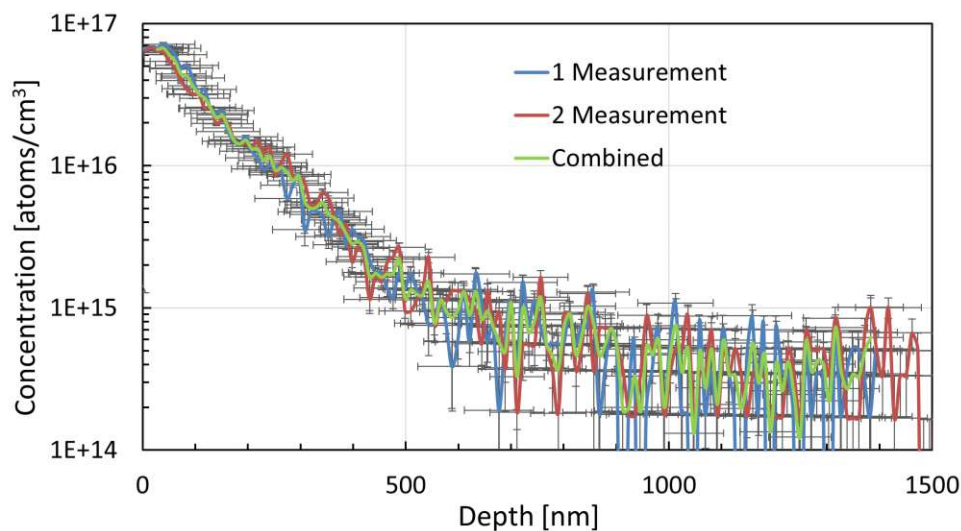
Fig. 5.16. Measured doping profile for the boron implant in the p-spray region of the test structure. The "Combined" plot represents the mean of the two measurements.

5.1.5 P^{++} (sensor backside)

The p^{++} region refers to the implant of the backside electrode used for biasing the sensor. As there should be no SiO$_2$ layer on top of the back side of the sensor, according to the specifications, oxygen primary ions were used from the start to measure the p^{++} region of the sample. Due to measured presence of aluminum in the silicon layer due to edge effects of the metal layer for the first test measurement, the analyzed region was reduced for all further measurements (see table 5.1). As a result new calibration measurements were conducted for boron with the modified conditions. Another effect of the analysed field size reduction in resolution to $1.13 \pm 0.421 \times 10^{15}$ atoms cm^{-3} could be achieved, reducing the sensitivity by roughly a factor of two compared to the previous calibration. As the backside doping profile

is expected to have the same concentration as the n^+ implant, the reduction in sensitivity can be considered acceptable. No SiO_2 layer was found at the sensor backside (see figure 5.17). The abrasion speed for the silicon region of this sample agrees with the one previ-

	Abrasion Speed [$\mathrm{nm\,s^{-1}}$]	Error [$\mathrm{nm\,s^{-1}}$]
Al	1.34	0.09
Si	2.54	0.05

Table 5.4. Abrasion speeds calculated for the different layers present on the back side of the sample.
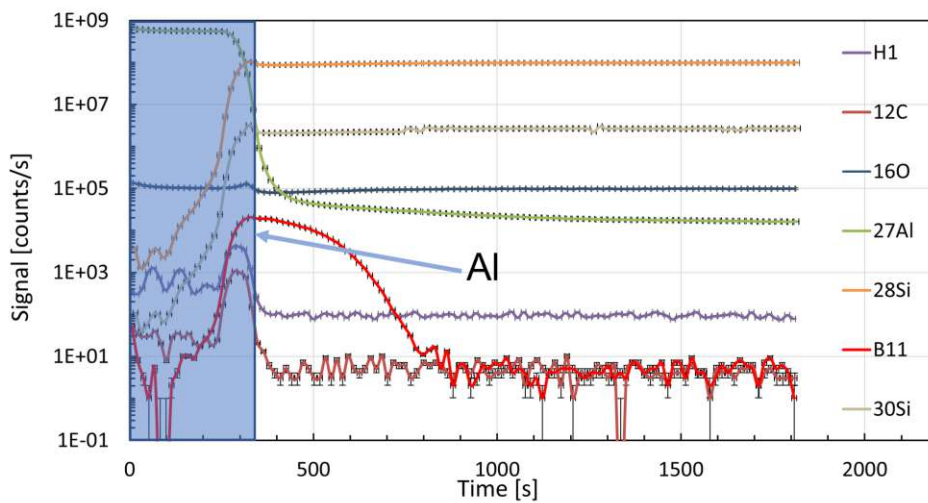
Fig. 5.17. Layer transition for the p^{++} region. Pre-silicon layers are marked with coloured boxes.

ously calculated using oxygen primary ions in the p-spray measurement. For aluminium, an even slower abrasion speed compared to previous caesium primary ion measurements is observed (see table 5.4). The metal layer thickness is estimated at 424 ± 8 nm, closer to the light area thickness measured at the p-spray region, supporting the theory that the dark region are over etched holes. As the metal layer on the backside was designed with openings to allow for charge injection via laser, two approaches were used to measure the doping profile. First the standard procedure was used, traversing through the metallization layer, while secondly a second measurement was also performed directly in a an opening, thus circumventing the aluminium layer completely. For the second measurement, the same boron profile was observed (see figure 5.18).
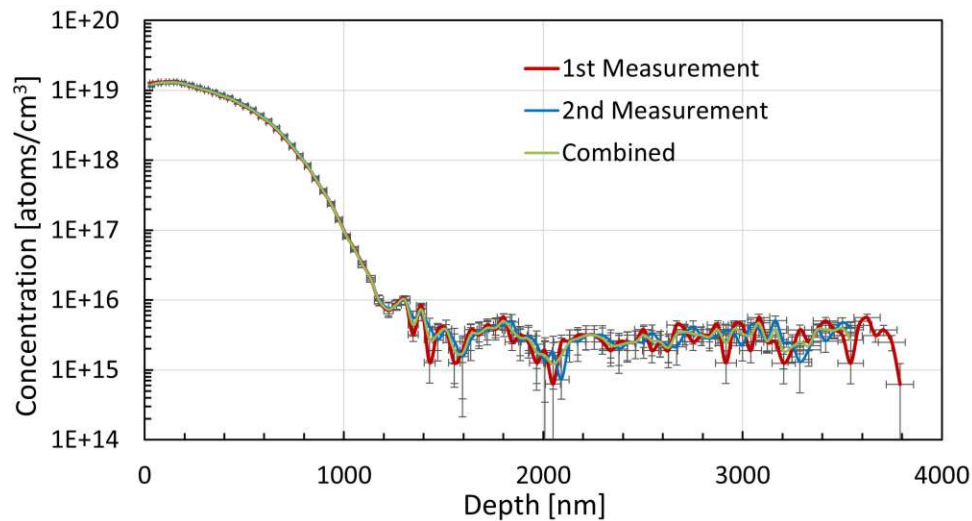
Fig. 5.18. Back side p^{++} implant profile for the two measurement and the combined mean profile .

5.1.6 Intermediate region

To test the effect of the uneven metal surface on the resolutions an additional measurement was performed in the region between the p-spray and n^+ implant, where only SiO_2 layers are present. As demonstrated in figures 5.19 and 5.7 the layer transitions are clearly visible. Two SiO_2 layers can be distinguished. The thickness of SiO_2 layer closest to the silicon is with 573 ± 18 nm equivalent to the one found at the p-spray region. Additionally,the same profile phosphorus can be found in it, where the preceding layer exhibits a constant high concentration of phosphorus. As this layer is not visible in the p-spray region, it can be theorized that it was removed for the deposition of the metal.
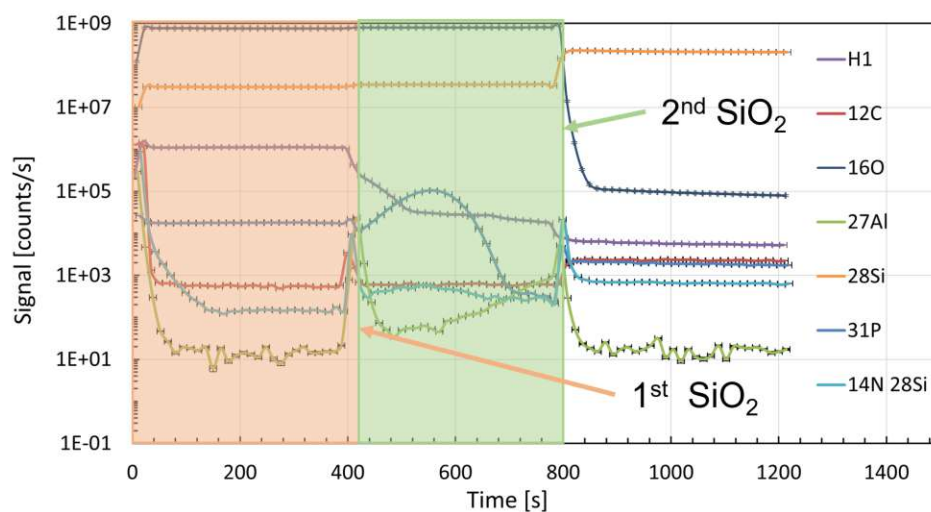
Fig. 5.19. Layer transition for the region between the two doping regions. Pre-silicon layers are marked with coloured boxes.

5.1.7 Summary

All doping profiles measured can be seen in figure 5.20. The n^+ implant has a peak concentration of $1.72 \pm 0.05 \times 10^{19}$ atoms cm^{-3} located at a depth of 4.5 nm inside the silicon. It reaches 50% of the implanted dose after 520 nm and reaches the detection limit at around 1000 nm. For the p-spray a peak concentration of $6.89 \pm 0.15 \times 10^{16}$ atoms cm^{-3} was measured at a depth of 16 nm. As this is a quite high value, being slightly higher than a standard concentration used to reach impact ionization in Low Gain Avalanche Diodes [117], this could potentially be a source of gain in the device. For the p^{++} implant a peak concentration of 1.85 $\pm 0.0793 \times 10^{19}$ atoms cm^{-3} was observed at a depth of 12.31 nm. Compared to the n^+ profile, it extends much deeper, dropping to a level of 10^{17} atoms cm^{-3} at 600 nm inside the bulk. For the doping profiles only the p-spray with its high peak concentration seems to be out of the expected range of values.
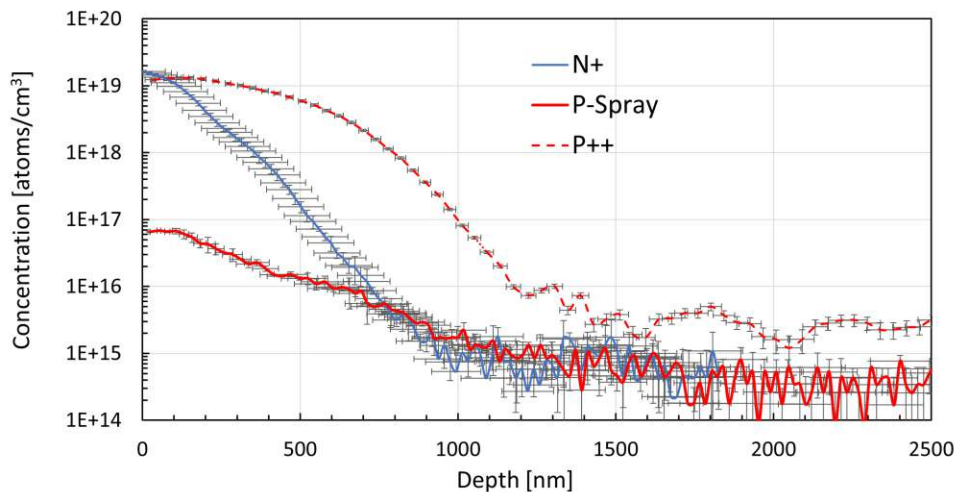
Fig. 5.20. Mean doping profiles measurement for the 200 μm ADVACAM test structures. Boron doping is displayed in red and phosphorus in blue.

6

Electrical characterization

6.1 Measurement setup

Before irradiation the leakage current (IV) and capacitance (CV) behaviour of all samples was studied to extract reference parameters for later studies. All CV and IV measurements were performed using the IV/CV setup of the solid-state detector (SSD) lab at CERN (see figure 6.1 a). The setup employs a cold chuck, which is used to apply a negative bias voltage to the backside of the sensors and to cool the sample. The sample is held in position by vacuum, applied through a small hole in the chuck to prevent movement during the contacting process and the measurements. The current is measured by connecting the top electrodes to the ground potential. For the guard-ring and the readout electrode the ground potential was applied through needles, which are brought in contact with the opening in the passivation of the corresponding electrode. While the needle used for the guard-ring is shorted directly to ground, the needle used for the pad measurement is connected to a measurement device depending on the type of measurement. Additionally the backside current of the sensor is measured through the power supply used for biasing. The needles are mounted on micro-positioners allowing for micrometer precision during sample contacting. A microscope, mounted on a movable arm, enables sample inspection during contacting. The whole setup is contained within a light tight box, which also functions as a Faraday cage. To prevent condensation during cooling of the samples and other effects related to humidity, the box can be flushed with dry air. The bias voltage was supplied by a Keithley 2410 sourcemeter, allowing voltages up to 1100 V. To switch between the IV and CV measurement configuration a switch box is used. For the IV measurement, the current is measured by a Keithley 6487 Picoammeter with a resolution of 10 fA [118] (see figure 6.1 b). CV measurements are performed with the help of an Agilent E4980A LCR meter. In a CV measurement configuration, two bias components are necessary. The DC component, responsible for sensor depletion and provided by the sourcemeter is added to the AC complement generated by the LCR meter. The two components are combined with the help of a bias tee (see figure 6.2).

For n-on-p sensors, a negative reverse-bias voltage is applied to the backside and the current measured at the readout electrode also has negative polarity. For easier readability only the absolute values of the bias voltage and current are used for all measurement and simulation plots.
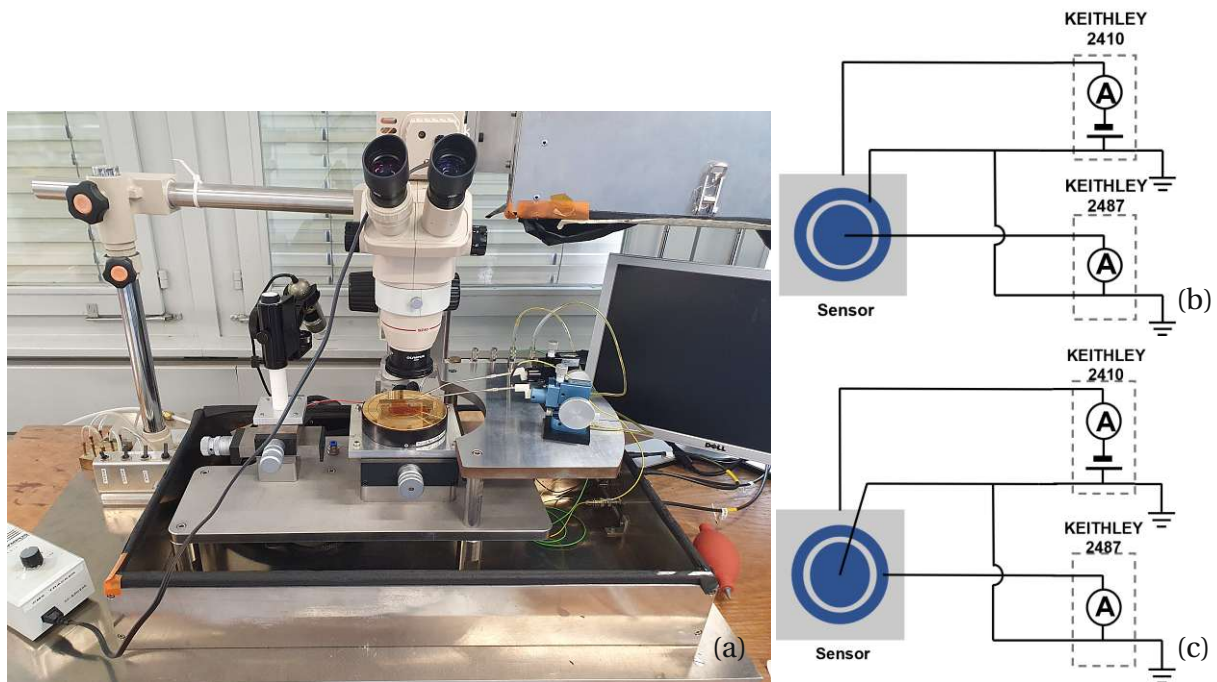
Fig. 6.1. a: IV/CV Setup at the SSD lab at CERN. **b**: Circuit diagram for the leakage current measurement of the pad.**c**: Circuit diagram for the leakage current measurement of the guard-ring.
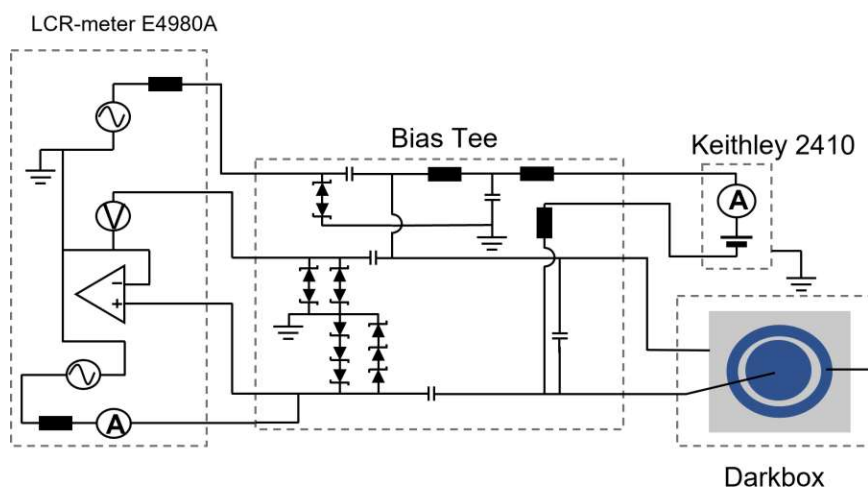
Fig. 6.2. Circuit diagram for the capacitance measurement of the pad.

6.2 IV

For all thicknesses, several big diodes were measured at room temperature. Voltage ramp-up is performed using 0.2 V steps with a stabilization time of 1 s. For each voltage point at least four consecutive measurements are performed in one second intervals and averaged to reduce noise and statistical effects. Small diodes were only measured to test their functionality before sending them for irradiation as their leakage current is in the same order of magnitude

as the resolution of the amperemeter (10 fA [119]). The reduced thickness of the contact layer, as a result of metal over-etching during fabrication, is susceptible to cause surface damage at needle contact. This enforced only light contacting, leading to an imperfect contact, which can be seen in erratic behaviour of the IV measurements at low bias voltage for some samples. For the first measurements the guard-ring was grounded to the same potential as the readout pad.
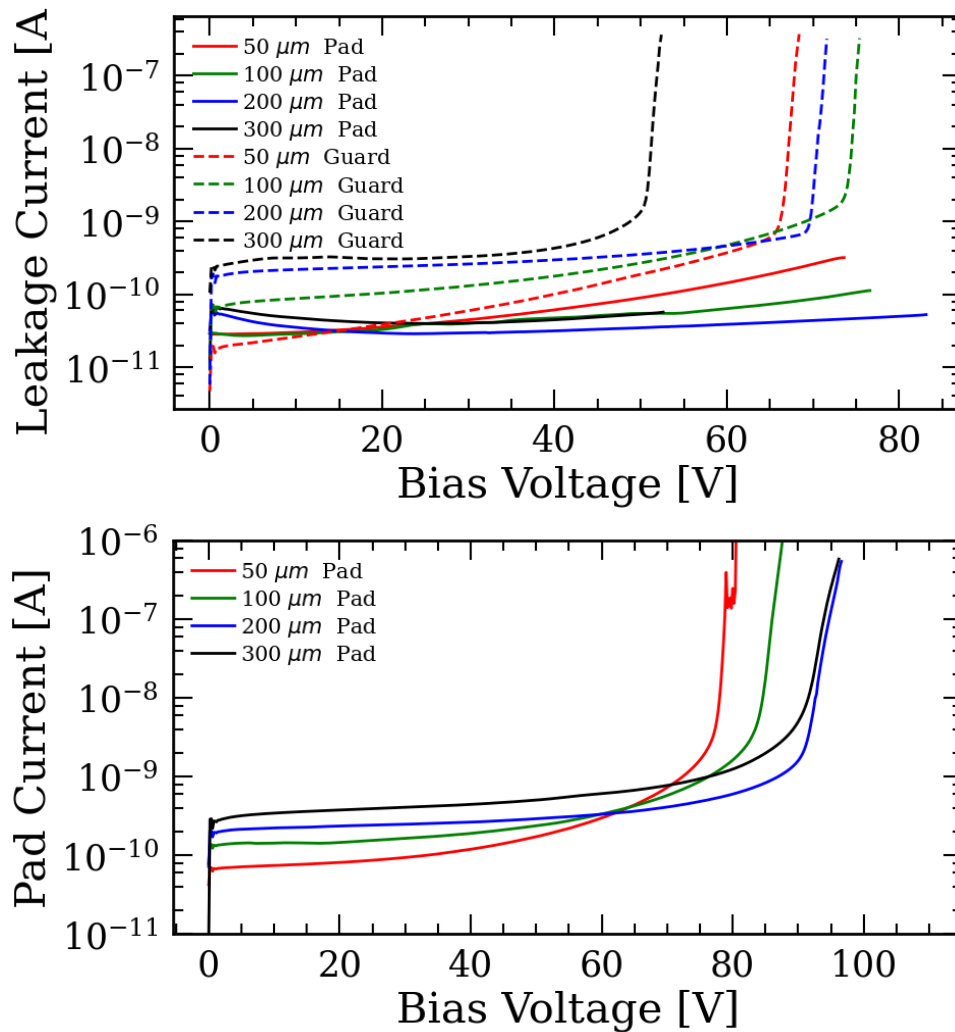
Fig. 6.3. Top: Pre-irradiation IV measurements of pad and guard-ring current for the big diodes at 25°C. **Bottom**: Pre-irradiation IV measurements of pad for the big diodes at 25°C after the guard-ring was left floating.

For all samples a diode behaviour was expected, with a near constant leakage current between full depletion and breakdown of the device. Breakdown happens when the increase of current with bias voltage changes drastically leading to currents high enough to damage the sensor. For all measured devices breakdown appeared earlier than expected from similar productions, with most of them breaking down around 80 V (see figure 6.3). A similar production of 200 μm thick silicon planar pixels produced for the Upgrade I VELO showed no breakdown up to 800 V (see figure 3.6). Breakdown hereby is defined as the point where the

total measured current reached the compliance current of 1 μA. The observed early break-down behaviour was also independently verified by the producer in several samples of this run. Due to the needed switch to a lower resolution of the total current measurement at a bias voltage of 21 V, the guard-ring and the pad cannot be measured with sufficient precision at the same time. Therefore another measurement was done where the contacting to the pad and guard was switched to allow a precise measurement of the guard-ring current. It can be seen that the breakdown originates from the guard-ring, whereas the breakdown condition is not reached in the pad. For all samples, the leakage current does not reach a plateau as would be expected for a fully depleted sensor. Instead an exponential increase in leakage current with bias voltage is observed, indicating a soft breakdown in the sensor due to the onset of impact ionization. This is a good indication that the reason for breakdown may also be present in the pad. It can be seen that the breakdown happens roughly independently of the thickness at the same voltage, with the 300 μm sensor breaking down even earlier than all other thicknesses (figure 6.3). No fundamental differences between small and big diodes except a lower leakage current were observed for the IV measurements (see figure 11.5 and figure 6.4).
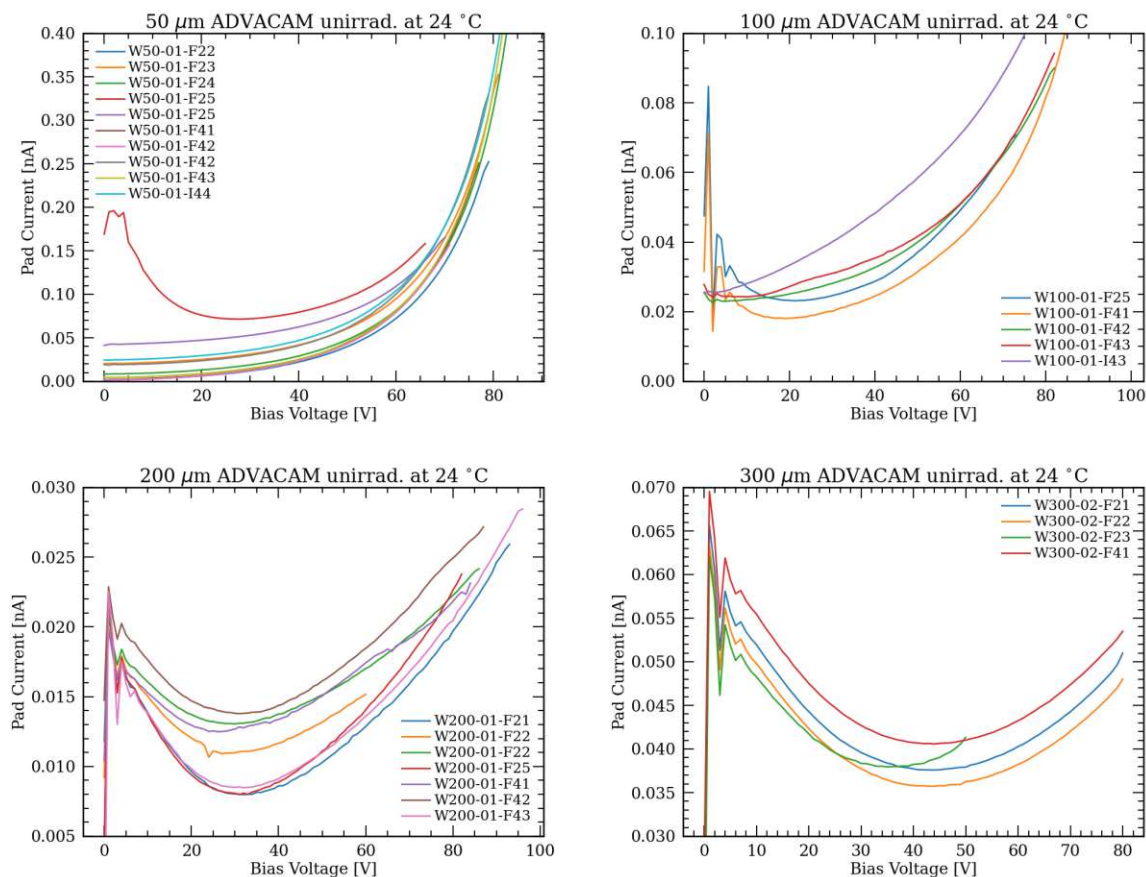
Fig. 6.4. Pre-irradiation IV measurements for the big diodes at room temperature with grounded guard-ring.

The thickness independence of the breakdown mechanism indicates that the increase of

field inside the bulk with bias voltage is not the reason for the breakdown. If this were the case, breakdown would happen at higher bias voltages for thicker sensors. As the breakdown happens for all samples roughly at the same voltage, a strong candidate could be the lateral growth of the depleted region. As the guard-ring has a lateral depletion inwards and outwards from the sensor center, whereas the pad only only depletes outwards, it could also explain the earlier breakdown in the guard-ring. If the guard-ring is left floating (figure 6.3) the expected diode behaviour is seen for the pad current with an exponential increase in leakage current close to the breakdown point. In addition, the overall current increases by two orders of magnitude for the thickest sensor.

Another visible effect is an initial decrease of the current with bias voltage, causing a dip in the IV curve. The voltage at which the dip occurs increases with thickness from around 20 V for the 100 μm sensors to around 45 V for 300 μm. This change in current is also more frequently observed in the thicker sensors where it is present in all measurements. For the 50 and 100 μm sensors it is only visible in a small number of samples. It has to be also mentioned here that the guard-ring current for most of the bias range is higher than the pad current, despite a smaller current generating volume (figure 6.3).
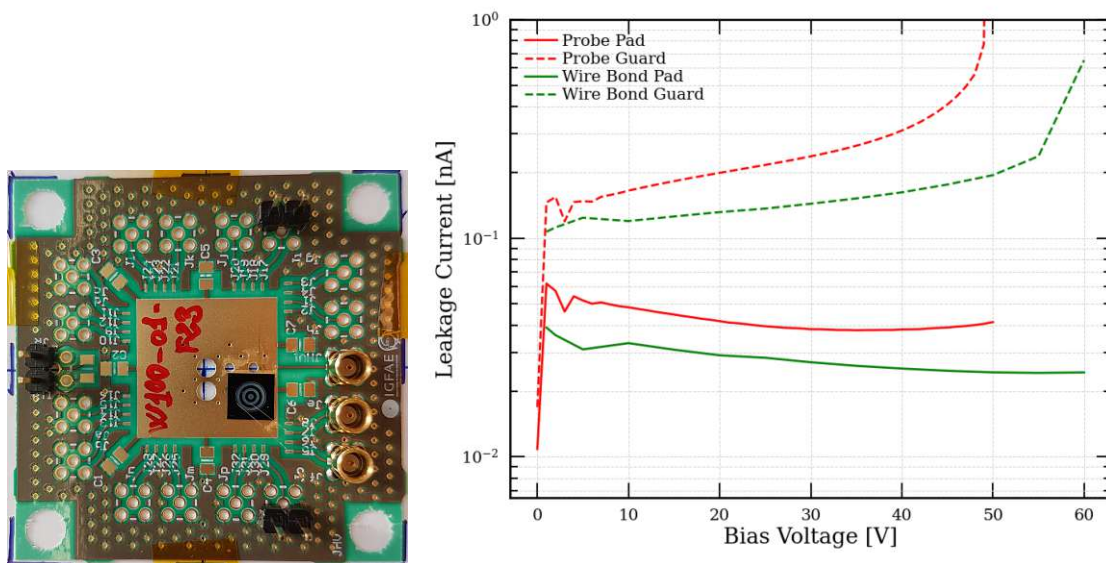
Fig. 6.5. Left: 300 μm big diode wire-bonded to a readout board. **Right**:Comparisons of the IV measurement using wire-bonds and needles.

To exclude a non-optimal contact as the reason for this behaviour, one diode was wire-bonded to a read out board and measured by attaching cables to the integrated MCX connectors (figure 6.5). A similar behaviour with respect to a needle measurement was also observed in this setup. The lower current for the guard-ring and the pad using the wire bonds is due to the overall lower noise of the Keithley 2470 sourcemeter used for the wire-bond measurement.

Some of the thinner sensors were observed to recover the expected diode behaviour after immediate remeasuring. As this phenomenon only occurs in the pad and not in the guard ring, one explanation could be the accumulation of charge at the SiO_2/Si interface of the oxide between the pad electrodes. An initial biasing would collect all the charges before the measurement is started. As the collection depends on the electric field inside the sensor, such a collection occurs at a fixed field value, which corresponds to lower bias voltages for thinner sensors. To test the effect, a measurement was performed after each sensor remained biased at -50 V for 30 min. The voltage point was chosen as most sensors seem to recover the normal behaviour after this value. The results can be seen in figure 6.3. No changes were observed for the thicker sensors, strongly suggesting that the change originated from the loss of contact of the guard-ring during the measurement. This happens when the needle moves of the guard-ring before the measurement. This was supported by the fact that the observed pad current shows the same behaviour and order of magnitude as a measurement with floating guard-ring.

6.3 CV

For the CV measurements all samples were measured at 1 kHz to ensure a faster time constant of the time dependent weighting field than the AC-signal period [120] [121]. The resulting measurements for big diodes can be seen in figure 6.6. The capacitance is plotted as $1/C^2$ to allow for an easy determination of the depletion voltage. For the 100, 200 and 300 µm a sharp decrease in capacitance ("step") is observed at 8 to 9 V. The 50 µm thick sensors exhibits this feature at 12 V. An additional plateau is observed before the step for this thickness, probably due to the sensor reaching depletion before the step occurs. For the small diodes the same step was measured, but at a lower voltage of 5 V and for all thicknesses at the same point (see figure 11.6). Such a step, commonly observed in LGADs [122], indicates a second diode like structure being depleted inside the sensor.

 As the guard and pad electrode implant have the same ratio between the surface areas for the big and small diode, their relative contribution to the capacitance should be the same and cannot be the reason behind the different step positions. For the 50 µm big diode the gap between the implants is bigger than the sensor thickness, whereas for the smaller diode this is not the case. For the thicker sensors the gap distance is always smaller than its thickness independent of the diode size. This difference between the 50 µm thick asmall and big diodes could lead to a different lateral growth of the depletion zone, changing the position of the step. This theory is supported by the fact that this feature moves to lower voltages for the smaller diodes. As the gap between the guard-ring and the pad is smaller for the smaller diodes, the maximal region that can be depleted laterally is smaller and therefore its lateral depletion is reached at lower voltages, resulting in the earlier step. The step feature was not observed on the CV measurements provided by the producer (ADVACM), due to the coarse
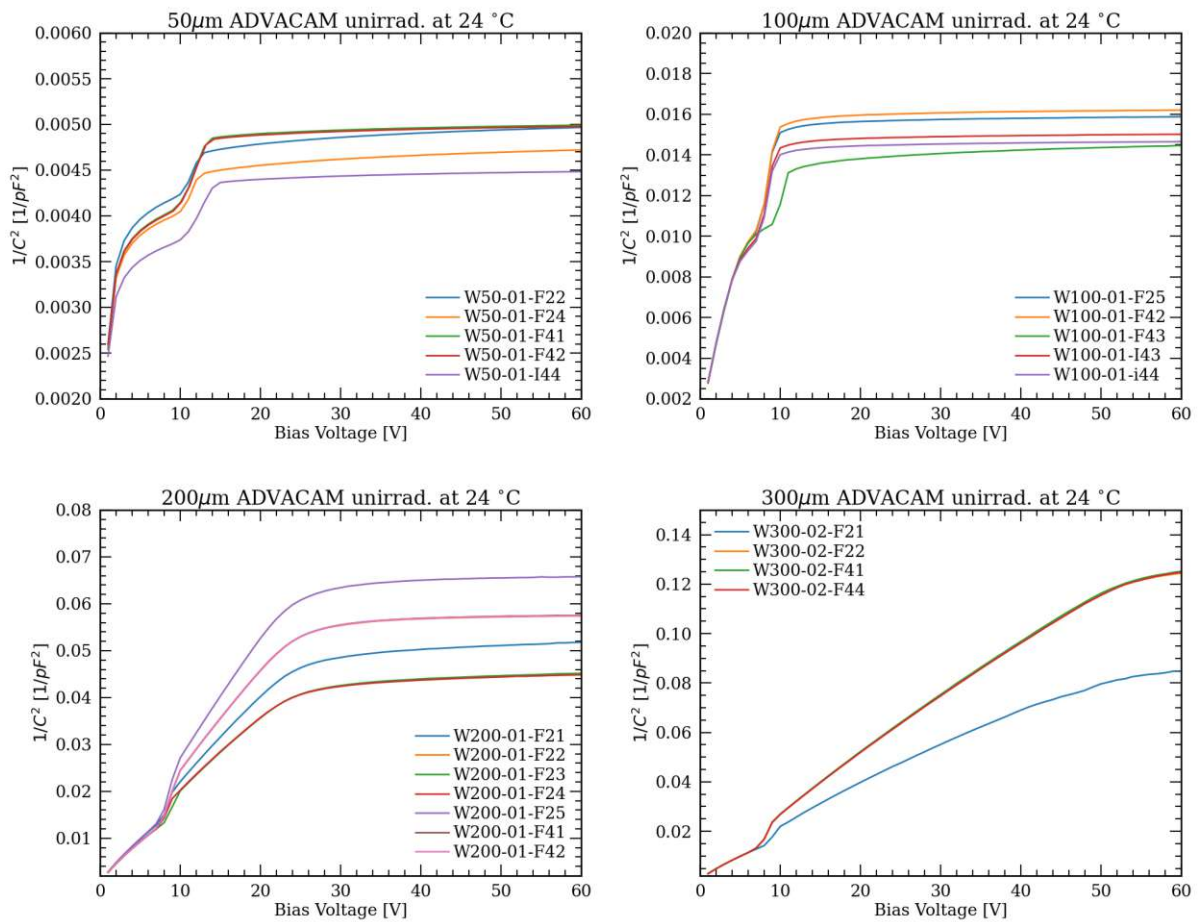
Fig. 6.6. CV measurements done on big diodes of different thicknesses.

step used in their studies.

To determine the depletion voltage of the sensors two straight lines were fitted on different parts of the curve and their intercept is used as the depletion voltage. One was fitted at the rising flank at low voltages, while the other was fitted to the stable region at the end of the measurement(see figure 6.7). A comparison of the measured depletion voltages to the results of the ADVACAM measurement can be seen in table 6.1.

From the measured depletion voltages the bulk doping concentration c was calculated with

$$c = \frac{2V_{\text{dep}}\epsilon\epsilon_r}{ed},\tag{6.1}$$

where ϵ stand for the vacuum permittivity, ϵ_r for the relative permittivity , e for the elementary charge and d for the sensor thickness. As all wafers should have the same bulk doping concentration, the values should agree across the thicknesses. For the 100 to 300 µm thick sensors similar concentration values were calculated, whereas for the 50 µm thick sensor one obtains twice the concentration of the other sensors. As the resistivity range specified in the
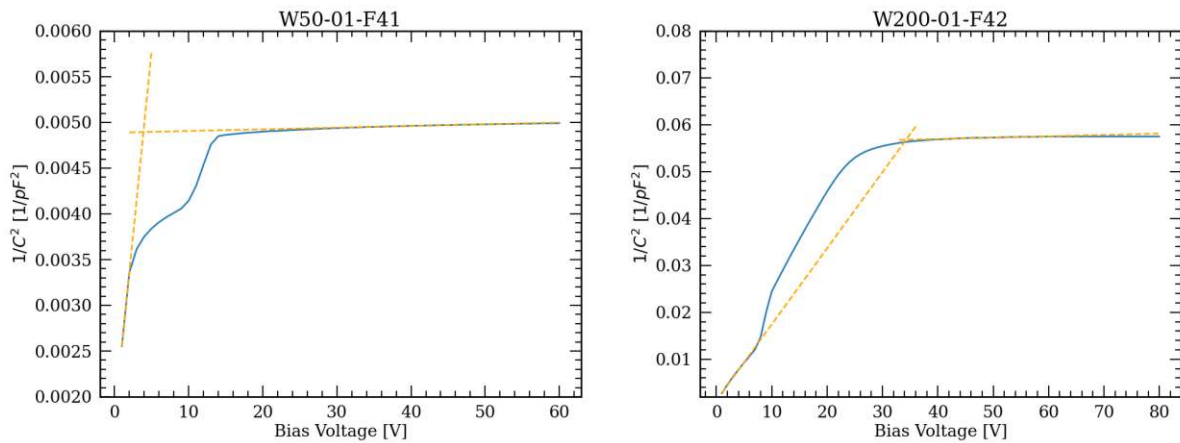
Fig. 6.7. Examples of the different fit regions for the depletion voltage calculation of a 50 μm (**left**) and 200 μm (**right**) diode. The orange dashed line represent the fitted curves.

production tender is in better agreement with the thicker sensors (see table 6.2), their concentration was assumed for all sensors. For the 50 μm thick sensors the occurrence of the step at around the same value as the expected depletion voltage could lead to wrong results in the calculation of the depletion voltage.

Thickness [μm]	V_{dep} Measurement [V]	calculated V_{dep} [V]
50	3.7	1.9
100	8.2	7.7
200	31.6	31
300	63.9	69.5

Table 6.1. Comparisons of the calculated depletion voltages with the expected depletion voltages for a bulk concentration of 1×10^{12} cm^{-3}

Thickness [μm]	Measurement [cm^{-3}]
50	1.9×10^{12}
100	1.1×10^{12}
200	1.1×10^{12}
300	9.2×10^{11}

Table 6.2. Bulk doping concentrations calculated from the measured depletion voltages. From the production specifications a concentration of around 1.3×10^{12} cm^{-3} is expected.

7

Simulation

7.1 Simulation setup

Simulations are an essential tool in the development of silicon sensors. They allow testing of hypotheses without the need for expensive and time consuming production of devices. They also allow for easy access to different properties of the detector and their interplay with each other. Technical Computer Aided Development (TCAD) is a sub-family of CAD software, optimized for modelling of semiconductor production and operation. It can be divided in three parts. First is the process simulation which can simulate all the processes needed to fabricate a semiconductor device. Second is the device simulation. It simulates the characteristics and performance under various conditions of a device. Finally, the circuit simulation allows to simulate a device integrated in an electrical circuit. Several commercial TCAD packages are available by Synopsys, Silvaco, Crosslight Software, Cogenda Software, Global TCAD Solutions and Tiberlab [123]. For this thesis, Sentaurus TCAD by Synopsys [124] is used.

As the doping profiles were extracted from the SIMS measurements, the process simulation step was not needed in this thesis. Instead the description and geometry, including doping profiles, of the device were specified explicitly as an input to the device simulation program. Device generation can be split in two parts, the creation of the object itself and the meshing of the geometry. Both steps are performed with the Sentarus Device Editor (sde). It allows the construction of the device similar to other CAD programs out of elementary geometric forms and Boolean operations. The dimensions of the sensor parts were obtained from the different masks used in the production process, provided by the producer. The description of the active layers was based on the doping profiles obtained from the SiMS measurements. To account for the part of dopants that were measured in the SIMS but were not integrated in the lattice and therefore do not contribute to the electric properties of the device, the total concentration was scaled down to 90% from the measured concentration. As the imported doping profile only describes the change of the profile in one dimension (as a function of sensor depth), the lateral profile also needs to be defined. For modelling the lateral extent of the implants the imported profile was used again with all depth values scaled down to 80%.

Sentaurus TCAD uses finite element methods to solve the Poisson and drift-diffusion differential equations in the stationary regime. To discretize these equations, the domain has to be divided in smaller volumes. This process is called meshing. Meshing is a crucial step, as inadequate meshing can lead to inconsistent device behaviour or to non-converging simulations. Additional, simulation time and memory load is directly proportional to the number of nodes

created during the meshing process. A compromise has to be found between a coarse mesh, needed to reduce simulation time, and a fine mesh to ensure converging results. It is therefore advised to change the meshing size to a finer mesh where the physical properties of the device are expected to change rapidly with position and to implement a wider mesh for the other regions. An example of such a mesh can be found in figure 7.1. Programmatically, this
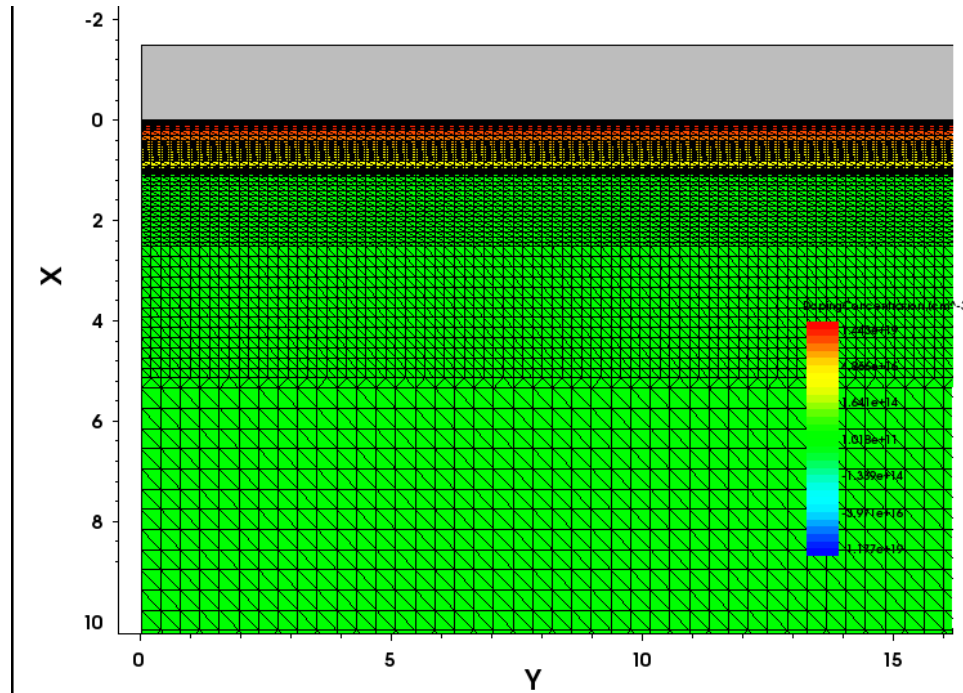
Fig. 7.1. Example of the meshing close to the readout electrode. Mesh size is decreasing at the pn-junction and the implant metal interface. Axes in μm.

can be achieved by defining by defining the maximum and minimum mesh size for different regions and letting the program ensure a smooth transition between these regions. Additionally, a refinement function can be used to control the mesh size inside each region based on a certain parameter (for example doping concentration). For every node the difference of the parameter to its value on adjacent nodes is calculated, if it exceeds a defined value the mesh size is adjusted until the difference is lower than the value. As mentioned before the mesh size plays a critical role in the behaviour of the sample. An example of the impact on meshing can be seen in figure 7.2, where different mesh sizes around the edge of the electrodes are tried for the same geometry, leading to different breakdown voltages and even to convergence problems in the guard-ring current. For this study the mesh is optimized to have a finer meshing along the implants and in the region between the implant of the guard-ring and the pad. A coarser mesh is used in the region after the guard-ring and in most of the bulk. In the inner part of the readout electrode and at the backside electrode the mesh size was only increased in the horizontal direction as no rapid changes are expected in this dimension.

Device simulation is performed using Sentaurus Device (sdevice). First the physical properties of each material and the physics models to be included in the simulation are defined.

Unless stated otherwise, the simulation results shown in this thesis were obtained using the standard material properties and the default parameters of the physics models. The next step is defining the parameters of the solver (for example, solver type, used CPU-cores, numerical error need for convergence,..). The solver is the algorithm that calculates the solution to the matrix system built from the different equations. This is followed by the parameters of the solving process itself. Two options are available: a quasi-stationary (see 11.1) or a transient simulation (see 11.2). Quasi-stationary simulations increase or decrease one parameter until a goal is reached, moving from one stable solution to the next. The step size is hereby defined dynamically, decreasing if no convergence is reached after the simulated step or increasing in the opposite case. This is done to ensure convergence when the device parameters can vary rapidly, while keeping the simulation time to a minimum. For additional control, a minimum and maximum of simulation points can be defined. In each of the simulated steps the predefined set of equations is solved. In most cases, this includes the Poisson equation, the electron and hole continuity equations. For capacitance simulation the AC-coupled option has to be used allowing the simulation of an AC signal. The transient option allows one to study the change of parameters as a function of time. Finally all parameters to be saved in the output file have to be defined.

The suite of tools is complemented by the programs Sentaurus Workbench and SVisual. The first is a graphical interface which can be used to control and schedule all aforementioned simulation tools, allowing for scenario building and definition of extensive simulation campaigns. The latter is a tool to visualize the simulation results and can be used to extract parameters from the output files for further analysis.

Thanks to the axial symmetry of the geometry, the diodes can be simulated in 2D using cylindrical coordinates (figure 7.3). 3D simulation would be possible in theory, but beyond the memory capabilities of available computing infrastructure. As this leads already to the limits of simulation for the mesh size, only preliminary IV studies of the unirradiated samples are simulated using the dimensions of the small diode test structures and then scaled up according to the relative difference in sensor area compared to the big diode. For all other simulations some simplifications had to be implemented and are discussed as they come up in each section.
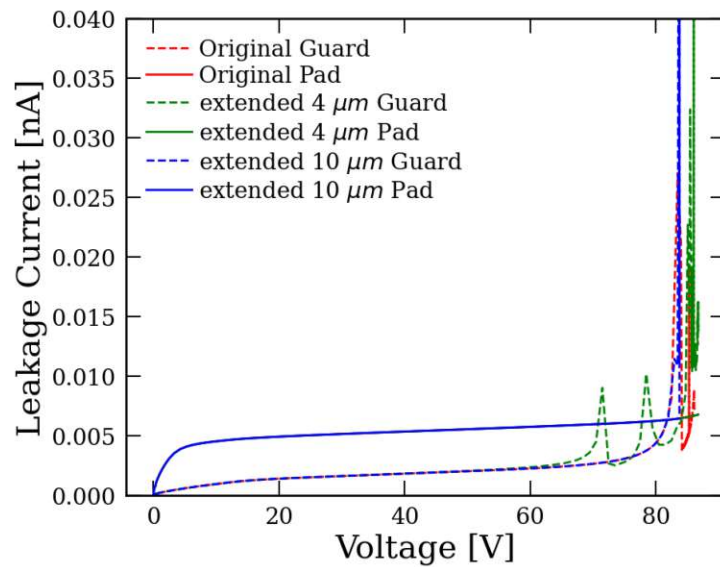
Fig. 7.2. IV simulation of a small 50 μm diode with different meshes. The original has only a finer mesh (10 nm gradually increased to 500 nm) around the pn-junction. These fine mesh was then extended laterally for 4 and 10 μm from the interface into the region between the guard ring and pad implant. Continuous lines represent the simulated pad current and dashed lines the current flowing through the guard ring.
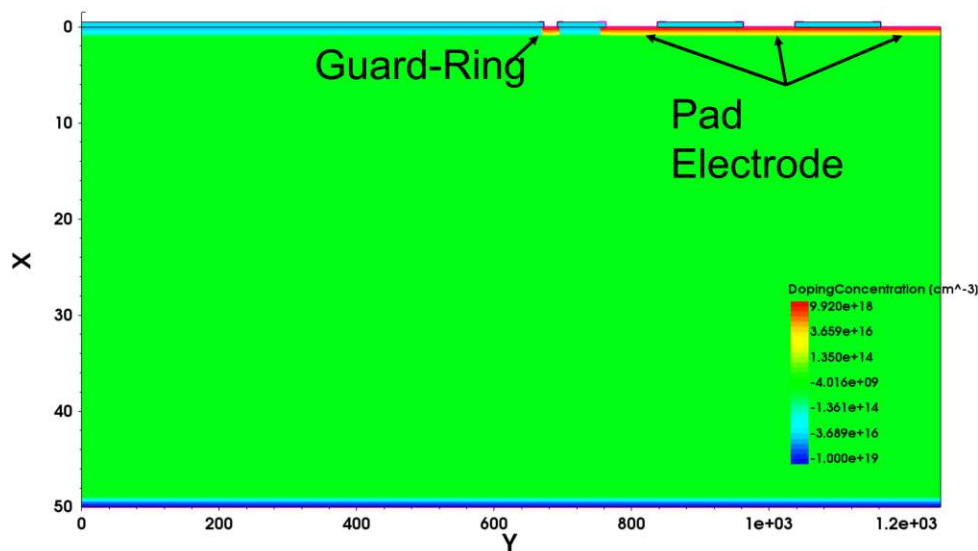
Fig. 7.3. Geometry used for IV simulations of a 50 μm small diode. Pink lines represent the simulated electrodes.

Impact ionization plays an import role in simulating our devices. Impact ionization occurs when the mean free path of a carrier for a given electric field allows the carrier to gain enough energy to create an additional electron-hole pair in its next collision. This effect leads to an increase in leakage current and in the worst case to a self-multiplying carrier avalanche resulting in a breakdown of the device. Impact ionization depends on the electrical field inside the sensor. For silicon, impact ionization begins around a critical field of 1×10^5 V cm^{-1}. In

a uniform electric field, the increase in leakage current can be described by a factor G [125] depending on the width of the region where impact ionization occurs d and the ionization coefficient α (which depends on the electric field)

$$G = e^{\alpha d}. \tag{7.1}$$

As α is different for the two carrier types, the main contributor to the impact ionization in silicon are electrons with them having a one order of magnitude higher ionization rate than holes for field values close to the critical field (see figure 7.4). This gain can not be used alone
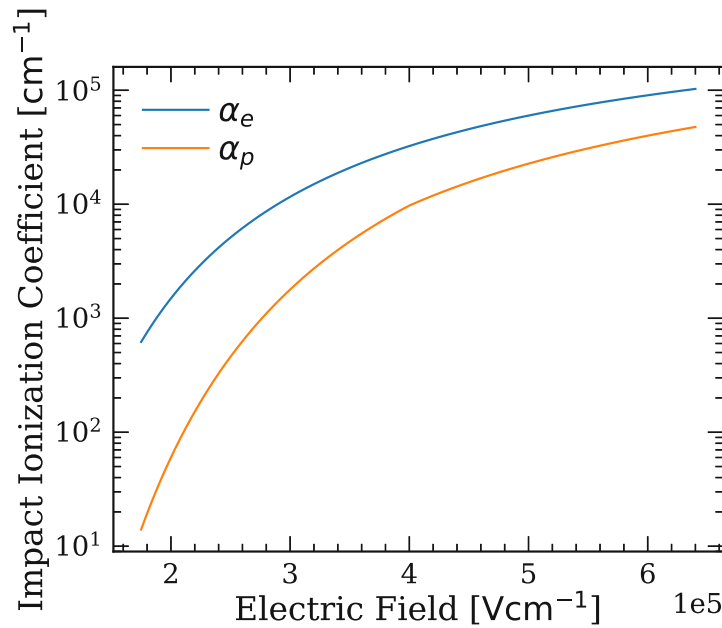
Fig. 7.4. Impact ionization coefficients for electrons and holes calculated using [126].

to describe the breakdown behaviour, as the interaction of the two carrier types plays an important role too. The ionization coefficient α itself has an exponential dependence on the electric field in the gain region E and can be described with the help of the material dependent parameters b and c, which have to be determined with experimental data [127]:

$$\alpha = b e^{-c/E} \tag{7.2}$$

In TCAD, several impact ionization models are implemented as extensions of the above described process. The most commonly used model is the Van-Overstraeten–de-Man model [126]. It scales the parameters b and c in equation 7.2 with a temperature-dependent factor

$$\gamma = \frac{\tanh\left(\frac{\hbar\omega}{2kT_0}\right)}{\tanh\left(\frac{\hbar\omega}{2kT}\right)}, \tag{7.3}$$

with $\hbar\omega$ being the energy of optical phonons, $T_0 = 300$ K being the reference temperature for

the parameters, T the simulated temperature and k the Boltzmann constant, leading to

$$\alpha = \gamma b e^{-\gamma c / E} \tag{7.4}$$

This allows to include the temperature dependent scattering of free carriers on optical phonons. It has to mentioned here that the Van-Overstraeten–de-Man model has two sets of the parameters b and c, depending on the electric field, with their switching point being a parameter of the model. The Van Overstraeten–de-Man model is used for all simulations done in this thesis if not stated otherwise. Other models implemented (Okuto [128], Lackner [129] UNINBO [130], UNNIBO2 [131]) in TCAD were tested. No significant difference in the predicted breakdown was observed between the different models, with the Van-Overstraeten–de-Man yielding the highest values (see figure 7.5). Due to an increased convergence stability under small mesh changes of the Van-Overstraeten–de-Man model it was used for all simulation.

For mobility, the Canali model [132] is used to implement high field velocity saturation. To account for the scattering of free carriers on ionized donors and acceptors and electron-hole scattering the Phillips Unified Mobility Model [133] was used which includes both effects in a single model. Bandgap narrowing is implemented using the Slotboom model [134]. For generation and recombination the Shockley-Read-Hall model [135] was used including models (the default parameters for τ_{max} were changed for electrons to 10^{-2} s and for electrons to 10^{-3} s) adding dependences on the doping concentration, temperature and the electric field. The oxide interface charge was simulated as a constant with a constant value of 10^{11} atoms cm^{-3}.
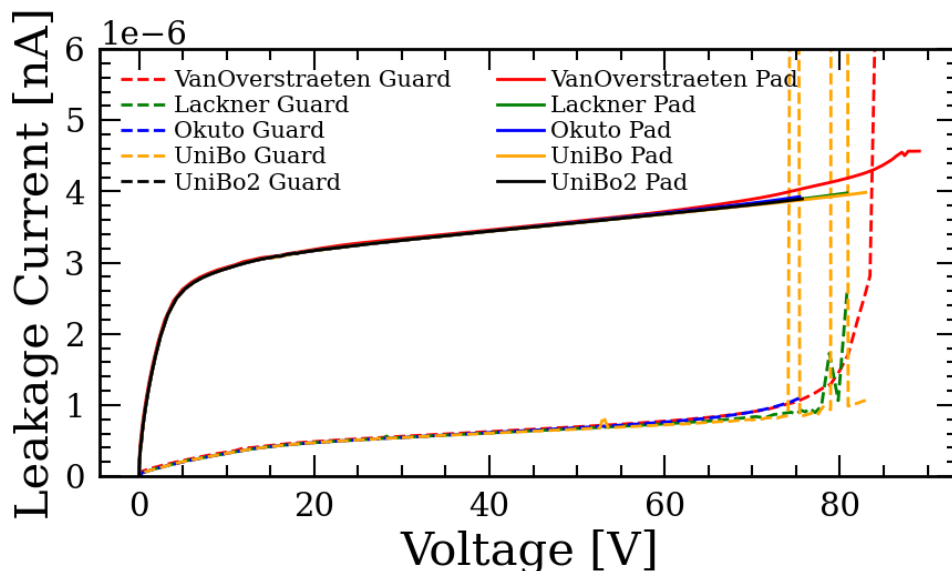
Fig. 7.5. Testing of the different impact ionization models implement for TCAD for a 50 μm small diode. The peaks in the guard-ring current at high voltages originates from a diverging simulation.

7.2 IV

The behaviour of the two types of diodes should only differ due to the difference in volume, thus expecting a multiplicative scaling between the leakage current of the small and the big diodes. Thus, to reduce simulation time simulations of the small diode are scaled up to the big diodes using their respective sensor area. The first focus was the recreation of the early breakdown. As the p-spray was suspected to be the reason of the breakdown, its doping profile was scaled down and compared to the initial simulation (see figure 7.6). For the actual p-spray concentration the breakdown occurs at 80 V, similar to the measurements. It can be seen that the breakdown moves to higher bias voltages, if the peak concentration of the p-spray is lowered. An additional simulation was performed, where the SiO_2/Si interface charge was removed resulting in a higher effective p-spray concentration (see figure 7.6). Breakdown is again moving towards higher values indicating that the region of breakdown is located somewhere close to the interface. By looking at the current density during the breakdown, one can see that the breakdown happens in the region where the gradient between the p-spray and the n^+ implant is the highest (as seen in figure 7.7). In this region, fields above $1.5 \times 10^5 \, \mathrm{V\,cm^{-1}}$ exist independent of bias voltage, leading to the production of excessive electron hole pairs through impact ionization. The electrons flow then to the closest electrode and are collected by it, whereas the holes follow the edge of the depleted region, until they form a conductive channel to the backside in the middle of the gap between guard-ring and pad. This process induces the observed breakdown.
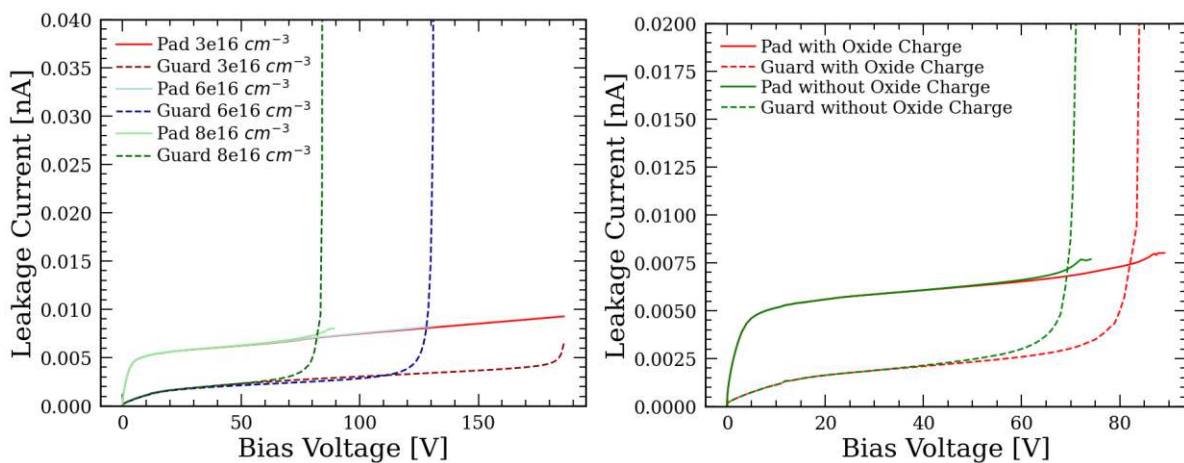
Fig. 7.6. Left: Tcad Simulation of a 50 μm small diode for different p-spray concentrations. The pad and guard-ring current are plotted separately. **Right**: Tcad Simulation of a 50 μm small diode with and without simulated oxide interface charge.

The reason for the breakdown being first visible in the guard-ring is due to the relatively longer interface region between its implant and the p-spray. Not only does this interface exist on both sides of the guard ring, leading to larger impact ionization fronts, but also, due to the size difference of the inner and outer circular interfaces. Neither the decrease of leakage
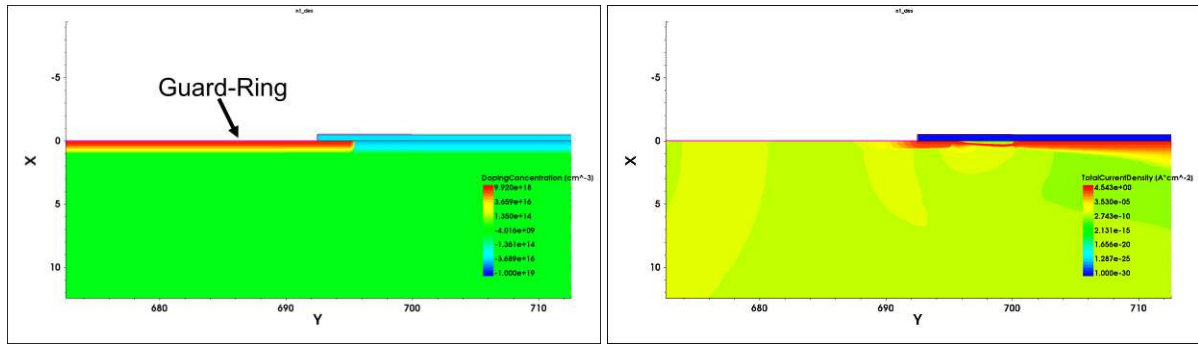
Fig. 7.7. TCAD Simulation of the big diodes. **Left**: Doping concentration at the right edge of the guard-ring. **Right**: Current density during breakdown at the right edge of the guard-ring.

current for low bias voltages nor the absolute values were reproducible for the 50, 100 and 200 µm thick simulated structures (figure 7.8). A possible reason behind is that the over-etching of the metal changes the overlap of the electrodes and therefore the electric field termination close to the region of impact ionization. If the p-spray was implemented after the electrode implant, another possible reason could be the change of profile at the electrode p-spray interface due to doping-enhanced diffusion. For the 300 µm thick sensor no converging meshing solution has been found inside the limits of the available memory.
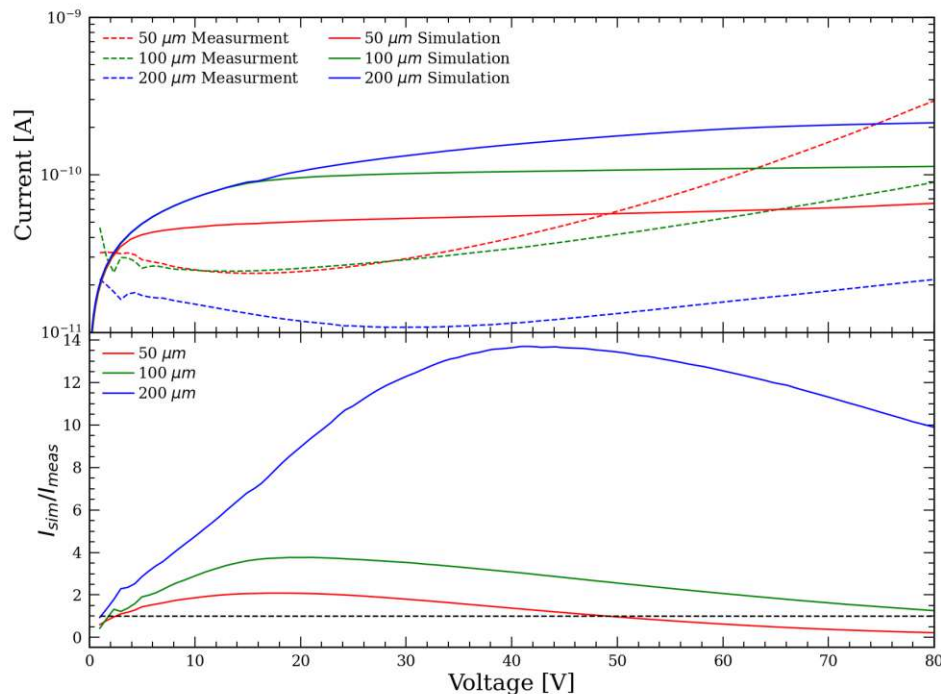
Fig. 7.8. Comparisons of the IV simulation for small diodes of different thickness scaled to the size of the big diodes with the mean leakage current of all measurements. The bottom plot shows the relative difference of the simulated current with the measured one.

Due to the high p-spray concentration the devices could potentially be treated as a npn-transistor, where guard ring and pad function as emitter and collector. The biasing of the backside would then work as a gate controlling the current. This would allow for current to flow from the pad to the guard-ring, leading to an overall lower pad current. As the total field needed for the gate to open fully is quite low this would explain the stop of this effect after a certain voltage. Additionally, this would explain the different inversion point in the IV behaviour for different thickness, as the highest field is reached later. To simulate this behaviour, a fixed potential difference was applied between the guard-ring and the pad. As this voltage difference should be quite low, only small voltage differences between pad and guard-ring are simulated (figure 7.9). No substantial changes in the region before 1V were observed. Increasing the bias in the guarding even leads to instant breakdown in the simulation.
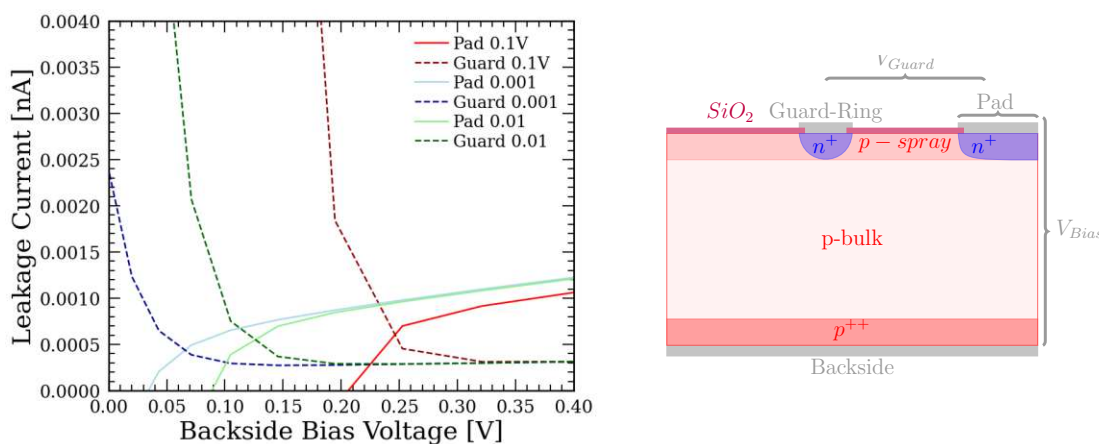
Fig. 7.9. Left: Leakage current simulations for a 50 μm small diode, where first the guard-ring potential was ramped up to different values (see legend) and then the backside bias was applied. **Right**: Sketch of the applied Voltages.

7.3 CV

To study the CV behaviour of the sensor, TCAD offers the possibility of including circuit simulations on top of the quasi stationary solution. Due to the significant computation time associated with AC circuits in TCAD, in the interest of understanding the origin of the secondary step of the IV curve, only the region between pad and guard-ring were simulated (figure 7.10). The simulated structure consists of only 40 μm of the guard ring and 200 μm of the pad electrode. This was done to increase the simulation speed and to circumvent convergence problems on the outer side of the guard-ring p-spray interface. To study the impact of such a simplification, a full simulation for the 50 μm thick sensor was performed and compared to the simplified simulation and the measurements. The simplified simulation results were scaled to the same area as the full simulation. As can be seen in figure 7.11, the "step" in the reduced simulation is much more pronounced with respect to the full simulation, whereas they agree on the position of the step. Both simulations exhibit a bigger capacitance than
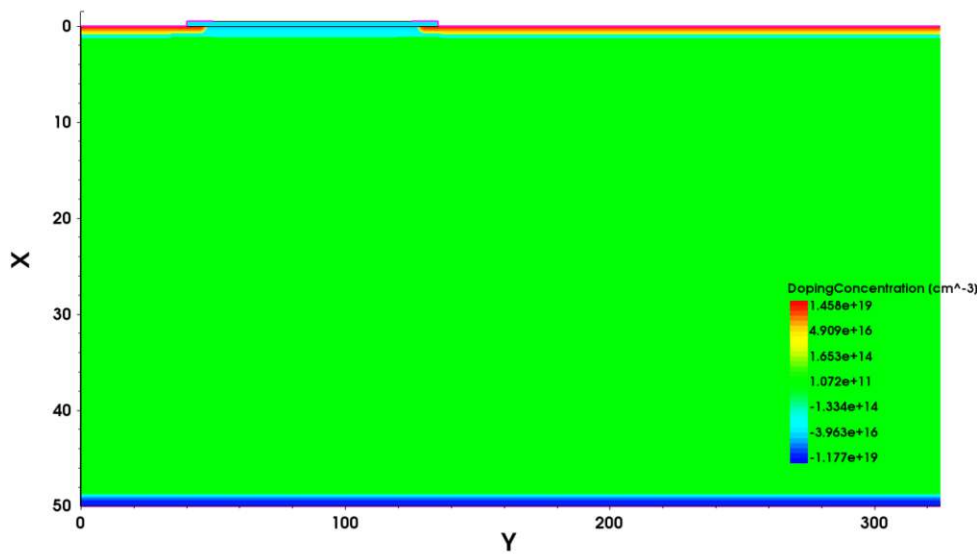
Fig. 7.10. Geometry used for CV simulations of a 50 µm big diode. Pink lines represent the simulated electrodes.

measured and the step occurs at higher voltages. In addition, simulation results, which are scaled up to achieve the same capacitance as the measurement before the "step", are plotted (figure 7.11). As the behaviour of the capacitance is qualitatively the same between the two simulation geometries it was concluded that the reduced simulation is sufficient to study the reason behind the step.
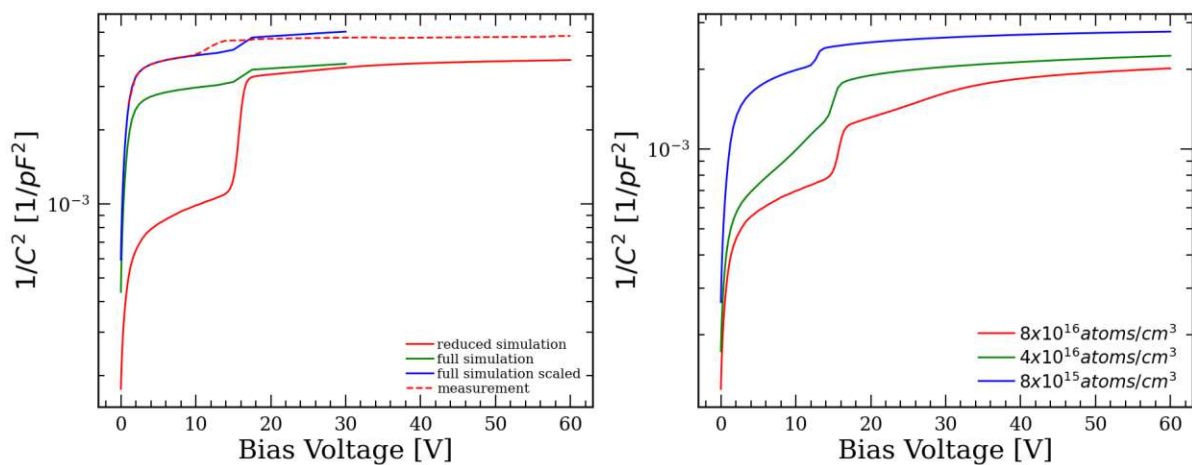
Fig. 7.11. Left: Comparison between the full and reduced CV simulations to the measurements of the 50 µm big diode. An additional graph is plotted where the full simulated is scaled up to exhibit the same capacitance before the step as the measurement. **Right**: CV simulation of different p-spray peak concentrations for a 50 µm big diode.

As the p-spray was again suspected to be the reason behind the step, a first study was performed by decreasing the p-spray concentration in the simulation. As can be seen in figure 7.11 the height of the step, its position and the capacitance after the step depends on the the p-spray concentration. With increasing p-spray concentration, the value of the capacitance

after depletion increases, the position of the step moves to higher voltages and the hight of the step slightly increases. To achieve the measured step position in simulations, the concentration of the p-spray has to be one order of magnitude lower than the concetration measured with SIMS.
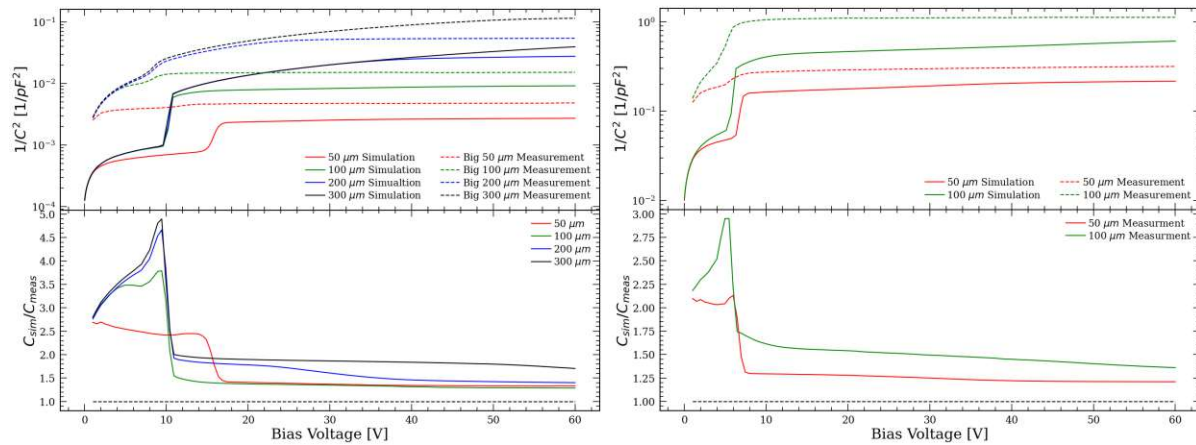
Fig. 7.12. Left: Comparison of CV Simulation of big diodes using the reduced geometry to the mean measured capacitance. **Right**: Comparison of CV Simulation of small diodes using the reduced geometry to the mean measured capacitance. The bottom plots show the relative difference of the simulated capacitance with the measured one.

To further investigate the reason behind the step the CV simulations were repeated for all thicknesses (figure 7.12). The tendency of the step position versus thickness was reproduced in simulation while in all scenarions the steps was observed at lower bias voltages than in measurements. This could indicate a surface sheet resistance reducing the applied voltage to the device. The difference between simulated and measured step positions is 2 V for all thicknesses. For the behaviour after depletion no agreement of the simulation with the measurements for the 100 to 300 μm diodes is seen, as no depletion is visible. In the figures 7.13 the space charge is plotted before and after the occurrence of the step for a 50 μm and 200 μm thick sensors. The border of the depleted region is marked with a white line. It can be seen that the step occurs for all samples when the same region in the gap between the guard ring and the pad is depleted. It was therefore suspected that the depletion of the full high field region at the p-spray interface is responsible for the step. For the 50 μm diodes the step occurs earlier as the perpendicular depletion is reached before the lateral depletion would reach the critical region. This changes leads to a modification of the lateral depletion and the earlier step.

7.4 Summary

Through SIMS measurements a detailed concentration profile of each implant in the test devices could be obtained. An unusually high p-spray concentration of 6.89×10^{16} atoms cm^{-3} was observed. IV and CV test measurements were performed before irradiation indicating an
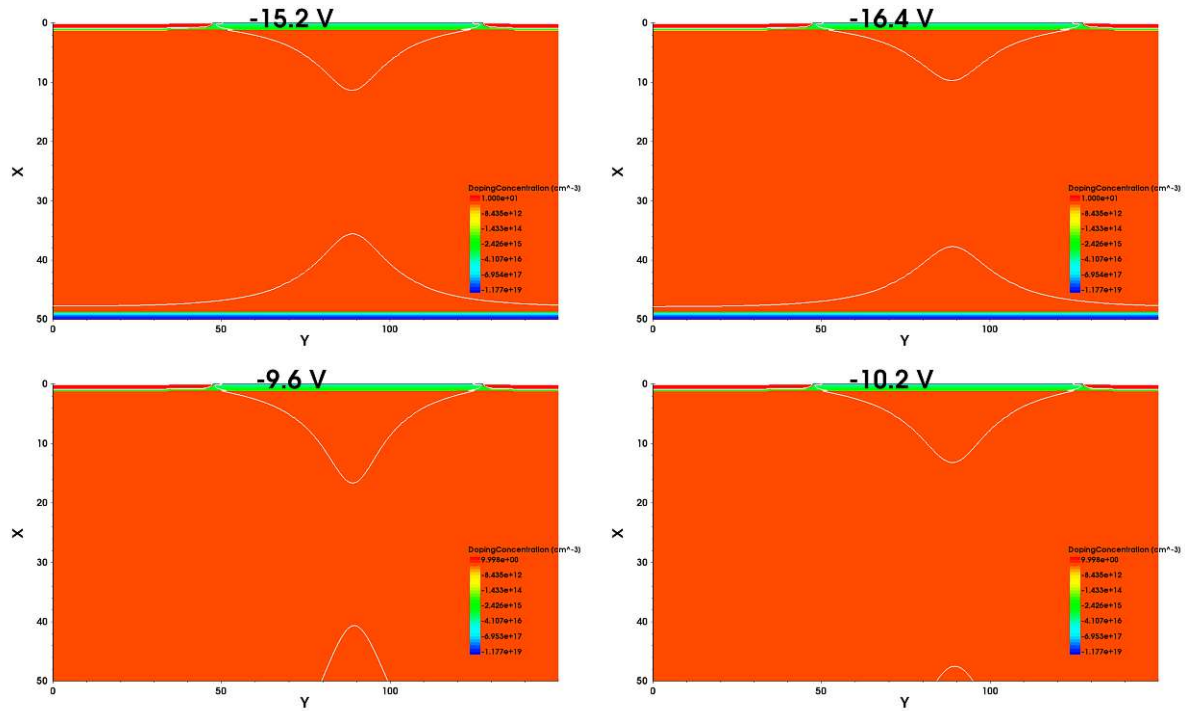
Fig. 7.13. Simulated depletion region (white line) before and after the step for a 50 μm (top) and 200 μm (bottom) big diode.

abnormal behaviour with respect to the expected performance of similar devices. With the help of simulation the reason of the early breakdown was understood to be due to the high p-spray concentration, leading to impact ionisation in the interface region between the p-spray and the n^+ implants. Several hypotheses for the decrease of leakage current at low bias voltages, especially in thick sensors have been tested, but no conclusive results have been found. For the CV measurement, a step in the capacitance has been observed, which again could be tracked down to originate from the p-spray. As all abnormal effects seem to originate from the p-spray, they should not be a concern for irradiated sensors due to the expected de-activation of the p-implant related to acceptor removal effects.

Irradiation

8

In the following chapters the effect of radiation damage on the planar silicon sensors, described in Chapter 2, will be studied. The main focus hereby lies on the leakage current as it determines the temperature needed to prevent thermal runaway and, together with the power consumption of the ASIC, determines the required cooling power. In addition its contribution to the shot-noise will affect the time and spatial resolution of the detector. The measured IV curves will be compared against TCAD simulations and analytic models predicting the leakage current change with radiation are tested for their validity at high fluences.

To cover the full fluence range relevant for the Upgrade II, four fluence points were chosen: 1×10^{15} n_{eq} cm^{-2}, 8×10^{15} n_{eq} cm^{-2} (max. fluence in scenario B), 6×10^{16} n_{eq} cm^{-2} and 1×10^{17} n_{eq} cm^{-2}. As the type of defects created by neutrons and protons differ (see 2.4), irradiations were performed with both types of particles at all fluence points.

8.1 Neutron irradiation

For neutron irradiation the samples were irradiated in the TRIGA Mark II reactor of the research center of the Jozef Stefan Institute, using the irradiation channels F4 and F19 located at the outer edge of the reactor [136]. These channels were chosen to limit the maximal reachable temperature during irradiation to 50 °C at the cost of a longer irradiation time to limit the amount of annealing during irradiation. For these channels a maximal fluence of 1.5×10^{12} 1MeV n_{eq} cm^{-2} s^{-1} can be achieved, leading to an irradiation duration of 17 h for the highest fluence. To minimise annealing during the transport of the irradiated samples back to CERN, a cool box was used for the transport and the temperature was constantly monitored. During the whole travel 12°C was not exceeded. The uncertainty on the fluence is 10% [137].

8.2 Proton irradiation

All proton irradiations were done at the IRRAD facility at CERN. It provides a beam of 24 GeV/c protons from the PS. Several beam focusing options were available, but to reduce the irradiation time the smallest beam size of 6×6 mm (full width at half maximum) was chosen, which was estimated to correspond to a rate of around 0.8×10^{14} p/cm^2/h for our samples. Accounting for the expected downtimes of the accelerator this would lead to an irradiation time of one year of PS operation time for 1×10^{17} n_{eq} cm^{-2}. To prevent uncontrolled annealing during this time, the sensors needed to be cooled for the whole duration. This was

achieved using a vortex cooler, keeping the samples at a constant temperature of -15 °C. As there was no suitable holding mechanism for the samples available a new support was designed and fabricated. The three main constraints for its design were the restriction on the material budget introduced into the beam, the radiation hardness of the material and the micrometer precision needed for the alignment of the samples. As no metal could be used due to its activation, Accura 25 [138] was chosen to be the base material. Its low coefficient of thermal expansion ensured no stress between the samples and the support during the cooling. Additionally, it could be 3D-printed with a precision of 0.1 mm. The support structure consists of a base plate mounted to the top of the vortex cooler box and up to four cages containing samples. A picture of the support mounted on the top of the vortex box can be seen in fig. 8.1. The cages can be separately removed allowing the removal of samples irradiated to lower fluences without removing the other samples. The samples themselves are mounted on Accura 25 cards, which contain different cut-outs depending on the sample type, ensuring the alignment of the samples with the beam. An example of such a card for four small diode samples can be seen in figure 8.1. Each cage has slots for up to 14 cards.
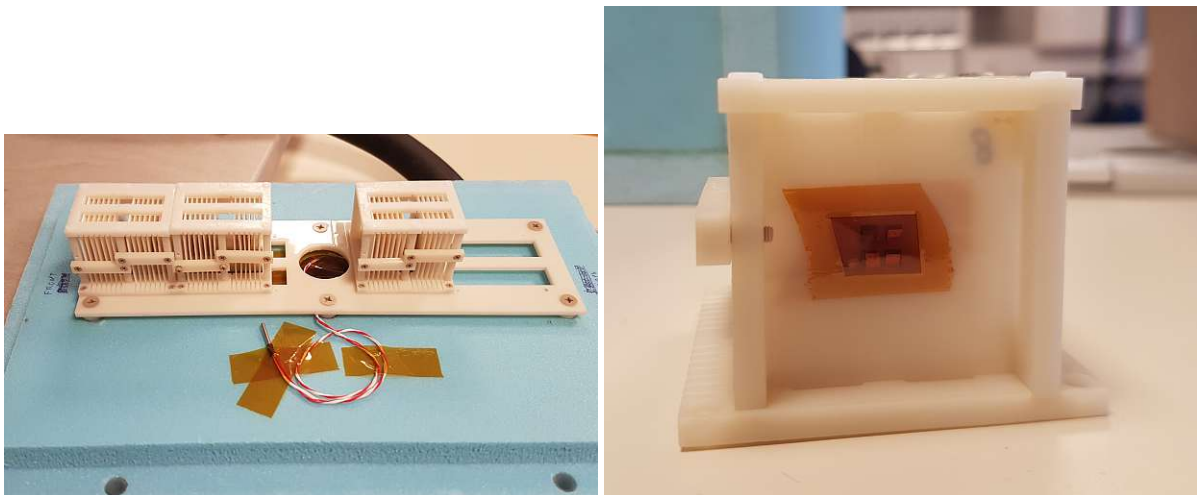
Fig. 8.1. Left: Support structure mounted on the top lid of the vortex cooling box with 3 mounted cages. **Right**: Front view of a card containing four small diodes.

The fluence was determined by inserting thin aluminum foils with the samples into the beam. During irradiation, some aluminum nuclei get converted into sodium. The activity originating from the gamma decay of sodium into calcium is proportional to the received fluence and can be used to calculate the fluence the aluminum received. With this method a resolution of 7% can be achieved. The irradiation goal for the proton irradiation was to achieve the same 1 MeV neutron equivalent fluence as for the neutron irradiation. This could only be achieved for 6×10^{16} n_{eq} cm^{-2} and 8×10^{15} n_{eq} cm^{-2} (see table 8.1). The final fluence of 1×10^{17} n_{eq} cm^{-2} could not be achieved because of unexpected downtimes of the PS.

Irradiation type	Fluence [$10^{15}\ n_{eq}\,\mathrm{cm}^{-2}$]	Uncertainty [$10^{15}\ n_{eq}\,\mathrm{cm}^{-2}$]
neutron	1	0.1
neutron	8	0.8
neutron	60	6
neutron	100	10
proton	0.39	0.03
proton	9	0.6
proton	68.8	4.8
proton	84.9	5.9

Table 8.1. Irradiation achieved for each sample type.

8.3 Annealing

After irradiation, each sample was annealed to reduce its leakage current. This was achieved by heating them for 60 min at 80 °C. A list of all annealing histories can be found in table 8.2. The samples that were neutron irradiated to $1 \times 10^{15}\ n_{eq}\,\mathrm{cm}^{-2}$ were annealed for a longer time since the preheated oven cooled down while the samples were placed inside it and was cooler than 80 °C for a substantial part of the annealing time. It was therefore decided to anneal them for a further ten minutes to have a similar annealing effect compared to the other samples. Using equation (2.21) one can calculate the expected α value. As can be seen in table 8.3, α is for all samples around $3 \times 10^{-17}\,\mathrm{A\,cm}^{-1}$ with only the neutron irradiated samples at 8×10^{15} $n_{eq}\,\mathrm{cm}^{-2}$ and $6 \times 10^{16}\ n_{eq}\,\mathrm{cm}^{-2}$ having a slightly lower α.

Irradiation type	Fluence [$n_{eq}\,\mathrm{cm}^{-2}$]	Annealing temperature [°C]	Annealing time [min]
neutron	1×10^{15}	78	70
neutron	8×10^{15}	82	60
neutron	6×10^{16}	82	60
neutron	1×10^{17}	81	60
proton	3.2×10^{14}	79	60
proton	7.4×10^{15}	79	60
proton	5.6×10^{16}	78	60
proton	6.9×10^{16}	80	60

Table 8.2. Annealing time and temperature for each fluence.

As mentioned before, the annealing of the samples during the neutron irradiation is not well

known. To better understand the implication of this additional annealing step, the alpha factor is first calculated only for the intentional annealing in the oven and in a second step with an additional annealing step during irradiation. For the used channels in the reactor a maximum temperature of 50 °C was measured, so this temperature was assumed during the whole irradiation duration. As the temperature would be in reality lower and would slowly ramp up over time this was done to calculate the maximal deviation possible. As the annealing happened during irradiation only a small fraction of the irradiation damage experienced the full annealing. Due to not having the exact irradiation and temperature timeline, the annealing is calculated after an assumed full radiation dose, slightly overestimating the effect of annealing. From table 8.2 it can be seen that the additional annealing inside the reactor leads in the worst case to a reduction of α by 2.67% and for the lowest fluence to a reduction by less than 1%. As the error of this is smaller than the error in the fluence measurement, it was concluded that this error can be neglected.

Irradiation type & Fluence [n_{eq} cm^{-2}]	α [10^{-17}A cm^{-1}] without reactor annealing	α [10^{-17}A cm^{-1}] with reactor annealing	Relative Change [%]
neutron 1×10^{15}	3.01	3.00	-0.04
neutron 8×10^{15}	2.90	2.89	-0.22
neutron 6×10^{16}	2.90	2.86	-1.52
neutron 1×10^{17}	2.94	2.86	-2.67
proton 3.2×10^{14}	3.02		
proton 7.4×10^{15}	3.02		
proton 5.6×10^{16}	3.06		
proton 6.9×10^{16}	2.98		

Table 8.3. Calculated α factors using equation 2.21 with the annealing times and temperatures from table 8.2 at 20 °C after annealing of the different samples. Comparison of the effect of an assumed annealing at 50 °C in the neutron reactor and no additional annealing.

For the two lowest proton fluences additional measurements were performed before the annealing process and compared to measurement after annealing to calculate the relative reduction in leakage current G_{Ann} [139]

$$G_{\mathrm{Ann}} = \frac{I_{\mathrm{NonAnnealed}}}{I_{\mathrm{Annealed}}}. \tag{8.1}$$

The results can be seen in figure 8.2. For 1×10^{14} n_{eq} cm^{-2} a mean reduction by a factor 2.3 is observed, whereas for the higher fluence this factor is closer to 2. To calculate the expected reduction the alpha factor after annealing was compared to an alpha factor with an annealing time of around 10 min at 24 °C, which would correspond to the warming of the sensor during the preperation of the measurement. For this case a reduction of leakage current by
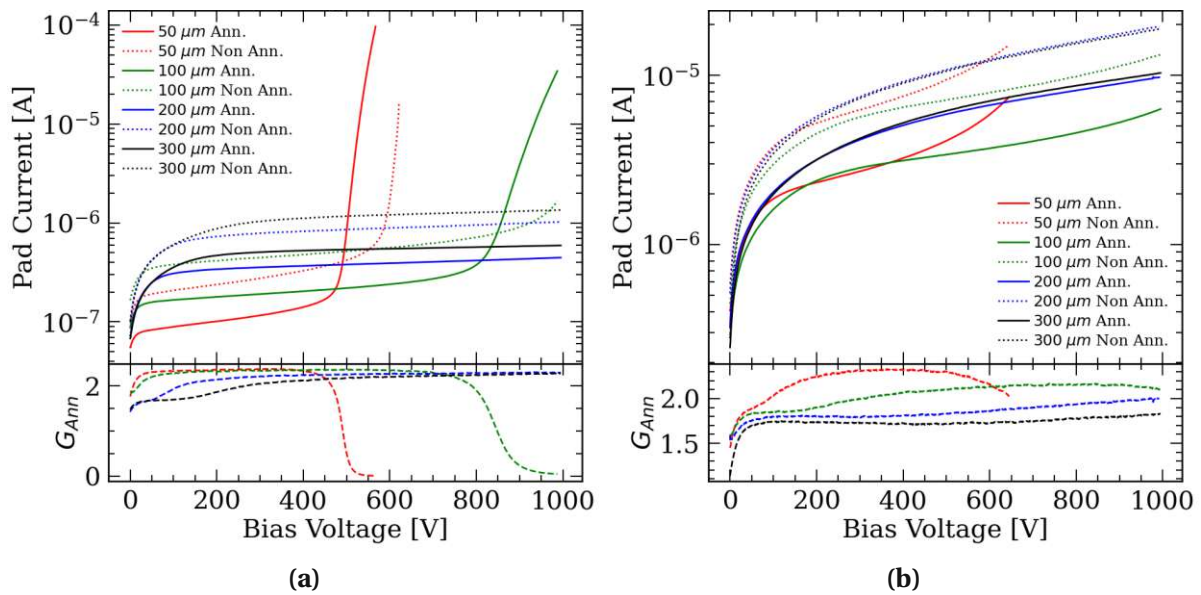
Fig. 8.2. Leakage current measurement at -20°C before and after annealing for different sensor thicknesses. The bottom plot shows the Relative reduction in leakage current after annealing. **a**: Measurement for 1×10^{14} n_{eq} cm^{-2} proton irradiated samples [139]. **b**: Measurement for 9×10^{15} n_{eq} cm^{-2} proton irradiated samples [139].

a factor of 2.4 is calculated. This indicates that for the higher fluence samples the actual annealing temperature may have been lower than the measured 79 °C. In all cases the thicker sensors exhibit a lower reduction of current after annealing than the thinner sensors. As all gain values seem to converge to the same value at high voltages, it is suspected that this effect originates from the difference in depletion volume of the sensors, with thicker sensors reaching the same volume at higher bias voltages.

For the lower fluences a decrease in breakdown voltage is observed, attributed to the annealing of the p-spray itself. After annealing the depletion region is also moving to higher voltages, as the samples were annealed past the beneficial annealing range, which leads to an increase in E_{eff}. For the higher fluence a similar behavior is observed. For the lowest fluence the breakdown happens earlier after annealing, which again can be attributed to the change in p-spray. An direct comparison of the measured of and calculated α factors is not addvised due to several reason discussed in section 9.2.2.

9

Leakage current

9.1 Measurements

The IV characteristics of the irradiated samples were measured in the same way as described in section 6. To prevent annealing of the samples during the measurement and to prevent thermal run-away the samples can not be measured at room temperature. To study the temperature scaling after irradiation each sample is measured at -10, -20 and -30 °C. As the behavior of the IV curves does not change drastically as a function of the temperature, -20 °C is used as the standard in this thesis. An extensive look at the temperature scaling behavior can be found in [139]. Figures 9.1 and 9.2 show the pad and guard current for sensors of different thickness for the different neutron irradiation levels. Due to the overall increase in leakage current the guard-ring current is not measured separately anymore, instead the combined current of pad and guard ring measured by the sourcemeter subtracted by the pad current is used. No breakdown for the 300 and 200 μm diodes is seen in the measurement range. Only for the 50 and 100 μmthick sensors at the lowest fluence a breakdown is still visible. The breakdown is shifted to higher voltage, consistent with the expected removal of the p-spray concentration. For 10^{15} n_{eq} cm^{-2}, no stable region is visible after depletion with an exponential increase until the onset of the breakdown. As the guard-ring current again reaches the breakdown before the pad for the lowest proton and neutron fluence the p-spray is suspected again to be the reason of the breakdown. For the lowest neutron fluence a sharp increase in guard-ring around 200 V is seen for all thicknesses. Only for the 50 μm and 100 μm thick sensors no saturation of the leakage current is observed. For the other thicknesses, a decrease in slope of the IV curve is seen achieving a higher leakage current as the pad. For the lowest proton irradiation level, no saturation of leakage current is seen for the guard-ring current. Since the guard-ring IV curve shows earlier breakdown and has an overall higher leakage current than the pad one, the breakdown behavior is again attributed the p-spray concentration and geometry. An increase of leakage current in the guard-ring due to surface currents is not considered, as the pad exhibits the same breakdown behavior as the guard-ring, and it can be therefore assumed that they share the same phenomenon behind their behavior. The reason of the difference in the slope of the breakdown between the proton and neutron irradiation can be attributed to the concentration depending on acceptor removal. As higher concentration increases the probability of the removal of a boron atom from its lattice position the relative reduction is higher the higher the concentration is. This leads to a smoothing of the doping layer profile and as a result a slower increase in current during breakdown. As the proton irradiation has a lower fluence the breakdown is expected to be steeper.

141

For non-irradiated sensors, the leakage current normally increases with increasing sensor thickness. For the lowest fluence the leakage current follows the same behavior with the thinnest sensor exhibiting the lowest current due to the lowest current generating volume. For the next higher fluence at 8×10^{15} n_{eq} cm^{-2} this difference is reduced. After 6×10^{16} n_{eq} cm^{-2} a reversed behavior is observed, with the thinner sensors exhibiting the highest leakage current for the same bias voltage. This indicates that the main contributor of the leakage current is not any more the thermal generated bulk current but a field dependent impact ionization. As mentioned before a double junction in the electric field is expected for all fluences above 1×10^{15} n_{eq} cm^{-2}, which leads to high field regions at both electrodes where impact ionization can happen.
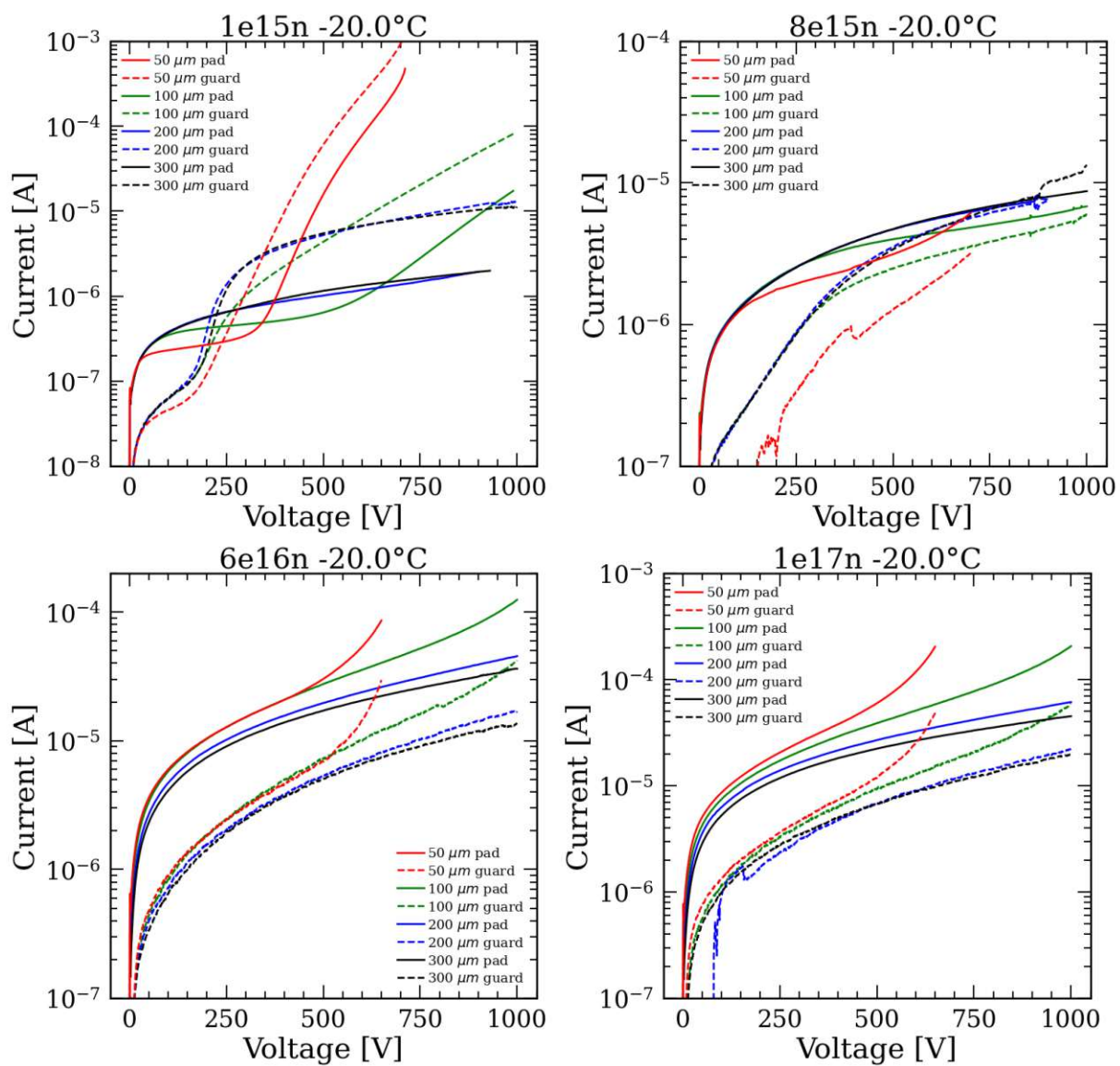
Fig. 9.1. Comparison of IV measurements for neutron irradiated diodes of different thickness for different fluences.
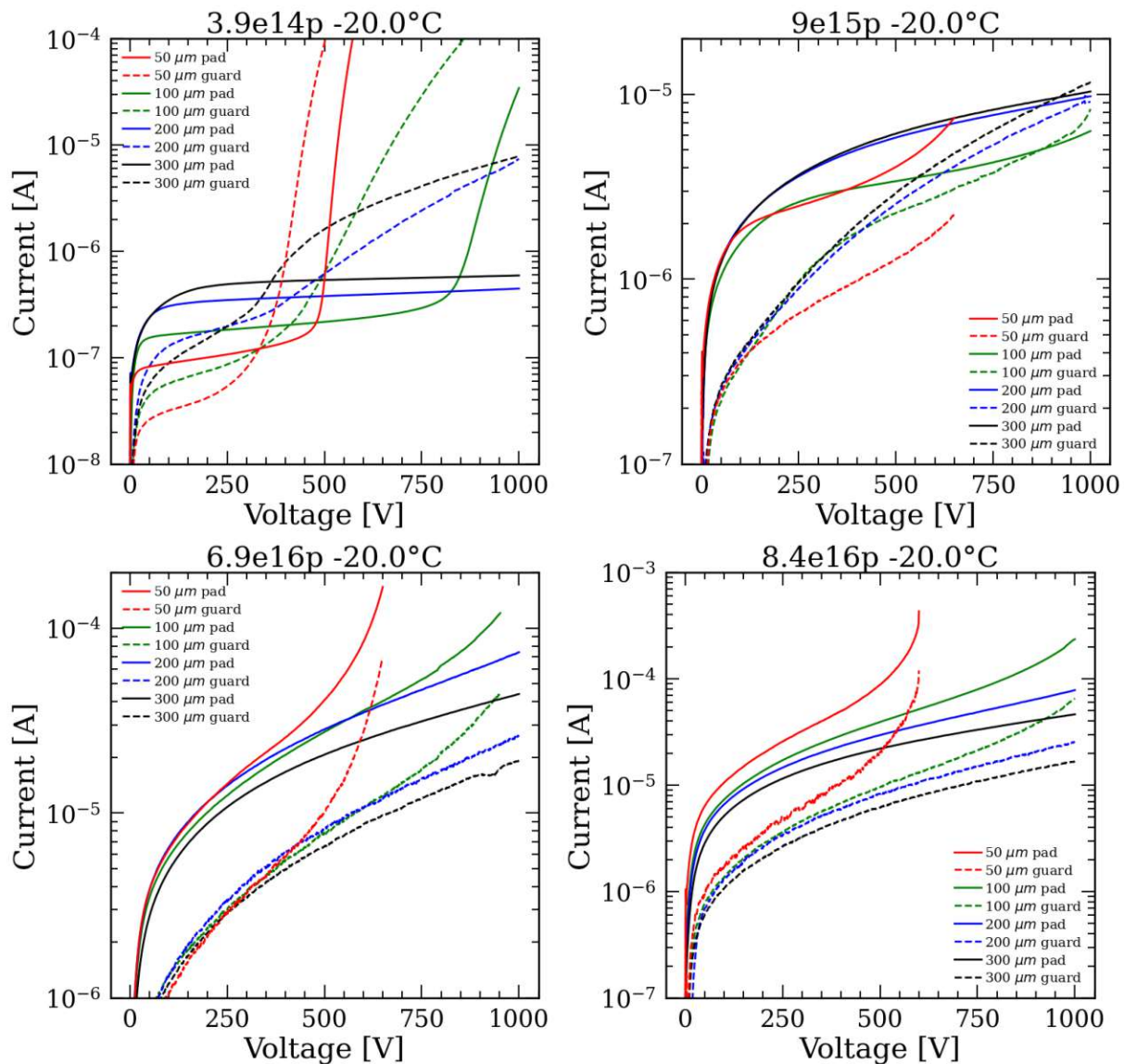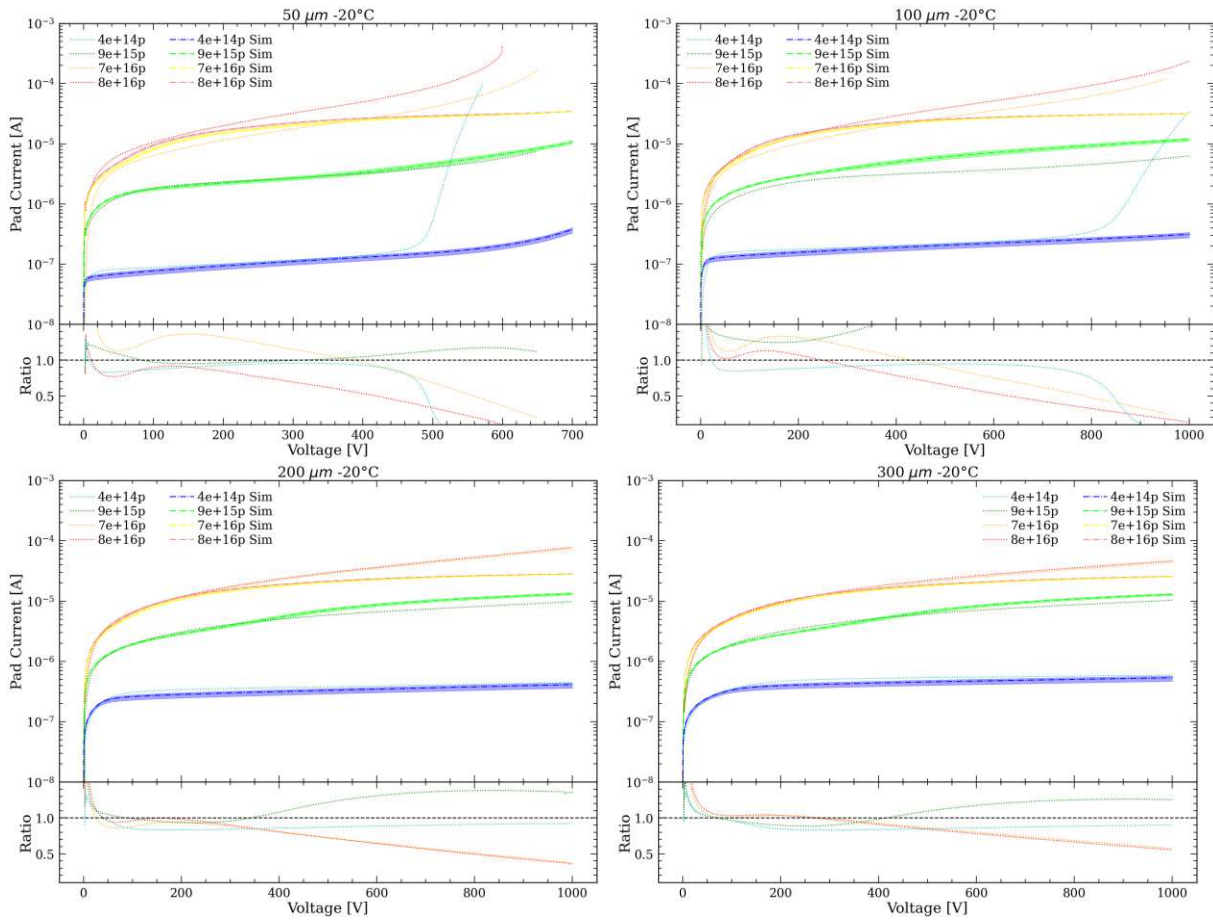
Fig. 9.2. Comparison of IV measurements for proton irradiated diodes of different thickness for different fluences.

9.2 Simulation

To better understand the observed features in the measured IV curves after irradiation, simulations were performed. In TCAD, radiation effects are modeled by manually defining trap states, specifying the concentration of the trap states as a function of fluence, their positions in the band gap, the type of defect and their electron and hole cross-sections. The position can hereby be defined as an absolute value or in relation to either the valence or conduction band. As the introduction of all known defect states would lead to prohibitively long simulation times, effective trap states are used which should combine the effect of several similar trap states into a single state. The parameters of these states are extracted by optimizing them through the comparison of simulation with measurement data. As these models

are often tuned for a certain type of sensor, irradiation type and energy, they may not lead to satisfactory results for environments far from their initial optimization. The number of traps introduced differs between the different models. Whereas the Perugia[140] and LHCb model [141] have three states, the Hamburg Penta Trap model [142] has five. For this study only the Penta Trap Model is used, as it has been shown to have a good agreement in the current behaviour up to 1×10^{16} n_{eq} cm^{-2} and was tuned using n-in-p sensors irradiated with protons with the same energy as used for the irradiation of the test samples. In this model a linear introduction rate g with fluence is assumed. A table with all the trap parameters implemented in TCAD can be found in 9.1. No parameter optimization was done for the model to evaluate the prediction for a general sensors case.

Defect Name	Type	Energy[eV]	g [cm^{-1}]	σ_e[cm^2]	σ_h[cm^2]
E30K	Donor	E_C-0.1	0.0497	2.3×10^{-14}	2.92×10^{-16}
V_3	Acceptor	E_C-0.458	0.6447	2.551×10^{-14}	1.511×10^{-13}
I_p	Acceptor	E_C-0.545	0.4335	4.478×10^{-15}	6.709×10^{-15}
H220	Donor	E_V+0.48	0.5978	4.166×10^{-15}	1.965×10^{-16}
C_iO_i	Donor	E_C+0.36	0.378	3.23×10^{-17}	2.036×10^{-14}

Table 9.1. Hamburg Penta Trap model parameters [142].

Hurkx tunnelling[143] was activated for the defect I_p and the tunnelling mass parameter of the holes was changed to 0.25 as recommended in [142]. The LHCb model was not used because of a strong saturation and overall lower leakage current observed at high fluences compared to the Penta Trap model. The Perugia model was not implemented as its parameters have to be changed depending on the fluence. To account for surface damage the oxide interface concentration is increased to 1×10^{12} cm^{-2}. To speed up the simulation only a 100 μm wide part of the pad electrode (reduced geometry) without the guard-ring was simulated and then scaled up to the full area. A comparison between the simulation of the full geometry and the reduced one can be seen in figure 9.3. As the two simulations are in good agreement, the reduced simulation is used where possible.

As the Penta Trap model does not account for the acceptor removal in the p-spray, all simulations at a fluence of 8×10^{15} n_{eq} cm^{-2} and higher are simulated with no p-spray implementation. For the lower fluences, if the p-spray is simulated, the concentration had to be corrected accordingly. As the p-spray reduction depends on the total concentration, a change of profile shape in addition to a reduction in concentration is expected. This is due to the fact that the relative removal of acceptors is higher for higher concentrations, leading to flatter profiles. To simulate this the measured doping profile was modified with [144]

$$N_\phi = N_0 \left(1 - e^{aN_0^{-b}} \right), \tag{9.1}$$

where N_0 represents the initial doping concentration, a and b are parameters with the val-
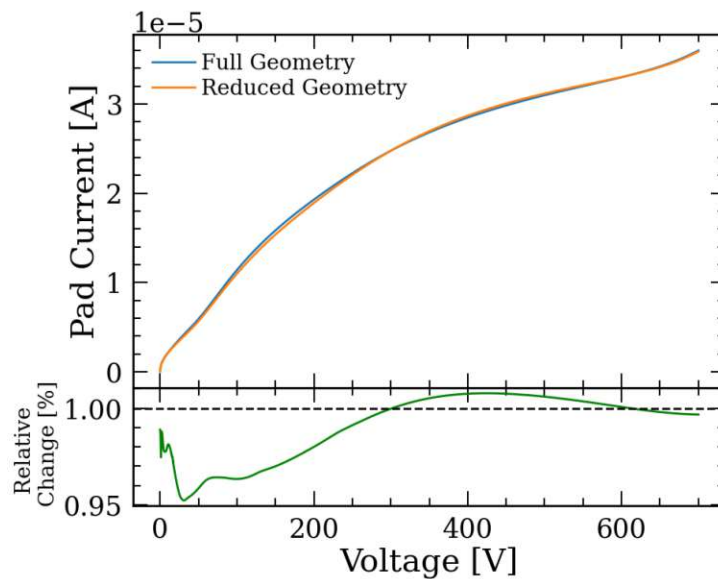
Fig. 9.3. Comparisons between the simulated full geometry and 100 μm cut out for a 50 μm thick diode irradiated up to $1\times10^{17}\,n_{eq}\,\mathrm{cm}^{-2}$. The green line represents the relative change between the simulations.

ues of $1.66\times10^{-6}\,\mathrm{cm}^3$ and 4.96×10^{-1}, respectively. The values of a and b where extracted from several N_ϕ values obtained from literature [145, 146, 147, 148]. The change in profile can be seen in figure 9.4a. In figure 9.4b a simulation using the full sensor geometry and the calculated p-spray profile for the $3.9\times10^{14}\,n_{eq}\,\mathrm{cm}^{-2}$ proton irradiated 50 μm thick sensor is compared to its measurement. Up to the breakdown region the simulation is in good agreement with the measurements, but the simulated breakdown happens earlier and it is softer. The difference is suspected to originate from the non-modelling of the annealing of the p-spray in the calculations. Another comparison was made to the reduced geometry used for other fluences. As no difference between the full geometry simulation and the reduced geometry simulation is observed before the breakdown (figure 9.4b) it was used for all further simulations.

A comparison of the simulations and the measurement data can be found in figure 9.5 and 9.6. The simulation results are represented as dashed lines, with the colored bands representing the error bar due to the uncertainty in the fluence measurement. The corresponding measurements are displayed as full lines. For most sensors the agreement between measurements and simulations is better than 30% for all fluences. An exception to this are the neutron irradiated 200 and 300 μm thick sensors at the lowest fluence. Here a non-saturating behavior is observed, suspected to be due to a change in depleting behavior because of the reduced p-spray concentration. Another indication for this is that this is not the case for the proton irradiated sensors. As the acceptor removal coefficient is higher for protons, more p-spray is removed for the device at similar fluences [149].

For fluences above $1\times10^{16}\,n_{eq}\,\mathrm{cm}^{-2}$ a diverging behavior between simulation and mea-

(a)

(b)
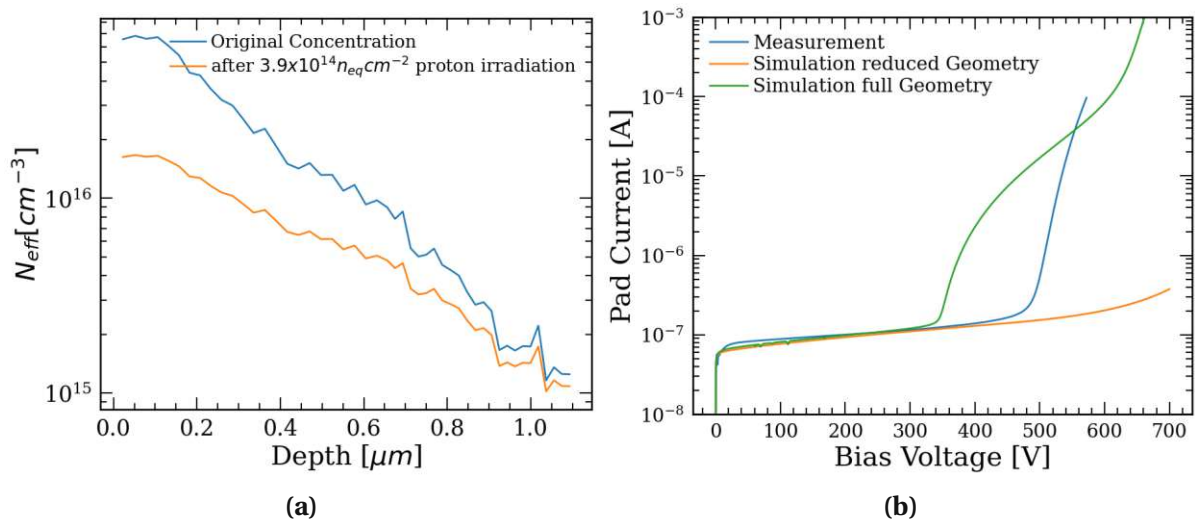
Fig. 9.4. a: Calculated change of the measured p-spray concentration after 3.9×10^{14} n_{eq} cm^{-2} proton irradiation. **b**: Comparison of the measured IV curve of the 50µm thick sensor irradiated up to 3.9×10^{14} n_{eq} cm^{-2} to a simulation using the full detector geometry and changed p-spray profile and simulation using only a 100 µm wide slice of the pad electrode.

surement with bias voltage is observed. At high bias voltages the simulated leakage current reaches a plateau, whereas the measured current continues to grow. This divergence is more pronounced for thinner sensors, with the thinnest sensors exhibiting a steeper than exponential growth at the highest bias voltages indicating the onset of breakdown. Another feature is the higher or equal leakage current for proton irradiated samples compared to neutron irradiated ones at the highest fluence. This could be an indication that the NIEL Hypothesis is not valid at these fluences.

As the Penta Trap model was designed with an annealing of 80 min at 60 °C the simulated current should be scaled down to 70% to account for the additional annealing done for our samples. As the simulation underestimates in most cases the leakage current, this would lead to a 30% reduction of the simulated leakage current (see figure 9.7). This is consistent with the lower-than-expected annealing factor and indicates that the annealing was done at a lower temperature than measured. Due to this the additional scaling was not applied for further simulation studies.

The saturation of the leakage current at high fluences could be an indication that the used impact ionization model may not describe impact ionization correctly for this high trap concentration. Therefore, all other impact ionization models were evaluated for the 100 µm thick diode at 1×10^{17} n_{eq} cm^{-2} (see figure 9.8). The different models produce only marginal differences and can not reproduce the diverging leakage current. Another possibility for the increased leakage current could be a higher accumulated charge at the interface or the introduction of generation / recombination centers at the silicon interface. To assess this hypothesis two different simulations were done: one where the interface charge was doubled compared to the values used before and one where the leakage current related traps from the
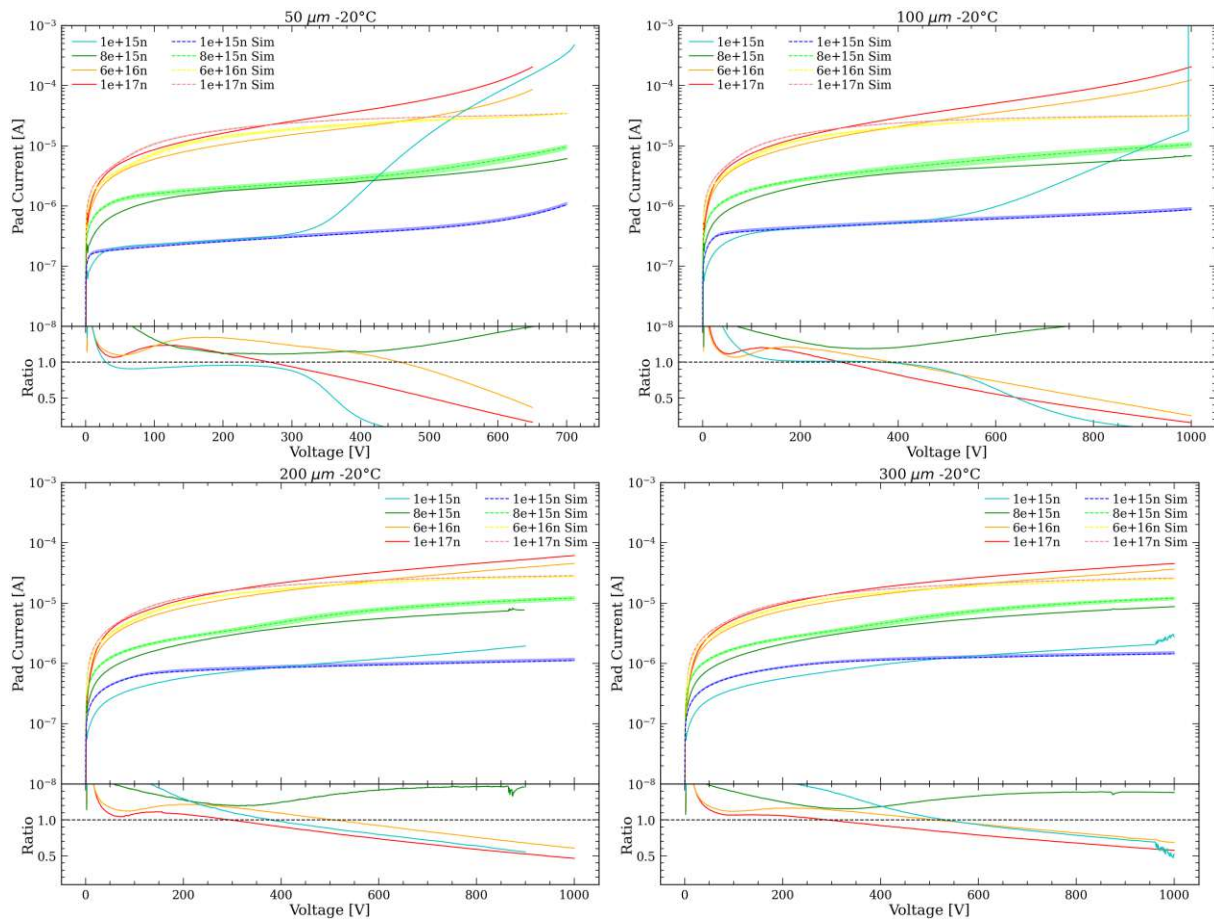
Fig. 9.5. Comparison of IV measurements for neutron irradiated diodes of different thickness for different fluences to simulated data. The colored band represents the uncertainty in the simulation due to the uncertainty in the fluence measurement. The bottom shows the ratio between simulation results and measurements.

Perugia surface damage model [150][151] were introduced. The parameters used for the traps can be found in table 9.2. The implemented surface damage had no significant effect on the impact ionization and the diverging behavior could not be reproduced (figure 9.9).

Type	Energy[eV]	g [cm^{-1}]	σ_e[cm^2]	σ_h[cm^2]
Donor	E_V+0.6	2×10^{12}	1×10^{-15}	1×10^{-16}
Acceptor	E_C-0.56	2×10^{12}	1×10^{-16}	1×10^{-15}

Table 9.2. Parameters of the Perugia surface damage model used in TCAD for irradiation of 1×10^{17} n_{eq} cm^{-2}.

To better illustrate the reason behind the higher leakage current for thinner detectors at higher fluences the current generated by the impact ionization is plotted against the current generated by all other sources. This was achieved by extracting the generation rate from the impact ionization and integrating it over the detector volume. The same was done for the combined

Fig. 9.6. Comparison of IV measurements for proton irradiated diodes of different thickness for different fluences to simulated data. The colored band represents the uncertainty in the simulation due to the uncertainty in the fluence measurement. The bottom shows the ratio between simulation results and measurements.

generation rate for all other process. As this does not account for the trapping and movement of charges in the detector, the resulting current cannot be directly compared to the simulated leakage current but can be used instead to give an idea of how the different effects behave relative to each other. As can be seen in figure 9.10a, for the lowest fluence the current generated by impact ionization is lower than the current generated by SRH-Generation at low voltages and depending on the sensor thickness overtakes the SRH current at later voltages. For the highest fluence impact ionization is several orders of magnitude higher than the SRH-Generation and is therefore the main contributor. This can also be illustrated by the electrical field (figure 9.11a and 9.11b). Close to the readout electrode a substantially higher electric field field is observed for $1 \times 10^{17}\ n_{eq}\,\mathrm{cm}^{-2}$ compared to $1 \times 10^{15}\ n_{eq}\,\mathrm{cm}^{-2}$. This in turn leads to an increased impact ionization for the higher fluence.
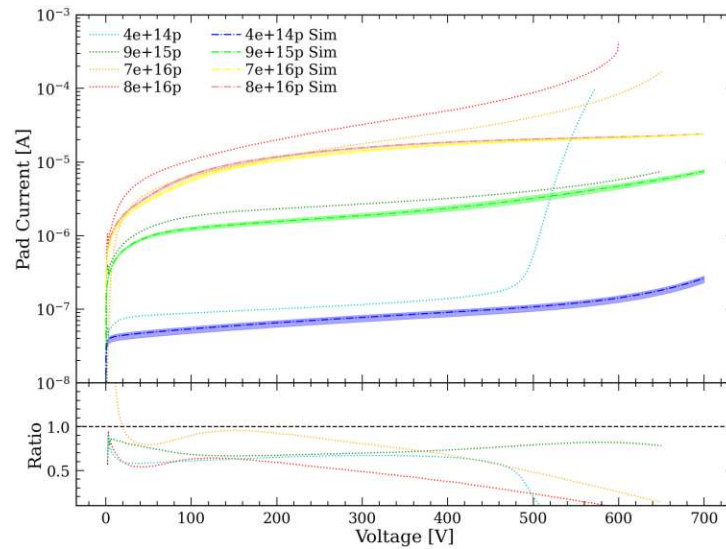
Fig. 9.7. Comparison of IV measurements for 50 μm diodes irradiated with protons at different fluences to simulated data after scaling the simulated data down to 70%. The colored band represents the uncertainty in the simulation due to the uncertainty in the fluence measurement. The bottom shows the relative difference of the simulation in regard to the measurement. The black dashed line represents no difference.
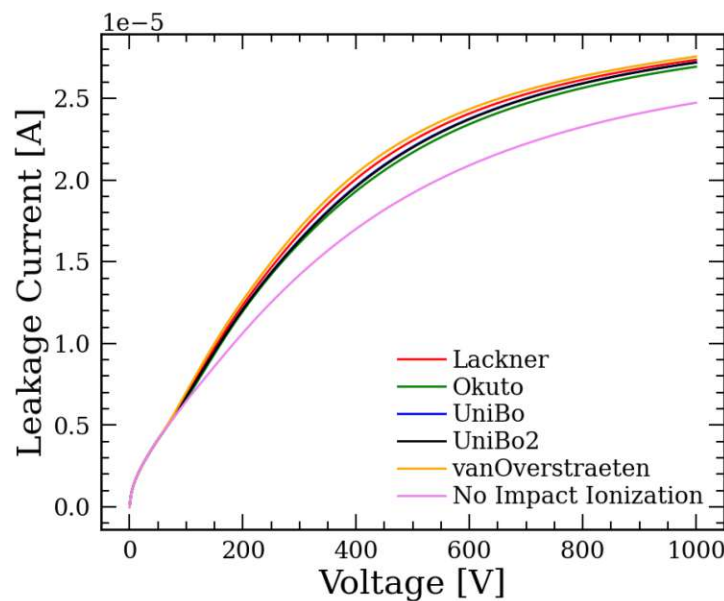
Fig. 9.8. Simulation of a 100 μm diode irradiated up to $1 \times 10^{17} \ n_{eq} \ \text{cm}^{-2}$ for different impact ionization models used in TCAD.

9.2.1 Temperature scaling of the leakage current

Another effect that was studied was the scaling of the leakage current with temperature. The standard parametrization of the temperature scaling behavior [139] is

$$I\left(T\right) \propto T^2 e^{\frac{-E_{eff}}{2k_b T}} , \tag{9.2}$$
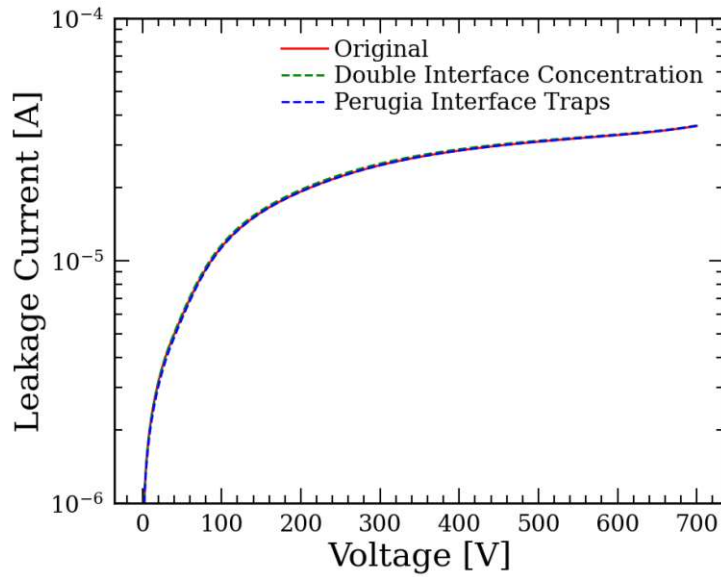
Fig. 9.9. Comparison of simulation of a 50 µm diode irradiated up to $1 \times 10^{17}\, n_{eq}\, \mathrm{cm}^{-2}$ using double the original oxide charge and including the Perugia surface trap model.

where E_{eff} represents a constant effective band gap used to describe the temperature dependence of the band gap in the observed temperature range. E_{eff} was calculated for each thickness and each fluence point by comparing the measured leakage current I_1, I_2 at different temperatures T_1, T_2 using

$$E_{eff} = 2k_b ln \left(\frac{T_1^2 I_2}{T_2^2 I_1} \right) \frac{T_1 T_2}{T_2 - T_1}. \tag{9.3}$$

This was done for all permutations of the three measured temperatures (-10°C,-20°C,-30°C) and the mean was calculated. As an example, the dependence of E_{eff} on the bias voltage for the different proton fluences for the 100µm thick sensor can be seen in figure 9.12. For the two lowest fluences a steady decrease in E_{eff} with increasing bias voltage is observed. For the two highest fluences E_{eff} increases instead exponentially with increasing bias voltage. To exclude internal heating of the sensors due the high leakage current as the reason behind the exponential increase, another measurement was done to evaluate the change of leakage current as a function of time. For this the 50 µm sensor irradiated to $1 \times 10^{17}\, n_{eq}\, \mathrm{cm}^{-2}$ was biased at 500 V and the leakage current was measured over a period of 30 min. As no change in leakage current was observed thermal runaway was excluded as an explanation. One probable reason behind this increase could be the temperature dependence of the impact ionization coefficient. This difference due to the double exponential scaling behavior of impact ionization as a function of temperature (see equation 3.6), should result in an exponential difference in the leakage currents. Comparing the value of E_{eff} determined from the measurements to simulation data, the behavior for the lowest fluences could be reproduced (figure 9.13), but the mean E_{eff} is higher in the simulation. For higher fluences the simulation results in the same behavior as the lower ones, while exhibit a higher mean E_{eff}. This contradicts the mea-
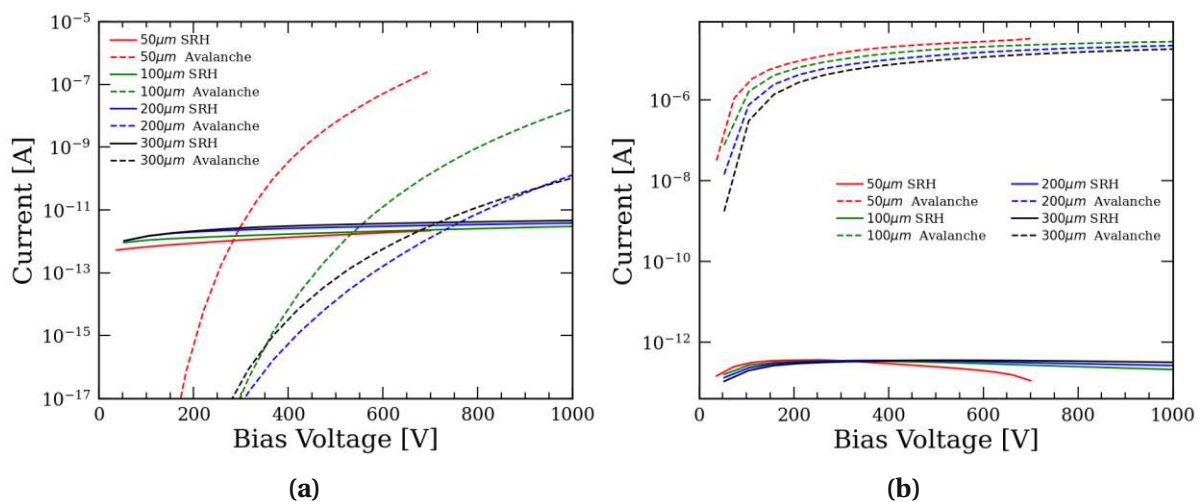
Fig. 9.10. Comparison of the current generated by impact ionization and other generation/recombination effects for sensors of different thickness. **a**: Simulation for a fluence of $1 \times 10^{15}\ n_{eq}\,\mathrm{cm}^{-2}$. **b**: Simulation for a fluence of $1 \times 10^{17}\ n_{eq}\,\mathrm{cm}^{-2}$.
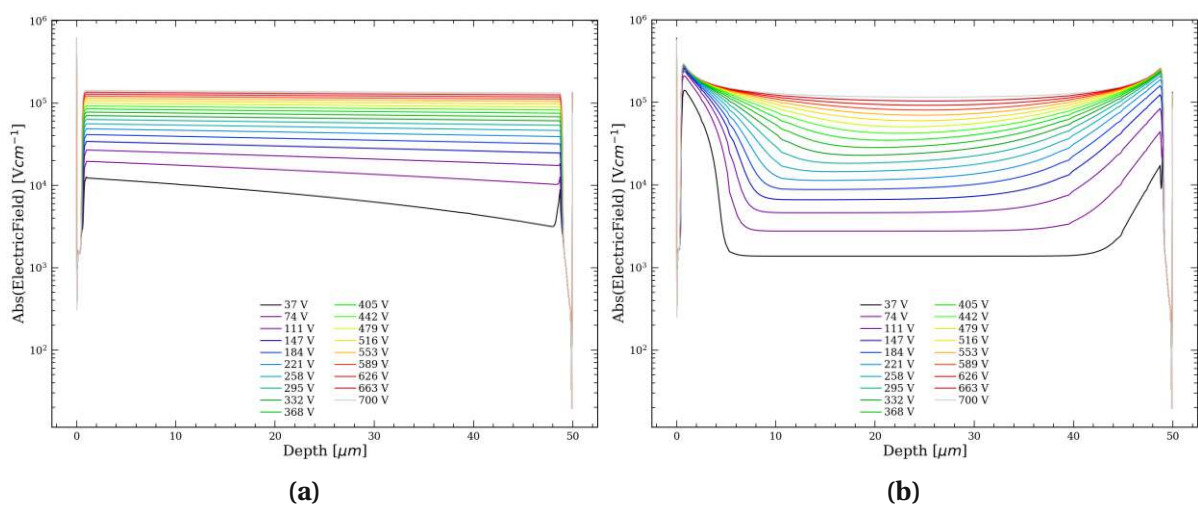
Fig. 9.11. Simulated electrical field inside a 50 μm thick sensor for different bias voltages. **a**: Simulation for a fluence of $1 \times 10^{15}\ n_{eq}\,\mathrm{cm}^{-2}$. **b**: Simulation for a fluence of $1 \times 10^{17}\ n_{eq}\,\mathrm{cm}^{-2}$.
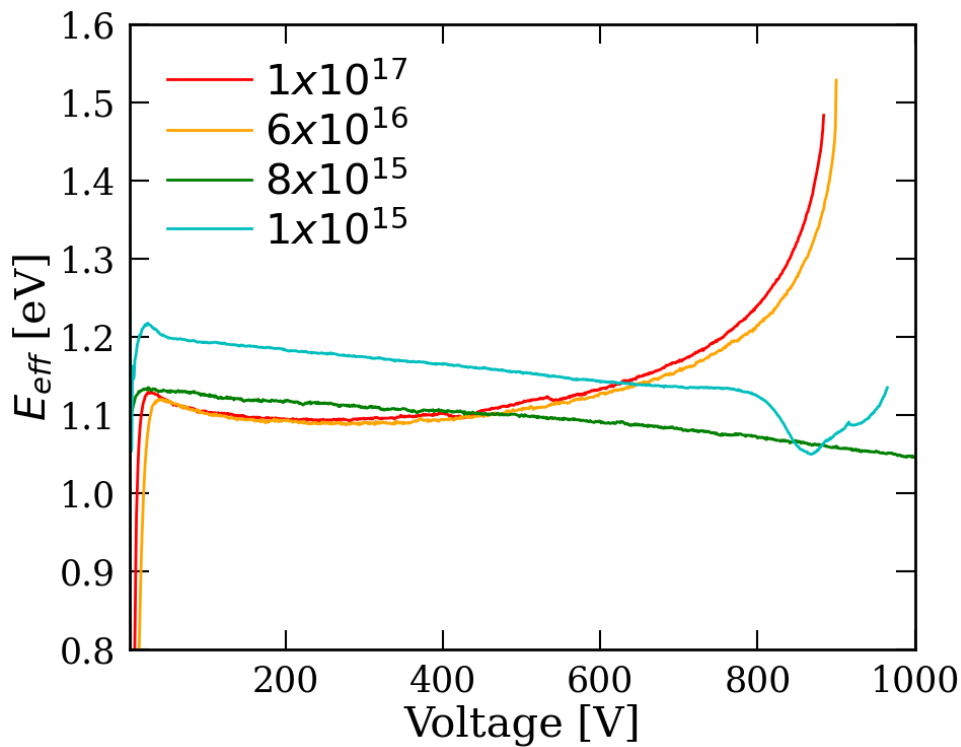
Fig. 9.12. Calculated E_{eff} as a function of bias voltages from measurements of a 100µm thick sensor at four proton irradiations (fluence levels in units of $n_{eq}\,\text{cm}^{-2}$).

surements, implying that there may still be an internal heating of the sensor, as described in [152]. To calculate a mean E_{eff} value from the measurement the mean of all voltage points
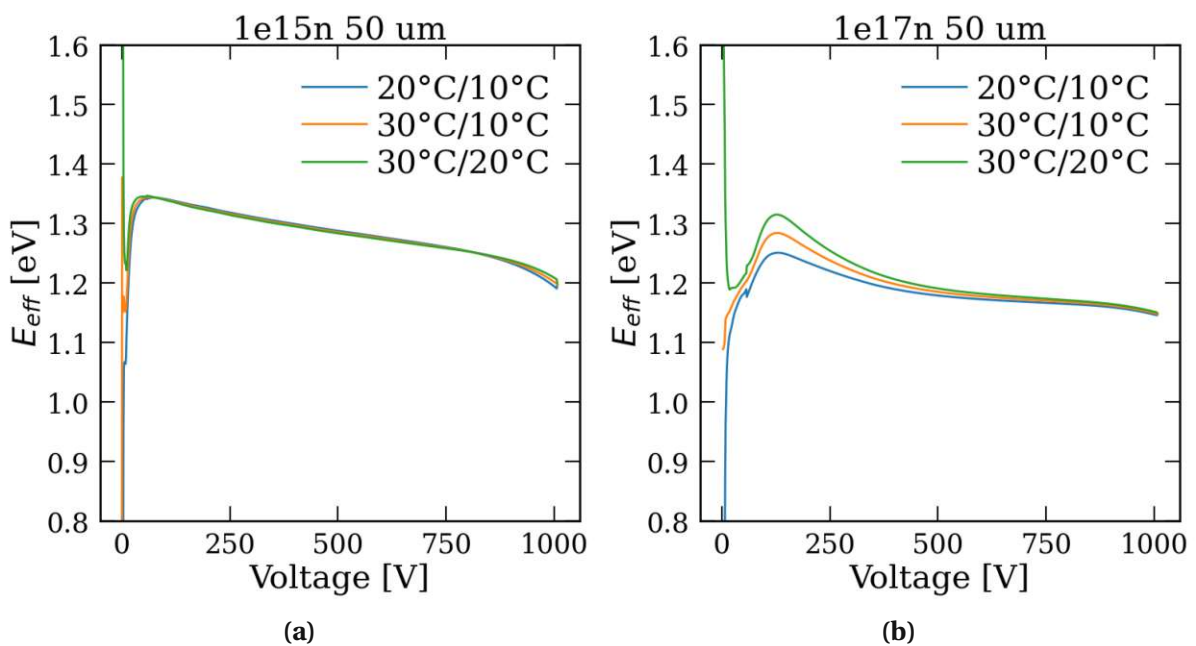
Fig. 9.13. E_{eff} calculated form simulated data for a 50 µm thick sensor at (**a**) $1 \times 10^{15}\,n_{eq}\,\text{cm}^{-2}$ (**b**) $1 \times 10^{17}\,n_{eq}\,\text{cm}^{-2}$.

was taken. For the highest fluence the region after the start of the exponential increase was excluded. The change of mean E_{eff} as a function of fluence and thickness can be seen in figure 9.14. A slight decrease of E_{eff} as a function of fluence is observed similar to the simulation results. This is expected as the introduction of trap states should lead to a decrease in band gap. For the highest fluence a mean E_{eff} of 1.07 ± 0.012 eV is measured, whereas for the lowest fluence this increase to 1.15 eV, this is much lower as the value of 1.21eV quoted in [153], but agrees with the value that was determined by the ATLAS experiment [154]. A more extensive study of E_{eff} can be found in [139].
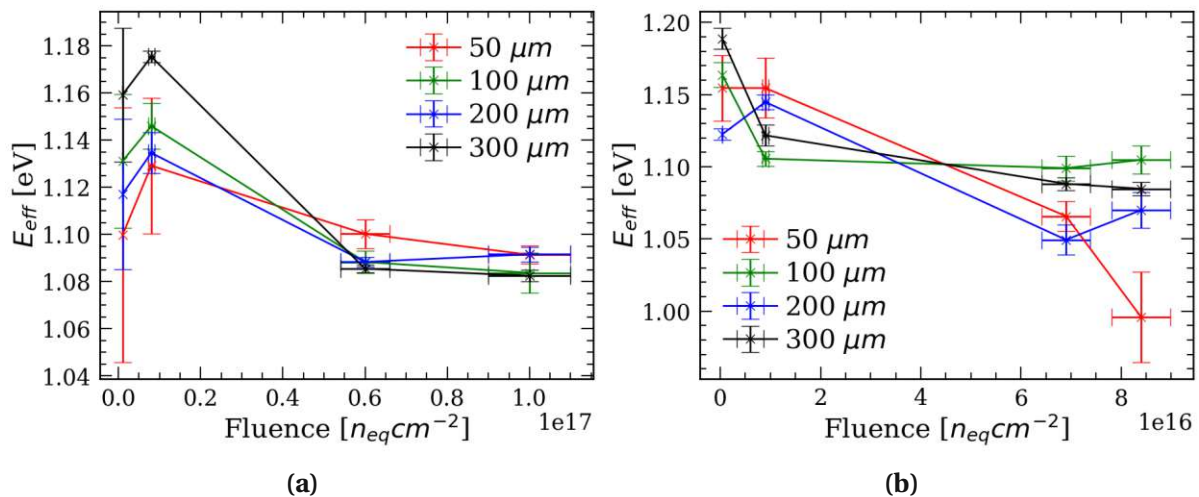
Fig. 9.14. Mean E_{eff} calculated as a function of fluence for different thicknesses after (**a**) neutron and (**b**) proton irradiation.

9.2.2 Leakage current scaling with fluence

An attempt was made to calculate the leakage current scaling factor α from the measured data. It was done by normalizing the irradiated current by the geometrical volume of the sensor (as the pre-irradiation leakage current is several orders of magnitude lower than after irradiation, ΔI was approximated by the leakage current) for each fluence point and fitting it with a straight line. The geometrical volume was chosen as a normalization constant, as at fluences in the order of 10^{16} n_{eq} cm^{-2} or higher the sensors do not deplete fully anymore and to compare the sensors of different thicknesses they have to be normalized by their respective current generating volume. From the slope of the fitted curve α was extracted. An example of the results for all neutron irradiations is shown in figure 9.15.

As can be seen no agreement between the different thicknesses was reached. The discrepancy is suspected to be due to several reasons. Firstly, a significant contribution to the leakage current comes from impact ionization, especially at high fluences, which is not uniform throughout the sensor volume. This leads the voltage points at which ΔI is evaluated has a significant impact on the resulting α. As no plateau of constant leakage current is reached after irradiation, the higher the reference voltage the higher the resulting α. Secondly, with
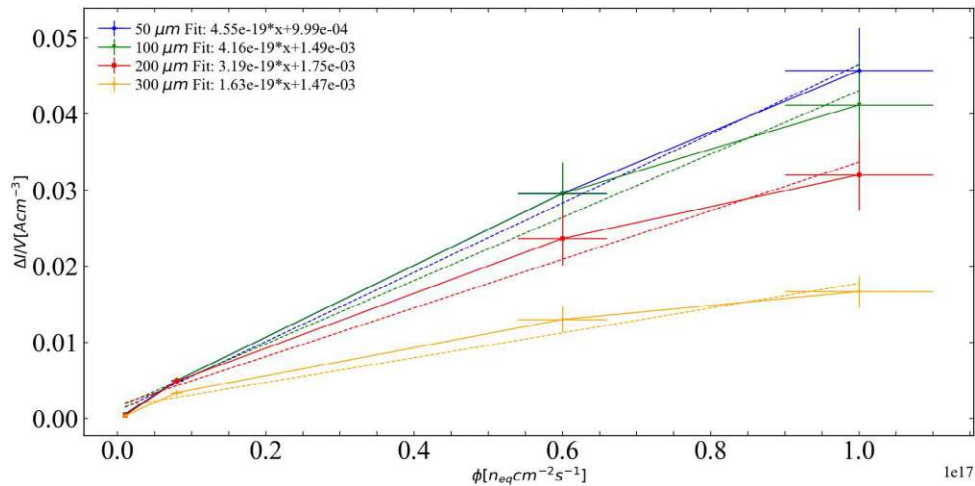
Fig. 9.15. Fits used to calculate α for sensor of different thickness after neutron irradiation.

the formation of a double junction the sensors does not deplete in a normal way anymore. Therefore the normalization of leakage current with the depleted volume is not possibel anymore. Lastly, as shown before, the temperature scaling behavior of the leakage current and therefore of α changes with temperature. One therefore cannot apply the standard temperature scaling to α, but instead each point of the fit used to determine α needs to be scaled separately and α needs to be recalculated. An example for this can be seen in figure 9.16, where the α was calculated assuming a fully depleted 50 μm thick sensor and scaling the α to 20 °C assuming $E_{\mathrm{eff}} = 1.15$eV. Were as for 4×10^{14} n_{eq} cm^{-2} and 10^{15} n_{eq} cm^{-2} the alpha is at 100 V with 3.2 A cm^{-1} close to the expected value of 3, but reaches values of around 4.4 and 4, respectively, before the breakdown. For higher fluences this discrepancy is increased further. Due to afore mentioned reason not further studies were done on α, as its purpose of a easy predictor of leakage current for different fluence was not valid in the fluence range of interest.

9.3 Summary

The shape of the IV curves of the irradiated samples was observed to change significantly with fluence. This can be explained by the fact that with increasing fluence, impact ionization and therefore the electrical field plays an increasing role. This is especially relevant for thinner sensor as high fields can be achieved already at low bias voltages. Up to a fluence of 8×10^{15} n_{eq} cm^{-2} TCAD simulations based on the Penta Trap model were found to be in agreement with measurements. At higher fluences the simulated IV curves show saturating behaviour, while the measurements exhibit a steeper increase in leakage current at high bias voltages.

For the temperature scaling a lower E_{eff} was measured than expected which leads to a slower
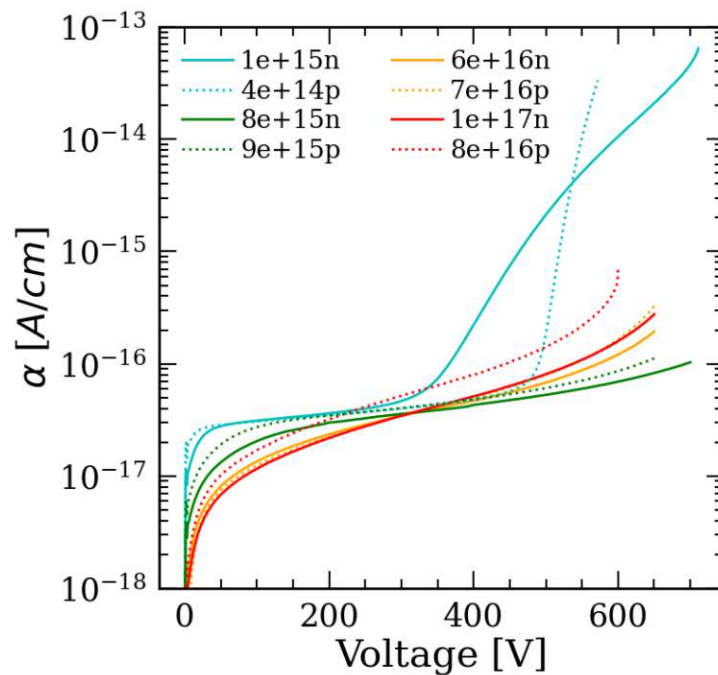
Fig. 9.16. α calculated from measurements as function of bias voltage assuming a fully depleted 50 µm thick sensor and scaling the α to 20 °C assuming $E_{\text{eff}} = 1.15\text{eV}$.

decrease in leakage current with temperature. This low E_{eff} could not be reproduced in simulations, which could indicate that the internal heating of the sensor may be responsible for the lower value. In addition, an exponential increase in E_{eff} as as function of bias voltage is observed for the measurements of the two highest fluence points, diverging from the standard scaling behaviour. Again this could be due to internal heating due to the additional current generated by difference in scaling of the impact ionization as a function of temperature. A decrease in E_{eff} with bias voltage is observed in all simulated fluences, similar to the observed decrease in the measurements for the tow lowest fluences. Overall the E_{eff} in the simulation is by 0.1 eV higher compared tot the measurement.

It was concluded that the linear scaling of the leakage current is not valid anymore for fluences above $8 \times 10^{15} \, n_{eq} \, \text{cm}^{-2}$. Firstly, as the sensors do not fully deplete anymore no simple scaling factor for different sensors geometries can be applied to compare them. Secondly, the dominance of impact ionization at these fluences does not allow one to define a meaningful reference voltage due to its field dependence.

Signal characteristics

In addition to the leakage current, another important aspect is the collected charge which (for a given threshold value) determines the efficiency of the sensor. A sufficiently high signal-to-noise ratio is also a prerequisite for achieving good time resolution. Another interesting parameter is the charge collection efficiency (CCE). It measures how much of the charge created by the interaction of a particle with the sensor is collected by the electrode.

10.1 Measurements

For this study, signals of the 50 µm thick sensors were measured for all neutron fluences and for the 100 µm thick sensors after a neutron fluence of 1×10^{15} n_{eq} cm^{-2} and 1×10^{17} n_{eq} cm^{-2}. To measure the signal before and after irradiation, the small diodes were wire-bonded to UCSC single channel readout boards [155]. The small diodes were used due to their lower capacitance which results in lower noise. The board has an integrated trans-impedance amplifier, which converts the induced current to a voltage signal with a gain of 470 Ω. Due to the small size of the guard ring electrode, it was only possible to wire-bond the pad electrode. The resulting change in depletion behaviour is not expected to have a significant impact on the signal. Another voltage amplifier[1] was added to the signal line to achieve an additional gain of 10. The amplified signals were readout by a Tektronix MSO64B oscilloscope. Initial laboratory tests using using a non-irradiated 50 µm thick diode biased at 40 V and a radioactive source mounted in a climate chamber showed noise peaks up to 11 mV. Setting the trigger threshold above this level would bias the measurement towards high charge deposits, only allowing for charge deposits in the tail of the Landau distribution to trigger the system. It was therefore decided to exclude the DUT (Device under Test) from the trigger. This can be done by placing sensors with a better signal to noise ratio and a similar size in front of and behind the DUT. If the trigger is set to the coincidence between these two, it can be assumed that the particle also went through the DUT. This was however not possible in the lab environment as the electrons emitted by the radioactive source would scatter drastically due to their low energy (2.2 MeV) on their way to the last sensor, reducing the rate of coincidences to near zero. It was therefore decided to measure the sensors in a test beam with high energy particles provided by the SPS accelerator at CERN.

For these measurements the sensors were mounted in the AIDA telescope [156] in the H6 beamline of the North Area at CERN. The telescope consists of six Mimosa detectors [157],

---

[1]Mini-Circuits ZX60-V63+

with three planes upstream and three planes downstream of the DUTs. This allows one to reconstruct the tracks of the particles crossing the telescope and to determine if a track went through a DUT. The beam used consisted of mostly 120 GeV/c protons. The trigger of the testbeam setup consists of a scintillator mounted in front of the telescope and a pixellated planar detector (FEI4)[158] mounted on a Mimosa plane behind the DUTs. The trigger signal is formed by a Trigger Logic Unit (TLU) out of the coincidence of the Region of Interest (ROI) of the FEI4 and the scintillator. The ROI is necessary as the FEI4 and scintillator are substantially larger than the DUTs and it allows to reduce the collected data by only triggering on tracks that went through the DUTs. To cool the sensors to -20 °C they were mounted in a Styrodur box with an internal cooler that was connected to a Glycol chiller. To prevent condensation of the samples the box was flushed with nitrogen. Each of the sensor boards is mounted on micro position stages which enable the alignment of the boards in x- and y-direction (see figure 10.2). Up to six sensors where measured at the same time and were read out by two oscilloscopes. The setup also included two LGAD sensors (also read out using the oscilloscopes) with similar size as the DUTs (1.3×1.3 mm to 1×1 mm). One LGAD was mounted before the first DUT to function as a time reference for the first three DUTs and one behind the last DUT as a reference for the last three. A sketch of the setup can be found in figure 10.1.
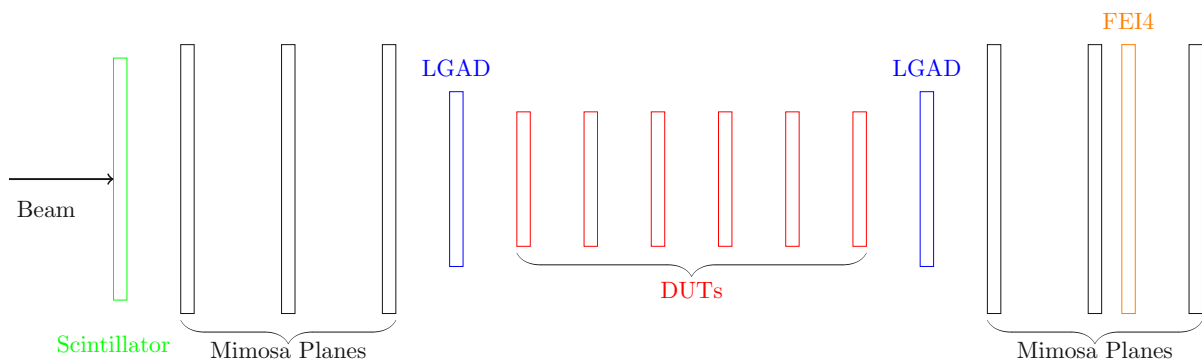
Fig. 10.1. Sketch of the Mimosa telescope with mounted DUTs.

The alignment of the sensors was done by triggering on the coincidence of the respective sensor and the FEI4. This allows one to see the imprint of the sensor in the pixelated matrix of the FEI4.

All sensors can then be aligned in relation to the FEI4 position. The accuracy is limited by the pixel size of the FEI4, which is 50 μm in x-direction and 250 μm in y-direction. The ROI

Fig. 10.2. Open cold box with with 5 DUTs and 2 LGADs mounted.

was then defined according to the imprint of the aligned sensors. An example of the imprint of a planar sensor on the FEI4 can be seen in figure 10.3.

The maximum bias voltage was initially chosen to be 10 V below the breakdown region of
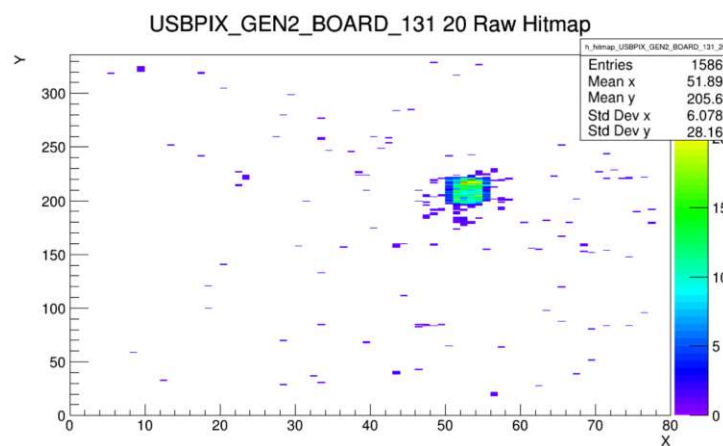
Fig. 10.3. Imprint of a planar diode on the FEI4 after triggering on the coincidence of the FEI4 and the sensors. x- and y-axis are switched. Axis units are pixels.

the sensor. For most sensors irradiated above $1 \times 10^{15} \, n_{eq} \, \mathrm{cm}^{-2}$ near constant noise were observed at this bias voltage, even when the beam was turned off. The maximal bias voltage was therefore reduced in these cases until the rate of spurious events was below one per minute. Two possible explanations for these spurious signals were considered: (1) a residual activity

from the irradiation and (2) the generation of thermal electron/hole pairs in regions of high field, allowing their amplification and creating an avalanche that is measured as a signal.

For each trigger signal sent by the TLU the oscilloscopes save the waveform data of each channel with a sampling rate of 25 GHz. As the beam is divided in spills of ~ 4 s with a period of typically about 30 s of no beam in-between the spills the waveform data of each event is first saved locally on the oscilloscope and then written out during the pause. For the highest bias voltages one million events were collected, whereas for the other bias points only 200 000 were collected. As no correlation between the reconstructed tracks and the oscilloscope data were found and as only 3/4 of the events contained a LGAD signal, a problem in the trigger and the telescope data stream was assumed. Therefore the reconstructed tracks were not included in the analysis.

While the LGAD signals are clearly distinguishable from the noise background due to their intrinsic gain, the DUT signals are much closer to the noise level. As a first step to understand and potentially reduce the noise contribution, the average waveform of all "noise events" (i. e. events with no visible LGAD signal) was calculated and subsequently converted to the frequency domain using a fast Fourier transform (FFT). For each oscilloscope channel, the noise frequency spectrum showed distinct peaks with the most prominent ones being shared around 3.1 and 4.9 GHz between the oscilloscopes. The peak at 4.9 GHz is suspected to originate from the WLAN switches installed in the setup, whereas the others are suspected to originate from the oscilloscope itself. The frequencies that are common in all channels of one oscilloscope were therefore filtered out to reduce the noise. Despite this filter the signal-to-noise ratio was nevertheless too low for a meaningful analysis of the time resolution and charge collection spectrum on an event-by-event basis (see figure 10.4).
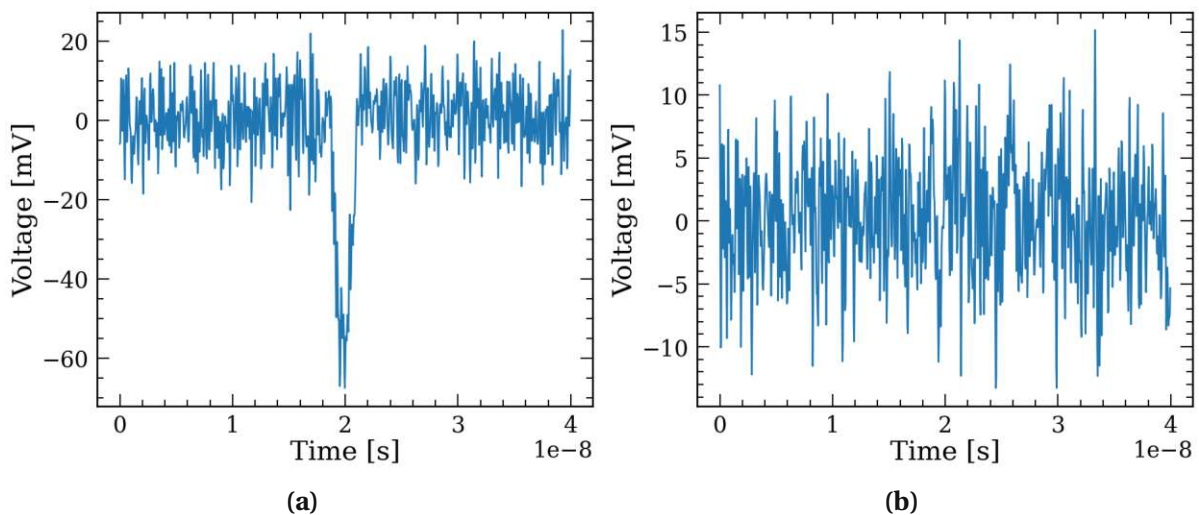
Fig. 10.4. Examples of a single waveform after applying a frequency filter for (**a**) an LGAD and (**b**) a planar diode.

To get an estimate of the sensor behaviour we then calculated the mean waveform of all data

samples which do have a signal in the corresponding LGAD. An example of the mean wave-form after the applied frequency filter can be found in figure 10.5.

(a) **(b)** **(c)**
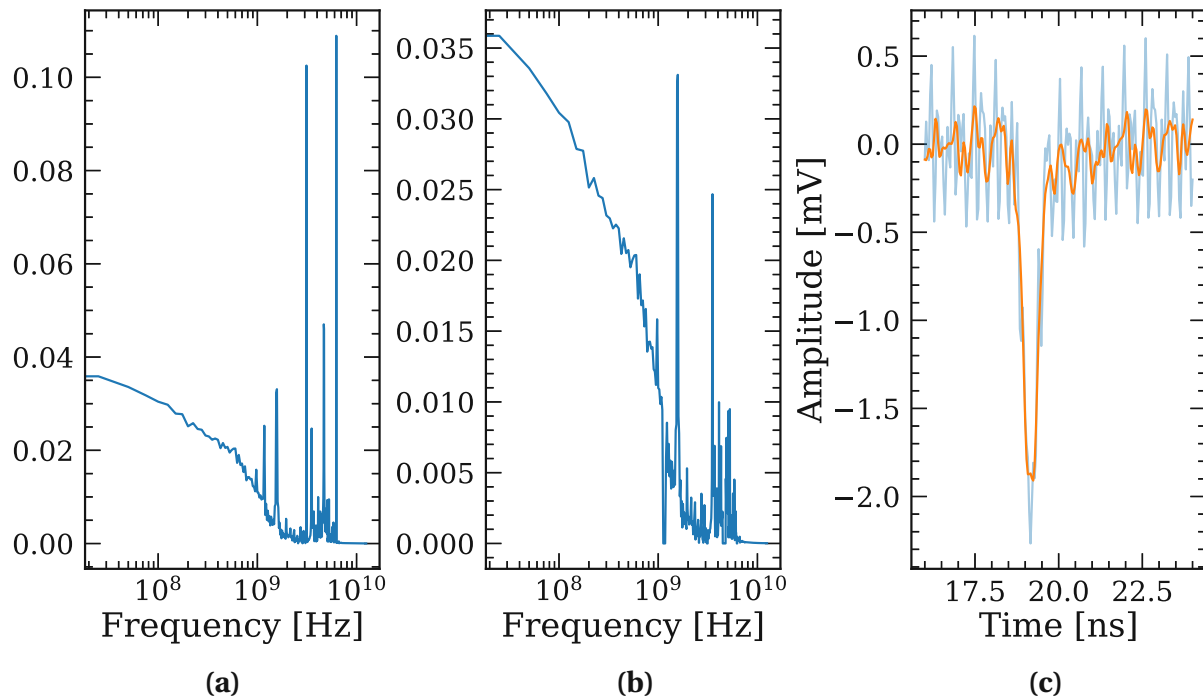
Fig. 10.5. a: Initial Fourier transformation of the mean signal of a 50 μm thick sensor irradiated to a fluence of $6 \times 10^{16}\, n_{eq}\,\mathrm{cm}^{-2}$. **b**: Fourier transformation of the mean signal after applying a frequency filter. **c**: Comparison of the mean signal before and after applying the filter.

The resulting mean waveforms for the highest bias voltage point for different fluences can be seen in figure 10.6a and 10.6b. For the 50 μm thick sensors, the amplitude increases for the two lowest fluences compared to the non-irradiated sample indicating charge multiplication. The result of the $1 \times 10^{15}\, n_{eq}\,\mathrm{cm}^{-2}$ irradiated sample is limited by the maximum voltage at 150 V and is expected to achieve higher gain at higher bias voltages. For the 100 μm thick sensors the signal before irradiation is around two times longer compared to the thinner sensors, as expected from the longer drift distance. For the $1 \times 10^{15}\, n_{eq}\,\mathrm{cm}^{-2}$ sample no change in amplitude is observed but the signal is shorter due to the trapping of the slower holes. For $1 \times 10^{17}\, n_{eq}\,\mathrm{cm}^{-2}$ the signal is substantially reduced in amplitude and signal width. The induced charged can be calculated by integrating over the signal. As some signals show an undershoot, which is suspected to originate from the transfer function of the first stage amplifier, the upper integration limit was set to the zero-crossing (start of the undershoot). The results for all different bias voltages can be found in figure 10.7a and 10.7b. All results are converted into e/h pairs. For the 100 μm non-irradiated sensor, one obtains using this method an average collected charge of 8000 e/h pairs which is between the expected most probable value of around 7400 and the mean restricted energy loss (assuming a cut-off energy of 0.2 MeV), calculated (using the Heed program interfaced to Garfield++[159]) to be
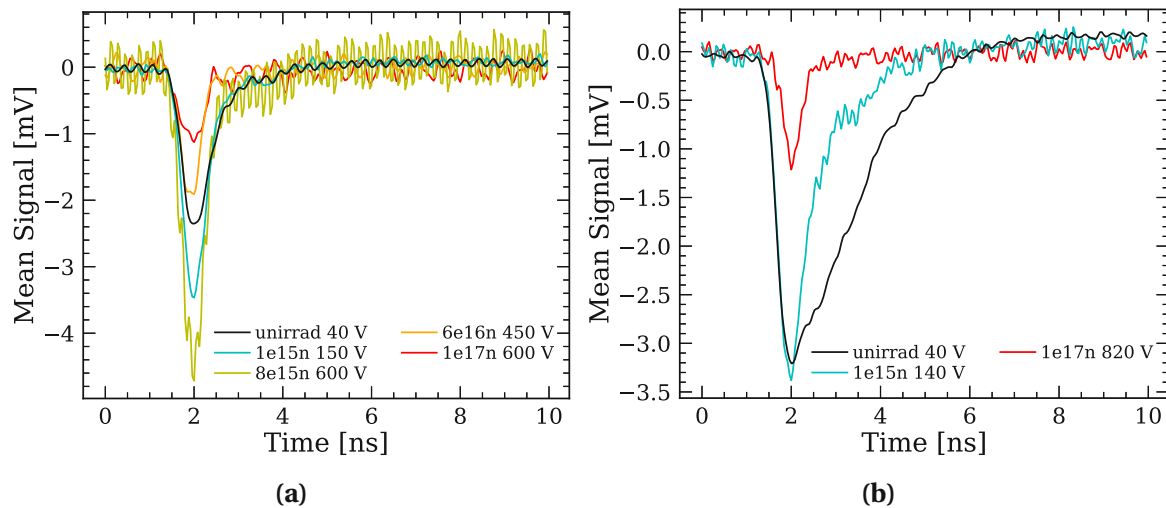
Fig. 10.6. a: Mean waveforms for the highest bias voltage point for different fluences for a 50 µm thick sensor. **b**: Mean waveforms for the highest bias voltage point for different fluences for a 100 µm thick sensor.

9344 electrons. For the 50 µm thick non-irradiated sensor the average collected charge calculated by integrating over the mean waveform is 3000 e/h pairs, which is below the expected MPV of 3300 e/h pairs and the mean restricted energy loss, 4672 e/h pairs. This could indicate a slightly lower gain than assumed in the calculation. In addition, due to the bigger size of the LGAD tracks that went through it may not traverse the DUT. This is especially the case when the sensors are not centred in the beam as was the case for the unirradiated measurements (see figure 10.8). It has to be therefore concluded that only a rough estimate can be concluded from the measurements, as the absolute values need to be confirmed with an additional measurement campaign. For 1×10^{15} n_{eq} cm^{-2} the 50 µm and 100 µm thick sensors show a slow increase of charge as a function of bias voltage. In the 100 µm thick sensor the change is substantially higher compared to the 50 µm thick sensor. It is therefore suspected that the sensor is not fully depleted in the measured range and the increase in the 50 µm thick one is due to the increase in field. At 8×10^{15} n_{eq} cm^{-2} the measured average collected charge for the 50 µm thick sensor shows a strong increase of charge with bias voltage over the whole measured range, which is consistent with charge multiplication. At the two highest fluences the 50 µm thick sensor exhibits a charge of only 1000 e/h pairs after a bias voltage of 400 V, with the sensor irradiated to 6×10^{16} n_{eq} cm^{-2} reaching a charge of 1600 e/h-pairs at 450 V. The sensor irradiated to 1×10^{17} n_{eq} cm^{-2} saturates after 500 V at 1200 e/h-pairs. The 100 µm thick sensor irradiated to 1×10^{17} n_{eq} cm^{-2} shows a similar behaviour as the 50 µm thick one: saturation is reached around the same voltage value and at roughly the same charge.
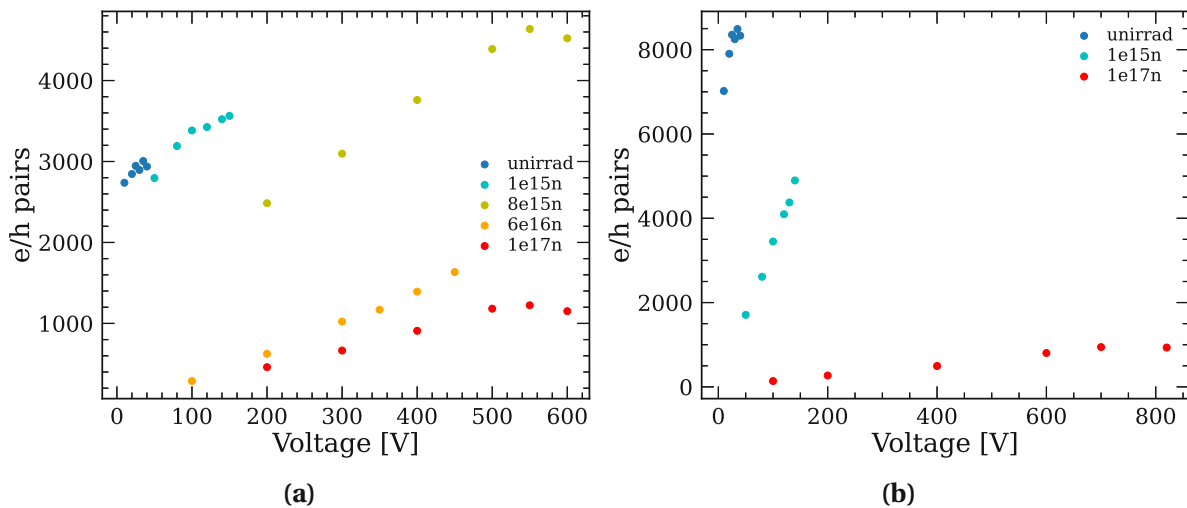
Fig. 10.7. Calculated charge as a function of bias voltage for different fluences for a (**a**) 50 µm thick sensor and a **b** 100 µm thick sensor.
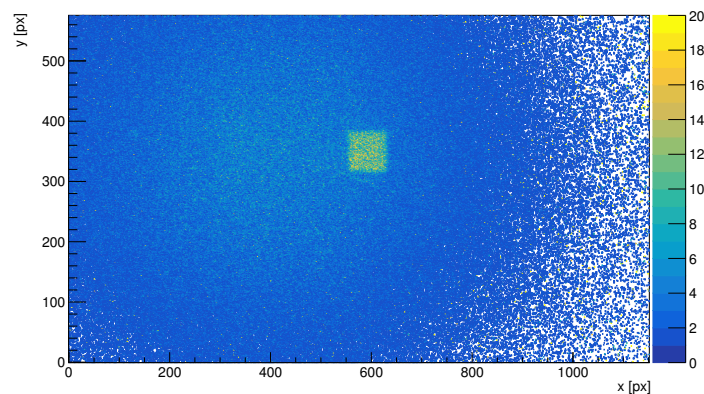
Fig. 10.8. Beam position compared to the position of the ROI used as a trigger for the measurement of the unirradiated samples as seen on a mimosa plane.

10.2 Simulation

The signal was simulated in TCAD by placing an initial distribution of 80 e/h-pairs per µm on a straight track in the middle of the sensor and performing a transient simulation. The lateral distribution of the deposited charge was chosen to be Gaussian with a standard deviation of 1 µm. The integral of the induced current on the pad electrode was then compared to the deposited charge to calculate the CCE. The resulting CCE of a 50, 100 and 200 µm thick sensor can be seen in figures 10.9a, 10.9b and 10.9c.

At the lowest fluence (1×10^{15} n_{eq} cm^{-2}), the 50 µm thick sensor shows a CCE of close to 100%. For the 100 µm thick sensor, the CCE saturates at 95% and for the 200 µm thick sensor the CCE saturates at 85% at this fluence. At 8×10^{15} n_{eq} cm^{-2} no saturation is seen any more for the 100 µm and 200 µm thick sensors and a maximum CCE of 80% and 45% is reached, respec-
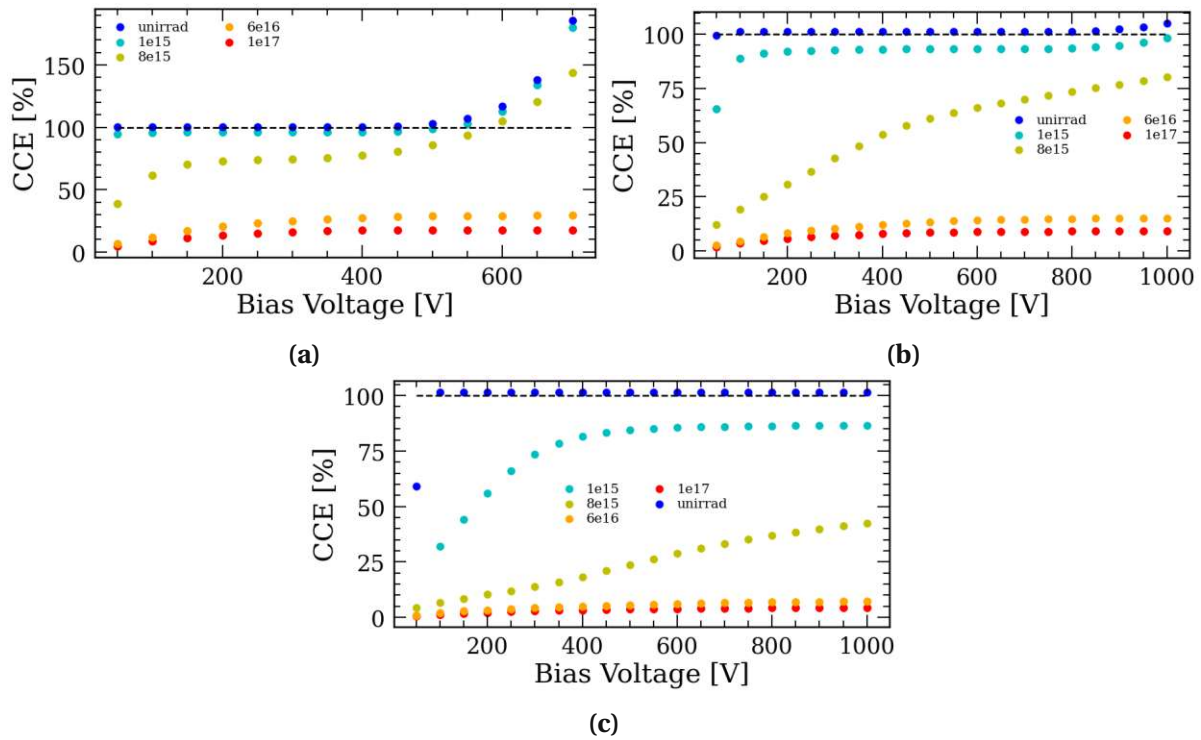
Fig. 10.9. Simulated CCE for a uniform deposited charge along the middle of the detector at different fluences for sensors with a thickness of 50 (**a**), 100 (**b**) and 200 (**c**) μm.

tively. The 50 μm sensor starts to saturate around 300 V at 70%. For both fluences the thinnest sensor exhibits gain after 550 V leading to a CCE at 700 V of around 180% for $1 \times 10^{15} \, n_{eq} \, \mathrm{cm}^{-2}$ and 143% for $8 \times 10^{15} \, n_{eq} \, \mathrm{cm}^{-2}$. For the 100 μm thick sensor an onset of gain in the simulated voltage range is observed only for the lowest fluence. For $6 \times 10^{16} \, n_{eq} \, \mathrm{cm}^{-2}$ the simulated CCE shows again a saturating behaviour at 30%, 15% and 7% for the 50 μm, 100 μm and 200 μm sensors, respectively. At $1 \times 10^{17} \, n_{eq} \, \mathrm{cm}^{-2}$ this is reduced further to 18%, 9% and 5%. This means that at the highest two fluences the collected charge is essentially the same for all thicknesses.

To explain this effect we consider the weighting field in the sensors. Due to the relatively big size of the pad compared to the thickness the weighting field is uniform along the sensor depth and is inversely proportional to the thickness. To calculate the depth dependence of the CCE, 80 e/h-pairs where deposited at certain depths in the 50 and 200 μm sensors for a fluence of $1 \times 10^{17} \, n_{eq} \, \mathrm{cm}^{-2}$. The CCE (normalized to 80 e/h-pairs) can be seen in figure 10.10. Due to the high fields close to the pad electrode (figure 9.11b) and the close collection distance a CCE of up to 25% could be reached in the first 10 μm of the sensor for the 50 μm thick sensor, whereas due to the lower field only a maximum of 6% is reached for the 200 μm thick sensor. After this region a near constant CCE is observed until a drop to 0% close to the backside electrode. This originates from the fact that the weighting field is uniform along the thickness and the current induced by a moving charge is therefore independent of position. As the velocity is close to saturation at the simulated bias voltages this leads to approximately
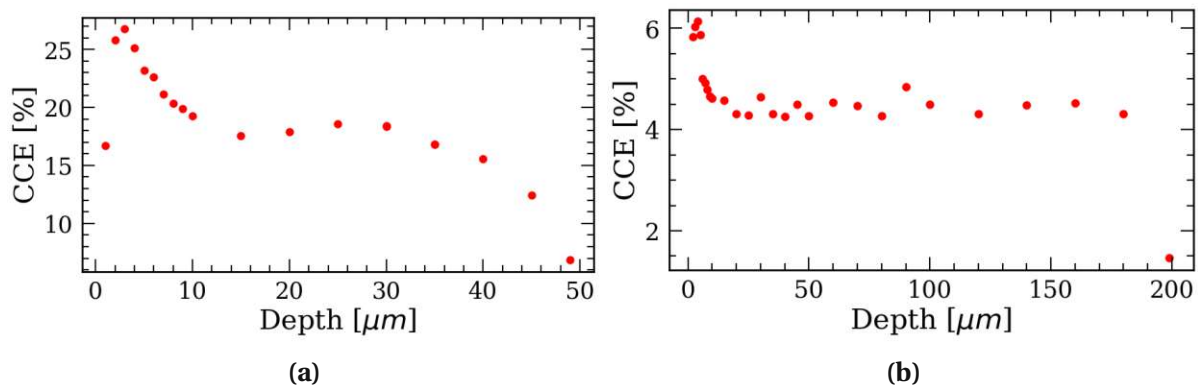
Fig. 10.10. Simulated CCE of 80 e/h-pairs placed at different depths in (**a**) 50 and (**b**) 200 µm thick sensor irritated to a fluence of $1 \times 10^{17}\ n_{eq}\,\mathrm{cm}^{-2}$. The pad electrode is located at a depth of 0.

the same distance a charge can travel until it is trapped. Due to the lower weighting field in the 200 µm thick sensor this results still in a smaller induced current compared to the thinner sensor. As impact ionization happens only close to the pad electrode an estimate of the mean free path can be made by determining the point where impact ionization becomes visible in the CCE. For both sensors the trapping distance can be estimated by measuring the depth of the gain region close to the readout electrode. This is done by measuring the distance between the peak of the gain peak and the point where it return to the baseline. A trapping distance of around 10 µm can be estimated for both thicknesses.

To compare the simulation with the measurements the CCE calculated by the simulation was scaled with the expected MPV. This should lead to overall lower charge than the measurements. The results can be seen in figure 10.11a and 10.11b. For the lowest fluence of the 50 µm thick sensors the saturation behaviour at low bias voltages of the simulation was not observed in the measurements, as in both the charge is constantly increasing with voltage. For the two highest fluences the simulation shows similar behaviour at low voltages, but the measurements show a higher charge at high bias voltages. The point of divergence is similar to where the measured leakage current diverges from the simulations. This could again indicate that the simulation underestimates the impact ionization inside the sensor. For the 100 µm thick sensors at the lowest fluence the measurement show still a depleting behaviour in the measured range while the simulation shows already saturation. This is suspected to be due to the remains of the p-spray. At the highest fluence the collected charge is lower at low bias voltages, but again reaches higher collected charge at high bias voltages. If the simulation is scaled to have the same charge as the first two measured point the point of diverging in gain is similar to the leakage current.
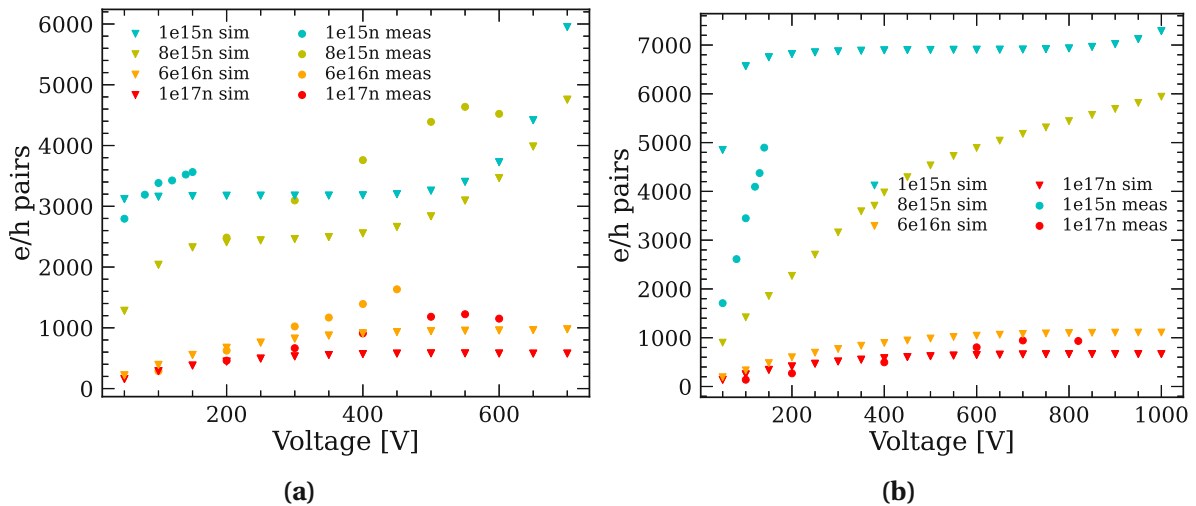
Fig. 10.11. Simulated signal charge assuming a deposited charge of 3300 (50 μm) and 7400 (100 μm) e/h-pairs compared to the measured mean signal for (**a**) 50 and (**b**) 100 μm thick irradiated sensor.

10.3 Summary

For the two lowest fluences the simulation predicts for the 50 μm thick sensor a constant charge until 500 V above which impact ionization leads to higher charge compared to an un-irradiated sensor. In the stable region the charge for the samples irradiated to $1\times10^{15}\,n_{eq}\,cm^{-2}$ close to the charge of the non-irradiated sensor, whereas for $8\times10^{15}\,n_{eq}\,cm^{-2}$ the charge is reduced to 70%. For the measured charge no stable region but a steady increase with bias voltage was observed. For the two highest fluences the simulation predicts a saturation after 200 V at 30% for $6\times10^{16}\,n_{eq}\,cm^{-2}$ and 18% for $1\times10^{17}\,n_{eq}\,cm^{-2}$. For the measured charge only for the highest fluences a saturation is observed, but at a higher voltage.

For the 100μm thick sensor a similar behaviour as the for the 50 μm thick sensor is observed, albeit with a lower saturation level (90%). For $8\times10^{15}\,n_{eq}\,cm^{-2}$ no saturation is observed, but the steepness of the increase in charge as function of voltages decreases after 500 V, reaching a maximal charge of 80% at the highest bias point. At the highest fluences the same behaviour as for the 50 μm thick sensor is seen.

With increasing fluence the collected charge becomes independent of sensor thickness, as the drift distance becomes significantly smaller than the sensor thickness. Due to the thickness dependent weighting field this leads to the same induced charge for all thicknesses. In a pixellated sensor this could reduce the effective area responsible for charge collection to several micrometer below the collection electrode.

Conclusion and Outlook

Planar silicon sensors are one of the candidate technologies considered for the Upgrade II of the LHCb Vertex Locator. The requirements are highly dependent on the layout of the detector, in particular on the distance of the sensors from the beam line.If the distance is kept the same as in Upgrade I (5.1 mm), the fluence in the sensors reaches up to $5 \times 10^{16}\ n_{eq}\,\mathrm{cm}^{-2}$. The simulations and measurements presented in this work indicate that the collected charge in a pad sensor at this fluence is of order 1000 e/h pairs and is independent of the sensor thickness (assuming a pad like weighting field). In a pixellated structure, the weighting field will be more concentrated around the readout electrode and the collected charge will therefore be reduced even more. Considering that in the Upgrade I VELO the ASICs are operated at a threshold of 1000 electrons, a significant reduction in the noise level would be required to achieve the required efficiency and it would be even more challenging to achieve the required time resolution. In addition, the fluence induced trapping and the concentrated weighting field will lead to a decrease in charge sharing between pixels, which in turn reduces the spatial resolution to the binary resolution. This makes a reduction in pixel size to around 43 µm necessary. Due to all the afore mentioned reasons the use of planar silicon sensors is not recommended for a Upgrade I layout detector.

The requirements in terms of radiation hardness and rate capability can be relaxed by increasing the distance of the sensors from the beamline. In order to maintain the same acceptance and performance (i. e. the same impact parameter resolution), the geometric layout of the detector needs to be re-optimised, the material budget needs to be reduced and the single-hit resolution needs to be improved. As shown in Section 4.2, a cylindrical RF foil is a better choice for these scenarios than a corrugated foil. To minimize the length of the detector the shape of of the sensor cut-out around the beam line plays a critical part. An octagonal shape would lead to the smallest detectors and the lowest needed change in detector parameters, whereas a hexagonal sensors would make the tiling with a single type of sensor tile possible. Using the simulation tool developed as part of this thesis work, different configurations were studied. For a distance of 11.1mm of the sensors from the beam line ("scenario B"), the same radiation damage as in the Upgrade I can achieved. To achieve the same performance as in Upgrade I the single-hit resolution has to be improved to 9 µm. The thickness of the RF-foil depends on its position, the sensor shape and the combined sensor and ASIC thickness and has to be reduced to 20 µm in most cases. For the foil two positions were considered. The current distance from the beam (3.5 mm) and an increased distance (8.6 mm), which allows the fabrication of the foil out of a single piece. The ASIC and sensor thickness must be be reduced to 100 µm in all cases, except for an octagonal sensor with a 20 µm thick

foil at 3.5 mm, where the thickness can stay the same as Upgrade I. If for this configuration the sensor and ASICs are reduced to 100 µm the foil thickness can be increased to 100 µm.

The simulations show that for a 100 µm thick sensor under scenario B conditions a collected charge of up to 6000 e/h-pairs can be expected, which is sufficient to distinguish signals from the noise, whereas for a 50 µm thick sensor a maximum of around 4000 e/h-pairs at high bias voltages can be achieved. As this operating region is close to the breakdown point and the collected charge being highly dependent on the received fluence, an extensive research campaign has to be implemented for the final sensors, to be able to adjust the biasing during operation correctly. To achieve the necessary timing resolution the 50 µm thick sensor would be preferable, but due to the afore mentioned restrictions, a 100 µm thick sensors is recommended, if further studies indicates that they can reach the required time resolution.

As the increased size of a scenario B would extend the detector far into RICH1, which can only be implemented with a redesign of the RICH detector, this scenario should be only considered if $8 \times 10^{15}\ n_{eq}\,\mathrm{cm}^{-2}$ is found to be the limit for the time resolution after irradiation or a reduction of the maximal η acceptance to around 4.3 is implemented. The most limiting factor for sensors in scenario B will be the reduction in pixel size. Assuming the same charge sharing as indicated by upgrade I studies the final pixel size should be located between 40 µm and 31 µm (binary resolution). As the Upgrade I studies where done with 200 µm thick sensors, as the sensor thickness is decreased charge sharing will be reduced and therefore reduces the upper limit of the pixel size.

If the foil is placed at 8.6 mm and the sensors are placed as close as possible to the foil (9.5 mm), called scenario C, the length of detector can be reduced by around 20 cm. This would allow for a single-hit resolution of 10 µm and a slight increase in fluence to $1 \times 10^{16}\ n_{eq}\,\mathrm{cm}^{-2}$. This would correspond to a pixel size of 44 µm. The current sensor and ASIC thickness can be kept, while the foil thickness needs to be reduced to 20 µm. If both, the ASIC and sensor thickness can be reduced to 100 µm the foil thickness can be increased for a foil at 8.6 mm to 40 µm and to 220 µm when the foil is placed at 3.5 mm. As the fluence would only increase by around 50% compared to scenario B, the detector performance is not expected to be drastically reduced compared to scenario B and therefore planar detectors are suspected to still be a valid solution for scenario C.

For the use of silicon hybrid planar sensors for fluences in the order of $1 \times 10^{16}\ n_{eq}\,\mathrm{cm}^{-2}$ and higher it has to be considered that the fluence scaling with irradiation is not applicable anymore, due the importance of impact ionization and therefore the electrical field inside the sensor. In addition, the temperature scaling behaviour for these fluences diverge from the relation used for un-irradiated sensors or lower fluences due to the difference in the temperature dependence of the current generated by impact ionization compared to the thermal generated current.

Appendix

11.1 Module Position

Module z-position [cm]
-4.91, -2.35, 0.21, 2.77, 5.33, 7.89, 10.45, 13.013, 15.57, 18.13, 20.69, 23.84, 31.24, 33.48, 35.96, 48.77, 56.63, 73.45, 87.97, 95.65, 98.15, 100.65, 103.15

Table 11.1. Layout for Scenario B with hexagonal aperture.

Module z-position [cm]
-4.90, -2.35, 0.21, 2.77, 5.33, 7.89, 10.45, 13.01, 15.57, 18.13, 20.69, 23.54, 29.90, 32.01, 34.33, 46.34, 58.95, 69.42, 82.85, 90.22, 92.72, 95.22, 97.72

Table 11.2. Layout for Scenario B with octagonal aperture.

Module z-position [cm]
-5.49, -2.93, -0.37, 2.19, 4.75, 7.31, 9.87, 12.43, 14.99, 17.55, 20.11, 23.16, 26.69, 28.61, 30.72, 41.67, 53.16, 68.95, 90.34, 92.84, 95.34, 97.84

Table 11.3. Layout for Scenario C with hexagonal aperture.

Module z-position [cm]
-5.49, -2.93, -0.37, 2.19, 4.75, 7.31, 9.87, 12.43, 14.99, 17.55, 20.11, 22.91, 25.55, 27.35, 29.33, 39.59, 50.36, 65.17, 69.01, 85.24, 87.74, 90.24, 92.74

Table 11.4. Layout for Scenario C with octagonal aperture.

11.2 SIMS Fits
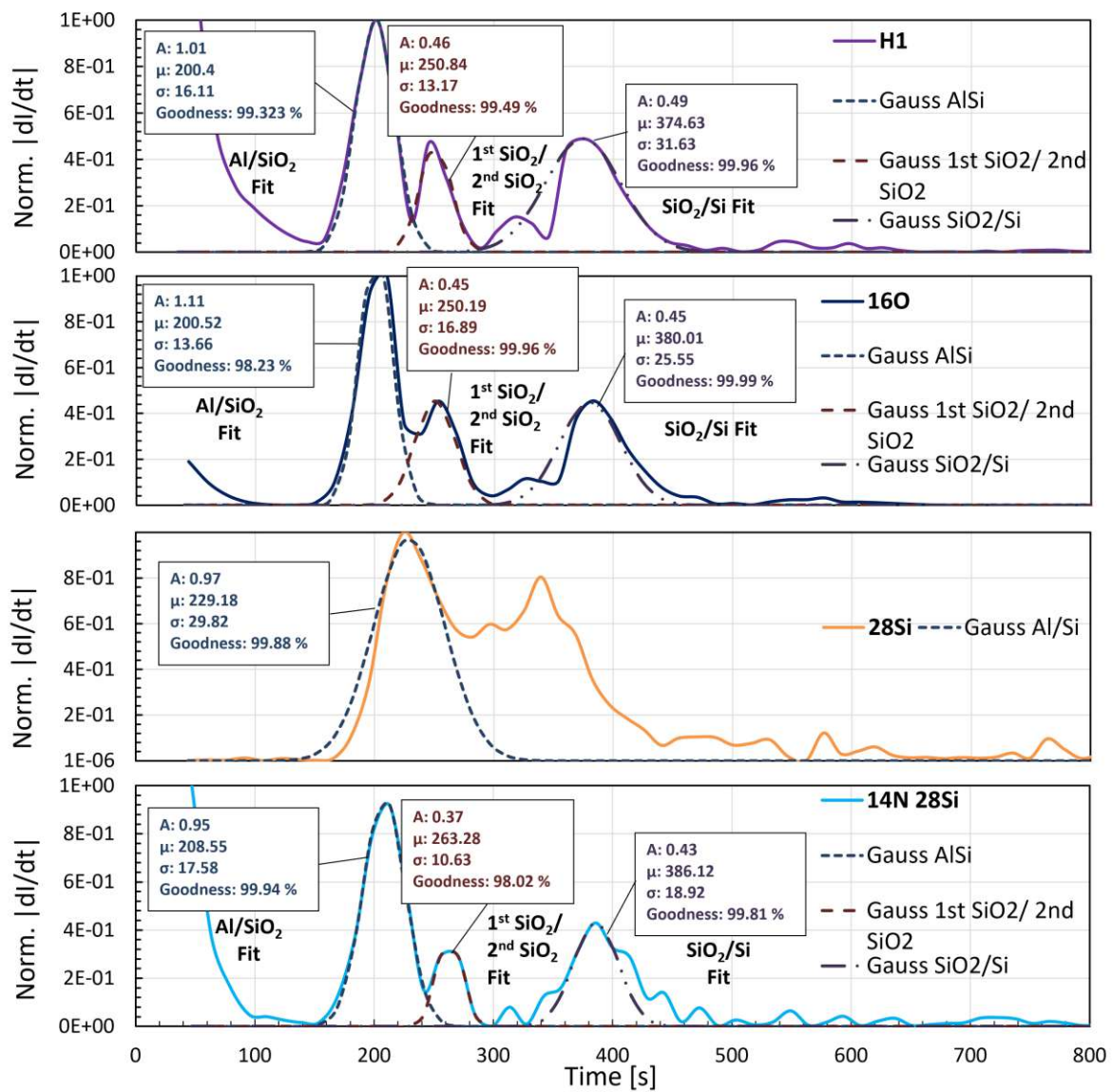
Fig. 11.1. First derivation of intensities of the count rate for different elements normalized to the highest value for the first measurement of the n^+ area. Transition points are fitted with gaussian curves. The fit parameters are displayed next to the fit.
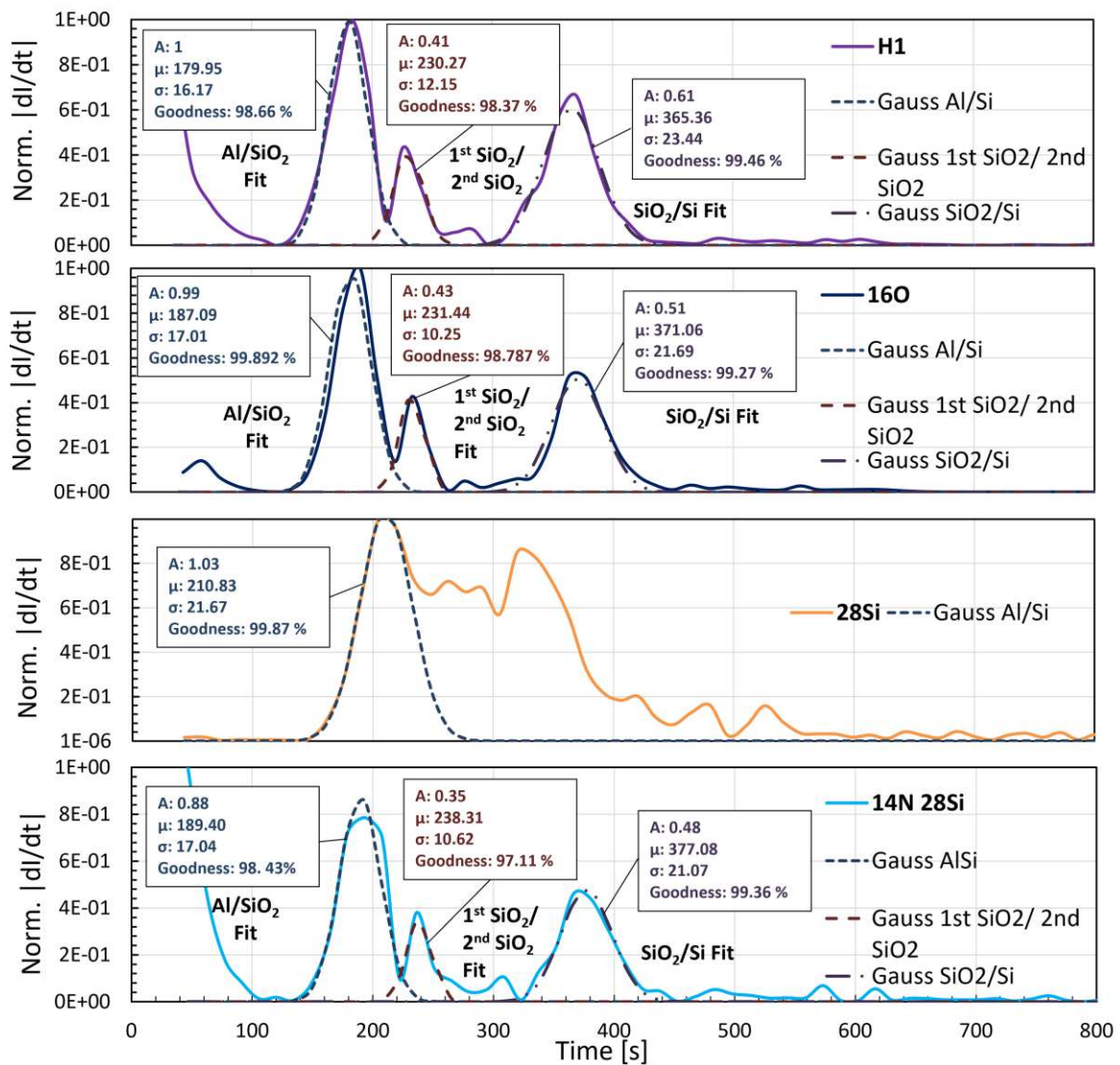
Fig. 11.2. First derivation of intensities of the count rate for different elements normalized to the highest value for the second measurement of the n^+ area. Transition points are fitted with gaussian curves. The fit parameters are displayed next to the fit.
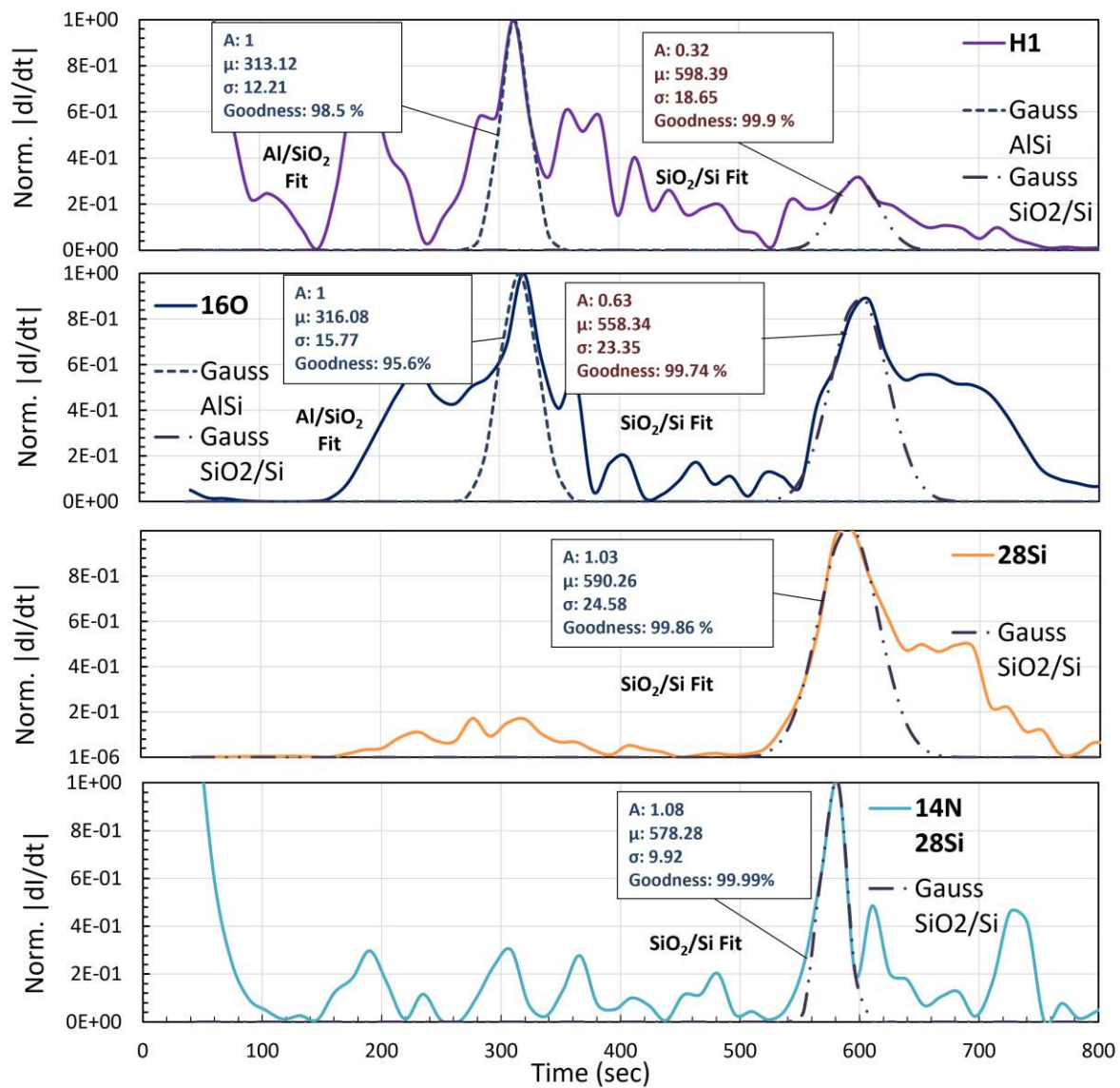
Fig. 11.3. First derivation of intensities of the count rate for different elements normalized to the highest value for the measurement of the p-spray area. Transition points are fitted with gaussian curves. The fit parameters are displayed next to the fit.
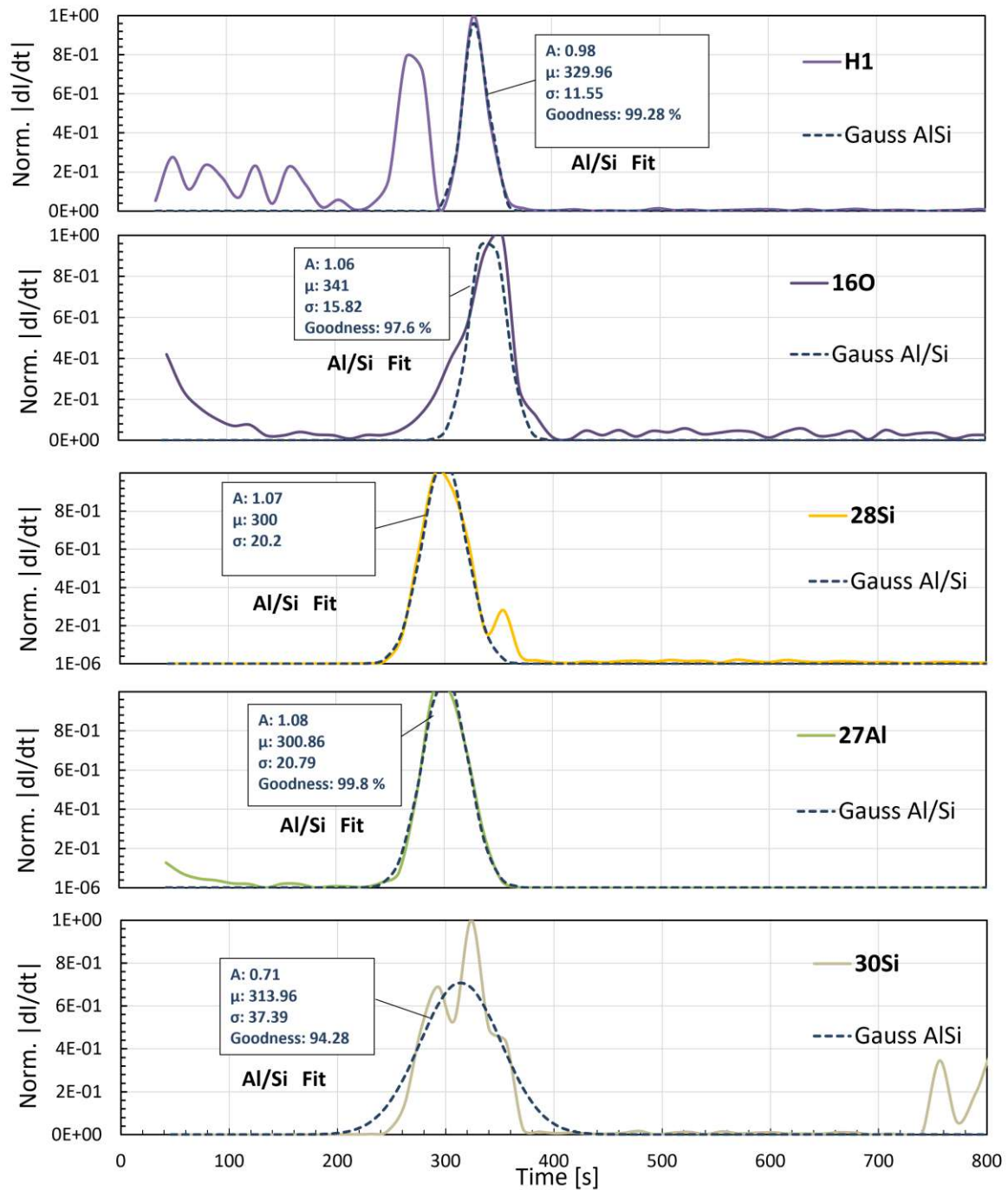
Fig. 11.4. First derivation of intensities of the count rate for different elements normalized to the highest value for the measurement of the p^{++} on the back side. Transition points are fitted with gaussian curves. The fit parameters are displayed next to the fit. Fits used to determine the layer transition points of the first measurement.

11.3 IV Measurements
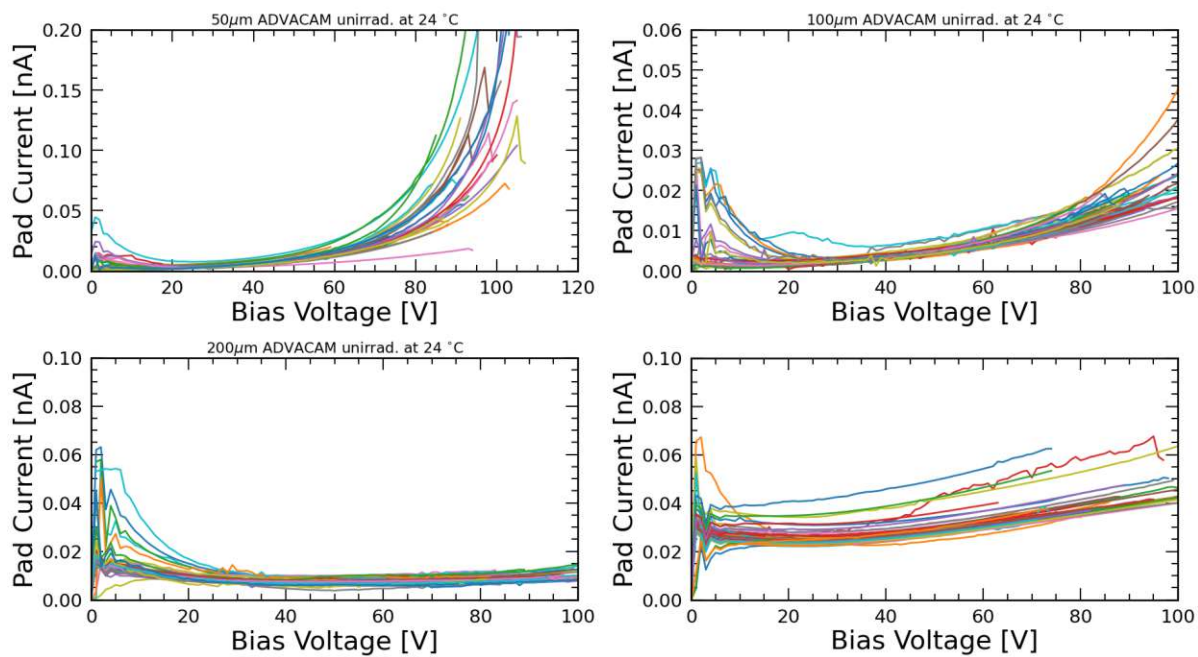
Fig. 11.5. Pre-irradiation IV measurements for the small diodes at room temperature
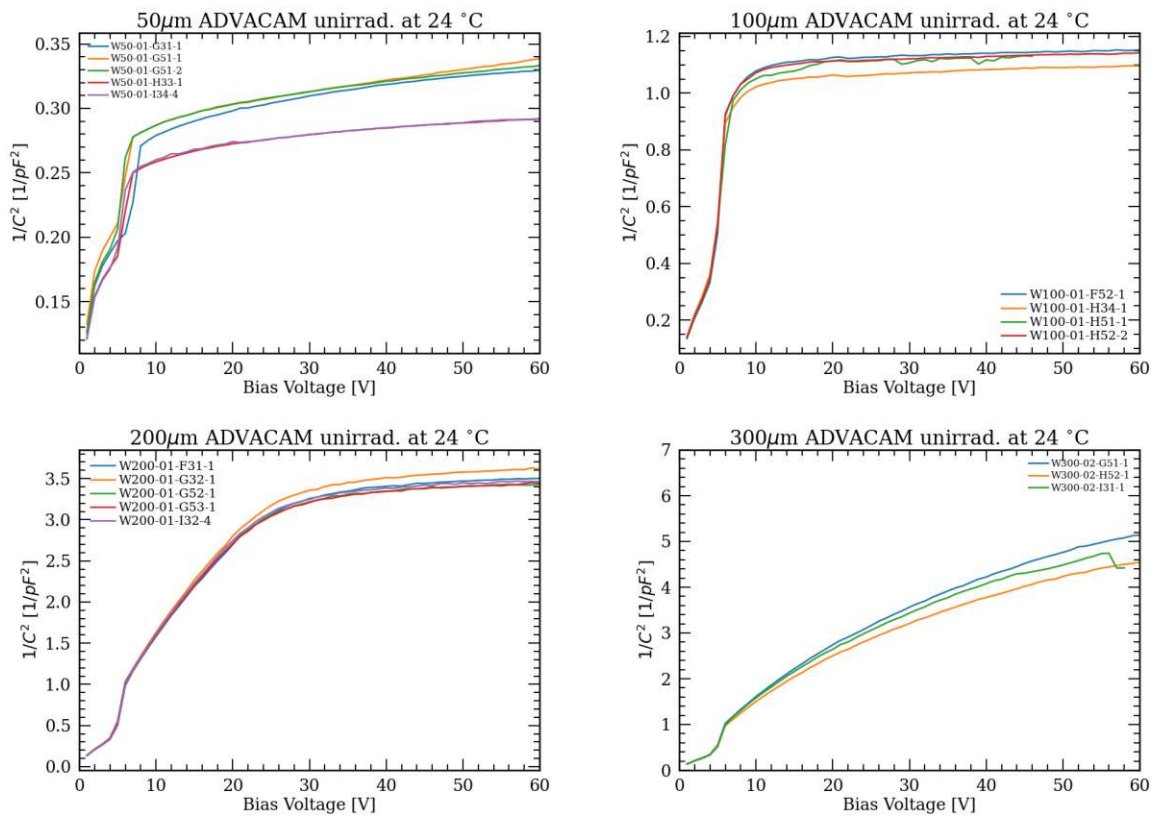
Fig. 11.6. CV measurements done on small diodes of different thicknesses

11.4 TCAD

```
File {
    Grid     = "/eos/home−j/jhaimber/TimingStudy/Meshes/2D/FinalMesh/IV_noPS_50_msh.tdr"
    Parameter= "sdevice.par"
    Plot=    "tdr/@tdrdat@"
    Current="plt/@plot@"
    Output= "log/@log@"
}
Electrode {
    {Name="pix1_electrode"   Voltage=0.0 Material = "Aluminum" Areafactor = 1}
    {Name="bot_electrode"    Voltage=0.0 Material = "Aluminum" Areafactor = 1}
}
Physics{
    Areafactor = 225 #scaling factor for current and charge
    Temperature = @Temperatur@
    Fermi #activate Fermi Statistic
    EffectiveIntrinsicDensity (BandGapNarrowining(Slotboom))
    Mobility (
        eHighFieldSaturation
        hHighFieldSaturation
        PhuMob( Phosphorus Klaassen )
    )
    Recombination (
        SRH (DopingDependence
            TempDependence
            ElectricField (Lifetime=Hurkx DensityCorrection = None)
            )
        eAvalanche (vanOverstraeten Eparallel)
        hAvalanche (vanOverstraeten Eparallel)
    )

}
Plot {
```

```
*---Density and Currents, etc
    eDensity hDensity
    IntrinsicDensity      EffectiveIntrinsicDensity
    TotalCurrent eCurrent hCurrent
    eMobility hMobility
    eVelocity hVelocity
    eSaturationVelocity hSaturationVelocity
    eDriftVelocity hDriftVelocity
    *eQuasiFermi hQuasiFermi
*---Fields and charges
    ElectricField/Vector Potential SpaceCharge
*---Doping Profiles
    Doping DonorConcentration AcceptorConcentration
*---Generation/Recombination
    SRH Band2Band * Auger
    SRHRecombination
    AvalancheGeneration eAvalancheGeneration hAvalancheGeneration
    eAlphaAvalanche hAlphaAvalanche
    * SurfaceRecombination
    TotalRecombination
*--- Lifetme
    *eLifetime hLifetime
*---Driving forces
    *eGradQuasiFermi hGradQuasiFermi
    *eEparallel hEparallel eENormal hENormal
*---Band structure/Composition
    *BandGap EffectiveBandGap
    *BandGapNarrowing
    *Affinity
    *ConductionBand ValenceBand
    *eQuasiFermiEnergy hQuasiFermiEnergy
*---Gate Tunneling
    * eBarrierTunneling hBarrierTunneling   BarrierTunneling
    * eDirectTunnel hDirectTunnel
*---Traps
    *TotalTrapConcentration
    *eTrappedCharge hTrappedCharge
    *eGapStatesRecombination hGapStatesRecombination
    * eInterfaceTrappedCharge hInterfaceTrappedCharge
}
Physics(MaterialInterface="Oxide/Silicon") {
                Charge(Conc = 1e12 )
}
Physics (material = "Silicon"){
        Traps(
                (Donor Level
                fromCondBand
                Conc = @<0.0497*Fluence>@
                EnergyMid = 0.1
                eXsection = 2.3e-14
                hXsection = 2.92e-16)

                (Acceptor Level
                fromCondBand
                Conc = @<0.6447*Fluence>@
                EnergyMid = 0.458
                eXsection = 2.551e-14
                hXsection = 1.511e-13)

                (Acceptor Level
                fromCondBand
                Conc = @<0.4335*Fluence>@
                EnergyMid = 0.545
                eXsection = 4.478e-15
                hXsection = 6.709e-15
                Tunneling(Hurkx))

                (Donor Level
                fromValBand
                Conc = @<0.5978*Fluence>@
                EnergyMid = 0.48
                eXsection = 4.116e-15
                hXsection = 1.965e-16)

                (Donor Level
                fromValBand
                Conc = @<0.378*Fluence>@
                EnergyMid = 0.36
                eXsection = 3.23e-17
```

```
                        hXsection = 2.036e−14)
            )
}
Math {
        Method = Blocked
        SubMethod = Pardiso
        Number_of_Threads = 16
        Cylindrical( yAxis= 0 )
        #Derivatives #sometimes helps convergence
        #AvalDerivatives #sometimes helps convergence
        RelErrControl #standard error control
        Digits=5 #
        #ErrRef(electron)=1.0e3
        #ErrRef(hole)=1.0e3
        Extrapolate # Extrapolate in quasi stationary
        Iterations=30
        #Notdamped=50 # Mat rosen daming activated after this amout of iterations
        #ExitOnFailure
        #MetalConductivity

}
Solve {
    * 1) initial solution
    Coupled (iterations=600) { Poisson }
    Coupled { Poisson Electron Hole }
    *
    QuasiStationary( InitialStep=1e−4
                     Maxstep=0.001
                     MinStep=1e−6
                     Increment=1.4
                     Decrement=2
                     Goal{name="bot_electrode" voltage = −700}
                     Plot { Range = (0 1) Intervals=20}

                )
         {

            Coupled {Poisson Electron Hole}

         }
}
```

Listing 11.1: Example of a quasi-stationary simulation of a irradiated diode.

```
File {
        Grid     = "/eos/home−j/jhaimber/TimingStudy/Meshes/2D/FinalMesh/IV_noPS_50_MIP_msh.tdr"
        Parameter= "sdevice.par"
        Plot=    "tdr/@tdrdat@"
        Current="plt/@plot@"
        Output= "log/@log@"
}
Electrode {
        {Name="pix1_electrode"  Voltage=0.0 Material = "Aluminum" Areafactor = 1}
        {Name="bot_electrode"   Voltage=0.0 Material = "Aluminum" Areafactor = 1}
}
Physics{
    Areafactor = 225 #scaling factor for current and charge
    Temperature = @Temperatur@
    Fermi #activate Fermi Statistic
    EffectiveIntrinsicDensity (BandGapNarrowining(Slotboom))
    Mobility (
        eHighFieldSaturation
        hHighFieldSaturation
        PhuMob( Phosphorus Klaassen )
    )
    Recombination (
        SRH (DopingDependence
             TempDependence
             ElectricField (Lifetime=Hurkx DensityCorrection = None)
             )
      eAvalanche (vanOverstraeten Eparallel)
      hAvalanche (vanOverstraeten Eparallel)
    )
   HeavyIon (
                Direction=(200.000000,0.000000)
                Location=(0,50.000000)
                Time=0.02e−9
                Length = 200.000000
```

```
                    wt_hi = 1.0
                    LET_f = 1.282E-5
                    Picocoulomb )
}
Plot {
*----Density and Currents, etc
    eDensity hDensity
    IntrinsicDensity      EffectiveIntrinsicDensity
    TotalCurrent eCurrent hCurrent
    eMobility hMobility
    eVelocity hVelocity
    eSaturationVelocity hSaturationVelocity
    eDriftVelocity hDriftVelocity
    *eQuasiFermi hQuasiFermi
*----Fields and charges
    ElectricField/Vector Potential SpaceCharge
*----Doping Profiles
    Doping DonorConcentration AcceptorConcentration
*----Generation/Recombination
    *SRH Band2Band * Auger
    AvalancheGeneration eAvalancheGeneration hAvalancheGeneration
    eAlphaAvalanche hAlphaAvalanche
    * SurfaceRecombination
*--- Lifetme
    *eLifetime hLifetime
*----Driving forces
    *eGradQuasiFermi hGradQuasiFermi
    *eEparallel hEparallel eENormal hENormal
*----Band structure/Composition
    *BandGap EffectiveBandGap
    *BandGapNarrowing
    *Affinity
    *ConductionBand ValenceBand
    *eQuasiFermiEnergy hQuasiFermiEnergy
*----Gate Tunneling
    * eBarrierTunneling hBarrierTunneling  BarrierTunneling
    * eDirectTunnel hDirectTunnel
*----Traps
    *TotalTrapConcentration
    *eTrappedCharge hTrappedCharge
    *eGapStatesRecombination hGapStatesRecombination
    * eInterfaceTrappedCharge hInterfaceTrappedCharge
}
Physics(MaterialInterface="Oxide/Silicon") {
                    Charge(Conc = 1e12 )
}
Physics (material = "Silicon"){
        Traps(
                (Donor Level
                fromCondBand
                Conc = @<0.0497*Fluence>@
                EnergyMid = 0.1
                eXsection = 2.3e-14
                hXsection = 2.92e-16)

                (Acceptor Level
                fromCondBand
                Conc = @<0.6447*Fluence>@
                EnergyMid = 0.458
                eXsection = 2.551e-14
                hXsection = 1.511e-13)

                (Acceptor Level
                fromCondBand
                Conc = @<0.4335*Fluence>@
                EnergyMid = 0.545
                eXsection = 4.478e-15
                hXsection = 6.709e-15
                Tunneling(Hurkx))

                (Donor Level
                fromValBand
                Conc = @<0.5978*Fluence>@
                EnergyMid = 0.48
                eXsection = 4.116e-15
                hXsection = 1.965e-16)

                (Donor Level
                fromValBand
```

```
                    Conc = @<0.378*Fluence>@
                    EnergyMid = 0.36
                    eXsection = 3.23e−17
                    hXsection = 2.036e−14)
        )
}
Math {
        Method = Blocked
        SubMethod = Pardiso
        Number_of_Threads = 16
        #Cylindrical( yAxis= 0 )
        #Derivatives #sometimes helps convergence
        #AvalDerivatives #sometimes helps convergence
        RelErrControl #standard error control
        Digits=5 #
        #ErrRef(electron)=1.0e3
        #ErrRef(hole)=1.0e3
        Extrapolate # Extrapolate in quasi stationary
        Iterations=30
        #Notdamped=50 # Mat rosen daming activated after this amout of iterations
        #ExitOnFailure
        #MetalConductivity
}
Solve {
    Load (FilePrefix="@Temperatur@_@Fluence@_@Voltage@")
    Transient(
                InitialTime = 0.0
                FinalTime= 1E−11
                InitialStep=0.5E−14
                MaxStep=1E−11
        ){
                Coupled (iterations=8, notdamped=15) { Poisson Electron Hole }
        }
    Load (FilePrefix="@Temperatur@_@Fluence@_@Voltage@")
    Transient(
                InitialTime = 1E−11
                FinalTime= 5E−11
                InitialStep=0.5E−14
                MaxStep=5E−13
        ){
                Coupled (iterations=8, notdamped=15) { Poisson Electron Hole }
        }
    Transient(
                InitialTime = 5E−11
                FinalTime= 3E−9
                InitialStep=5E−13
                MaxStep=1E−10
        ){
                Coupled (iterations=8, notdamped=15) { Poisson Electron Hole }
        }
}
```

Listing 11.2: Example of a transient simulation of a irradiated sample after loading a pre-simulated quasi-stationary file.

List of Figures

184

186

List of Tables

Bibliography

[1] Particle Data Group. "Review of Particle Physics". In: *Progress of Theoretical and Experimental Physics* 2022.8 (Aug. 2022). 083C01. ISSN: 2050-3911. DOI: `10.1093/ptep/ptac097`. eprint: `https://academic.oup.com/ptep/article-pdf/2022/8/083C01/45434185/ptac097\_19\_miscellaneous\_searches\_and\_searches\_in\_other\_sections.pdf`. URL: `https://doi.org/10.1093/ptep/ptac097`.

[2] Paul Langacker. *The standard model and beyond; 1st ed.* Series in high energy physics, cosmology, and gravitation. Boca Raton, FL: Taylor and Francis, 2010. URL: `https://cds.cern.ch/record/1226768`.

[3] Wikimedia Commons. *Standard Model of Elementary Particles.* 2022. URL: `https://en.wikipedia.org/wiki/File:Standard_Model_of_Elementary_Particles.svg`.

[4] Antonio Pich. "The Standard Model of Electroweak Interactions". In: (2012). DOI: `10.48550/ARXIV.1201.0537`. URL: `https://arxiv.org/abs/1201.0537`.

[5] N. G. Cooper. "Los Alamos Science, Number 25 – 1997: Celebrating the neutrino". In: (Dec. 1997). DOI: `10.2172/569122`. URL: `https://www.osti.gov/biblio/569122`.

[6] *Convention for the establishment of a European organization for nuclear research: Paris, 1st July, 1953 : as amended. Convention pour l'établissement d'une Organisation européenne pour la Recherche nucléaire. Paris, le 1er juillet 1953 : telle qu'elle a été modifiée.* Geneva: CERN, 1971. URL: `https://cds.cern.ch/record/330625`.

[7] Fabienne Marcastel. "CERN's Accelerator Complex. La chaîne des accélérateurs du CERN". In: (2013). General Photo. URL: `https://cds.cern.ch/record/1621583`.

[8] Lyndon Evans and Philip Bryant. "LHC Machine". In: *Journal of Instrumentation* 3.08 (Aug. 2008), S08001. DOI: `10.1088/1748-0221/3/08/S08001`. URL: `https://dx.doi.org/10.1088/1748-0221/3/08/S08001`.

[9] Michael Benedikt and R Garoby. "High Brightness Proton Beams for LHC: Needs and Means". In: (2005). DOI: `10.5170/CERN-2005-006.203`. URL: `https://cds.cern.ch/record/815739`.

[10] B G Taylor. "Timing distribution at the LHC". In: (2002). DOI: `10.5170/CERN-2002-003.63`. URL: `https://cds.cern.ch/record/592719`.

[11] The ALICE Collaboration and K Aamodt et al. "The ALICE experiment at the CERN LHC". In: *Journal of Instrumentation* 3.08 (Aug. 2008), S08002. DOI: 10.1088/1748-0221/3/08/S08002. URL: https://dx.doi.org/10.1088/1748-0221/3/08/S08002.

[12] The ATLAS Collaboration and G Aad et al. "The ATLAS Experiment at the CERN Large Hadron Collider". In: *Journal of Instrumentation* 3.08 (Aug. 2008), S08003. DOI: 10.1088/1748-0221/3/08/S08003. URL: https://dx.doi.org/10.1088/1748-0221/3/08/S08003.

[13] The CMS Collaboration and S Chatrchyan et al. "The CMS experiment at the CERN LHC". In: *Journal of Instrumentation* 3.08 (Aug. 2008), S08004. DOI: 10.1088/1748-0221/3/08/S08004. URL: https://dx.doi.org/10.1088/1748-0221/3/08/S08004.

[14] The LHCb Collaboration and A Augusto Alves Jr et al. "The LHCb Detector at the LHC". In: *Journal of Instrumentation* 3.08 (Aug. 2008), S08005. DOI: 10.1088/1748-0221/3/08/S08005. URL: https://dx.doi.org/10.1088/1748-0221/3/08/S08005.

[15] CERN. *Luminosity Sceanrios of HL-LHC*. URL: http://lhc-commissioning.web.cern.ch/schedule/images/2023/rampup_2022_YETS19weeks_2p.pdf (visited on 05/22/2023).

[16] O. et al. Aberle. *High-Luminosity Large Hadron Collider (HL-LHC): Technical design report*. CERN Yellow Reports: Monographs. Geneva: CERN, 2020. DOI: 10.23731/CYRM-2020-0010. URL: https://cds.cern.ch/record/2749422.

[17] Burkhard Schmidt. "The High-Luminosity upgrade of the LHC: Physics and Technology Challenges for the Accelerator and the Experiments". In: *Journal of Physics: Conference Series* 706.2 (Apr. 2016), p. 022002. DOI: 10.1088/1742-6596/706/2/022002. URL: https://dx.doi.org/10.1088/1742-6596/706/2/022002.

[18] R. L. Workman et al. "Review of Particle Physics". In: *PTEP* 2022 (2022), p. 083C01. DOI: 10.1093/ptep/ptac097.

[19] "56 - ON THE ENERGY LOSS OF FAST PARTICLES BY IONISATION". In: *Collected Papers of L.D. Landau*. Ed. by D. TER HAAR. Pergamon, 1965, pp. 417–424. ISBN: 978-0-08-010586-4. DOI: https://doi.org/10.1016/B978-0-08-010586-4.50061-4. URL: https://www.sciencedirect.com/science/article/pii/B9780080105864500614.

[20] Marius M. Halvorsen. *Optimisation of Silicon Pixel Sensors for Timing Applications*. Master's thesis. June 2020.

[21] S Meroli, D Passeri, and L Servoli. "Energy loss measurement for charged particles in very thin silicon layers". In: *Journal of Instrumentation* 6.06 (June 2011), P06013. DOI: 10.1088/1748-0221/6/06/P06013. URL: https://dx.doi.org/10.1088/1748-0221/6/06/P06013.

[22] Norbert Kolanoski Hermann; Wermes. *Teilchendetektoren. Grubdlagen und Anwendungen*. Springer, 2016.

[23] Gerald R. Lynch and Orin I. Dahl. "Approximations to multiple Coulomb scattering". In: *Nuclear Instruments and Methods in Physics Research Section B: Beam Interactions with Materials and Atoms* 58.1 (1991), pp. 6–10. ISSN: 0168-583X. DOI: `https://doi.org/10.1016/0168-583X(91)95671-Y`. URL: `https://www.sciencedirect.com/science/article/pii/0168583X9195671Y`.

[24] Mini Physics. *Band-diagram*. 2010. URL: `https://www.miniphysics.com/wp-content/uploads/2010/12/Band-diagram.png` (visited on 06/14/2023).

[25] S.M. Sze. *Semiconductor Devices: Physics and Technology*. John Wiley & Sons Singapore Pte. Limited, 2012. ISBN: 9780470873670.

[26] Thomas Bergauer. *Grundlagen der Teilchendetektoren*. 2018. URL: `https://www.oeaw.ac.at/fileadmin/Institute/HEPHY/PDF/ausbildung/teilchendetektoren/VO-4-2018-SemiconductorDetectors.pdf` (visited on 06/12/2023).

[27] Zhong He. "Review of the Shockley–Ramo theorem and its application in semiconductor gamma-ray detectors". In: *Nuclear Instruments and Methods in Physics Research Section A: Accelerators, Spectrometers, Detectors and Associated Equipment* 463.1 (2001), pp. 250–267. ISSN: 0168-9002. DOI: `https://doi.org/10.1016/S0168-9002(01)00223-6`. URL: `https://www.sciencedirect.com/science/article/pii/S0168900201002236`.

[28] Peter Svihra. "Developing a Silicon Pixel Detector for the Next Generation LHCb Experiment". Presented 17 Jan 2022. 2021. URL: `https://cds.cern.ch/record/2806219`.

[29] Gabriele Giacomini. "LGAD-Based Silicon Sensors for 4D Detectors". In: *Sensors* 23.4 (2023). ISSN: 1424-8220. DOI: `10.3390/s23042132`. URL: `https://www.mdpi.com/1424-8220/23/4/2132`.

[30] N. Cartiglia et al. "Beam test results of a 16ps timing system based on ultra-fast silicon detectors". In: *Nuclear Instruments and Methods in Physics Research Section A: Accelerators, Spectrometers, Detectors and Associated Equipment* 850 (2017), pp. 83–88. ISSN: 0168-9002. DOI: `https://doi.org/10.1016/j.nima.2017.01.021`. URL: `https://www.sciencedirect.com/science/article/pii/S0168900217300219`.

[31] V.A.K. Temple. "Junction termination extension (JTE), A new technique for increasing avalanche breakdown voltage and controlling surface electric fields in P-N junctions". In: *1977 International Electron Devices Meeting*. 1977, pp. 423–426. DOI: `10.1109/IEDM.1977.189277`.

[32] S.I. Parker, C.J. Kenney, and J. Segal. "3D — A proposed new architecture for solid-state radiation detectors". In: *Nuclear Instruments and Methods in Physics Research Section A: Accelerators, Spectrometers, Detectors and Associated Equipment* 395.3 (1997). Proceedings of the Third International Workshop on Semiconductor Pixel Detectors for Particles and X-rays, pp. 328–343. ISSN: 0168-9002. DOI: `https://doi.org/10.1016/`

S0168-9002(97)00694-3. URL: `https://www.sciencedirect.com/science/article/pii/S0168900297006943`.

[33] Nicole Apadula et al. *Monolithic Active Pixel Sensors on CMOS technologies.* 2022. arXiv: `2203.07626 [physics.ins-det]`.

[34] V A.J. Van Lint et al. "Mechanisms of radiation effects in electronic materials. Vol. 1". In: (Jan. 1980). URL: `https://www.osti.gov/biblio/6854931`.

[35] Felix Wizemann. "Temperature Scaling of Leakage Current in Irradiated Silicon Sensors". PhD thesis. Tech. U., Dortmund (main), 2019. DOI: `10.17877/DE290R-20491`.

[36] L. Rossi et al. *Pixel Detectors. From Fundamentals to Applications.* Heidelberg: Springer Berlin, 2006.

[37] Michael Moll. "Radiation damage in silicon particle detectors: Microscopic defects and macroscopic properties". Ph.D. Thesis (Advisor: G. Lindstrom); Dissertation, Universität Hamburg, 1999. Dissertation. Universität Hamburg, 1999, p. 251. DOI: `10.3204/PUBDB-2016-02525`. URL: `https://bib-pubdb1.desy.de/record/300958`.

[38] A. Vasilescu RD50 Collaboration and G. Lindstroem. *Displacement damage in silicon.* 2023. URL: `https://rd50.web.cern.ch/niel/`.

[39] Michael Moll. "Displacement Damage in Silicon Detectors for High Energy Physics". In: *IEEE Transactions on Nuclear Science* 65.8 (2018), pp. 1561–1582. DOI: `10.1109/TNS.2018.2819506`.

[40] G Kramberger et al. "Modeling of electric field in silicon micro-strip detectors irradiated with neutrons and pions". In: *JINST* 9.10 (2014), P10016. DOI: `10.1088/1748-0221/9/10/P10016`. URL: `https://cds.cern.ch/record/2634242`.

[41] V. Chiochia et al. "Simulation of heavily irradiated silicon pixel sensors and comparison with test beam measurements". In: *IEEE Transactions on Nuclear Science* 52.4 (2005), pp. 1067–1075. DOI: `10.1109/TNS.2005.852748`.

[42] Christian Elsässer. $\bar{b}b$ *production angle plots.* URL: `%7Bhttps://lhcb.web.cern.ch/lhcb/speakersbureau/html/bb%5C_ProductionAngles.html%7D%7Bhttps://lhcb.web.cern.ch/lhcb/speakersbureau/html/bb%5C_ProductionAngles.html%7D` (visited on 12/13/2022).

[43] Reyes Alemany-Fernandez, Fabio Follin, and Richard Jacobsson. "The LHCb Online Luminosity Control and Monitoring". In: *4th International Particle Accelerator Conference.* 2013, TUPFI010.

[44] B. Muratori and T. Pieloni. "Luminosity levelling techniques for the LHC". In: (2014). Comments: 5 pages, contribution to the ICFA Mini-Workshop on Beam-Beam Effects in Hadron Colliders, CERN, Geneva, Switzerland, 18-22 Mar 2013, pp. 177–181. DOI:

10.5170/CERN-2014-004.177. arXiv: 1410.5646. URL: https://cds.cern.ch/record/1957033.

[45] Paula Collins. *Radiation Damage in LHCb VELO*. URL: https://indico.cern.ch/event/663851/contributions/2711526/attachments/1561115/2457785/radddam_paula_RD50_31.pdf.

[46] LHCb Collaboration and CMS Collaboration. "Observation of the rare Bs0 → μ+μ-decay from the combined analysis of CMS and LHCb data". In: *Nature* 522.7554 (May 2015), pp. 68–72. DOI: 10.1038/nature14474. URL: https://doi.org/10.1038%2Fnature14474.

[47] LHCb Collaboration. "Measurement of the $B_s^0 \to \mu^+\mu^-$ Branching Fraction and Search for $B^0 \to \mu^+\mu^-$ Decays at the LHCb Experiment". In: *Phys. Rev. Lett.* 111 (10 Sept. 2013), p. 101805. DOI: 10.1103/PhysRevLett.111.101805. URL: https://link.aps.org/doi/10.1103/PhysRevLett.111.101805.

[48] LHCb Collaboration. "Measurement of the CP-Violating Phase ϕ_s in the Decay $B_s^0 \to J/\psi\phi$". In: *Phys. Rev. Lett.* 108 (10 Mar. 2012), p. 101803. DOI: 10.1103/PhysRevLett.108.101803. URL: https://link.aps.org/doi/10.1103/PhysRevLett.108.101803.

[49] Federico Betti. *Observation of CP violation in charm decays at LHCb*. 2019. arXiv: 1905.05428 [hep-ex].

[50] LHCb Collaboration. "Observation of $J/\psi p$ Resonances Consistent with Pentaquark States in $\Lambda_b^0 \to J/\psi K^- p$ Decays". In: *Phys. Rev. Lett.* 115 (7 Aug. 2015), p. 072001. DOI: 10.1103/PhysRevLett.115.072001. URL: https://link.aps.org/doi/10.1103/PhysRevLett.115.072001.

[51] LHCb Collaboration. "Model-Independent Study of Structure in $B^+ \to D^+ D^- K^+$ Decays". In: *Phys. Rev. Lett.* 125 (24 Dec. 2020), p. 242001. DOI: 10.1103/PhysRevLett.125.242001. URL: https://link.aps.org/doi/10.1103/PhysRevLett.125.242001.

[52] LHCb collaboration and R. Aaij et al. *The LHCb upgrade I*. 2023. arXiv: 2305.10515 [hep-ex].

[53] *Letter of Intent for the LHCb Upgrade*. Tech. rep. Geneva: CERN, 2011. URL: http://cds.cern.ch/record/1333091.

[54] LHCb Collaboration. *Framework TDR for the LHCb Upgrade: Technical Design Report*. Tech. rep. 2012. URL: https://cds.cern.ch/record/1443882.

[55] LHCb Collaboration. *LHCb VELO Upgrade Technical Design Report*. Tech. rep. CERN-LHCC-2013-021. LHCB-TDR-013. Nov. 2013. URL: https://cds.cern.ch/record/1624070.

[56] LHCb Experiment LHCb Collaboration. *Future physics potential of LHCb*. Tech. rep. Geneva: CERN, 2022. URL: https://cds.cern.ch/record/2806113.

[57]   LHCb Collaboration. *LHCb magnet: Technical Design Report*. Technical design report. LHCb. Geneva: CERN, 2000. URL: `https://cds.cern.ch/record/424338`.

[58]   LHCb Collaboration. *LHCb Tracker Upgrade Technical Design Report*. Tech. rep. 2014. URL: `https://cds.cern.ch/record/1647400`.

[59]   "LHCb detector performance". In: *International Journal of Modern Physics A* 30.07 (Mar. 2015), p. 1530022. DOI: 10.1142/s0217751x15300227. URL: `https://doi.org/10.1142%2Fs0217751x15300227`.

[60]   LHCb Collaboration. *LHCb reoptimized detector design and performance: Technical Design Report*. Technical design report. LHCb. Geneva: CERN, 2003. URL: `https://cds.cern.ch/record/630827`.

[61]   Gianluigi Casse et al. "Evidence of enhanced signal response at high bias voltages in planar silicon detectors irradiated up to 2.2×1016neqcm-2". In: *Nuclear Instruments and Methods in Physics Research Section A: Accelerators, Spectrometers, Detectors and Associated Equipment* 636.1, Supplement (2011). 7th International ""Hiroshima"" Symposium on the Development and Application of Semiconductor Tracking Detectors, S56–S61. ISSN: 0168-9002. DOI: `https://doi.org/10.1016/j.nima.2010.04.085`. URL: `https://www.sciencedirect.com/science/article/pii/S0168900210009393`.

[62]   T. Poikela et al. "VeloPix: the pixel ASIC for the LHCb upgrade". In: *Journal of Instrumentation* 10.01 (Jan. 2015), p. C01057. DOI: 10.1088/1748-0221/10/01/C01057. URL: `https://dx.doi.org/10.1088/1748-0221/10/01/C01057`.

[63]   Peter Svihra. "The Design and Construction of LHCb VELO Upgrades Modules". In: (2019). Poster-2020-1041. DOI: 10.1109/NSS/MIC42101.2019.9059693. URL: `https://cds.cern.ch/record/2727215`.

[64]   LHCb Collaboration. "Microchannel cooling for the LHCb VELO Upgrade I". In: *Nuclear Instruments and Methods in Physics Research Section A: Accelerators, Spectrometers, Detectors and Associated Equipment* 1039 (2022), p. 166874. ISSN: 0168-9002. DOI: `https://doi.org/10.1016/j.nima.2022.166874`. URL: `https://www.sciencedirect.com/science/article/pii/S0168900222003394`.

[65]   "The LHCb Upgrade I". In: (2022). For submission to: JINST; Contact authors: Giovanni Passaleva, Massimiliano Ferro-Luzzi; Reviewers: (chair), , John Walsh (EB); DP-2022-002, ; Institutes: Barcelona, Spain. PNPI, Gatchina, Russia. Bristol, United Kingdom. Zurich, Switzerland. MISIS, Russia. Cagliari, Italy.. URL: `https://cds.cern.ch/record/2836445`.

[66]   Oscar Augusto de Aguiar Francisco et al. "Microchannel cooling for the LHCb VELO Upgrade I". In: *Nuclear Instruments and Methods in Physics Research Section A: Accelerators, Spectrometers, Detectors and Associated Equipment* 1039 (Sept. 2022), p. 166874.

DOI: `10.1016/j.nima.2022.166874`. URL: `https://doi.org/10.1016%2Fj.nima.2022.166874`.

[67] Freek Sanders. *x section of VELO Upgrade Detector*. URL: `%7Bhttps://lbtwiki.cern.ch/bin/view/VELO/VeloUpgradePresentationMaterial#General_plots_about_upgrade%7D` (visited on 05/02/2023).

[68] Freek Sanders. "Velo RF foil installation. Forum on Tracking Detector Mechanics". In: (2021). URL: `https://cds.cern.ch/record/2770596`.

[69] Ina Carli. "Upstream Tracker - The silicon strip tracking detector for the LHCb Upgrade". In: *PoS* ICHEP2020 (2021), p. 724. DOI: `10.22323/1.390.0724`. URL: `https://cds.cern.ch/record/2783293`.

[70] Sz. Bugiel et al. "SALT, a dedicated readout chip for high precision tracking silicon strip detectors at the LHCb Upgrade". In: *Journal of Instrumentation* 11.02 (Feb. 2016), p. C02028. DOI: `10.1088/1748-0221/11/02/C02028`. URL: `https://dx.doi.org/10.1088/1748-0221/11/02/C02028`.

[71] A.B.R. Cavalcante et al. "Refining and testing 12,000 km of scintillating plastic fibre for the LHCb SciFi tracker". In: *Journal of Instrumentation* 13.10 (Oct. 2018), P10025. DOI: `10.1088/1748-0221/13/10/P10025`. URL: `https://dx.doi.org/10.1088/1748-0221/13/10/P10025`.

[72] Olivier Girard et al. *Characterisation of silicon photomultipliers based on statistical analysis of pulse-shape and time distributions*. 2018. arXiv: `1808.05775` `[physics.ins-det]`.

[73] A Massafferri. "SciFi, the new Tracker of the LHCb experiment". In: *JINST* 15.08 (2020), p. C08006. DOI: `10.1088/1748-0221/15/08/C08006`. URL: `http://cds.cern.ch/record/2749158`.

[74] LHCb Collaboration. *LHCb calorimeters: Technical Design Report*. Technical design report. LHCb. Geneva: CERN, 2000. URL: `https://cds.cern.ch/record/494264`.

[75] LHCb Collaboration. *LHCb PID Upgrade Technical Design Report*. Tech. rep. 2013. URL: `https://cds.cern.ch/record/1624074`.

[76] LHCb Collaboration. *LHCb RICH: Technical Design Report*. Technical design report. LHCb. Geneva: CERN, 2000. URL: `https://cds.cern.ch/record/494263`.

[77] Ayan Batyrkhanov. "MaPMT Relative Efficiency Measurements for the LHCb RICH Upgrade". In: *JPS Conf. Proc.* 27 (2019), p. 012004. DOI: `10.7566/JPSCP.27.012004`. URL: `https://cds.cern.ch/record/2727527`.

[78] Massimiliano Fiorini. "The upgrade of the LHCb RICH detectors". In: *Nuclear Instruments and Methods in Physics Research Section A: Accelerators, Spectrometers, Detectors and Associated Equipment* 952 (2020). 10th International Workshop on Ring Imaging Cherenkov Detectors (RICH 2018), p. 161688. ISSN: 0168-9002. DOI: `https://doi.`

org/10.1016/j.nima.2018.12.003. URL: https://www.sciencedirect.com/science/article/pii/S0168900218318011.

[79] R Djeliadine, O Iouchtchenko, and V F Obraztsov. *LHCb hadron trigger and Hcal cell size and length optimization.* Tech. rep. Geneva: CERN, 1999. URL: https://cds.cern.ch/record/691688.

[80] LHCb Collaboration. *Expression of Interest for a Phase-II LHCb Upgrade: Opportunities in flavour physics, and beyond, in the HL-LHC era.* Tech. rep. Geneva: CERN, 2017. URL: https://cds.cern.ch/record/2244311.

[81] CERN (Meyrin) LHCb Collaboration. *Framework TDR for the LHCb Upgrade II - Opportunities in flavour physics, and beyond, in the HL-LHC era*. Tech. rep. Geneva: CERN, 2021. URL: https://cds.cern.ch/record/2776420.

[82] LHCb Collaboration. *Considerations for the VELO detector at the LHCb Upgrade II.* Tech. rep. LHCb-PUB-2022-001, CERN-LHCb-PUB-2022-001. 2022.

[83] LHCb Collaboration. *Physics case for an LHCb Upgrade II - Opportunities in flavour physics, and beyond, in the HL-LHC era.* Tech. rep. LHCB-PUB-2018-009, CERN-LHCC-2018-027, LHCC-G-171. 2016.

[84] A. Doblas et al. *Inverse Low Gain Avalanche Detector (iLGAD) Periphery Design for X-Ray Applications.* 2022. arXiv: 2202.01552 [physics.ins-det].

[85] S. Ayyoub et al. *A new approach to achieving high granularity for silicon diode detectors with impact ionization gain.* 2021. arXiv: 2101.00511 [physics.ins-det].

[86] G. Paternoster et al. "Trench-Isolated Low Gain Avalanche Diodes (TI-LGADs)". In: *IEEE Electron Device Letters* 41.6 (2020), pp. 884–887. DOI: 10.1109/LED.2020.2991351.

[87] L. Castillo García et al. "Characterization of Irradiated Boron, Carbon-Enriched and Gallium Si-on-Si Wafer Low Gain Avalanche Detectors". In: *Instruments* 6.1 (2022). ISSN: 2410-390X. DOI: 10.3390/instruments6010002. URL: https://www.mdpi.com/2410-390X/6/1/2.

[88] E. L. Gkougkousis. *Parametric process optimization for Indium, Gallium and Boron dopants using TCAD simulation modeling.* 16th Trento Workshop on Advanced Silicon Radiation Detectors. 2021. URL: https://indico.cern.ch/event/983068/contributions/4223170/.

[89] G. Dalla Betta and M. Povoli. "Progress in 3D Silicon Radiation Detectors". In: *Front. in Phys.* 10 (2022), p. 927690. DOI: 10.3389/fphy.2022.927690.

[90] Markus Piller et al. "Generic Analog 8 Bit DAC IP Block in 28nm CMOS for the High Energy Physics Community". In: *2022 Austrochip Workshop on Microelectronics (Austrochip).* 2022, pp. 5–8. DOI: 10.1109/Austrochip56145.2022.9940783.

[91] L. Piccolo et al. "First measurements on the Timespot1 ASIC: a fast-timing, high-rate pixel-matrix front-end". In: *Journal of Instrumentation* 17.03 (Mar. 2022), p. C03022. DOI: `10.1088/1748-0221/17/03/c03022`. URL: `https://doi.org/10.1088/1748-0221/17/03/c03022`.

[92] Neville Harnew et al. "TORCH: a large area time-of-flight detector for particle identification". In: *Nucl. Instrum. Methods Phys. Res., A* 936 (2019), pp. 595–597. DOI: `10.1016/j.nima.2018.10.099`. arXiv: `1810.06658`. URL: `https://cds.cern.ch/record/2645864`.

[93] Peter Jenni et al. *The high resolution spaghetti hadron calorimeter: proposal.* Tech. rep. Geneva: CERN, 1987. URL: `https://cds.cern.ch/record/181281`.

[94] Michael Thomas Alexander. "Constraints on Mixing and CP-Violation in the Neutral Charmed Meson System at LHCb". Presented 06 Jul 2012. 2012. URL: `http://cds.cern.ch/record/1494111`.

[95] Markus Frank et al. *AIDASoft/DD4hep.* webpage: http://dd4hep.cern.ch/. Oct. 2018. DOI: `10.5281/zenodo.592244`. URL: `https://doi.org/10.5281/zenodo.592244`.

[96] M Frank et al. "DD4hep: A Detector Description Toolkit for High Energy Physics Experiments". In: *Journal of Physics: Conference Series* 513.2 (June 2014), p. 022010. DOI: `10.1088/1742-6596/513/2/022010`. URL: `https://dx.doi.org/10.1088/1742-6596/513/2/022010`.

[97] M Clemencic et al. "The LHCb Simulation Application, Gauss: Design, Evolution and Experience". In: *Journal of Physics: Conference Series* 331.3 (Dec. 2011), p. 032023. DOI: `10.1088/1742-6596/331/3/032023`. URL: `https://dx.doi.org/10.1088/1742-6596/331/3/032023`.

[98] Michał Mazurek, Marco Clemencic, and Gloria Corti. "Gauss and Gaussino: the LHCb simulation software and its new experiment agnostic core framework". In: *PoS* ICHEP2022 (Nov. 2022), p. 225. DOI: `10.22323/1.414.0225`.

[99] S. Agostinelli et al. "Geant4—a simulation toolkit". In: *Nuclear Instruments and Methods in Physics Research Section A: Accelerators, Spectrometers, Detectors and Associated Equipment* 506.3 (2003), pp. 250–303. ISSN: 0168-9002. DOI: `https://doi.org/10.1016/S0168-9002(03)01368-8`. URL: `https://www.sciencedirect.com/science/article/pii/S0168900203013688`.

[100] R. Frühwirth. "Application of Kalman filtering to track and vertex fitting". In: *Nuclear Instruments and Methods in Physics Research Section A: Accelerators, Spectrometers, Detectors and Associated Equipment* 262.2 (1987), pp. 444–450. ISSN: 0168-9002. DOI: `https://doi.org/10.1016/0168-9002(87)90887-4`. URL: `https://www.sciencedirect.com/science/article/pii/0168900287908874`.

[101] Giovanni Passaleva. "Status and highlights from the LHCb experiment". In: (2018). URL: https://cds.cern.ch/record/2633797.

[102] A.Mihul M.Pentia G.Iorgovan. *Multiple Scattering Error Propagation in Particle Track Reconstruction.* June 1994. URL: https://arxiv.org/pdf/hep-ex/9406006.pdf.

[103] Thomas Bird et al. *VELO upgrade studies and layout optimisations.* Tech. rep. Geneva: CERN, Nov. 2014. URL: https://cds.cern.ch/record/1968565.

[104] Nicolas Mounet. "The LHC Transverse Coupled-Bunch Instability". Presented 2012. 2012. DOI: 10.5075/epfl-thesis-5305. URL: https://cds.cern.ch/record/1451296.

[105] Roderik Bruce et al. *Parameters for aperture calculations at injection for HL-LHC*.* Tech. rep. CERN-ACC-2016-0328. *Research supported by EU FP7 HiLumi LHC Grant agreement 284404. Geneva: CERN, Feb. 2016. URL: https://cds.cern.ch/record/2237427.

[106] Roderik Bruce et al. *Updated parameters for HL-LHC aperture calculations for proton beams.* Tech. rep. CERN-ACC-2017-0051. Geneva: CERN, July 2017. URL: https://cds.cern.ch/record/2274330.

[107] B. Jayant Baliga. "High-voltage device termination techniques a comparative review". English. In: *IEE Proceedings I (Solid-State and Electron Devices)* 129 (5 Oct. 1982), 173–179(6). ISSN: 0143-7100. URL: https://digital-library.theiet.org/content/journals/10.1049/ip-i-1.1982.0037.

[108] Charles W. Magee, William L. Harrington, and Richard E. Honig. "Secondary ion quadrupole mass spectrometer for depth profiling—design and performance evaluation". In: *Review of Scientific Instruments* 49.4 (1978), pp. 477–485. DOI: 10.1063/1.1135438. eprint: https://doi.org/10.1063/1.1135438. URL: https://doi.org/10.1063/1.1135438.

[109] MultiMedia LLC. *Group d'Etude de la Matière Condensée.* URL: https://www.sciences.uvsq.fr/laboratoire-gemac (visited on 03/10/2023).

[110] Washington State University St. Louis. *Secondary Ion Mass Spectrometer.* URL: https://eps.wustl.edu/sims.

[111] CAMECA. *IMS 7F Brochure.* URL: https://www.cameca.com/-/media/ametekcameca/acameca/download-library/sims/ims-7f-auto/ims-7f-auto_product-brochure.pdf?la (visited on 03/10/2023).

[112] J.W. McDonald et al. "Surface charge compensation for a highly charged ion emission microscope". In: *Ultramicroscopy* 101.2 (2004), pp. 225–229. ISSN: 0304-3991. DOI: https://doi.org/10.1016/j.ultramic.2004.06.008. URL: https://www.sciencedirect.com/science/article/pii/S0304399104001445.

[113] Viktoriia Gorbenko. "Caractérisation par faisceaux d'ions d'hétérostructures III-V pour les applications micro et optoélectroniques". 2015GREAT140. PhD thesis. 2015. URL: http://www.theses.fr/2015GREAT140/document.

[114] Evangelos Gkougkousis. "Background studies on the H→ZZ→4l channel at LHC Run 1. Prospects of the bbH(→γγ) mode and studies for an improved pixel detector system for the ATLAS upgrade towards HL-LHC". PhD thesis. Universite Paris-Saclay, 2016.

[115] Vagelis Gkougkousis. "Detailed process characterization of carbonated LGADs through Secondary Ion Mass Spectroscopy". 17th "Trento" Workshop on Advanced Silicon Radiation Detectors. 2022. URL: https://indico.cern.ch/event/1096847/contributions/4742738/.

[116] Richard C. Jaeger. *Introduction to Microelectronic Fabrication.* USA: Addison-Wesley Longman Publishing Co., Inc., 1987. ISBN: 0201146959.

[117] N. Moffat et al. "Low Gain Avalanche Detectors (LGAD) for particle physics and synchrotron applications". In: *Journal of Instrumentation* 13.03 (Mar. 2018), p. C03014. DOI: 10.1088/1748-0221/13/03/C03014. URL: https://dx.doi.org/10.1088/1748-0221/13/03/C03014.

[118] *6487 Picoammeter Specifications.* Rev. A. Tektronix. Oct. 2002.

[119] Keithley. *Model 6487 Picoammeter Refence Manual.* English. Version Rev D. Keithley. Oct. 28, 2020. 317 pp.

[120] W. Riegler. "An application of extensions of the Ramo–Shockley theorem to signals in silicon sensors". In: *Nuclear Instruments and Methods in Physics Research Section A: Accelerators, Spectrometers, Detectors and Associated Equipment* 940 (2019), pp. 453–461. ISSN: 0168-9002. DOI: https://doi.org/10.1016/j.nima.2019.06.056. URL: https://www.sciencedirect.com/science/article/pii/S0168900219309015.

[121] J. Schwandt and R. Klanner. "On the weighting field of irradiated silicon detectors". In: *Nuclear Instruments and Methods in Physics Research Section A: Accelerators, Spectrometers, Detectors and Associated Equipment* 942 (2019), p. 162418. ISSN: 0168-9002. DOI: https://doi.org/10.1016/j.nima.2019.162418. URL: https://www.sciencedirect.com/science/article/pii/S0168900219309891.

[122] Gabriele Giacomini. "Fabrication of Silicon Sensors Based on Low-Gain Avalanche Diodes". In: *Frontiers in Physics* 9 (Apr. 2021), p. 618621. DOI: 10.3389/fphy.2021.618621.

[123] Wikipedia. *Technology CAD.* 2023. URL: https://en.wikipedia.org/wiki/Technology_CAD.

[124] Synopsys. *Synopsys TCAD.* 2023. URL: https://www.synopsys.com (visited on 03/13/2023).

[125] Helmuth Spieler. *Semiconductor Detector Systems*. Vol. v.12. Semiconductor Science and Technology. Oxford: Oxford University Press, 2005. ISBN: 978-0-19-852784-8.

[126] R. Van Overstraeten and H. De Man. "Measurement of the ionization rates in diffused silicon p-n junctions". In: *Solid-State Electronics* 13.5 (1970), pp. 583–608. ISSN: 0038-1101. DOI: https://doi.org/10.1016/0038-1101(70)90139-5. URL: https://www.sciencedirect.com/science/article/pii/0038110170901395.

[127] A. G. Chynoweth. "Ionization Rates for Electrons and Holes in Silicon". In: *Phys. Rev.* 109 (5 Mar. 1958), pp. 1537–1540. DOI: 10.1103/PhysRev.109.1537. URL: https://link.aps.org/doi/10.1103/PhysRev.109.1537.

[128] Y. Okuto and C.R. Crowell. "Threshold energy effect on avalanche breakdown voltage in semiconductor junctions". In: *Solid-State Electronics* 18.2 (1975), pp. 161–168. ISSN: 0038-1101. DOI: https://doi.org/10.1016/0038-1101(75)90099-4. URL: https://www.sciencedirect.com/science/article/pii/0038110175900994.

[129] Thomas Lackner. "Avalanche multiplication in semiconductors: A modification of Chynoweth's law". In: *Solid-State Electronics* 34.1 (1991), pp. 33–42. ISSN: 0038-1101. DOI: https://doi.org/10.1016/0038-1101(91)90197-7. URL: https://www.sciencedirect.com/science/article/pii/0038110191901977.

[130] S. Reggiani et al. "Electron and hole mobility in silicon at large operating temperatures. I. Bulk mobility". In: *IEEE Transactions on Electron Devices* 49.3 (2002), pp. 490–499. DOI: 10.1109/16.987121.

[131] E. Gnani et al. "Extraction Method for the Impact-Ionization Multiplication Factor in Silicon at Large Operating Temperatures". In: *32nd European Solid-State Device Research Conference*. 2002, pp. 227–230. DOI: 10.1109/ESSDERC.2002.194911.

[132] C. Canali et al. "Electron and hole drift velocity measurements in silicon and their empirical relation to electric field and temperature". In: *IEEE Transactions on Electron Devices* 22.11 (1975), pp. 1045–1047. DOI: 10.1109/T-ED.1975.18267.

[133] D.B.M. Klaassen. "A unified mobility model for device simulation—I. Model equations and concentration dependence". In: *Solid-State Electronics* 35.7 (1992), pp. 953–959. ISSN: 0038-1101. DOI: https://doi.org/10.1016/0038-1101(92)90325-7. URL: https://www.sciencedirect.com/science/article/pii/0038110192903257.

[134] J.W. Slotboom and H.C. de Graaff. "Measurements of bandgap narrowing in Si bipolar transistors". In: *Solid-State Electronics* 19.10 (1976), pp. 857–862. ISSN: 0038-1101. DOI: https://doi.org/10.1016/0038-1101(76)90043-5. URL: https://www.sciencedirect.com/science/article/pii/0038110176900435.

[135] W. Shockley and W. T. Read. "Statistics of the Recombinations of Holes and Electrons". In: *Phys. Rev.* 87 (5 Sept. 1952), pp. 835–842. DOI: 10.1103/PhysRev.87.835. URL: https://link.aps.org/doi/10.1103/PhysRev.87.835.

[136]   JSI. *Mark II Triga Reactor, Properties of Irradiation Channels*. 2021. URL: `https://ric.ijs.si/en/info-za-uporabnike/lastnosti-obsevalnih-kanalov/` (visited on 03/15/2023).

[137]   I. Mandić et al. "Measurements with silicon detectors at extreme neutron fluences". In: *Journal of Instrumentation* 15.11 (Nov. 2020), P11018–P11018. DOI: 10.1088/1748-0221/15/11/p11018. URL: `https://doi.org/10.1088%2F1748-0221%2F15%2F11%2Fp11018`.

[138]   Paolo Fessiaa. *The new 3D printing facility at the CERN polymer lab*. 2013. URL: `https://indico.cern.ch/event/271447/` (visited on 03/15/2023).

[139]   Eloi Pazos Rial. "Electrical Characterization of Irradaited Silicon Planar Sensors". MA thesis. Universidade de Santiago de Compostela, July 2023.

[140]   Arianna Morozzi et al. "TCAD advanced radiation damage modeling in silicon detectors". In: *PoS* Vertex2019 (2020), p. 050. DOI: 10.22323/1.373.0050.

[141]   Å. Folkestad et al. "Development of a silicon bulk radiation damage model for Sentaurus TCAD". In: *Nuclear Instruments and Methods in Physics Research Section A: Accelerators, Spectrometers, Detectors and Associated Equipment* 874 (2017), pp. 94–102. ISSN: 0168-9002. DOI: `https://doi.org/10.1016/j.nima.2017.08.042`. URL: `https://www.sciencedirect.com/science/article/pii/S0168900217309282`.

[142]   Joern Schwandt et al. *A new model for the TCAD simulation of the silicon damage by high fluence proton irradiation*. 2019. arXiv: `1904.10234 [physics.ins-det]`.

[143]   G.A.M. Hurkx, D.B.M. Klaassen, and M.P.G. Knuvers. "A new recombination model for device simulation including tunneling". In: *IEEE Transactions on Electron Devices* 39.2 (1992), pp. 331–338. DOI: 10.1109/16.121690.

[144]   E. L. Gkougkousis. *End of Life Radiation damage estimation for Velo*. URL: `%7Bhttps://indico.cern.ch/event/1253808/contributions/5288453/attachments/2600826/4491105/LHCbWeek%20_VeloRadDamage.pdf%7D`.

[145]   G. Kramberger et al. "Radiation effects in Low Gain Avalanche Detectors after hadron irradiations". In: *Journal of Instrumentation* 10.07 (July 2015), P07006. DOI: 10.1088/1748-0221/10/07/P07006. URL: `https://dx.doi.org/10.1088/1748-0221/10/07/P07006`.

[146]   E - L Gkougkousis et al. "Comprehensive technology study of radiation hard LGADs". In: *Journal of Physics: Conference Series* 2374.1 (Nov. 2022), p. 012175. DOI: 10.1088/1742-6596/2374/1/012175. URL: `https://dx.doi.org/10.1088/1742-6596/2374/1/012175`.

[147]   Katharina Kaska. "Characterization of radiation damage in detectors made from different silicon materials". PhD thesis. Technische Universität Wien, Nov. 2014.

[148]   P. D. de Almeid. "Measurement of the acceptor removal rate in silicon pad diodes". 30th RD50 Workshop. 2017. URL: https://indico.cern.ch/event/637212/contributions/2608666/attachments/1471954/2355527/Acceptor_Removal_Measurements_-_RD50_2.pdf.

[149]   Michael Moll. "Acceptor removal - Displacement damage effects involving the shallow acceptor doping of p-type silicon devices". In: *PoS* Vertex2019 (2020), p. 027. DOI: 10.22323/1.373.0027. URL: https://cds.cern.ch/record/2747752.

[150]   Patrick Asenov et al. "TCAD modeling of bulk radiation damage effects in silicon devices with the Perugia radiation damage model". In: *Nuclear Instruments and Methods in Physics Research Section A: Accelerators, Spectrometers, Detectors and Associated Equipment* 1040 (2022), p. 167180. ISSN: 0168-9002. DOI: https://doi.org/10.1016/j.nima.2022.167180. URL: https://www.sciencedirect.com/science/article/pii/S0168900222005459.

[151]   Arianna Morozzi et al. "TCAD Modeling of Surface Radiation Damage Effects: A State-Of-The-Art Review". In: *Frontiers in Physics* 9 (Feb. 2021). DOI: 10.3389/fphy.2021.617322.

[152]   Moritz Wiehe et al. "Measurements of the reverse current of highly irradiated silicon sensors to determine the effective energy and current related damage rate". In: *Nucl. Instrum. Methods Phys. Res., A* 877 (2018), pp. 51–55. DOI: 10.1016/j.nima.2017.09.021. URL: https://cds.cern.ch/record/2294507.

[153]   A Chilingarov. "Temperature dependence of the current generated in Si bulk". In: *Journal of Instrumentation* 8.10 (Oct. 2013), P10003. DOI: 10.1088/1748-0221/8/10/P10003. URL: https://dx.doi.org/10.1088/1748-0221/8/10/P10003.

[154]   ATLAS Collaboration. "Modelling radiation damage to pixel sensors in the ATLAS detector". In: *Journal of Instrumentation* 14.06 (June 2019), P06012–P06012. DOI: 10.1088/1748-0221/14/06/p06012. URL: https://doi.org/10.1088%2F1748-0221%2F14%2F06%2Fp06012.

[155]   Vagelis Gkougkousis. *UCSC single channel readout board*. URL: %7B%5Chref%7Bhttps://twiki.cern.ch/twiki/bin/view/Main/UcscSingleChannel%7D%7D (visited on 07/26/2023).

[156]   I. Rubinskiy. "An EUDET/AIDA Pixel Beam Telescope for Detector Development". In: *Physics Procedia* 37 (2012). Proceedings of the 2nd International Conference on Technology and Instrumentation in Particle Physics (TIPP 2011), pp. 923–931. ISSN: 1875-3892. DOI: https://doi.org/10.1016/j.phpro.2012.02.434. URL: https://www.sciencedirect.com/science/article/pii/S1875389212017889.

[157]   A. Kravchenko and H. Jansen. *MIMOSA26 sensor*. URL: https://twiki.cern.ch/twiki/bin/view/MimosaTelescope/MIMOSA26 (visited on 08/02/2023).

[158] M. Garcia-Sciveres et al. "The FE-I4 pixel readout integrated circuit". In: *Nuclear Instruments and Methods in Physics Research Section A: Accelerators, Spectrometers, Detectors and Associated Equipment* 636.1, Supplement (2011). 7th International ""Hiroshima"" Symposium on the Development and Application of Semiconductor Tracking Detectors, S155–S159. ISSN: 0168-9002. DOI: https://doi.org/10.1016/j.nima.2010.04.101. URL: https://www.sciencedirect.com/science/article/pii/S0168900210009551.

[159] Heinrich Schindler. *Garfield++*. URL: %7Bhttps://garfieldpp.web.cern.ch/garfieldpp/%7D (visited on 07/26/2023).